INVESTIGATION OF SHEAR CONNECTION SYSTEMS FOR PARTIALLY COMPOSITE INSULATED CONCRETE AND DOUBLE WYTHE CAVITY MASONRY WALLS

by

Benedict Nosazemen Egbon

A thesis submitted in partial fulfillment of the requirements for the degree of

Doctor of Philosophy

in

STRUCTURAL ENGINEERING

Department of Civil and Environmental Engineering
University of Alberta

ABSTRACT

Insulated concrete and double wythe cavity masonry walls are commonly used on building exteriors. Both wall types consist of inner and outer layers known as wythes, which surround an insulation layer, and these wythes are joined by mechanical devices known as shear connectors. In insulated concrete walls the inner and outer wythes are made entirely of concrete while that of double wythe cavity masonry walls are mostly made of bricks and Concrete Masonry Units, respectively. Overall, the structural performance of both walls is largely influenced by the shear connection system, and existing shear connection systems are currently being challenged by larger insulation thicknesses needed to meet stricter energy requirements. At the core of these changes to the thermal requirement for building envelopes, the structural load on walls such as the dead and live load are relatively unchanged, which means innovative considerations on how the load is transferred through the walls must be made. These innovative considerations, such as new shear connection mechanisms often create additional composite action in walls. Experimental, finite element, and analytical approaches can be used to quantify the amount of composite action developed in the walls, but existing approaches are cumbersome or limited to only uncracked conditions.

This thesis presents a study focused on increasing composite action using new shear connection mechanisms as well as developing a unified analytical model to analyze the behaviour of partially composite insulated and double wythe cavity masonry walls. While both walls are similar in composition, double wythe cavity masonry walls are not completely sandwiched due to an air gap that allows for moisture drainage. This airgap is absent in insulated concrete walls due to superior moisture resistance. This means different methods have to be developed to improve the shear connection system for both walls. Rectangular and trapezoidal notches were created in different insulation types and used along with inclined GFRP connectors to improve the shear connection strength in insulated concrete walls, while a novel inclined connector was developed at the University of Alberta for double wythe cavity masonry walls. Small-scale longitudinal shear

testing was executed for both shear connection systems, and the notches increased the shear connection strength by as much as 50%, with the rectangular notch shown to be more effective due to proper locking mechanism with the insulation. Meanwhile, the inclined novel masonry connector proffered larger shear strength per connector cross-sectional area than existing traditional plate connectors, in some cases up to 212%.

To compliment experimental tests, analytical expressions were developed to predict the strength of the shear connection schemes. A simplified analytical model was developed to predict the load-deflection response of both walls under flexural loading and more importantly, the amount of composite action generated by such shear connection mechanisms in full-scale walls. The analytical model was validated with experimental tests from literature, with an average test to predicted strength ratio of 0.94 with a coefficient of variation (COV) of 0.18 for insulated concrete walls. For double wythe cavity masonry walls, this ratio was 0.72 with a COV of 0.29. Among other factors examined along with the shear connection schemes in full-scale walls, the shear connector inclination and spacing influenced the degree of composite to a larger extent than others.

PREFACE

This thesis is the original work of Benedict Nosazemen Egbon, executed under the supervision of Dr. Douglas Tomlinson. From this research, three journal papers and two conference papers have been published to date. The publications are listed below.

Journal Papers

1. **Egbon, B.** and Tomlinson, D. (2021). "Experimental investigation of longitudinal shear transfer in insulated concrete wall panels with notched insulation. "*Journal of Building Engineering*, **43**(103173). https://doi.org/https://doi.org/10.1016/j.jobe.2021.103173
2. **Egbon, B.,** and Tomlinson, D. (2024). Simplified load-deflection analytical model for partially composite insulated concrete wall panels under flexural loading. *Engineering Structures*, **304** (117637). https://doi.org/10.1016/j.engstruct.2024.117637
3. **Egbon, B.,** Baron-Bello, L., Cruz, C., and Tomlinson, D. (2024). Experimental Longitudinal Shear Testing of Novel and Traditional Shear Connectors in Double-Wythe Cavity Masonry Walls. Engineering Structures, **305** (117745). https://doi.org/10.1016/j.engstruct.2024.117745

Conference Papers

1. **Egbon, B.** and Tomlinson, D. (2023). "Structural Evaluation of Notched Insulation in Precast Concrete Sandwich Panels." In: Walbridge, S., et al. Proceedings of the Canadian Society of Civil Engineering Annual Conference 2021. CSCE 2021. Lecture Notes in Civil Engineering, vol 241. Springer, Singapore. https://doi.org/10.1007/978-981-19-0511-7_25
2. Baron-Bello, L., **Egbon, B.**, Cruz, C., Tomlinson, D. (2023). "Longitudinal shear resistance of steel plate connectors in masonry cavity walls". In 14th National Masonry Conference. TMS.

ACKNOWLEDGEMENTS

Firstly, I want to thank my Lord and Saviour, Jesus Christ, for his help and strength during my years of study. Indeed, ***For the Lord giveth wisdom: out of his mouth cometh knowledge and understanding (Proverbs 2 vs 6).***

I want to thank my first teachers in life, my parents, Mr. Vincent Egbon (Epa 1.) and Barr. Mrs. Veronica Egbon, for giving me the essentials of life. I would not be here today without them. Though we were not rich you always taught me the virtue of hard work and satisfaction (***Philippians 4:12***), which have helped form my perspectives in life. I still remember my father (who always wanted me to be a medical doctor) shouting *time-time* while me and my siblings got ready for school as kids, and mum reading throughout the night while she studied to be a Lawyer. Indeed, they were setting me up for the future. To my grand father who is still going strong at the age of 102, I thank you for your obsession with education, which was transferred to my mother. I cannot forget your sacrifice in providing us with your car (your beloved *Benz 230*) to ride to school.

Special thanks to my wife, Benedicta Egbon, for her sacrifice, encouragement, and support throughout my program. Above all, I want to also thank her for bearing my daughters, Ariadne Egbon (***mi love***), Alicia Egbon (***my love***), Katarina Egbon (***moya lyubov***), and maybe more later. To my children and descendants, I hope that my achieving this milestone will encourage you to accomplish greater things. A Ph.D. must be the minimum standard and achievement for you all.

My sincere gratitude to my supervisor, **Dr. Douglas George Tomlinson**, for agreeing to accept and nurture me as a researcher with patience and grace during my program. Dr. Tomlinson is always generous with his time and thoughts, even those which are sometimes framed as *any way that's just a separate thing*. Most importantly, his red lines of correction always improved my work. I also want to thank **Dr. Ying Hei Chui**, **Dr. Carlos "Lobo" Cruz-Noguez, Dr. Mustafa Gül**, **and Dr. Robert Driver** for their insight and feedback during my program.

I want to also thank Greg Miller and Cameron West at the I. F. MORRISON Structures Laboratory. They developed and made significant improvements to my project setups, and I am grateful. Also, a big thank you to other students in the Tomlison research group, Ambar, Helmi, Sergio (power play), Brittney, Danny, Abdullah, Arnold, and Raphael, for their assistance during the concrete pour.

My sincere appreciation to Dr. Mark Hagel and Monica Guzman, for their immense contribution to my masonry work plan. The Zoom meetings I had with them were always rich with information and they helped to implant invaluable industry perspective to my work.

Sincere gratitude for the funding by the National Sciences and Engineering Research Council of Canada through the Discovery Grants Program (Project Title: "Integrity of Shear Connection Mechanisms in Precast Concrete Insulated Wall Panels"), the Collaborative Research and Design Program (Project Title: "Resilient Concrete Masonry Walls to meet the needs for the Next Generation of Low-rise Structures"), and Alliance Grants Program (Project Title: Robotic Wall Construction using Innovative Building Blocks and Processes for Enhanced Productivity, Safety, and Sustainability"). Funding and support were also provided through the Masonry Contractors Association of Alberta (MCAA), Canada Masonry Design Centre (CMDC), and the Canadian Concrete Masonry Producers Association (CCMPA).

My special gratitude to *Uncle Zero means nothing*, my Math teacher in primary school, who made me love the act/art of addition and subtraction. I want to also thank Prof. Douglas Osula, Prof. Sylvester Osuji, Prof. Jacob Ehiorobo, Dr. Nwankwo Ebuka, Dr. Osaretin Enadeghe, Dr. Ngozi Ihimekpen, Mr. Festus Okunbor, *The Sunmboye Family*, Engr. Eric Ikogho, and Engr. Emmanuel Edet for their contributions to my education over time. Big thanks to Mr. Wojtek Dowgiert for his encouragement throughout my program especially during the dark times of COVID. I wish this work had been completed before ***Prof. Douglas Osula*** passed away from this life. I cannot remember a dull moment with him. *Requiescat in pace.*

To the living, *TEMPUS FUGIT, MEMENTO MORI*

TABLE OF CONTENTS

LIST OF TABLES

LIST OF FIGURES

1. INTRODUCTION

Insulated concrete walls and double wythe cavity masonry walls are common components in residential and industrial buildings. On their own, buildings account for over 40% of global energy usage and 33% of global greenhouse gas emissions (Huovila et al. 2009, Peng, 2016). In Canada, heating for buildings accounts for 65% of greenhouse gas emissions (GHG) (Stinson, 2017) of which 20% is lost due to poor wall insulation (Natural Resources Canada 2021). To reduce energy demands brought about by increased economic activities and heat loss through the walls, building codes are being updated to meet stricter requirements such as using larger insulation thickness. This means walls even built a decade ago are no longer desirable for new construction.

Both wall types have been used as interior and external members of buildings for many years. Double-wythe cavity masonry walls usually have bricks and Concrete Masonry Units (CMUs) as external and internal layers (wythes), respectively, while insulated concrete walls have concrete as both layers. The main difference between both wall types is that an air gap is present in cavity masonry walls to allow for drainage of moisture and is absent in insulated concrete walls as concrete is less permeable to moisture than masonry. Both walls have insulation between the external layers that is placed for thermal purposes, and both layers are joined by mechanical devices known as shear connectors. This shear connector transfers longitudinal shear between the layers and could make both layers act as a single unit (fully composite) or individually (non composite). Most times both wall types tend to act as partially composite systems which is an intermediate behaviour between non and fully composite systems.

The common form of construction for both wall types is a combination of onsite and precast construction. The components of masonry walls which include Concrete Masonry Units (CMUs) and bricks are usually built offsite and assembled onsite. Insulated concrete walls can be completely built as precast members or onsite in the absence or proximity of precast facilities. Precast construction has enabled building contractors and owners to achieve 23-27 points in the Leadership in Energy and Environmental Design (LEED) system rating, of which 26 points are

needed for LEED certification (VanGeem 2006, CPCI 2020). This may be further enhanced by using Fibre Reinforced Polymers (FRP) as connectors (Belarbi et al. 2016) because of their lower thermal conductivity, which has been shown to achieve 1.7 times the thermal efficiency of a similarly built steel-reinforced wall (Woltman et al. 2017).

When composite action/strength is the sole consideration, designers can opt for fully composite walls, of which fully composite walls are more prone to thermal bowing. As an alternative, designers can design walls to be non-composite which are less susceptible to thermal bowing but have lesser structural capacity/composite action. At the moment, designers are faced with the need to have more thermally efficient building envelopes which is often achieved through larger insulation thickness between the wythes. However, this increase in insulation thickness adversely affects the structural strength of the connectors and consequently the amount of composite action reached by the walls. This means walls built with existing connectors could lose a significant amount of composite action.

Amidst changes to the thermal requirement for building envelopes, the structural load on buildings such as the dead and live load, has been largely constant which means new considerations on how the load is transferred through the walls must be made.

1.1 RESEARCH NEEDS

1.1.1 Current trend

The design of insulated concrete and double-wythe cavity masonry walls involves consideration of thermal and structural demands. However, this thesis is only focused on the structural behaviour. With the intent of improving the thermal efficiency of buildings, energy codes are being updated to require larger insulation thickness. This increase in insulation thickness challenges the appeal for composite action desired by engineers, as the connectors joining the wythes will lose stiffness which would affect the wall's composite behaviour.

The choice of connector type also presents a challenge, whereby composite action achieved particularly through steel reduces energy efficiency (Pantelides et al. 2008, Woltman et al. 2017,

Noël 2012). Even the use of connecting materials with low thermal conductivity such as FRP, often leads to lower levels of composite action due to their lower stiffness, especially GFRP. Also, FRPs have a low temperature resistance (ACI PRC 440.2-23), and often require additional resin coating for improved fire resistance (ACI PRC 440.2-23, Branco et al. 2010, Kandola et al. 2002). Again, these resin coatings are costly and reduce the mechanical properties (Petersen et al. 2015, Shahari et al. 2021). This means innovative processes have to be developed to achieve the desired level of composite action while maintaining the thermal integrity of a member.

1.1.2 Insulated concrete walls

Interventions for insulated concrete walls can be focused on the connectors and insulation. Although insulation has been shown to contribute towards composite action (Joseph et al. 2018, PCI 2011), its structural role is considered unreliable due to variation in insulation-concrete bond quality, which also depends on the type of insulation (Insel et al. 2006). In the past, researchers have used surface treatments such as mesh-patterning and sandblasting to increase the insulation-concrete bond strength, with sandblasting being the most effective. However, the level of such interventions was not reported, which makes it difficult to replicate. Stimulating insulation with shear keys is a concept that has been used in lightweight sandwich panels with FRP skin (Mathieson and Fam 2014, Mitra 2010, Mostafa et al. 2013). However, the effect of using insulation shear keys to increase composite action in insulated concrete walls with inclined shear connectors has not been investigated.

1.1.3 Double wythe cavity masonry walls

Unlike insulated concrete walls, interventions for double-wythe cavity masonry walls are restricted to the connectors due to the airgap which prevents any shear contribution from the insulation. Insulation used for masonry cavity walls is also commonly mineral wool which has negligible stiffness compared to the rigid polystyrene foams used in insulated concrete walls. However, there is a dearth in the development of innovative connectors for double-wythe cavity

masonry walls in Canada, with the predominantly used wall connectors developed in the 1970s and 1980s.

Inclined connectors have been used in insulated concrete walls where it showed improved structural performance due to better utilization of their material properties. However, the use of inclined connectors has not been utilized in double-wythe cavity masonry walls.

1.1.4 Quantifying composite action in insulated concrete and double wythe cavity masonry walls

The strength and stiffness of the shear connection system are usually evaluated using push-through tests such as those conducted by Arevalo (2019), Bunn (2011), Egbon and Tomlinson (2023), and Williams and Hamid (2005). When the shear connection mechanism is changed, it then becomes necessary to determine the amount of composite action generated by such interventions in full walls. This is usually done through experimental testing, numerical or analytical modelling of full walls. To achieve this, an understanding of how the walls behave under loading is needed.

Walls undergo various amount of deformation overtime, and the common sources of deformation include out of plane loads (wind) as well as environmental factors which include temperature differential (difference in temperature between the external and internal wythe) and humidity (expansion and contraction of the wythes). When partially composite walls undergo deformation, one wythe tries to move relative to the other, and internal forces are generated in the wythes. The internal forces create strain discontinuity (a deviation from plane sections) between the wythes which is physically manifested along the wall as a relative slip between wythes and is largest at the end of the wall. This slip is resisted by connectors through longitudinal shear contribution, and the shear contribution depends on its strength and stiffness.

As with other load sources, out of plane loads can act as positive (towards the wythe) and negative (suction, away from the wythe), and the connectors are expected to have adequate strength in both directions in order to contribute significantly to the strength and stiffness of walls.

When both wythes act separately (non-composite, Fig. 1.1a) the strain discontinuity is largest and there is zero longitudinal shear contribution (i.e., connectors have zero stiffness). In partially composite walls (Fig. 1.1b) the strain discontinuity is between that of a non-composite section and fully composite section. In fully composite sections, there is no strain discontinuity (Fig. 1.1c) and connectors provide complete longitudinal shear transfer (i.e. connectors have infinite stiffness).

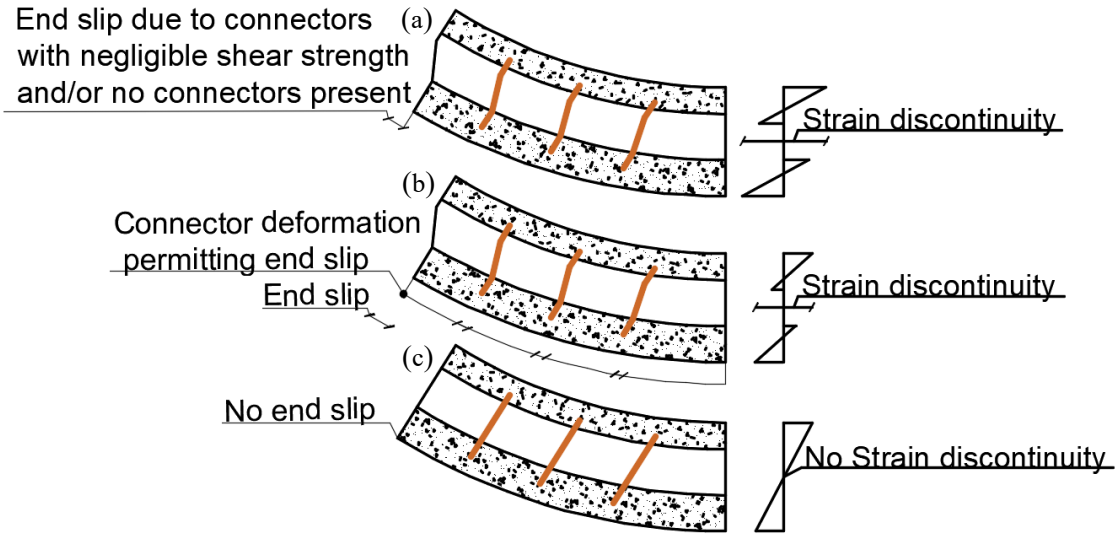

Figure 1.1: Classification of composite action in walls (a) Non (b) partially (c) fully composite

More so, there are similarities in design provisions for both wall types contained in respective concrete and masonry design codes and standards (CSA S304-14 2019, CSA-A23.3 2019), (ACI 318 2019, TMS 402/602 2016), (BS EN 1992 (Eurocode 2), BS EN (Eurocode 6)). While both wall types resist load through the same mechanism, the outer wythe in double wythe cavity masonry walls are usually unreinforced which creates different actions after cracking.

Knowing the load transfer mechanism is similar for both wall types mean existing analytical models developed for one wall type can be adapted to analyze the other wall type. Some of the models to predict the load-deflection response of walls include Gombeda et al. (2017), Tomlinson and Fam (2016a) (developed for partially composite insulated concrete walls) and Sakr and Neis (2001) (developed for double wythe cavity masonry walls). While these models predict the load-deflection response of both walls, there has been no attempt to use analytical models developed for partially composite insulated concrete walls to analyze double wythe cavity masonry walls,

and vice-versa. This is because existing analytical models for both wall types have several iteration steps which makes them difficult to follow and adapt for other cases.

Simpler models such as Pacholok 1989, Papanikolas et al. 1990, Al-Rubaye et al. 2021, and Olsen and Maguire 2016 only predict the load and deflection of both walls up to cracking and not at yielding of longitudinal reinforcement or at ultimate, which is also of interest to designers.

This means that a simplified and unified model is needed to predict the entire load-deflection response for both walls, and the model should be developed in a simplified manner such that it is easily adopted by designers without intensive additional learning and execution resources.

1.2 RESEARCH OBJECTIVES

The objective of this research was to;

1. Develop methods to better assess the amount of composite action in insulated concrete and double wythe cavity masonry walls.

To achieve the objective of this thesis, the following tasks were executed:

1. Conduct a review of literature on shear connection systems for both wall types.
2. Carry out push-through tests on notched and unnotched small-scale insulated concrete walls with inclined connectors and develop analytical expressions to predict the strength of the shear connection system.
3. Similar to Task 2, conduct small-scale shear testing on a novel connector as well as traditional connectors for double-wythe cavity masonry walls, and also develop analytical expression to predict their strength.
4. Develop and validate a designer-friendly analytical model to predict the load-deflection response of full-scale non-load bearing insulated concrete walls under flexural loading. Conduct a parametric analysis on the effect of connector spacing, type, and size, on composite action. Other parameters include longitudinal reinforcement ratio, wythe thickness, and wall length.

5. Adopt the model developed in Task 4 (insulated concrete walls) for non-load bearing double wythe cavity masonry walls under flexural loading. Conduct a parametric analysis on the amount of composite action developed by the novel and traditional connectors evaluated in Task 3. Other parameters examined include loading direction (pressure, suction), longitudinal reinforcement ratio, cavity width, wall length, and connector spacing.

Due to a prolonged laboratory closure due to major renovations and the COVID-19 Pandemic, full-scale experimental wall tests could not be conducted to evaluate the amount of composite action developed by the shear connection systems developed in Task 2 and 3 above, leaving analytical or finite element modelling as the only feasible options.

1.3 RESEARCH SCOPE

Although the design of insulated concrete and double wythe cavity masonry walls involve thermal and structural considerations, this thesis is only focused on the structural performance of both walls. Also, long-term actions that may affect wall behaviour such as creep, swelling, and shrinkage, are beyond the scope of this study. In addition, the walls considered are simply supported non-prestressed walls under static symmetric flexural loading only, while the effect of superimposed axial loads is beyond the scope of this thesis. The walls examined are single-storey walls without interruptions from intermediate floors.

In place of full-scale experimental tests, simplified analytical expressions were developed to determine the amount of composite action developed by the shear connection systems. Analytical modelling was chosen over Finite Element Modelling (FEM) as it enables the wall behaviour to be determined using mechanical formulations that are known to designers and can be executed using simple hand or spreadsheet calculations that are easy to follow. Also, computations for analytical modelling are inexpensive, often requiring far less computational space and time in comparison to FEMs. In addition, designers often utilize FEM software as a “black box” where

users do not often have extensive knowledge of finite element modelling, leading to erroneous interpretations and results.

In this thesis, the connectors examined are those which have sufficient axial stiffness that would make the wythes in the walls deflect together and remain parallel during loading. As such, walls where the wythes do not deflect together are beyond the scope of this research. The connectors examined in this research are those with regular geometries such that properties (e.g., moment of inertia) can be easily determined.

Due to availability of materials, connectors for the insulated concrete walls examined in this study were made from protruded Glass Fibre Reinforced Polymers (GFRP) bars. While GFRP's have a lesser thermal conductivity than steel, they could not be utilized for the cavity masonry walls due to the need to bend and drill holes (slots) in the main connector to accommodate a smaller embedment tie as shown later in Section 4.2.1. If these slots and bends were made on the GFRP material, this would lead to a reduction in its mechanical properties such as its tensile strength by up to 50% (Nanni et al. 1998, Imjai et al. 2017, Jagadeesh et al. 2023). This is why steel connectors were used for the cavity masonry walls.

The walls examined are those under one-way action while walls under two-way bending are beyond the scope of this study. In addition, the walls examined are single-storey walls without interruptions from intermediate floors.

1.4 THESIS OUTLINE

This thesis is sub-divided into two parts which relate to small-scale testing and analytical modelling of full-scale wall behaviour of insulated concrete walls and double-wythe cavity masonry walls. After the introduction, the next chapter presents a review of literature related to both wall types and the four subsequent chapters comprise journal manuscripts.

Chapter 2: Literature review – Provides background knowledge on insulated concrete and double-wythe cavity masonry walls. Chapter 2 accomplishes Task 1 of the research objectives.

Chapter 3: Experimental investigation of longitudinal shear transfer in insulated concrete wall panels with notched insulation – This chapter is from a published paper (Journal paper 1 in Preface), and it presents results from experimental testing of concrete panels with rectangular and trapezoidal notches used in combination with truss-shaped GFRP connectors. This chapter completes Task 2 of the research objectives.

Chapter 4: Experimental longitudinal shear testing of novel and traditional shear connectors in double-wythe cavity masonry walls – This chapter (Journal paper 2 in Preface, under review), presents results from the experimental longitudinal testing of a novel masonry connector against existing plate connectors. This chapter completes Task 3 of the research objectives.

Chapter 5: Simplified load-deflection analytical model for partially composite insulated concrete wall panels under flexural loading – This chapter (Journal paper 3 in Preface, under review) presents a simplified analytical model to predict the load-deflection response of full-scale walls and validated with previous experimental data. Chapter 5 accomplishes Task 4 of the research objectives.

Chapter 6: Analytical flexural model for partially composite double wythe cavity masonry walls – This chapter, which is from a manuscript under preparation, presents the application of the analytical model for insulated concrete walls to double-wythe cavity masonry walls. The contribution of the novel connector (discussed in Chapter 4) towards composite action is compared to existing masonry connectors. This chapter completes Task 5 of the research objectives.

Chapter 7: Conclusion

This chapter summarizes the results from prior chapters with research contributions and recommendations for future studies.

Appendix A: Load-Slip Response of Connectors in Insulated Concrete Walls

Appendix B: Design Example for Insulated Concrete Wall Under Flexural Loading

Appendix C: Formulations For the Load-Slip Response of Masonry Connectors

Appendix D: Design Example for Double Wythe Cavity Masonry Wall Under Flexural Loading

2. LITERATURE REVIEW

2.1 DOUBLE-WYTHE CAVITY MASONRY WALLS

Double wythe masonry cavity walls (Fig. 2.1a) are mostly used as exterior walls in many residential, commercial, and industrial structures. This wall type is typically constructed onsite, with the outer wythe made of brick veneer or Concrete Masonry Units (CMUs), while the inner wythe is made of CMUs and called the structural wythe (Wang et al. 1997). The cavity encloses an insulation layer which is placed for thermal purposes and does not contribute to the structural response of the wall system. An air-gap of at least 25 mm is created after the veneer and serves as a water drainage path (Langmans et al. 2017, Brick Industry Association 2018, Allen and Iano 2009). A vapour or moisture barrier is attached to the warmer side of the insulation to prevent the entry of water vapour due to condensation (Clayford 2003, Hatzinikolas et al. 2015).

Modern double-wythe cavity walls are joined using connectors which are the main contributors to wall strength (Sakr and Neis 2001, Wang et al. 1997). Connectors are usually made of steel, and the structural contribution from a connector is dependent on its size (diameter/thickness) and embedment length. In addition, the connector strength is also influenced by the anchorage provided by mortar joints, and the thickness of the mortar joint typically ranges between 10 and 15 mm (Cascardi et al. 2020, Petersen et al. 2012, Martins et al. 2017). CSA A370:14 (2018) limits the size of flat and round connectors to 50% and 67% of the mortar thickness, respectively.

2.2 INSULATED CONCRETE WALLS

Insulated concrete wall panels, also called sandwich panels, are typically made of an insulation core material positioned between concrete layers, also known as wythes. The core material is usually added for thermal purposes (Joseph et al. 2017, Goudarzi et al. 2016) while the wythes provide a combination of structural resistance and architectural features (Fig. 2.1b). Insulated wall panels are used in a variety of applications, most commonly as exterior walls in residential buildings, commercial facilities, and industrial complexes. This wall type is typically fabricated

in a precast facility, shipped to site, and then attached to the structure (Norris and Chen 2016, PCI 2011). This off-site means of production facilitates shortened construction time, financial savings, better quality control, durability, and improved safety (Tomek 2017).

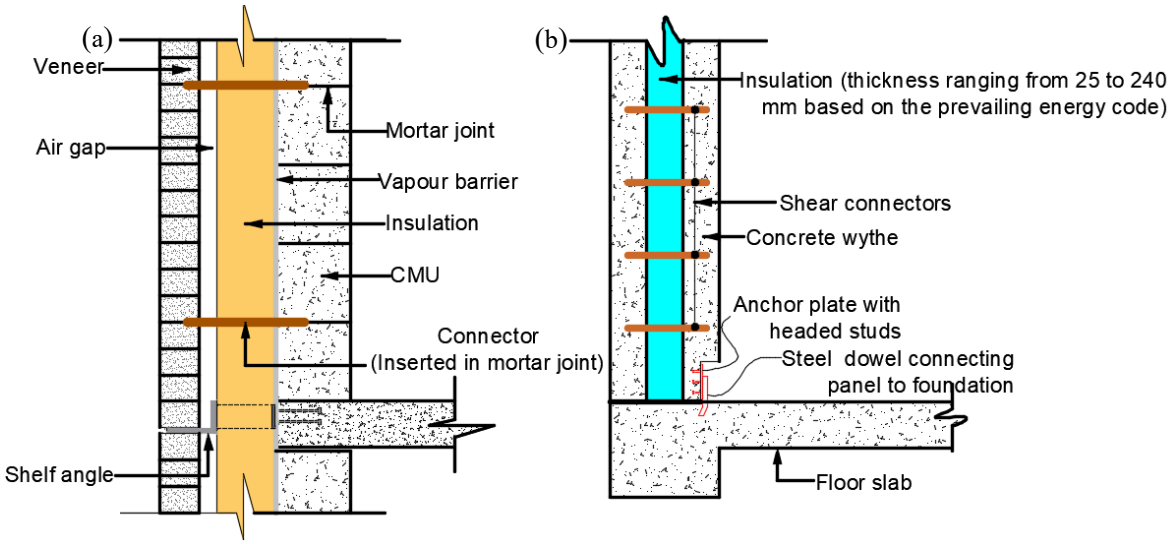

Figure 2.1: (a) Double-wythe cavity masonry wall (b) insulated concrete wall

2.3 SIMILARITIES AND DIFFERENCES BETWEEN INSULATED CONCRETE WALLS AND DOUBLE WYTHE MASONRY CAVITY WALLS

Over time, insulated concrete and double wythe cavity masonry walls have been used in similar applications, most commonly as exterior walls in single and multi-storey residential, commercial, and industrial structures, respectively (Martins et al. 2017, PCI 2011). Most insulated concrete walls are produced in off-site precast facilities while double wythe cavity masonry walls are usually constructed on-site. On-site construction is usually applied for double-wythe cavity masonry walls due to the sensitivity of the connector-mortar joints to movement during transportation. However, when it is uneconomical to use a precast facility due to its remoteness from a job site, insulated concrete walls are constructed on-site, just like double wythe cavity masonry walls.

The outer wythe of insulated concrete walls is reinforced while that of double wythe cavity walls (brick) is usually unreinforced. Knowing this, designers often adopt insulated concrete walls due to the additional strength from the reinforced outer wythe. However, in cases where strength is not an important consideration, double wythe cavity masonry walls are chosen due to the

superior aesthetic appearance of brick (Martins et al. 2016). In addition, as masonry blocks are more permeable to water than concrete, designers often prefer to start the foundation of walls using concrete and continue with the same material (concrete) in the superstructure.

Apart from the difference in the wythe material, the means of shear transfer in both wall systems is mostly through connectors that link wythes together (Bunn 2011). In insulated concrete walls, the structural role of the insulation is debatable and considered unreliable (Insel et al. 2006). This is because the insulation-concrete bond quality depends on the type of insulation which includes Expanded (EPS) and Extruded (XPS)Polystyrene, Polyisocyanurate, and Polyurethane, (Joseph et al. 2018, Mathieson and Fam 2014, PCI 2011). Amongst these insulation types, larger shear strength has been achieved in panels with EPS due to its rougher surface profile (Naito et al. 2012, Hassan and Rizkalla 2010, Frankl et al. 2008). In double-wythe cavity masonry walls, the shear contribution from insulation is zero because the insulation is adhesively bonded with a vapour barrier to one wythe and a space is left from the other wythe which serves as a drainage path (Fig. 2.1a) (Hatzinikolas et al. 2015). The vapour barrier is mostly required for cavity masonry walls because masonry is more permeable to vapour than concrete. Without a vapour barrier in double wythe cavity masonry walls, the integrity of the insulation and connectors would be reduced, often creating discomfort to occupants in the form of mould (Natural Resources Canada 2021).

Both wall types are built with energy and structural considerations to minimize heat loss without which, results in larger carbon footprint and financial cost of operation, and failure (Natural Resources Canada 2020). Energy considerations are detailed in energy codes that are currently prescribing higher R-values for buildings which can be attained by increasing insulation thickness (National Research Council of Canada 2017) and by using thermally efficient materials such as FRP as connectors. However, composite action is adversely affected by measures such as larger insulation thicknesses in both wall types (Bunn 2011, Choi et al. 2019). This is because

larger insulation thickness results in a larger connector span, which leads to a reduction in connector stiffness and contribution towards composite action. (Bunn 2011, Choi et al. 2019).

Under loading, strain discontinuity is created between the wythes. This strain discontinuity accumulates along the wall in the form of slip between the wythes and is largest at the end of the wall, and this slip is resisted by the connectors in the form of longitudinal shear contribution. When both wythes act separately (non-composite) the strain discontinuity is largest, in partially composite walls the strain discontinuity is lesser compared to non-composite sections while in fully composite sections, there is no strain discontinuity. Also, there are similarities in design provisions for both wall types contained in respective concrete and masonry design codes and standards (CSA S304-14 2019, CSA-A23.3 2019), (ACI 318 2019, TMS 402/602 2016), (Eurocode 2, Eurocode 6).

2.4 ROLE OF CONNECTORS AND ASSESSING BEHAVIOUR OF INSULATED CONCRETE AND DOUBLE WYTHE CAVITY MASONRY WALLS

The design of single wythe concrete and masonry walls is commonly taught in undergraduate and graduate civil engineering programs. However, this design process differs from that of insulated concrete and double wythe cavity masonry walls which is made complicated due to the need to account for the slip between the wythes. The amount of slip between the wythes is determined by the stiffness of the shear connection system, while the strength of the shear connection system determines how much longitudinal shear they can contribute to walls (Fig. 2.2).

The amount of longitudinal shear varies based on the connector type and this means that methods of evaluating the strength of the connectors are critical in understanding the behaviour of walls. The behaviour of insulated concrete and double wythe cavity masonry walls is classed into three categories which are discussed in Section 2.5.

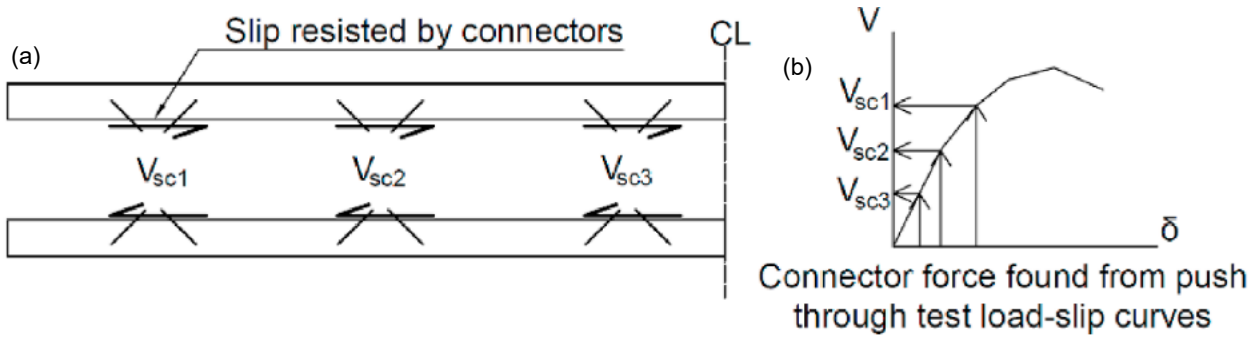

Figure 2.2: (a) Longitudinal shear generated in wall section (b) individual shear contribution from shear connection (Arevalo and Tomlinson 2020)

2.5 COMPOSITE ACTION

Both wall types under consideration are constructed using shear connectors which are a major factor affecting wall strength and stiffness (Arslan et al. 2020, Jaiden 2017). Depending on the desired nature of the wall, which is influenced by structural and thermal demands, walls are designed to act as non (Fig. 2.3c), partially, and fully-composite members (Fig. 2.3a). Generally, non-composite walls are thicker than fully composite walls (PCI 2011), and since there is no restraint to slip between the wythes, are more suitable for conditions where little or no thermal bowing is desired (Losch 2003, PCI 2010). In real-life, walls tend to act between these extremes as partially composite walls (Fig. 2.3b) (Frankl et al. 2011, O'Hegarty and Kinnane 2020).

Non-composite members have negligible shear transferred between the wythes which means that the wythes act independently. In these applications, the shear connectors act as ties to prevent delamination of the exterior wythe under self-weight or wind loads. For partial composite walls, only a percentage of the load needed for full composite action is transferred between wythes. In full-composite walls, the forces developed within the section are transferred between adjacent wythes, with the shear connector being the largest contributor to strength and stiffness (Benayoune et al. 2008, Bush and Stine 1994, Kazem et al. 2015, Morcous et al. 2011, Pessiki and Mlynarczyk 2003, Reneckis et al. 2004).

Often, the term "fully composite action" is broadly used in describing walls. However, it should be correctly used to refer to the amount of composite action based on stiffness and strength. A fully composite panel by strength means there are sufficient connectors needed to make both

wythes act together at peak load. For a full composite panel by stiffness, there is no slip (i.e., strain discontinuity) between the wythes meaning that the full moment of inertia of the panel can be used.

Specifically for double-wythe masonry walls, full-composite action by strength used to be achieved by filling the joint between the wythes (collar joint) with mortar or grout (TEK 16-01A 2006). A similar approach of using solid concrete zones was formerly used in insulated concrete walls (Frankl et al. 2008, Suryani and Mohamad 2012). However, this method rids the insulation of its thermal benefits by creating thermal bridges through the insulation. This means that the realization of large strength and stiffness, which full-composite sections offer, can impede the thermal benefits such as high R-values. This is a major concern that needs to be addressed especially with the development of new energy codes that are prescribing larger R-values for buildings.

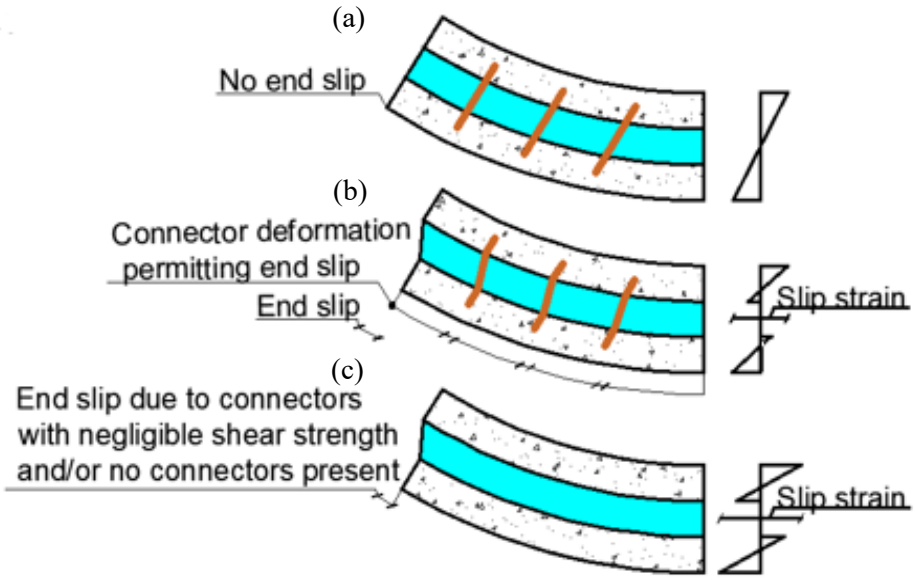

Figure 2.3: Classification of walls (a) Full composite (b) partially composite (c) non-composite

2.6 SHEAR CONNECTION TESTING

Connector responses (Fig. 2.2b) can be classified as dowel-type (Fig. 2.4a) where they transfer forces via beam action or truss-type (Fig. 2.4b) where they transfer forces using axial connector properties (Woltman et al. 2013, Tomlinson et al. 2016).

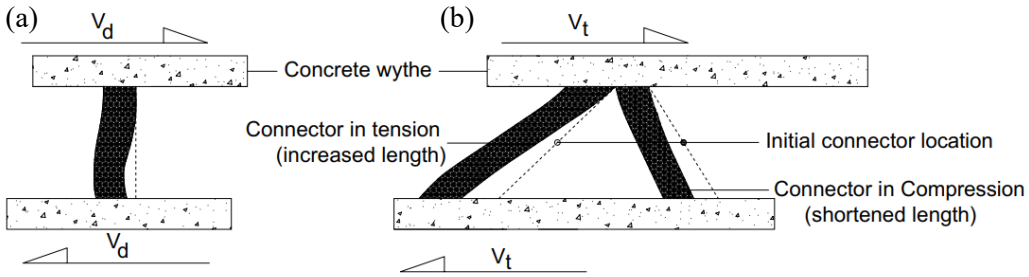

Figure 2.4: Classification of connector behaviour (a) dowel action (b) truss action

Unlike double wythe masonry walls, more innovative schemes have been developed in the aspect of connectors for insulated concrete walls. They include the use of discrete and distributed connectors (Naito et al. 2012, Sopal 2013, Einea et al. 1994, Maximos et al. 2007). Discrete connectors are placed at specified intervals/locations along a wall while distributed connectors are continuous along the wall. Common connectors for double wythe masonry (Fig. 2.5) and insulated concrete walls (Fig. 2.6) are generally examined under compression, tension, or shear. While connectors for insulated concrete walls have no strict limit for thickness, the diameter of masonry wall ties is limited to two-thirds of the mortar joint for round and helical shapes, and 50% for flat configurations (CSA A370). This is to ensure the surrounding mortar has sufficient cover to resist the forces developed in the connector (CSA A370).

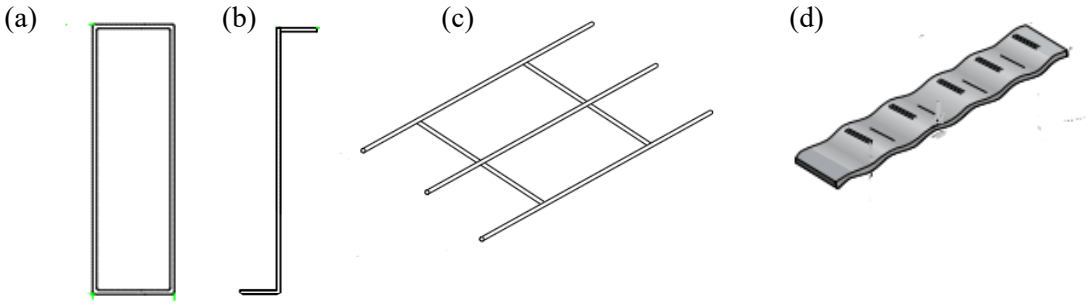

Figure 2.5: Common Masonry wall ties (a) Rectangular (b) Z (c) Ladder (d) Corrugated (CSA A370:14)

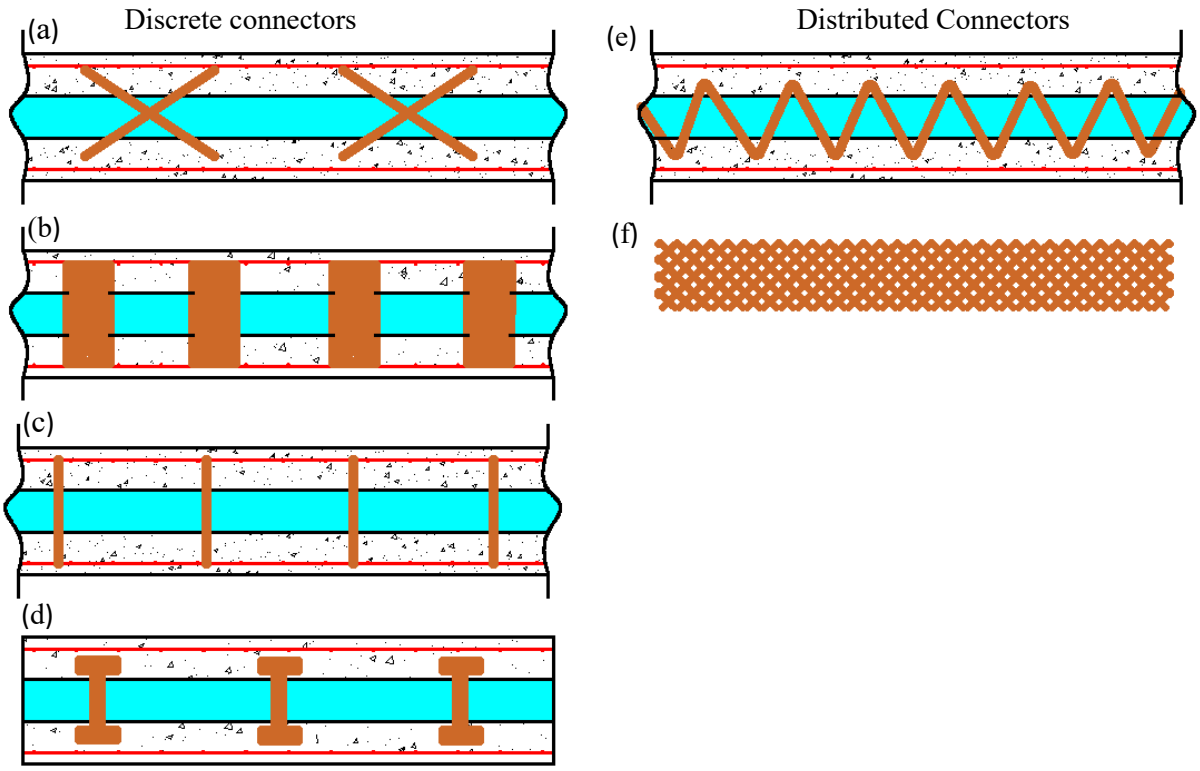

Figure 2.6: Insulated concrete walls with different connector types (a,b,c,e shown along the wall length, with (d) along the wall width) (a) truss bar connectors (b) Plate-type connectors (c) Pin-type connector (d) Profiled Connector (I-section) (e) Bent bar truss connector (f) Grid type truss connector

Tension and compression tests primarily reveal the axial capacity of connectors, and the axial strength of connectors may affect the amount of composite action in walls (Arslan et al. 2020, Sakr and Neis 1997). This is because connectors with sufficient axial strength ensure the wythes deflect together and remain parallel to each other while resisting load. The shear response is often assessed using push-through testing. Push-through tests are usually small-scale tests, and this test reveals the connector's ability to contribute longitudinal shear to the wall, which is the main determinant of the amount of composite action in walls (Hodicky et al. 2014, Sakr and Neis 2001).

Tension, compression, and shear properties for connectors are usually carried out using small-scale assemblies where the connector is inserted between wythes of both wall types. This is done to replicate conditions in real walls where the connectors interact with wall components such as concrete, mortar, and grout. Many experimental tests have been conducted on the behaviour of connectors under tension and compression (Arslan et al. 2020, Hatzinikolas et al. 1979, Corradi et

al. 2017, Hatzinikolas et al. 1983; Martins et al. 2016), Skroumpelou et al. 2018), and a typical test setup is shown in Fig. 2.7.

In interpreting the results from tension and compression loading, CSA A370:14 (2018) specifies that masonry connectors under compression and tension should have an ultimate strength of at least 1 kN, although the rationale for this value is not stated. Meanwhile, there is no minimum specification for connectors in insulated concrete walls but are generally required to be at least stiff enough to resist loads induced during handling and erection (Lee and Pessiki 2006a).

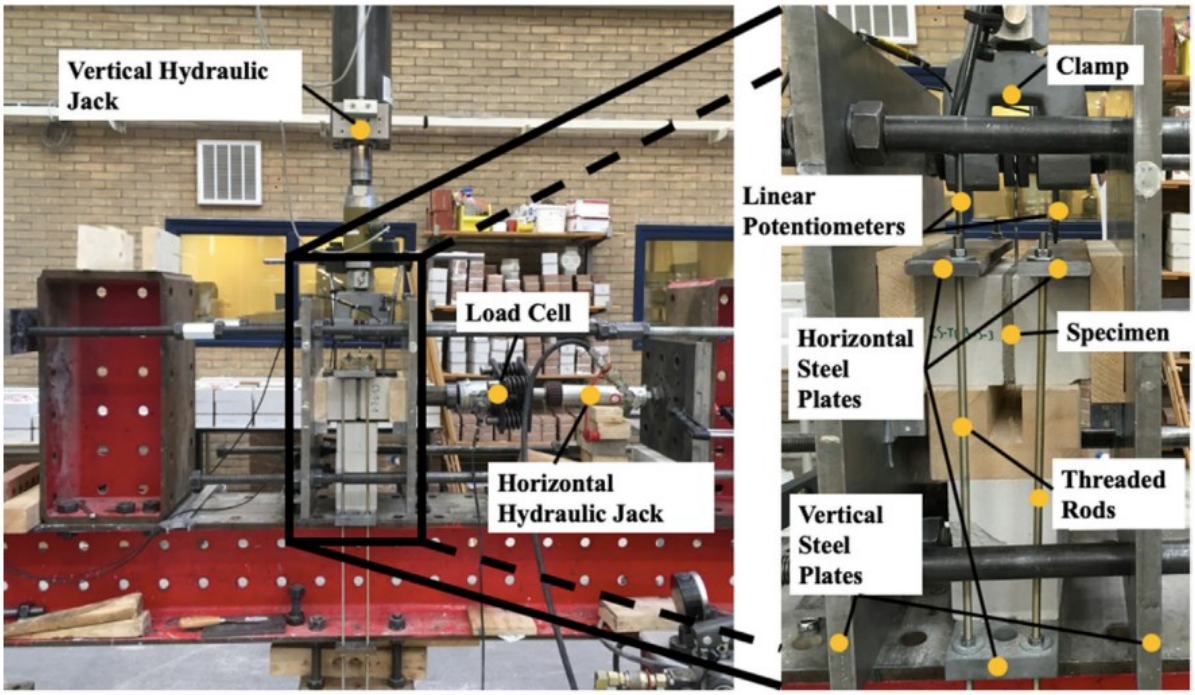

Figure 2.7: Tension and compression test setup for connectors (Arslan et al. 2020)

For shear testing, there is more literature related to the testing of connectors used in insulated concrete walls in comparison with double wythe cavity masonry walls. One reason for this is the fact that more insulated concrete walls are built in practice which attracts more research funding and attention. Also, since the brick in double wythe cavity masonry walls is usually unreinforced and thought to be placed for architectural and hygrothermal purposes only (Vanpachtenbeke et al. 2020), designers are not inclined to investigate innovative connectors schemes in cavity masonry walls. In addition, the superior resistance of concrete to vapour in comparison with masonry blocks/bricks reduces the formation of mould (Natural Resources Canada 2021, Pope 2021), leading to more adoption and attention to insulated concrete walls.

Many experimental studies on connectors for double-wythe cavity masonry walls focused on completely enclosed walls (stone walls or keyed joints) or external strengthening schemes (FRP strengthening) as seen in Szyszka et al. (2018), Magenes et al. (2012), Dizhur et al. (2014), Binda et al. (2006), and Maccarini et al. (2018). Even recent tests by Corradi et al. (2017) examined already existing wall ties. In CSA A370:14 (2018), there is no minimum requirement for the shear strength of connectors. To date, the only prominent test found during the literature review that related to shear testing of connectors in double wythe cavity masonry walls was conducted by Williams and Hamid (2005) as shown in Fig. 2.8. The test which examined the in-plane behaviour of connectors, revealed that the strength and stiffness of connectors depended on adequate anchorage with component parts as well as with masonry parts.

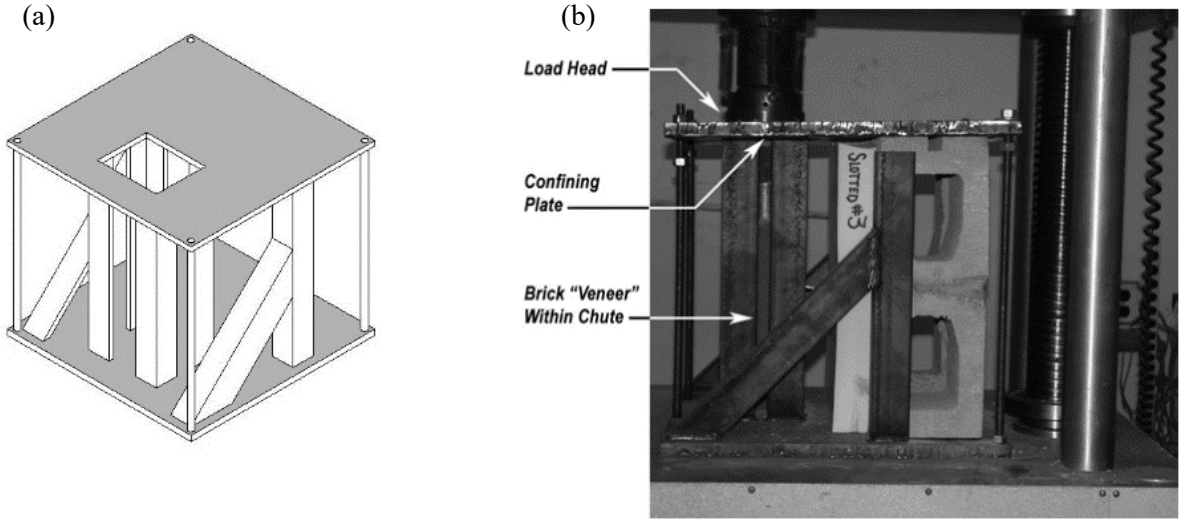

Figure 2.8: In-plane shear testing of masonry connectors (Williams and Hamid 2005) (a) test frame (b) specimen under load

Push-through tests for insulated concrete walls were initially developed for composite concrete-steel beams (Einea 1992). For FRP grid connectors, AC422 specifies the application of load parallel to at least two semi-continuous or continuous connector rows. Current shear testing of insulated concrete walls usually consists of three concrete wythes and two rigid insulation layers (Fig. 2.9). This set-up for shear testing is to ensure the connectors are loaded symmetrically and not subjected to prying forces which are unrepresentative of real-life applications.

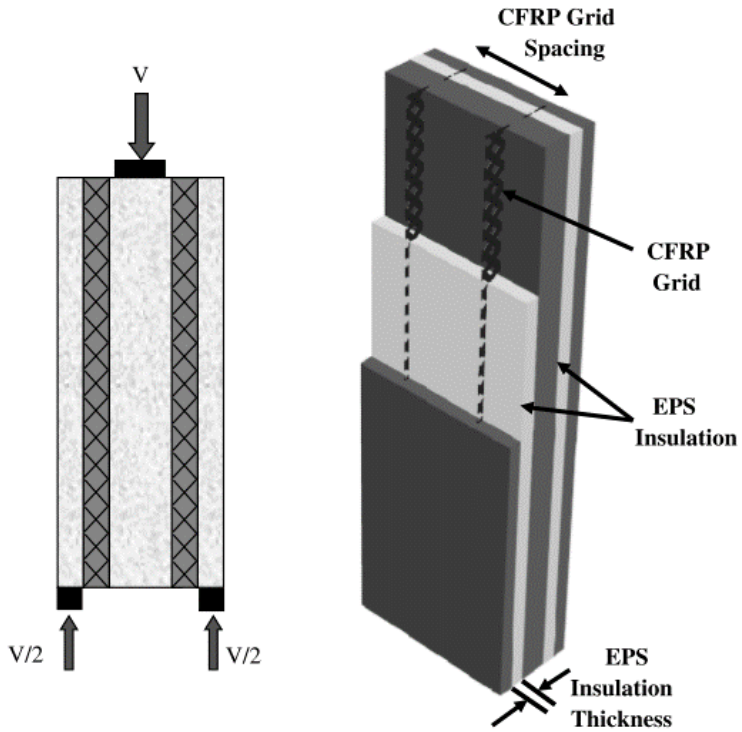

Figure 2.9: Typical shear test setup for connectors in insulated concrete walls (Hodicky et al. 2014)

A significant benefit is reported for steel and FRP connectors when utilized as trusses (inclined connectors) rather than dowels (vertical slotting of connectors) (Bunn 2011, Tomlinson et al. 2016, Sopal 2013). This is due to using the connector's material axial properties instead of their flexural properties as in dowel action. In plate-type connectors, larger stiffness and shear flow are achieved with increased plate thickness and insertion depth (Goudarzi et al. 2016).

Connector behaviour is also affected by the insulation layer thickness. An increase in insulation thickness generally resulted in a decrease in the shear connection strength (Fig. 2.10) due to the reduction in connector stiffness over the larger insulation layer combined with the increase of prying forces other than shear (Choi et al. 2019, Bunn 2011, Hodicky et al. 2014).

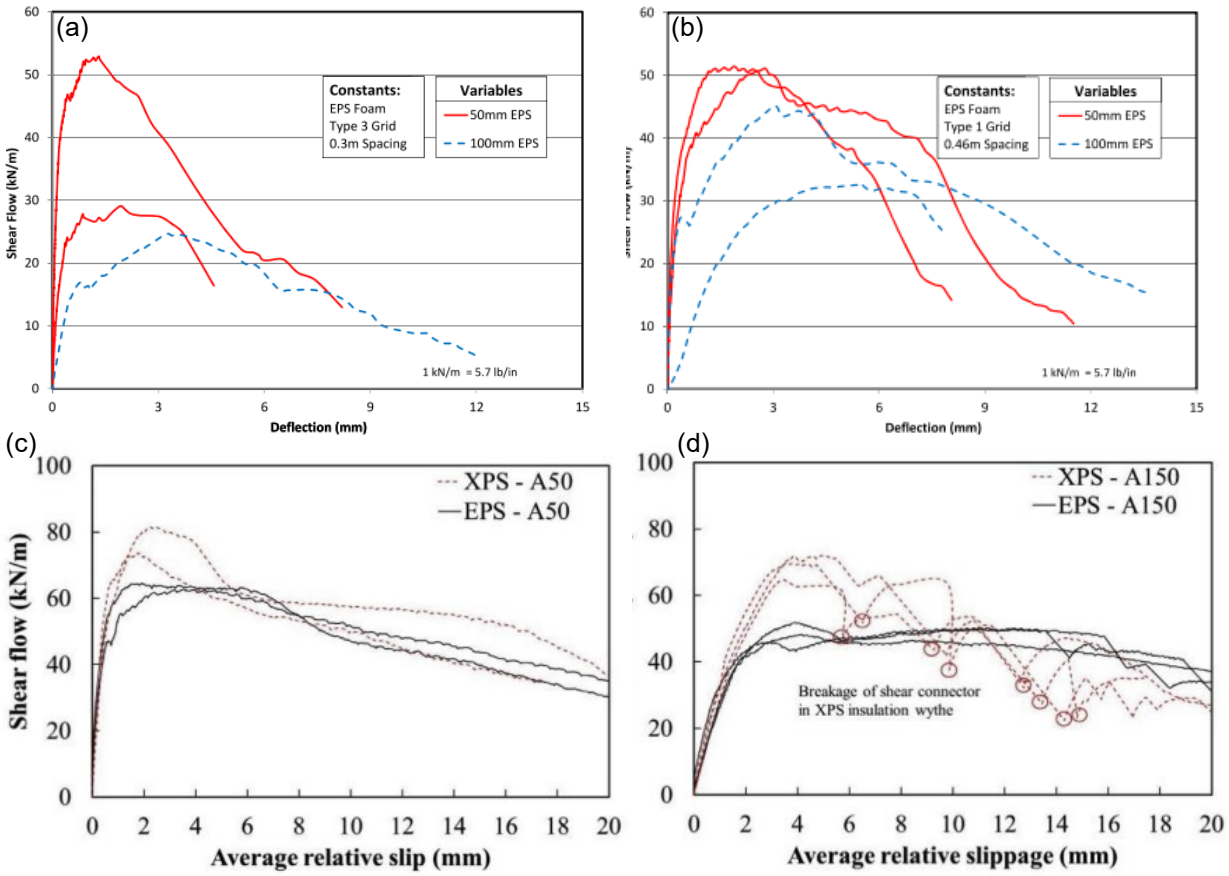

Figure 2.10: Effect of insulation thickness on shear connection strength. Soriano (2013) – 50 vs 100 mm insulation thickness (a) 300 mm connector spacing (b) 460 mm connector spacing. Choi et al. (2019) with insulation thicknesses of (c) 50 (d) 150 mm

On its own, insulation appeared to play a significant role in the shear connection strength (Fig. 2.11). This has been shown in bonded (no barrier at the concrete-insulation interface) versus unbonded (vapour barrier or sheet placed over the concrete-insulation interface) panel tests, and bonding the insulation with concrete increased the shear connection strength (Tomlinson et al. 2016, Soriano 2013). However, the structural role of the insulation is debatable and considered unreliable for insulated concrete wall panels (Insel et al. 2006). This is because of the variation in insulation-concrete bond quality which varies with the type of insulation which includes Expanded and Extruded Polystyrene (EPS, XPS), Polyisocyanurate, Polyurethane, (Joseph et al. 2018, Mathieson and Fam 2014, PCI 2011). Amongst these insulation types, larger shear strength has been achieved in panels with EPS due to its rougher surface profile (Naito et al. 2012, Hassan and Rizkalla 2010, Frankl et al. 2008). While the role of insulation is debatable in insulated concrete walls, it is not even considered in double-wythe cavity masonry walls. This is because, in double-

wythe cavity masonry walls, the insulation is adhesively bonded with a vapour barrier to one wythe, leaving a space from the other wythe (airgap). This space/gap gives its nomenclature as a cavity wall and makes the insulation shear contribution negligible for these walls.

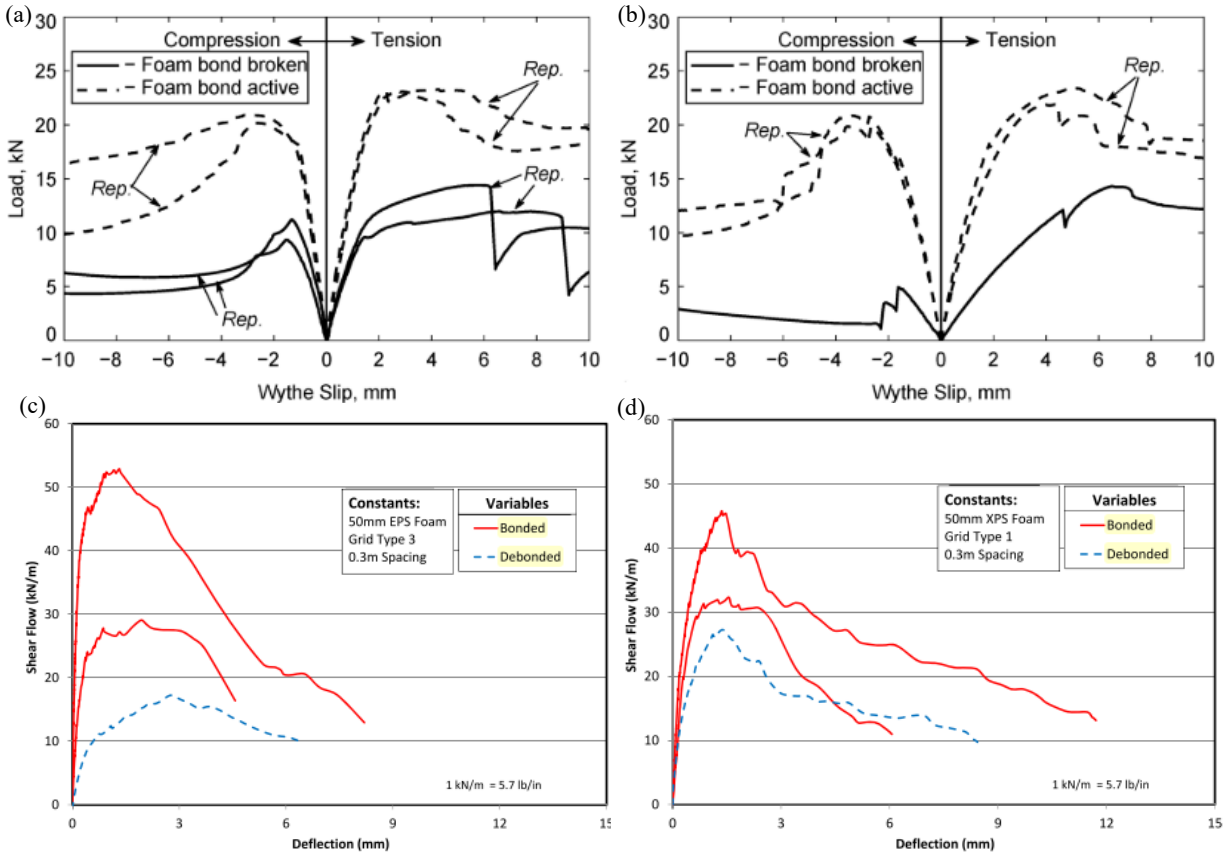

Figure 2.11: Effect of insulation bond with concrete. Tomlinson et al. (2016) with 6 mm thick shear connectors (a) steel (b) Basalt FRP. Soriano (2013) with 50 mm thick insulation (c) EPS (d) XPS

The failure modes of connectors under tension, compression, and shear include connector pullout (when insufficient embedment length is provided), rupture (when embedment length is large such that it makes the connector reach its maximum material strength), and material breakout (when a cone-like piece of the connector host material forms under loading) (Cox et al. 2019, Egbon and Tomlinson 2021, Tomlinson et al. 2016). Other failure modes include connector buckling (when the connector reaches its elastic buckling capacity) and punching failure (when a portion of the connector host material is pushed out towards the opposite direction of loading) (Arslan et al. 2021).

2.7 FLEXURAL TESTING OF WALLS

While push-through tests are effective at evaluating shear connection performance using small-scale specimens, full-scale walls are assessed using flexural tests (Fig. 2.12) which require more instrumentation, additional costs, and additional test facility capabilities. Common flexural test methods are three and four-point bending or using airbags/loading trees (Bush and Stine 1994, Newberry 2011, Carbonari et al. 2012). Four-point bending is usually preferred to 3-point bending due to the uniform stress and strain in a larger area of the test specimen, which is typically between the load points (Hammant 1971, Ferdous et al. 2018). For airbag testing, a uniform load is applied on the full wall face, to better simulate the effects of wind loading (Davies 2001).

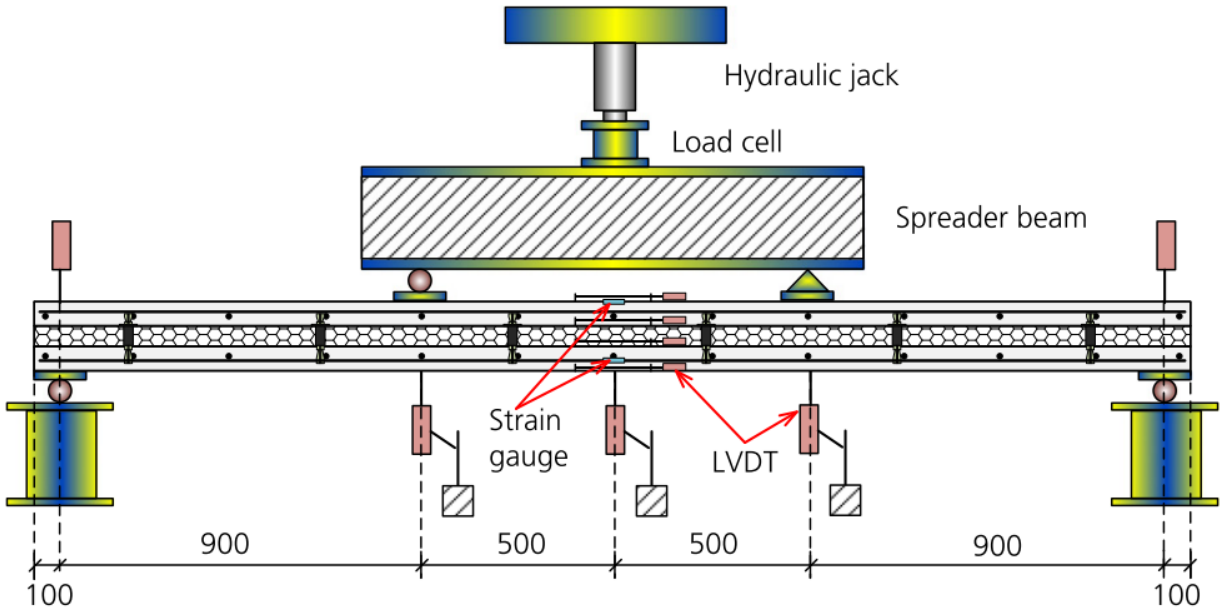

Figure 2.12: Typical flexural test setup: Four point bending (Huang et al. 2018)

Einea et al. (1994) tested bonded and unbonded insulted concrete walls with GFRP truss connectors. Results showed the unbonded panels reached strengths that were 26% lesser than that of bonded specimens, meaning that the insulation seemed to contribute to the shear connection strength. Salmon et al. (1997) tested insulated concrete walls with truss type GFRP and steel shear connectors. The study showed large degree of composite action by strength for panels with GFRP. However, panels with GFRP connectors had lesser degree of composite action by stiffness but were less prone to thermal bowing effects. This means that composite action by strength is not the same as composite action by strength, and this is confirmed in flexural tests by Chen et al. (2020)

and Tomlinson (2015). Also, Chen et al. (2020) showed that Carbon FRP shear connectors were able to produce a reasonable degree of composite action by strength compared to steel shear connectors. Frankl et al. (2011) also tested six insulated concrete walls under flexural load and with CFRP shear connectors and showed that the stiffness and deflections of insulated concrete walls are affected by the configuration of the shear transfer mechanism, which also includes insulation. The study also showed how solid concrete zones can lead to fully composite panels, similar to findings in Frankl et al. 2008 and Gleich (2007). However, solid concrete zones increase the effects of thermal bridging and condensation issues.

In Canada, tests on double-wythe cavity masonry walls stagnated since the start of the millennium, with most tests reported in the literature conducted between the 1970s and early 2000s. Brown and Elling (1979), Hatzinikolas et al. (1997), Hatzinikolas et al. (1990), and Sakr and Neis (1997) showed connectors greatly influenced the stiffness and strength of double wythe cavity masonry walls. Hatzinikolas et al. (1997) reported that while the strength of more than one connector in a row of connectors (along the width) is the total of all the connector strength, the aggregate strength could be reduced due to construction imperfections which could cause load concentration in only some connectors.

Goyal et al. (1994) showed the suitability of using CMUs made of sawdust in double wythe cavity masonry walls. The study showed that the strength of walls reduced with increase in cavity width and reduction in the CMU size. The study also showed that while the shear strength of connectors is important, the wall strength is also affected by the compressive strength of the connectors, as some walls failed due to axial buckling of the connectors.

2.8 PREVIOUS NUMERICAL AND ANALYTICAL MODELS

Huang and Dai (2019) modelled insulated concrete walls with GFRP plate connectors using ABAQUS. Concrete was modelled using 8-node solid elements, with connectors as shell elements with orthotropic properties and the Hashin damage model, suitable for modelling the damage evolution of elastic-brittle materials like FRP. The model predicted test results within 6.0 and 8.5%

for initial stiffness and peak load, respectively. However, the model could not reproduce the post-peak behaviour due to the implemented smeared crack approach, which was unable to account for the formation of diagonal cracks in the GFRP plate connectors. A similar finite element model by Huang and Hamed (2019) modelled insulated concrete walls with truss connectors. The model made simplifications to existing models such as modelling connectors as truss elements instead of beam elements and produced reasonable results with reduced computation time. From verification studies, the model showed the appropriateness of assuming partially composite insulated concrete panels to act under one-way action.

Tomlinson et al. (2016) developed analytical models for dowel and truss type connectors, where the contribution from dowel action was low compared to truss action, in some cases, contributing only 2% to connector resistance. An empirical model by the International Code Council (ICC) Evaluation Service uses deformation measurements obtained from double-shear tests to compute the shear modulus of grid connectors. The model was modified for non-grid connectors by Choi et al. (2015) and was further modified by Choi et al. (2019) to determine the shear deflection and shear flow of grid connectors. This builds on Bunn (2011) where the shear flow capacity was determined using design coefficients for the insulation type and thickness, grid orientation, and spacing obtained from a multi-variable solver tool. In addition, Choi et al. (2019) showed a decrease in shear flow with increasing insulation thickness, which can be attributed to additional demand on the connector.

Initial analytical models for composite structures were developed in the late 1940s and early 1950s, and based on differential equations for steel-concrete composites and timber structures (Stüssi, 1947, Granholm, 1949, Newmark et al. 1951). These studies formed the basis of other models developed in the 1960s (Holmberg and Plem 1965, Allen 1969) that focused on concrete walls. In Holmberg and Plem (1965), the formulations were for the elastic behaviour of concrete panels with steel truss connectors while Allen 1969 developed analytical expressions for walls with a soft core (insulation) and thin skin (metal or fibreglass) but without shear connectors.

In comparison to insulated concrete walls, there are fewer analytical models for double wythe cavity masonry walls. Initial models for double wythe cavity masonry walls such as the finite element models by Pacholok (1989) and Papanikolas et al. (1990) modelled the connector as a fixed-hinge beam, with the part embedded in the CMU assumed to be fixed while the part in the veneer assumed to be a hinge. Similarly, Zmavc (1991) developed analytical expressions for cavity masonry walls but the model only predicts the load and deflection at cracking, just like Pacholok (1989) and Papanikolas et al. (1990). Similarly, analytical models for insulated concrete walls like Olsen and Maguire (2016) and Al-Rubaye et al. (2021) only predict the load and deflection at cracking and not up to wall longitudinal reinforcement yielding and peak load, which is also of interest to designers. The two models simplify the wall evaluation process by assuming the maximum end connector slip to be linear at wall cracking but this may not always be the case.

The model by Sakr and Neis (2001) predicts the entire load-deflection response for cavity masonry walls, but relies on empirical factors for the effective wall stiffness, and has several iteration steps which create a barrier to usage. Comparable models developed for insulated concrete walls like Tomlinson and Fam (2016a) involve integrating differential strains along the wall which makes the solution complicated just like Gombeda et al. (2017) where the principle of virtual work is used to evaluate the rotation at connector locations from which the slip is obtained. Teixeira et al. (2016) used test data for the connector load-slip response which simplifies the procedure in Tomlinson and Fam (2016a) and Gombeda et al. (2017), but it still involves several iteration steps, making it complex to use.

2.9 THERMAL BEHAVIOUR OF WALLS

Apart from structural loads which create deformations on wall elements, another source of deformation is from temperature and moisture gradients in the environment where the wall is located. This thermal demand on walls is often manifested in the form of an out-of-plane deflection or bowing of walls (Pozo-Lora 2018).

Thermal efficiency of walls is quantified using R-Value and calculation for the R-Values of buildings in North America is usually done per ASHRAE (2021). The methods used in calculating the thermal efficiency in ASHRAE (2021) include the parallel flow method, zone method, and the isothermal plane method. In the three methods, the thermal resistances of the materials are treated as electrical resistances that are arranged in parallel, series, or a combination of both to evaluate the thermal resistance of the member (Lee and Pessiki 2006a). Although the zone method overpredicts the R-Values, it is more effective to determine the R-Values of walls with widely spaced sources of thermal bridges such as steel connectors (Lee and Pessiki 2008). Later, Lee and Pessiki (2008) developed a revised zone method which better predicts the R-Values in walls with different connector sizes, spacing, and material conductivities.

Experimentally assessing the thermal behaviour of walls is difficult due to challenges in fabricating a reliable thermal testing system, and the complex interaction between environmental and structural sources of bowing which include humidity, temperature, shrinkage, and creep (Losch 2003). Losch (2003) showed that thermal bowing is worse in walls with stiff connectors, as the differential slip between the wythes is restricted, leaving the wall to bow outwardly. This means that fully composite walls are bound to bow more than non-composite walls. Also, air-conditioning can cause the inner layer to dry faster and shrink quicker than the outer wythe, thereby causing an outward bow which can be permanent or vary over time. The study also reported that bowing can be created in walls due to differences in the elastic modulus of the inner and outer wythes.

Hotbox experiments, used to experimentally evaluate R-value, by Van Geem and Shirley (1987) reported thermal lag between 5 and 6 hours irrespective of the connector type, and the thermal lag is dependent on the heat storage capacity of the wall components. Experimental tests by Post (2006) on three 12.2 m long walls subjected to a temperature differential of approximately 38°C, examined the influence of connectors on thermal fatigue and bowing of walls. The results showed that the outward bowing of walls is dependent on the degree of fixity at the retrained end

of the wall. In addition, recommendations were made for better evaluation of the thermal fatigue behaviour of walls, and these included testing specimens where the insulation-concrete interface is unbonded.

McCall (1985) demonstrated the thermal effect of steel on walls, where a 38% reduction in thermal efficiency was observed in walls with a mere 0.08% of the wall cross-sectional area made of steel connectors. Using GFRP and a Hotbox setup (Fig. 2.13), Woltman (2014) and Woltman et al. (2017) reported a reduction in thermal bridging.

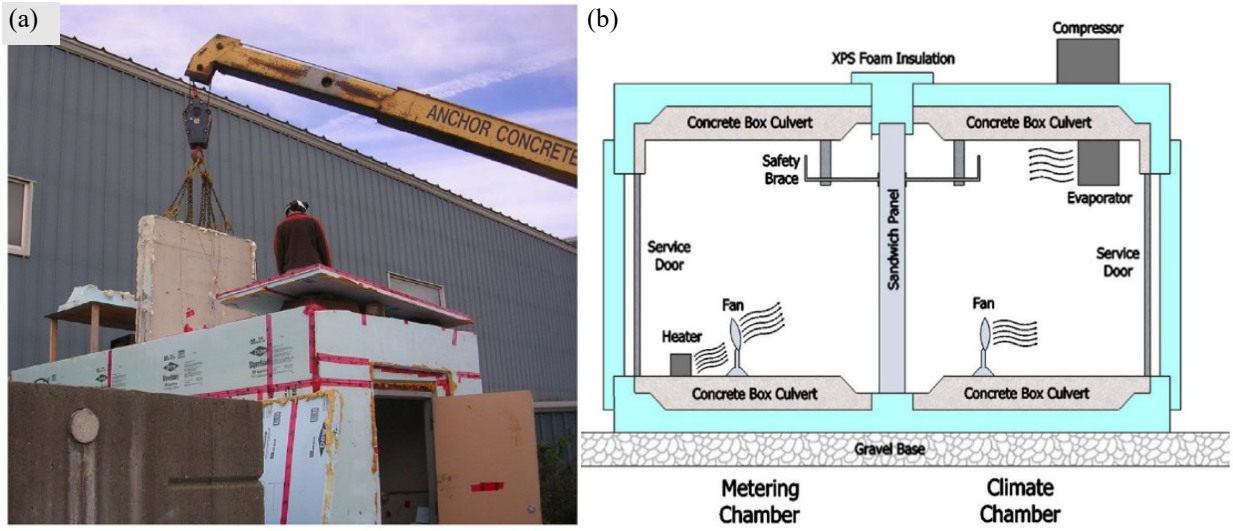

Figure 2.13: Woltman et al. (2017). (a) installation of wall into Hotbox (b) Hotbox schematics

Finite element models by Lee and Pessiki (2006a) and Lee and Pessiki (2006b) on insulated concrete walls found better thermal efficiency for three-wythe walls (three concrete layers) than two-wythe walls (two concrete layers) due to the increased length of the thermal path. It also reported better thermal performance for walls with staggered insulation and that the ASHRAE Handbook method does not correctly predict the thermal response of walls with staggered thermal bridges.

Ismaiel (2022) developed two methods of evaluating the R-Values of cavity masonry walls. The first was developing multipliers and simple design charts to easily estimate the R-Value for cavity masonry walls with different thermal insulation, connectors, and CMU and brick densities. The other method involved adjusting methods in the ASHRAE Handbook (parallel flow and isothermal plane method) to better account for thermal bridges at the brick and slab intersections.

The accuracy of the developed adjusted method was within 2% of values obtained from steady-state finite element models, which was better than that of the isothermal and parallel flow methods which gave accuracies of 19% and 25%, respectively.

2.10 DIGITAL IMAGE CORRELATION

Digital Image Correlation (DIC) is a non-contact optical measurement technique used to obtain the full-field measurements of strains and displacement of objects. It operates by relating sets of pixels or voxels in digital photographs for an element at various phases of deformation and enables a full field 2D or 3D deformation vector field and strain map to be generated. For best results, a speckle pattern on the object should be carefully made within a range of contrast and intensity (Sause 2016), often using spray paint (Dutton 2012). Tomlinson and Fam (2016b) utilized DIC to track relative slip between wythes at the ends of full-size walls as well as the movement of a vertical anchor rod used in the self-reacting frame that occurred due to rotation at the load points and during the elimination of wobbling while loading. This was necessary to estimate the moment capacity developed in their analytical model.

Vervloet et al. (2019) used DIC to monitor the effect of the face thickness on the load-bearing and failure behaviour of concrete sandwich walls with textile-reinforced cement composites, and it was able to capture the failure mode change from global buckling to wrinkling of the face including the debonding between the core and face. Dzaye et al. (2019) also used DIC in investigating the 3-D displacement and strain of an assorted composite such as fresh cementitious paste brought about by water evaporation and related cement hydration. All through the studies mentioned, DIC serves as an alternative to other motion-measuring devices such as Linear Variable Differential Transformers (LVDTs), as it was able to measure the non-uniform displacement and expansive strain.

2.11 GAPS IN LITERATURE

2.11.1 Insulated concrete walls

While several schemes such as sandblasting and mesh-patterning have been used to increase the insulation-concrete bond strength of insulation, these schemes are not reliable and difficult to replicate. In this research, shear keys (notches) will be used to provide a consistent improvement to the insulation-concrete bond strength. Shear keys have been used for activating insulation in sandwich panels with FRP skins, but it has not been used as a means to increase composite action in insulated concrete walls. This thesis will present push-through shear tests on insulated concrete panels with rectangular and trapezoidal notches and compare the results with panels without notches.

2.11.2 Double wythe cavity masonry walls

Inclined connectors have been used in insulated concrete walls and showed improved shear connection performance, but this has not been utilized in double wythe cavity masonry walls. In this thesis, the shear connection strength of a novel inclined connector is compared to traditional connectors used in masonry walls.

2.11.3 Simplified analytical models to predict full-scale response of walls

While both insulated concrete and double wythe cavity masonry walls are built with similar configurations (wythe-insulation-wythe) and act compositely based on a common factor which is the type of shear connection, there has not been an attempt to develop a unified model for the analysis of both wall types. This thesis presents a unified analytical model that would be used to determine the amount of composite action generated due to various shear connection systems. The developed analytical model would be such that it is implemented with a similar framework for both walls and can be executed with a simple spreadsheet.

3. EXPERIMENTAL INVESTIGATION OF LONGITUDINAL SHEAR TRANSFER IN INSULATED CONCRETE WALL PANELS WITH NOTCHED INSULATION

3.1 INTRODUCTION

Reinforced concrete sandwich wall panels, also known as insulated wall panels, are typically made of two reinforced concrete layers (i.e. wythes) that surround a lightweight foam insulation core. Panels are usually precast and are suitable for small and large building construction applications. The insulation's thermal performance combined with the added quality control and architectural capabilities of precast concrete leads to a lightweight and cost-effective option compared to solid concrete panels (Leung 1984, Choi et al. 2015). Structurally, panels are classified as fully composite (wythes act together to resist loads), non-composite (wythes resist loads independently), or partially composite (wythes transfer load between themselves as a percentage of full-composite panels (i.e. composite action)). Practically all panels in use are partially composite by stiffness to some degree.

The level of composite action is heavily influenced by the material and geometry of the shear connectors that link the wythes together. Composite action is usually evaluated through a combination of direct shear push-through tests (used to assess and compare connection mechanisms) and flexural tests (used to evaluate panels as a whole). Designers debate which level of composite action is preferred. High levels of composite action generally lead to lighter (i.e. more structurally efficient) panels at the cost of increasing concerns from thermal bowing (Arevalo and Tomlinson 2020, Pozo-Lora and Maguire 2020) and a reduction in thermal efficiency, particularly when using steel connectors. This concern leads to some designers preferring low composite action walls which are heavier but have minimized risk of bowing.

Traditional connectors such as steel pins, wire trusses, or solid concrete zones result in structurally efficient systems (Benayoune et al. 2008, Tomlinson 2015, Salmon and Einea 1995). However, these materials reduce energy efficiency because of thermal bridging (Frankl et al. 2008, PCI 2011, Rizkalla et al. 2009, Woltman et al. 2017). Fibre-Reinforced Polymer (FRP) connectors

are often used as an alternative to steel connectors due to their low thermal conductivity (Erki and Rizkalla 1993, Alnahhal et al. 2006) which has been observed in thermal tests (Keenehan et al. 2012, Kinnane et al. 2020). However, the lower stiffness of FRP (particularly Glass FRP (GFRP)) relative to steel leads to lower composite action than a similarly designed panel with steel connectors (Chen et al. 2015, Yossef and Chen 2018). FRP pin-type connectors were initially used for panels with low composite action (Waldron 2004) but FRP trusses were developed in the 1990s to give partial composite action by stiffness and fully composite action by strength (Salmon et al. 1997). Today, FRP connectors are available in many arrangements including grids (Bunn 2011, Frankl et al. 2008, Hassan and Rizkalla 2010, Kim and You 2015, Sopal 2013), pin-type connectors (Woltman et al. 2013), and inclined connectors (Tomlinson et al. 2016).

Although the level of composite action is dominated by shear connectors, the insulation contribution is large enough that it should not be ignored (Bunn 2011, Gara et al. 2012, Tomlinson et al. 2016). It is widely reported that Extruded Polystyrene (XPS) insulation has a lower shear capacity than Expanded Polystyrene (EPS) owing to EPS' rougher surface. Researchers have used minor surface treatments such as mesh-patterning and sandblasting to increase the insulation-concrete bond strength of XPS (Choi et al. 2016, Oh et al. 2013, Sopal 2013) with sandblasting being the most effective. Activating insulation with shear keys is a concept that has been used in sandwich panels with FRP skins with some effectiveness (Jakobsen et al. 2007, Mitra 2010, Mostafa et al. 2013). However, at the time of conducting this research, the effect of using insulation shear keys to increase composite action in insulated concrete walls with shear connectors has not been investigated. Relative slip, insulation debonding, and insulation or concrete crack propagation can be monitored with Digital Image Correlation (DIC), which is a non-contact method of measuring deformation fields in a specimen. DIC has previously been used to measure the slip and rotation in sandwich panels (Arevalo and Tomlinson 2020, Tomlinson 2015) as well as monitor crack formation and propagation (De Munck et al. 2019).

As mentioned in Section 1.1.4 of this thesis, when full-scale partially composite walls are loaded under out of plane loading, one wythe tries to slip relative to the other wythe. This relative slip between the wythes is resisted by the shear connection system, which is a sub-set of the full-scale wall, and can be replicated using small-scale push-through test. In the pushthrough test set-up (shown later in Section 3.6), the middle wythe pushes (shears) relative to the outer wythes (with the shear connector and insulation resisting the applied shear load), thereby creating a similar mechanism in full-scale walls.

The objective of this study is to evaluate the effect of adding notches on the load-slip performance of shear connection mechanisms with different insulation types using direct shear push-through tests. The variation of notch shape will reveal the most efficient shape and failure mechanism. DIC will be used to evaluate insulation contribution and failure modes (i.e. debonding or tearing). In addition, load-unload cycling was used to evaluate the degradation of shear connection stiffness under load.

3.2 EXPERIMENTAL PROGRAM

3.2.1 Specimen description

The performance of different insulation and notch configurations was evaluated. Test specimens measured 375 ×300 × 600 mm (Fig. 3.1) and were designed to be loaded in double shear (simulating two panels back-to-back) to simplify the test setup which is an approach used in previous studies (Kim and You 2015, Naito et al. 2012, Tomlinson et al. 2016, Woltman et al. 2013). Each specimen used 250 mm long GFRP bars inclined at 45° (i.e. forming an 'X' shape) as shear connectors.

Three commonly used rigid insulation types (EPS, XPS, and PIR), were considered in this test program. The insulation thickness of 75 mm (reduced to 50 mm at notches) was selected based on PCI (2011) guidelines and is commonly used in contemporary construction in Canada. A notch depth of 25 mm was chosen since this leaves a minimum insulation thickness of 50 mm at the notch which is greater than the least concrete cover (Sylaj et al. 2018) to ensure the structural and

thermal integrity of the insulation. For similar reasons, the notch width (along the panel length) was kept at 25 mm. In addition, this was intended to foster adequate contact (i.e. shear key behaviour) between concrete and insulation necessary for structural-insulation contribution as well as to provide enough width (approximately three times the aggregate size) for concrete to properly consolidate in the notch. Trapezoidal notches were cut at an 18° angle to divide the notch into three equal parts across its width. Notches were offset on both sides of the insulation to increase the heat flow path and prevent the formation of mirrored cracks that reduce thermal and structural efficiency.

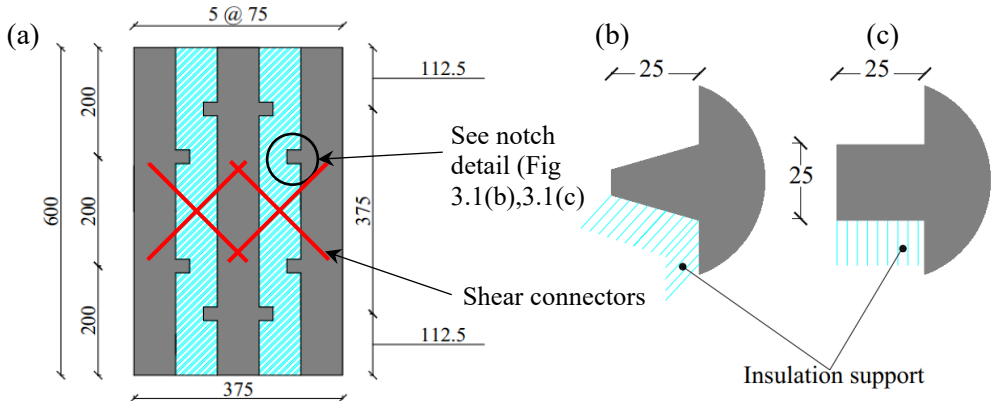

Figure 3.1: Specimen details (a) overall specimen layout and dimensions (b) trapezoidal notch detail and (c) rectangular notch detail. All dimensions in mm.

3.3 TEST MATRIX

Eight specimen configurations were tested with three repetitions completed for each configuration for a total of 24 tests (Table 3.1). Specimens were identified using a three-character code. The first character is the notch type (N – no notch, R – rectangular notch, T – trapezoidal notch) the second character is the insulation type (X-XPS, E-EPS, P-PIR), and the third character is the GFRP connector diameter (nominally 9.5 mm and 16.0 mm). Considering the availability of materials and previous testing by Arevalo and Tomlinson (2020) which focused on XPS along with using 16 mm connectors, only specimens with XPS had trapezoidal notches and were tested with 16 mm connectors in this study to serve as a means of comparison.

Table 3.1: Test Matrix

Specimen ID	Insulation Type	Nominal connector diameter, mm	Measured connector diameter, mm[a]	Notch type (Fig. 3.1)
NX-9.5[b]	XPS	9.5	10.4	N/A
NX-16[b]	XPS	16.0	16.0	N/A
RX-9.5[c]	XPS	9.5	10.4	Rectangular
TX-9.5[c]	XPS	9.5	10.4	Trapezoidal
RX-16[c]	XPS	16.0	16.0	Rectangular
NE-9.5[c]	EPS	9.5	10.4	N/A
RE-9.5[c]	EPS	9.5	10.4	Rectangular
RP-9.5[c]	PIR	9.5	10.4	Rectangular

[a] – connector diameter measured via immersion testing as per CSA S807:19 (2019)
[b] – Load-slip data from Arevalo and Tomlinson (2020)
[c] – one specimen from this data set was tested under load-unload cyclic loading.

Push-through tests cannot be directly used to calculate the degree of composite action in full-scale panels because composite action depends on member properties like connector spacing and panel length (Tomlinson 2015) as well as in Chapter 5 of this thesis. However, previous testing showed that NX-9.5 and NX-16 were at the upper end of strength and stiffness compared to other push-through tests in the literature (Arevalo and Tomlinson 2020). This indicates that, if other member properties are equal, these connectors would be more composite than many other connector systems.

3.4 FABRICATION PROCESS

The fabrication process of the push-through specimens is illustrated in Fig 3.2. Notches were first cut in the insulation (Fig. 3.2(a)) using an electric saw. A drilling device placed on a 45° wedge, and with a diameter smaller than that of the connector was used to make borings into the insulation. A smaller drill size was used to ensure adequate grip between the connector and insulation before and during pouring. Welded wire reinforcement was placed at mid-depth of the future wythes and supported using spacers (Fig. 3.2(b)). For ease of construction and to ensure concrete could flow into the notch areas, push-through samples were cast vertically using self-consolidating concrete (SCC) with a maximum aggregate size of 9 mm (Fig. 3.2(c), (d)). A tape was used to hold the

insulation in place before inserting specimens into the formwork (Fig. 3.2(b)). The tape was cut and removed from specimens before testing.

Full-scale sandwich panels are typically fabricated on flat tables in precast facilities by casting one wythe, adding insulation, and then casting the second wythe. This technique limits the applicability of insulation notches since concrete would not be able to flow into notches. However, panels could be cast on their sides (Arevalo and Tomlinson 2020, Hou et al. 2019) or vertically (Tomlinson and Fam 2014) to ensure notches behave as expected. Side or vertical casting is advantageous as it can reduce stresses from stripping and lifting as well as save precast plant space (Tomlinson and Fam 2018).

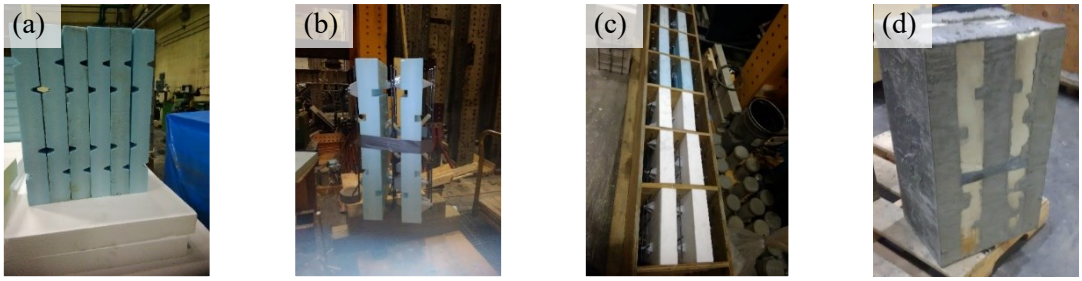

Figure 3.2: Specimen fabrication (a) XPS insulation with pre-cut notches, (b) Assembly of sample components (connectors, reinforcement, and insulation), (c) Specimens in formwork and, (d) Demoulded sample.

3.5 MATERIALS

The SCC mixture used in the walls is commercially available and is commonly used to cast similar walls in Alberta. The design strength of this mixture was 50 MPa. The average concrete compression strength, determined using tests on 100 × 200 mm cylinders as per ASTM C39/C39M−20 (2020) was 52.9 MPa at 28 days with a standard deviation of 2.0 MPa. Push-through tests were completed when the concrete was between 90 and 120 days old. The average compressive strength during this period was 57.0 MPa with a standard deviation of 1.8 MPa. There were no noticeable changes in strength from cylinders tested at the start and those at the end of the push-through test period. The concrete was flow tested immediately before casting as per ASTM C1611/C1611M-18 (2018) and had a flow of 700 mm.

Smooth steel welded wire mesh with a diameter of 5.76 mm and a square grid spacing of 100 mm, providing a reinforcement ratio of 0.0035, was used in the specimens.

High modulus GFRP bars were used as shear connectors and placed at 45° with cut lengths of 250 mm, providing a 25 mm clear cover between the ends of the bar and the exterior concrete surface. Two bar diameters (nominally 9.5 and 16.0 mm) were considered in this program. The actual bar areas were determined using immersion testing following CSA S807:19 (2019). In comparison with steel, FRP has lesser bond strength with concrete (Maranan et al. 2015) which means adequate embedment has to be provided. In this study, all connectors were embedded 72 mm along their length into each concrete wythe. This embedment length is larger than embedment lengths seen in similar push-through test (Naito et al. 2012, Cox et al. 2019, Huang and Dai 2019) that use FRP.

The GFRP bars have a modulus of elasticity and tensile strength of 60 GPa and 1200 MPa respectively, provided by the manufacturer and based on nominal properties.

Three different insulation materials were tested: XPS, EPS, and PIR. The tension and compressive strength of the three insulation materials were tested according to ASTM C165 (2017). Results from these tests as well as density and U-value are provided in Table 3.2.

Table 3.2: Insulation material properties

Property	XPS	EPS	PIR
Tensile strength, MPa	0.61 ± 0.02	0.25 ± 0.03	0.10 ± 0.03
Compressive strength, MPa	0.31 ± 0.01	0.13 ± 0.01	0.16 ± 0.01
Density, kg/m3	27.1	24.0	29.9
U-Value[a], W/m.K (per 25 mm)	0.020	0.031	0.023

[a] – Manufacturer's reported value. Other properties measured based on ASTM C165 (2017)

3.6 TEST SETUP AND INSTRUMENTATION

Test specimens were loaded through the centre wythe using a 529 kN hydraulic actuator at a rate of 1 mm/min to allow for initial settling of the specimens. After initial settling (when the average wythe slip read 0.5 mm), the loading rate was increased to 2 mm/min. The bottom faces of the outer wythes were supported by 75 × 75 mm steel supports (Fig. 3.3(a)), while the sides were

restrained to prevent excessive wythe rotation using steel blocks measuring 320 × 300 × 20 mm clamped to the loading platform (Fig. 3.3(b)). Tests were stopped once the load decreased to two-thirds that of the peak load.

After initial testing and as observed in Arevalo and Tomlinson (2020), the shear connection system may become damaged (i.e. lose stiffness and have permanent deformation) if connectors are subject to large enough forces like those in a stiff panel subject to a large temperature differential. To investigate this damage, load-unload cycling was carried out on some samples (Table 3.1) using the setup presented earlier. Load-unload cycling was done by loading specimens to 40 kN and then reducing the load to 20 kN. This force, i.e. 20 kN per connector, was selected as it was the estimated maximum force in 9.5 mm GFRP connectors with the same design as those tested here under a temperature differential of 20°C (Arevalo and Tomlinson (2020). Specimens were then reloaded until they averaged 1 mm slip, relaxed to one-third the load value corresponding to 1 mm slip, loaded until 2 mm slip, relaxed to one-third the load value at 2 mm, loaded until 3 mm slip, relaxed to one-third the load value at 3 mm, then loaded to failure. The loading rate for load-unload cycling was the same as that for monotonic testing (1 mm/min until settling then 2 mm/min afterwards).

Relative slip between wythes was measured using Linear Variable Differential Transformers (LVDTs) mounted on each of the exterior wythes on the front and back of the specimen (four LVDTs total). A small aluminum angle was attached to the inner concrete wythe to serve as a reference. Reported LVDT readings were averaged values from all four LVDTs. There were no significant differences between the LDVT readings until well after the peak load was reached in all tests. DIC was also used to measure deformations and evaluate notch effectiveness. A Canon EOS Rebel T7i camera captured images every 15 seconds, with a resolution of 6000 × 4000 pixels. This interval was chosen to capture three key stages during testing (debonding, start of tearing, and rupture of insulation) that are time-traced to load data for assessment using VIC-2D software.

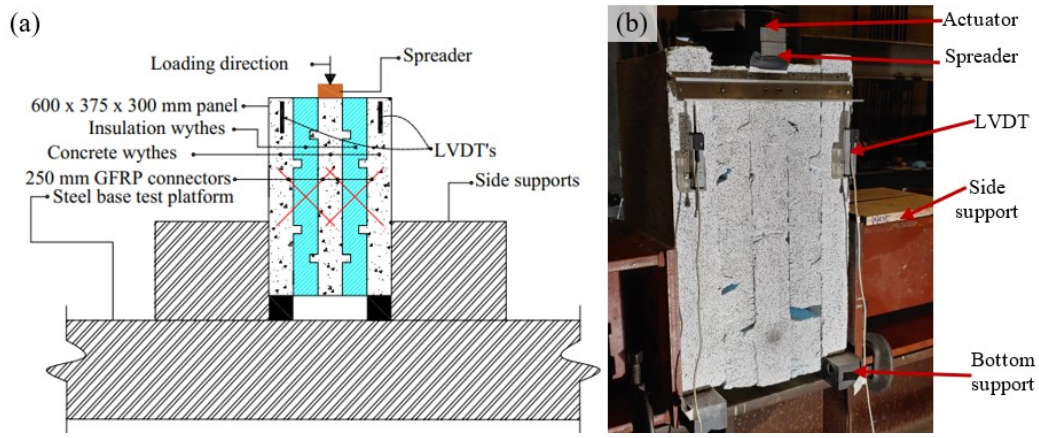

Figure 3.3: (a) Schematic diagram (b) Photo of test setup.

3.7 RESULTS

3.7.1 General load-slip relationship – monotonic testing

Averaged load-slip results, showing the general response of all three tests for each specimen type, are shown in Fig. 3.4. Load-slip curves for each test are shown in Fig. 3.5. In all tests, the reported load is the total load applied to the specimen (i.e. load read by the load cell attached to the actuator). The general results from each of the 24 tests are shown in Table 3.3. Differences in load values for some repetitions are relatively large which has been observed in previous push-through tests (Tomlinson et al. 2016, Woltman et al. 2013). These differences are attributed to specimen handling and variability compounded by the combination of concrete, connector, insulation, and geometric variability.

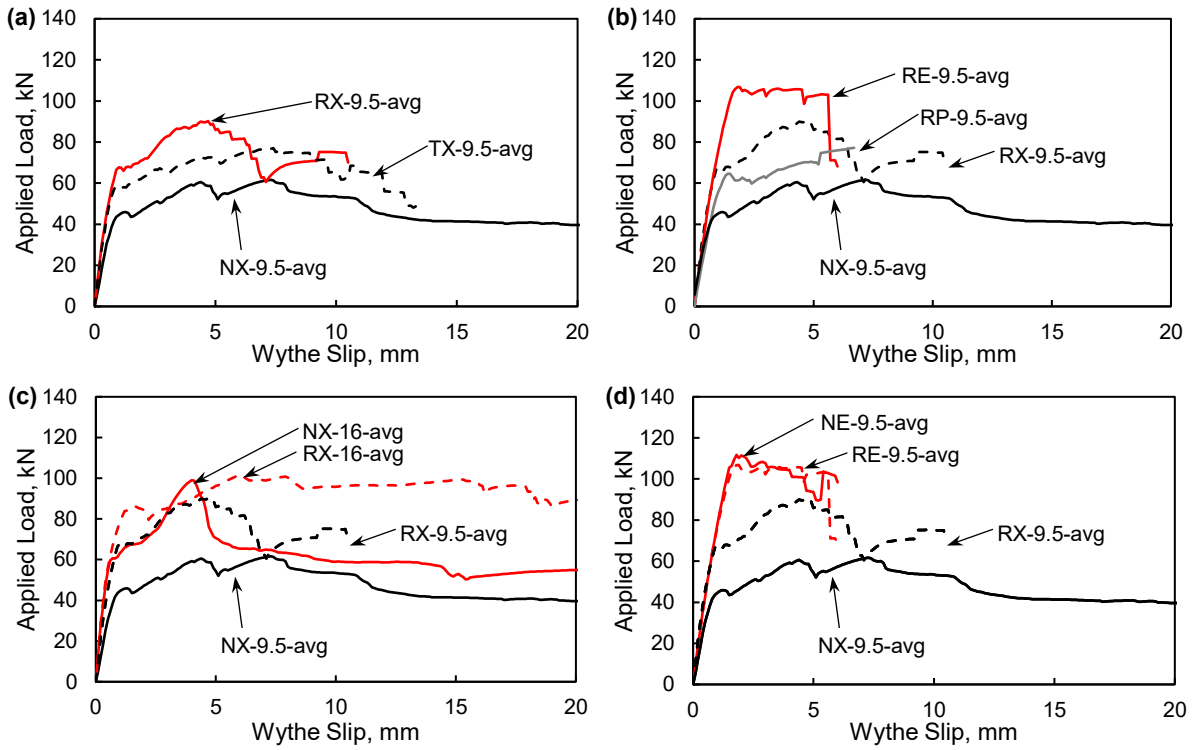

Figure 3.4: Averaged load-slip responses. Reference line showing average response of NX-9.5 included on each plot. (a) effect of notch type, (b) effect of insulation type, (c) effect of connector size and (d) effect of insulation

Table 3.3: Results from direct shear push-through tests. Load values are the total load applied per specimen.

	Proportional Limit, P.L.			Peak Load			Shear Flow		Deformability Index (DI)	Stiffness	
ID	Load, kN	Mean, kN	Slip at P.L, mm	Load, kN	Mean, kN	Slip at peak, mm	Maximum shear flow, kN/m	Mean, kN/m		Stiffness, kN/mm (Eq. 3.1)	Mean, kN/mm
NX-9.5	47.7 34.6 33.5	38.6 ±7.9	0.81 0.71 0.49	58.6 64.1 67.4	63.4 ±4.5	7.77 10.6 4.41	48.8 53.4 56.2	52.0 ±4.0	18.6	71.1 60.0 67.7	66.3 ±5.7
NX-16	51.5 55.1 50.3	52.3 ±2.5	0.47 0.40 0.48	95.7 83.6 107	95.3 ±11.5	4.22 12.2 4.08	79.8 69.7 89.2	79.3 ±9.0	26.9	136.0 125 103.2	121.4 ±16.7
RX-9.5	53.8 51.9 52.4 a	52.7 ±1.0	0.61 0.63 0.59	101 97.1 87.4	95.1 ±6.9	4.39 5.90 5.18	84.2 80.9 72.8	79.3 ±6.4	15.3	98.7 91.8 99.2	96.6 ±4.1
TX-9.5	45.9 45.6 48.2 a	46.6 ±1.4	0.60 0.59 0.49	71.4 80.4 89.4	80.4 ±9.0	7.23 4.56 8.07	59.5 67.0 74.5	67.3 ±7.0	20.4	83.7 82.3 102.74	89.6 ±11.4
RX-16	50.4 51.1 50.9 a	50.8 ±0.4	0.44 0.47 0.38	111 102 107	107 ±4.7	18.0 5.61 8.49	92.5 85.0 89.2	88.7 ±4.2	52.2	112.9 114.2 151.7	126.3 ±22.0
NE-9.5	41.3 51.5 41.0 a	44.6 ±6.0	0.50 0.60 0.47	133 105 112	117 ±14.6	2.35 1.41 1.95	110.8 87.5 93.3	97.3 ±11.4	9.5	80.0 82.9 91.5	84.8 ±6.0
RE-9.5	48.8 51.3 50.3 a	50.1 ±1.3	0.57 0.57 0.60	110 114 102	109 ±6.2	3.64 2.07 2.05	91.7 95.0 85.0	91.3 ±5.0	9.7	78.6 87.7 90.0	85.4 ±6.0
RP-9.5	30.5 34.1 35.2 a	33.3 ±2.5	0.48 0.54 0.58	64.3 82.7 73.8	73.6 ±9.2	4.90 6.63 1.99	53.6 68.9 61.5	62.0 ±8.0	18.7	64.1 60.5 66.7	63.8 ±3.1

± indicates standard deviation

[a]load-unload cyclic test

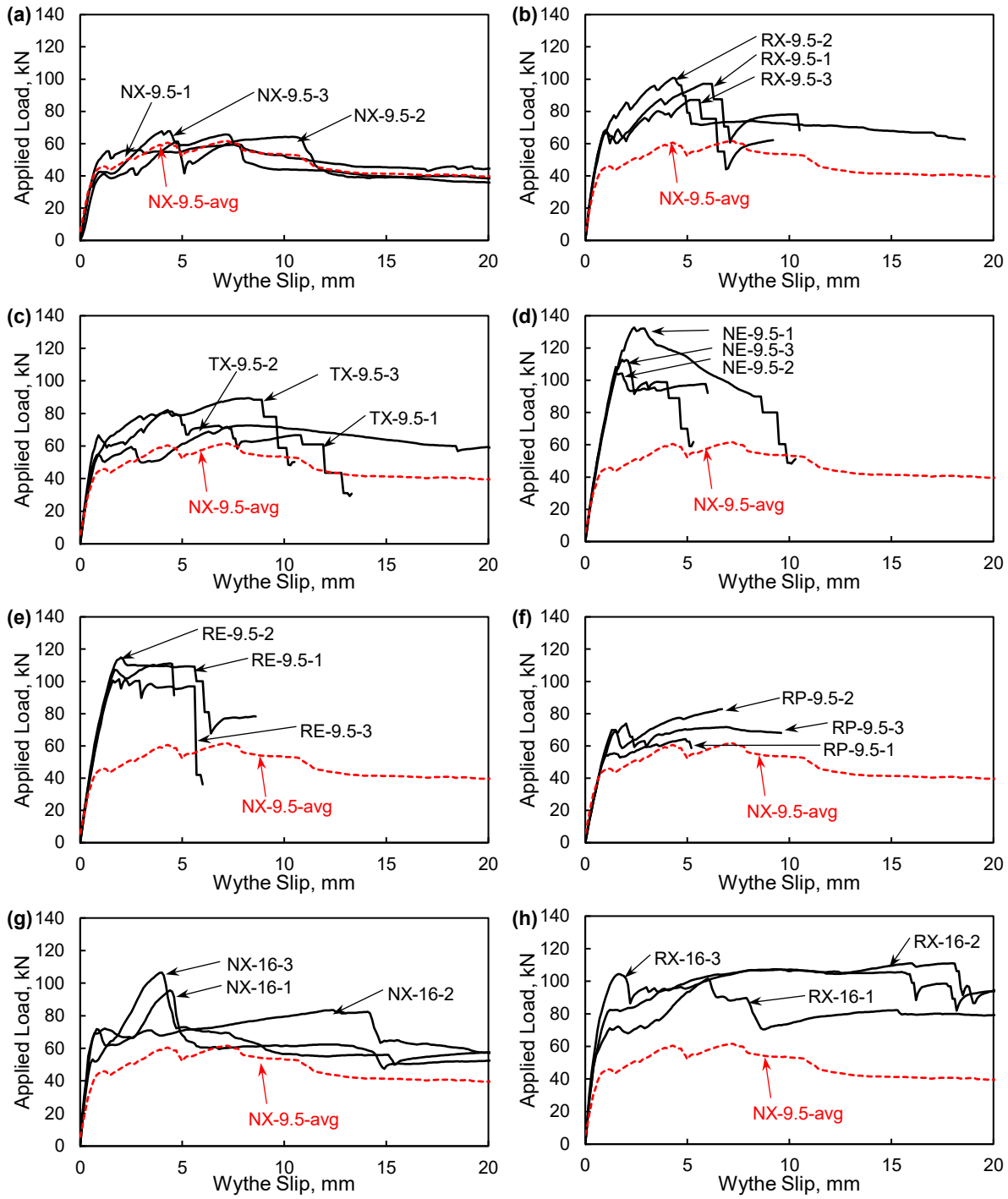

Figure 3.5: Load-slip responses. Reference line with average response of NX-9.5 included on each plot. Load-unload cycles not shown for clarity (data presented in Fig. 3.6). All loads are the total load applied on the specimen (a) NX-9.5 (b) RX-9.5 (c) TX-9.5 (d) NE-9.5 © RE-9.5, (f) RP-9.5, (g) NX-16, (h) RX-16

The general load-slip response can be grouped into three phases. The first phase is linear with relatively high stiffness. The second phase, characterized by load exceeding the proportional limit (i.e. the point where the response first becomes non-linear), had considerably lower stiffness and occasional load drops. The final phase, which occurred once the peak load was reached, is

characterized by sudden or gradual drops in load depending on the failure mode. The transition points between these phases are reported in Table 3.3. While the peak load is easily identifiable from Fig. 3.4 and 3.5, the proportional limit is not and was evaluated by determining the point where the initial linear response departs its secant as per Arevalo and Tomlinson (2020).

3.7.2 General load-slip relationship – load-unload cyclic testing

The load-slip responses of specimens subject to load-unload cycling are shown in Fig. 3.6. For all specimens, the response is essentially linear for the first loading phase (0 to 40 kN), a trend also observed in the unloading/reloading stages. As slip increased, specimens lost stiffness and experienced residual deformation during unloading and reloading cycles. The overall 'backbone' response of these tests, including peak load and proportional limit, of the load-unload cycling, were similar to the monotonic tests (Fig. 3.5) with variations attributed to general specimen variability rather than damage from load-unloading cycles.

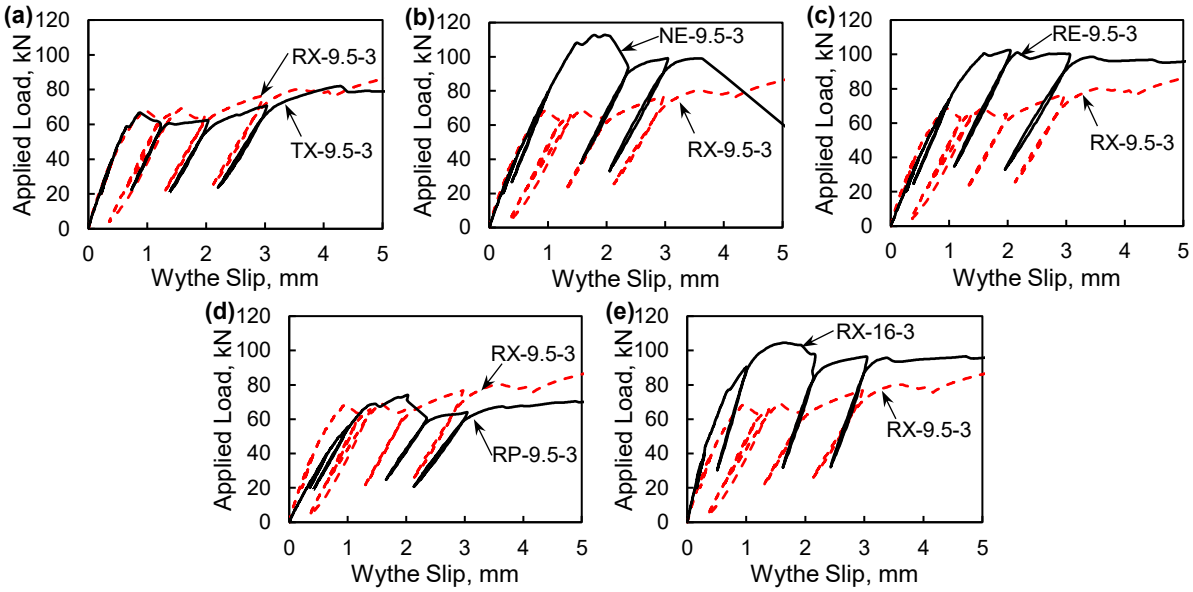

Figure 3.6: Load-slip relationship from load-unload cyclic testing. Response up to 5 mm slip shown for clarity (full response in Fig. 3.5) (a) RX-9.5 and TX-9.5 (b) NE-9.5 (c) RE-9.5 (d) RP-9.5 (e) RX-16

3.7.3 Stiffness

The procedure used in calculating the initial shear connection stiffness, k_p, shown in Table 3.3 follows the secant method used by Arevalo and Tomlinson (2020). The stiffness is evaluated using slip ($s_{p_{40\%}}, s_{p_{10\%}}$) and load ($F_{p_{40\%}}, F_{p_{10\%}}$) values at 10 and 40% of the peak load (Eq. 3.1). If $F_{p40\%}$

was greater than the proportional limit, the proportional limit load and slip were taken as the upper limit.

$$k_p = \frac{F_{p_{40\%}} - F_{p_{10\%}}}{s_{p_{40\%}} - s_{p_{10\%}}} \tag{3.1}$$

In the load-unload cycling tests, the stiffness of the reloading branches was calculated using a secant based on the point where the specimen was initially reloaded (i.e. one-third of the initial unloading force) and the point where the specimen was reloaded to 80% of the initial unloading force. This secant was extrapolated to the x-axis to determine permanent deformation (Fig. 3.7).

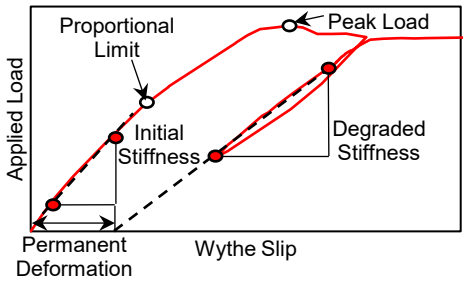

Figure 3.7: Illustration of initial stiffness, degraded stiffness, and permanent deformation.

3.7.4 Post-test inspection and failure modes

For NX-9.5 and RX-9.5, the dominant failure mode was the pull-out of the connectors (Fig. 3.8(a)) with some evidence of connector crushing (Fig. 3.8(b)). For NX-16, concrete crushed locally around the connectors (Fig. 3.8(c)). At the peak load of notched specimens with XPS insulation, the insulation suddenly ruptured horizontally (Fig. 3.8(d)). Some notches broke off in some specimens (Fig. 3.8(d)) but this occurred well after peak load was reached. There were consistent formations of horizontal bands on the insulation at notches that indicate foam crushing (Fig. 3.8I) which illustrates their effectiveness at transferring loads. For TX-9.5, failure was by connector rupture (Fig 3.8(f)) accompanied by foam crushing and prying at the notch interface (Fig 3.8(g)). Prying is defined as a wedging action that shifts the insulation away from the concrete wythe. For EPS samples (NE-9.5, RE-9.5), failure was initiated through insulation diagonal splitting (Fig 3.8(h)). For RE-9.5, this failure mode is consistent with Mitra (2010) for panels with semi-circular shear keys and PVC insulation. NE-9.5 and RE-9.5 ultimately failed by either rupturing or pull-

out of the connectors (Fig 3.8(a), 8(f)). Unlike the XPS specimens, EPS remained attached to the concrete, illustrating that the concrete-insulation bond was still active (Fig. 3.8(i)).

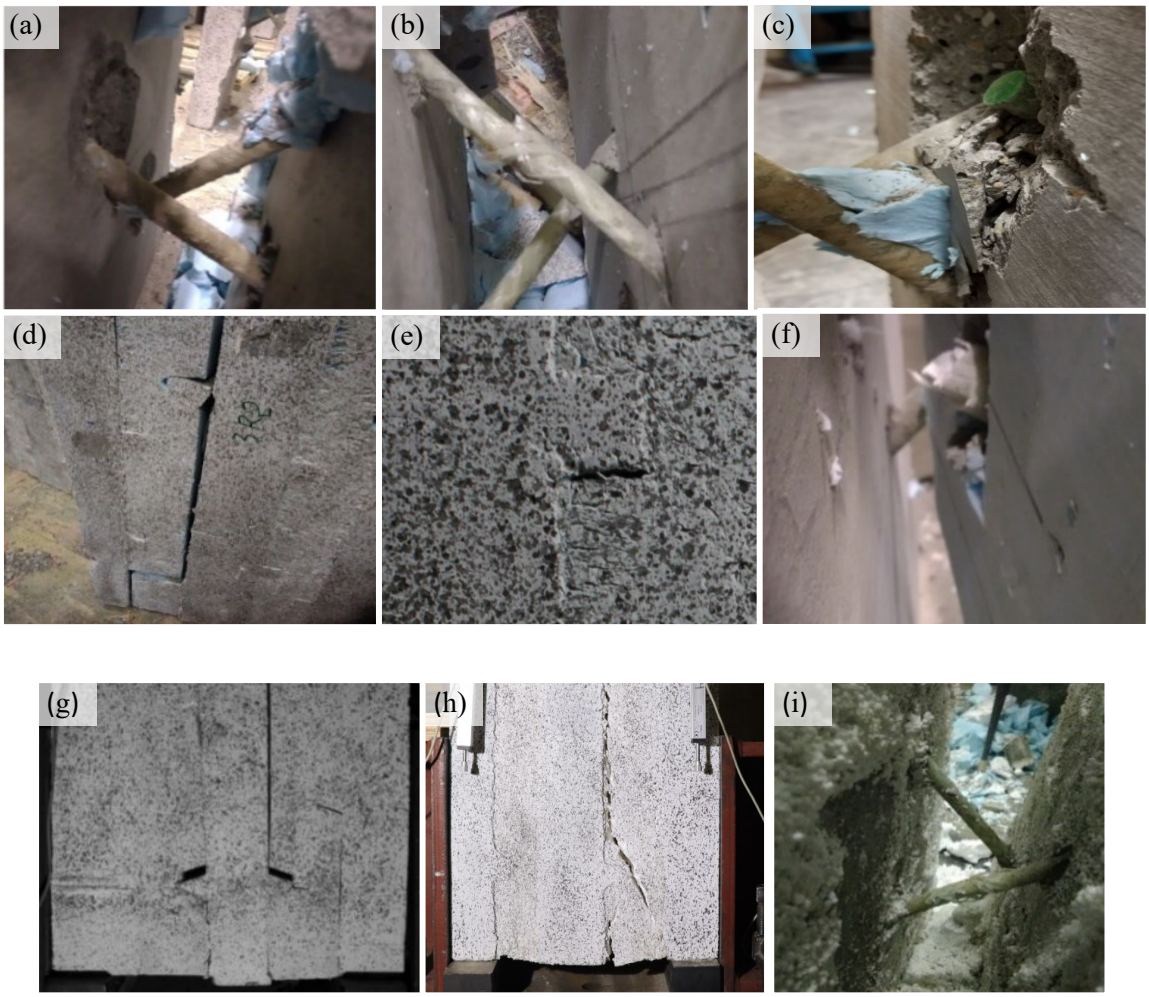

Figure 3.8: Post-test investigation (a) connector pull-out (b) compression failure of connector (c) Blow-out of concrete around the connector (d) breaking of notches and tensile failure of insulation at rectangular notch interface © crushing of insulation bearing against notches (f) connector rupture (g) insulation bearing failure and prying around trapezoidal notch (h) diagonal splitting of insulation (i) EPS bonded to concrete.

3.7.5 Deformability index (DI)

The Deformability Index (DI) is analogous to ductility (which is more appropriate for steel-reinforced concrete structures). The method from Theriaule and Benmokrane (1998) was used to calculate DI in each test (Table 3.4). Other methods (e.g. curvature approaches) exist but are not used here since these panels are not subject to bending.

$$DI = \frac{P_U \, \delta_u}{P_{PL} \, \delta_{PL}} \tag{3.2}$$

The subscripts U and PL refer to the peak value and proportional limit, while P and δ indicate the respective load and deflection.

3.7.6 Digital Image Correlation (DIC) analysis

DIC was used to evaluate the effectiveness of the notch and insulation. The insulation contribution was categorized into three major stages as illustrated in Fig. 3.9. These transitions developed as the vertical displacement increased. At Stage 1, the insulation to concrete bond fails, shown in DIC by a sudden colour change at the concrete/insulation interface (Fig. 3.9(a), Fig. 3.9(d)). At Stage 2, the insulation starts to tear away from the notch as stress concentrations at the notch initiate a crack in the insulation (Fig. 3.9(b), Fig. 3.9I). At Stage 3, the insulation layer tears completely through (Fig. 3.9(c), Fig. 3.9(f)), which occurred immediately after the peak load was reached. The load corresponding to each stage is reported in Table 3.4. Some specimens (e.g. XPS without notches) only saw Stage 1 since the insulation contribution was largely lost once the insulation-concrete bond failed. Other specimens (e.g. EPS) only saw Stages 2 and 3 as the insulation-concrete bond remained active for the entirety of the test (Table 3.4).

Table 3.4: Stages of Notch Contribution

Stage	RP-9.5, kN	NE-9.5, kN	RE-9.5, kN	RX-9.5, kN	TX-9.5, kN	RX-16, kN
1 (insulation-concrete bond failure)	53.5	120.1	90.5	N/A	58.3	N/A
2 (initiation of insulation tearing)	53.5	N/A	103.7	65.1	65.2	76.5
3 (insulation rupture)	53.5	N/A	109.7	97.2	69.2	78.1

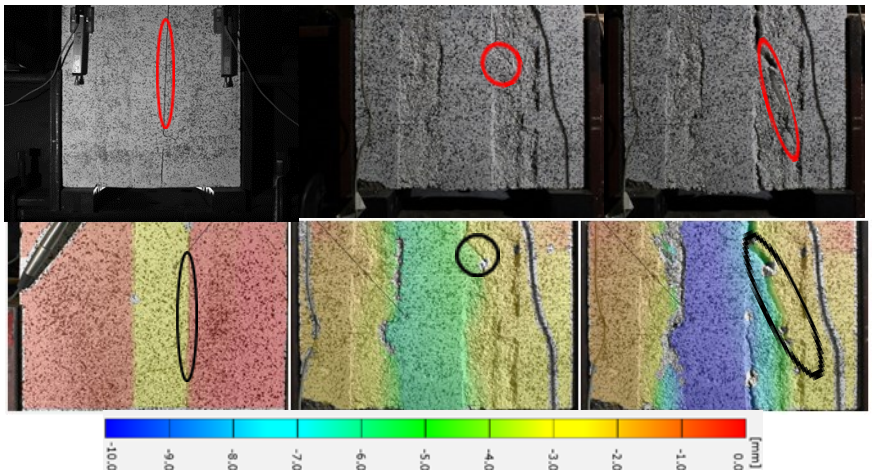

Figure 3.9: Stages of Insulation Contribution (a) Stage 1 photo: insulation debonding between notches, (b) Stage 2 photo: initiation of tear at notches, (c) Stage 3 photo: complete tear of insulation at notches, (d) Stage 1 DIC colourmap © Stage 2 DIC colourmap, and (f) Stage 3 DIC colourmap. All DIC colourmaps use the same scale and show vertical deformations.

Vertical deformation fields from DIC are shown in Fig. 3.10. These results are from four tests (NX-9.5-3, RX-9.5-1, TX-9.5-2, and RE-9.5-1) selected as representatives (the other tests had similar results). Major principal strain fields effective at indicating local damage due to insulation bond failure, concrete cracking, or insulation tearing are shown in Fig. 3.11. These strain readings are based on adjacent DIC text patches and can be distorted since cracking at the concrete-insulation interface (i.e. discontinuities) affects the ability of DIC to accurately track strains. The fields in Fig. 3.10 and 3.11 are shown at four parts of each test to facilitate comparison between parameters early into the test (1 mm), after the proportional limit (3 mm), close to the peak load (5 mm), and post-failure (10 mm).

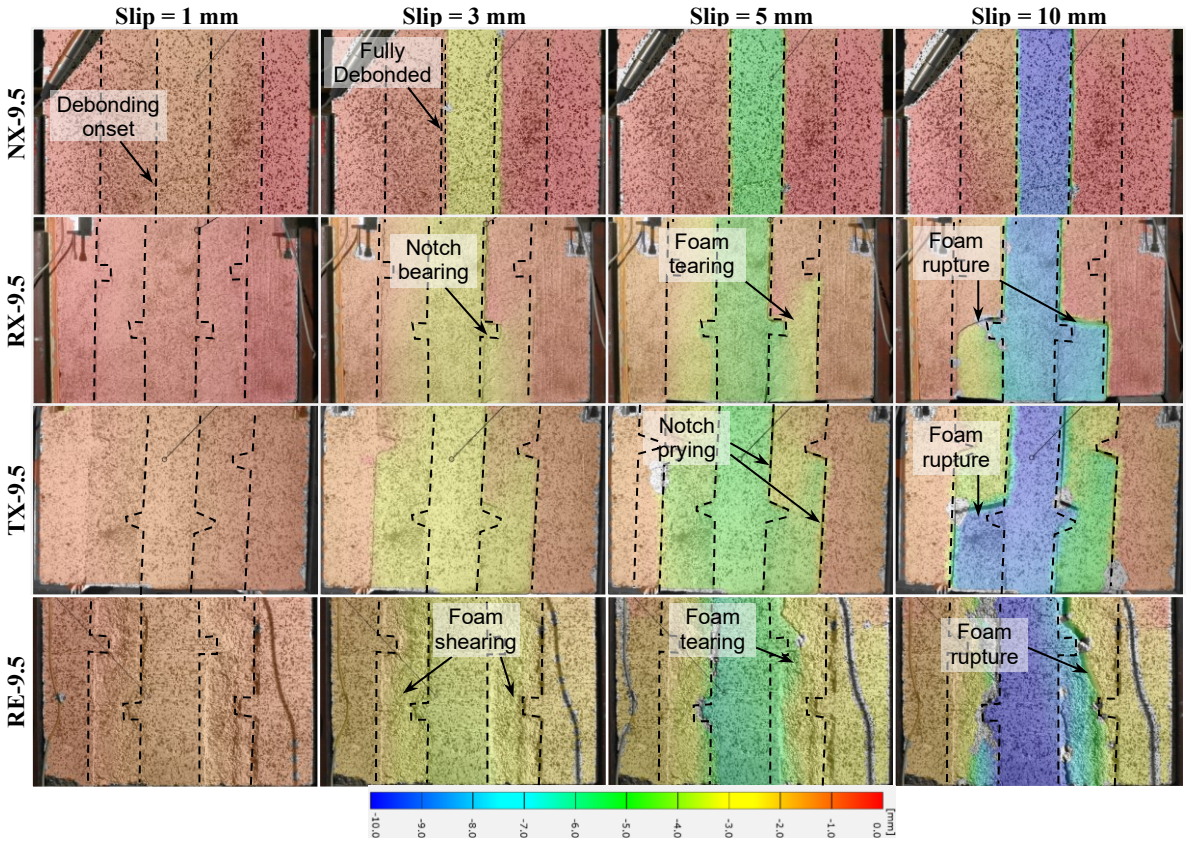

Figure 3.10: DIC vertical deformation fields. Selected tests are representative (other tests from the same parameter behaved similarly). Concrete-insulation interfaces indicated with dashed black lines. All images were plotted on the same scale (note: negative deformation = downwards).

3.8 CHAPTER DISCUSSION

3.8.1 Connector size

As expected, peak load increases with connector size. For panels with XPS insulation and without notches (NX-9.5, NX-16), the load at the proportional limit and peak load increased by an average of 36 and 50% respectively when the connector diameter increased from 9.5 mm to 16 mm. Although larger bars have larger load capacity, the increase is not proportional to the increase in connector area (2.4 times). The reduced effectiveness of the larger connectors is attributed to the failure mode changing from connector rupture or pullout to concrete crushing and indicates that, for the considered wythe proportions and materials, it is more effective to use smaller connectors. For specimens with XPS and notches (RX-9.5, RX-16), the change in bar diameter had minimal effect on the proportional limit and peak load (Table 3.3), indicating that the 16 mm connector attracted more of the load which reduced the insulation contribution.

In XPS specimens without notches (NX-9.5, NX-16), stiffness increased 1.8 times when larger connectors were used. This shows that connectors dominate the stiffness of systems without notches where the insulation contribution is limited even early into the test. The effect of connector diameter on stiffness was considerably reduced (down to 1.3 times) for XPS specimens with notches (RX-9.5, RX-16). The 16 mm connectors' axial stiffnesses (which dominates how the load is carried by the connectors when wythes slip relative to each other (Tomlinson et al. 2016) are considerably higher than the shear stiffness of the insulation. This means that enabling insulation to contribute via notches had a negligible effect on stiffness between NX-16 and RX-16. However, the insulation contribution was more apparent between NX-9.5 and RX-9.5 since the load carried by the connectors relative to the insulation was reduced.

Interestingly, the peak loads and proportional limits of NX-16 and RX-9.5 were very similar, which shows that in place of increasing connector size, notches can be used to increase the capacity of shear connections by engaging the foam. However, NX-16 was considerably stiffer than RX-

9.5 so if higher stiffness is desired it is more effective to use larger connectors than to add notches to the insulation for systems such as those considered in this paper.

DI is used to quantify the amount of warning expected before failure. Tests with 16 mm connectors had larger DI, attributed mostly to their lesser deformations at the proportional limit relative to the 9.5 mm connectors. This indicates that panels with larger connectors show a more pronounced non-linear response. However, since larger connectors also prompt more slip under thermal bowing (Arevalo and Tomlinson 2020) they are more likely to become non-linear under temperature effects.

3.8.2 Notch shape in panels with XPS insulation

The effect of notch shape on panel response is shown in Fig. 3.4(a). As mentioned in Section 3.7, the stiffness of the unnotched XPS specimens was lower than their notched counterparts because the insulation bond failed early in the test. This is shown in Fig. 3.11, where insulation debonding is noticeable for NX-9.5 even at 1.0 mm slip. Insulation debonding was also observed in notched specimens but the insulation force transfer mechanism changes to bear against notches and allow the insulation to contribute to the panel stiffness after Phase 1.

Rectangular notches were effective at increasing the proportional limit (averaging 37%) and peak load (averaging 50%) relative to tests without notches. Trapezoidal notches were also effective but to a lesser degree, increasing the proportional limit (averaging 21%) and the peak load (averaging 27%) compared to a test without notches. The reason trapezoidal notches are less effective is that trapezoidal notches act as wedges that pry the insulation away from its bearing surface, consequently reducing its capacity (Fig. 3.11). The benefit of this action is that these tests deform more before failure (Fig. 3.4(b)) leading to a higher DI (20.4) for TX-9.5 compared to RX-9.5 (15.3). The additional tension in connectors caused by prying also increased the risk of connector rupture in tension (Fig. 3.8(b), Fig. 3.8(f)). Note that RX-9.5 had lower DI than NX-9.5 (18.6) which is attributed to the lower proportional limit load in NX-9.5.

The effectiveness of the notches between the proportional limit and peak load can be seen in DIC deformation (Fig. 3.10) and strain fields (Fig. 3.11). Considering the deformation at 3 mm in Fig. 3.10 and 3.11, which is most representative of the response between the proportional limit and the peak load, the abrupt colour change between wythes and insulation in NX-9.5 indicates that there is a discontinuity (i.e. bond failure) between the middle wythe and the insulation. Though discontinuity was also observed in RX-9.5 and TX-9.5, the deformation field is continuous where the notch bears against the insulation in compression, indicating that the notches are effectively transferring forces to the insulation. Near the end of this stage, insulation began to crush locally against the notch in compression (Fig. 3.8I) and tear beginning at the region of the notch interface that is in tension (i.e. Phase 2 in Fig. 3.9) which caused occasional load or stiffness drops. Drops in load and stiffness in this region are also attributed to the connectors themselves, particularly localized crushing at the connector/concrete interface and non-linearity of the connectors caused by longitudinal shear on the resin but the onset of these factors could not be determined directly.

Specimens with rectangular notches failed soon after reaching the peak load by insulation rupture (Fig. 3.4(b)), which was abrupt and occurred horizontally (Fig. 3.8(d), Fig. 3.10). Around the same time, noises were heard within the specimen indicating connector failure (e.g. pullout, crushing) but these failures were unable to be tracked visually until after the test was complete.

As mentioned earlier, notch contribution is not observed with larger connectors as the load at the proportional limit was 3% lower for RX-16 (relative to NX-16) while the peak capacity was 12% higher. This is due to the higher stiffness of the larger diameter connectors which makes them attract more load, thereby reducing the insulation's effectiveness and contribution. Meanwhile, panels with smaller diameter connectors experienced greater insulation contribution.

From the phased insulation contribution monitored through DIC (Fig. 3.9 and Table 3.4), RX-9.5 and RX-16 did not experience Phase 1 due to the locking mechanism provided by the notches but those with small connectors (9.5 mm) carried 49% additional load relative to those without notches before the notch tears through the insulation. On average this additional load gain is 6.1%

and 5.8% for TX-9.5 and RE-9.5 respectively and negligible for RX-16 and RP-9.5 (Table 3.4). The panels made with EPS and without notches (NE-9.5) do not have the sequential transition from Phase 1 to Phases 2 and 3 as the insulation-concrete bond remained active for the entirety of the test (refer to Fig. 3.10 and 3.11 where necessary).

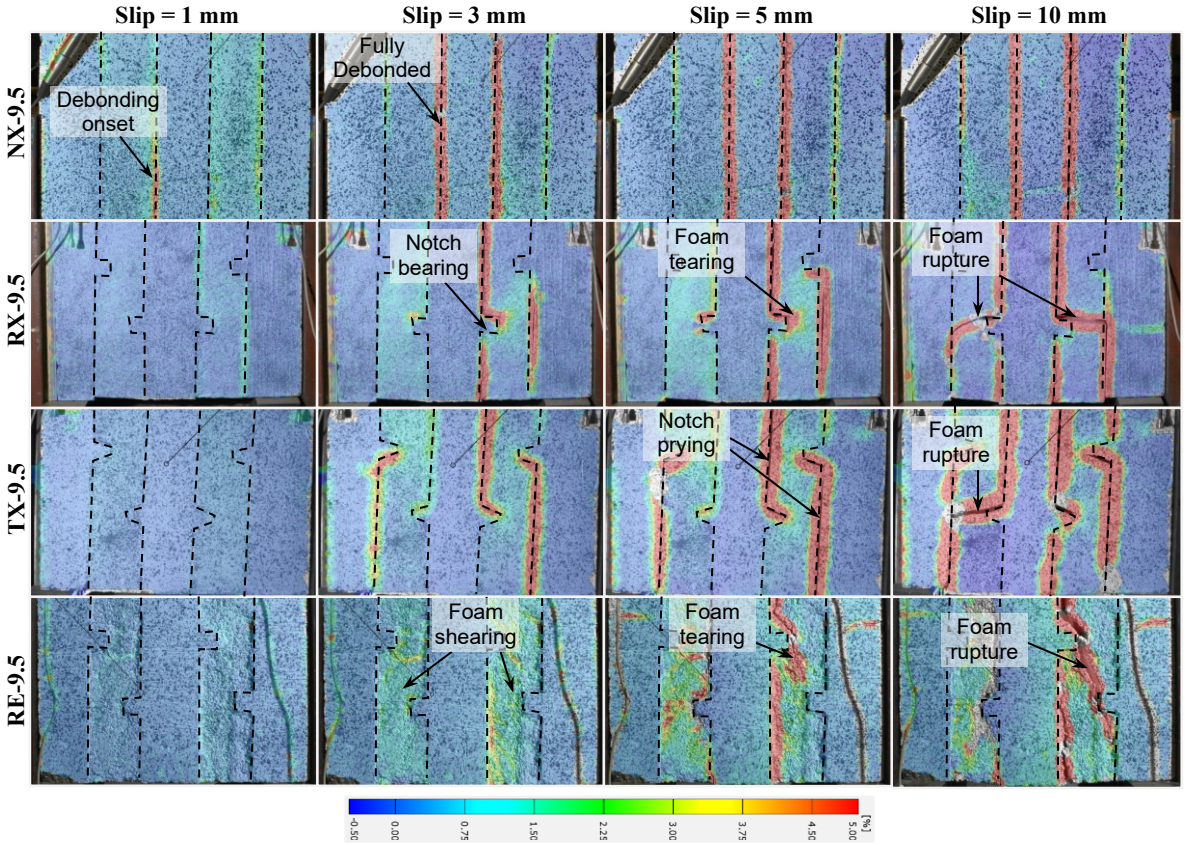

Figure 3.11: DIC major strain readings comparing adjacent texture patches for qualitative assessment of insulation-concrete bond and cracking. Selected tests are representative (other tests from the same parameter behaved similarly). Concrete-insulation interfaces indicated with dashed black lines. All images were plotted on the same scale (note: positive strain = tension).

3.8.3 Insulation types and notch effectiveness

The unnotched EPS tests (NE-9.5) had, on average, 16% larger proportional limits and 46% larger peak loads relative to the unnotched XPS (NX-9.5). Similarly, the stiffness of NE-9.5 was 27% higher, on average, than NX-9.5. Although the EPS used in this test has a lesser compressive strength than the XPS, these increases are primarily attributed to the additional contribution of the insulation that was lost in NX-9.5 once the insulation-concrete bond failed.

The notches were noticeably less effective for EPS tests than their XPS counterparts (Fig. 3.4(d)), with notched EPS tests mostly having lower strength and stiffness. Although notched EPS

specimens (RE-9.5) were seen to have larger proportional limits than NE-9.5, variability is large enough that the effect of notches slightly increasing the shear stiffness of EPS by reducing the insulation thickness at the notch location cannot be confirmed. Notched EPS panels were slightly weaker than the unnotched EPS panels. This is contradictory to the findings with XPS and attributed to the different force transfer mechanism through EPS. The insulation-concrete bond lost early in NX-9.5, remained active until failure in NE-9.5 which reduced the effectiveness of the notches (i.e. notch contribution is minimal if the insulation-concrete bond remains active). The insulation failure plane, diagonal for RE-9.5 and NE-9.5 then rectangular for RX-9.5, shows different force transfer mechanisms between EPS and XPS.

Diagonal cracks in EPS infer that the principal tensile stress acted on an angle and was dominated by shear, which also shows that the insulation bond was active. In the notched XPS tests, where insulation failed on a horizontal crack, had principal tensile stresses acting in the direction of the wythe slip. The location of these cracks on the tension side of the notch shows that stress concentrations are caused by the notch-initiated insulation failure (between Stage 2 and Stage 3 of the notch contribution illustrated in Fig. 3.9). The diagonal crack in RE-9.5 passed between notches in a shorter path than that in NE-9.5, which reduced the amount of insulation acting in tension and led to the decrease in capacity from NE-9.5 to RE-9.5.

The PIR insulation used in RP-9.5 had a fibreglass facing which was bonded to the PIR as part of the fabrication process. This facing was rough enough to give RP-9.5 adequate concrete-insulation bond throughout the test, leading to similar force transfer mechanisms to the EPS tests (including the same diagonal failure plane). However, the PIR used in the tests had lower compressive and tensile strength than XPS so its contribution to panel resistance was lower, only giving a slight increase in peak load (16%) relative to unnotched panels where the insulation-concrete bond failed early into the test (NX-9.5).

Similar to what was observed with strength, notches were considerably more effective at increasing the stiffness of tests with XPS insulation. Notch effectiveness is attributed to the failure

of the insulation-concrete bond in NX-9.5 early into the test while RX-9.5 and TX-9.5 were able to redistribute insulation force demands to the notches. Notches did not significantly affect the stiffness of tests with EPS and the insulation-concrete bond remained active throughout the test. Despite the higher density of PIR due to the glass-facing, the PIR insulation had lower tensile strength, and the panels noticeably had lower stiffness than the other tests. These findings also indicate that notches are effective for insulation types with higher strength.

The panels with EPS insulation had lower DI and showed less warning of failure than the other systems. This is attributed to the general response of the EPS panels, which did not have the pronounced lower stiffness region that occurred after the proportional limit that was seen in tests with XPS or PIR insulation.

3.8.4 Stiffness degradation and permanent deformation

The load-slip curves were presented in Fig. 3.6. These curves were processed as illustrated in Fig. 3.7 to determine the specimen stiffness and permanent deformation. These values are reported in Fig. 3.12.

All specimens lost stiffness as the slip upon unloading increased (Fig. 3.12(a)). Loss of stiffness is attributed to damage in the specimen. Initially, the damage is linked to localized concrete crushing around the connectors and continual failure of the insulation-concrete bond (in tests with XPS insulation). Later on, closer to failure, damage is also caused by the onset of insulation crushing (in RX-9.5, TX-9.5, and RX-16), concrete cracking around the connectors, and connector non-linearity.

These trends differed based on insulation type and are best observed when looking at the percentage of stiffness retained (Fig. 3.12(b)). Stiffness loss was more gradual in tests with EPS and PIR insulation because the insulation-concrete bond remained active in those tests, which was not the case for tests with XPS insulation. The losses in RX-9.5 and TX-9.5 were beyond the initial proportional limit at even low slip (1 mm) and behaved very similar to each other (Fig. 3.6(a)). Though the notches were effective at transferring forces through the insulation, there was still a

notable loss of stiffness after Phase 1 of the insulation contribution as well as once the insulation at the notch began to crush later in the tests. RX-16 did not lose stiffness as quickly as RX-9.5 since the 16 mm connectors accounted for a larger proportion of the stiffness in those tests.

Similarly, EPS and PIR specimens had smaller residual deformation than those with XPS (Fig. 3.12I). This was particularly evident at around 1 mm where the panels with XPS insulation had around three times the residual deformation of those with EPS because the insulation-concrete bond was still active in the EPS and PIR tests. Later on, the response was more so dictated by damage in the concrete and shear connectors which showed similar responses in all tests with residual deformation accounting for half to two-thirds of the maximum deformation by the time the wythe slip reached 3 mm.

These results show that significant connection stiffness is lost under repeated loading even under low (~1 mm) magnitudes of relative wythe slip. Similarly, walls with the same connector configuration as NX-9.5 had slips exceeding 1 mm under a thermal gradient of 20°C (Arevalo and Tomlinson, 2020) which represents loading situations that panels experience in practice. The loss of stiffness was observed in these panels with stiff connectors in that study. Loss of shear connection stiffness, particularly in regions near the end of the panel that are expected to slip more than others, is also expected to reduce the thermal bowing under future load cycling since bowing is a function of connector stiffness. However, this comes at the cost of permanent deformation (some bow may be permanent) and higher deflections under external loads like wind. These effects may not be as pronounced with less stiff connection systems (e.g. pin-type connectors) since stresses induced on connectors and concrete are reduced under the same amount of relative wythe slip.

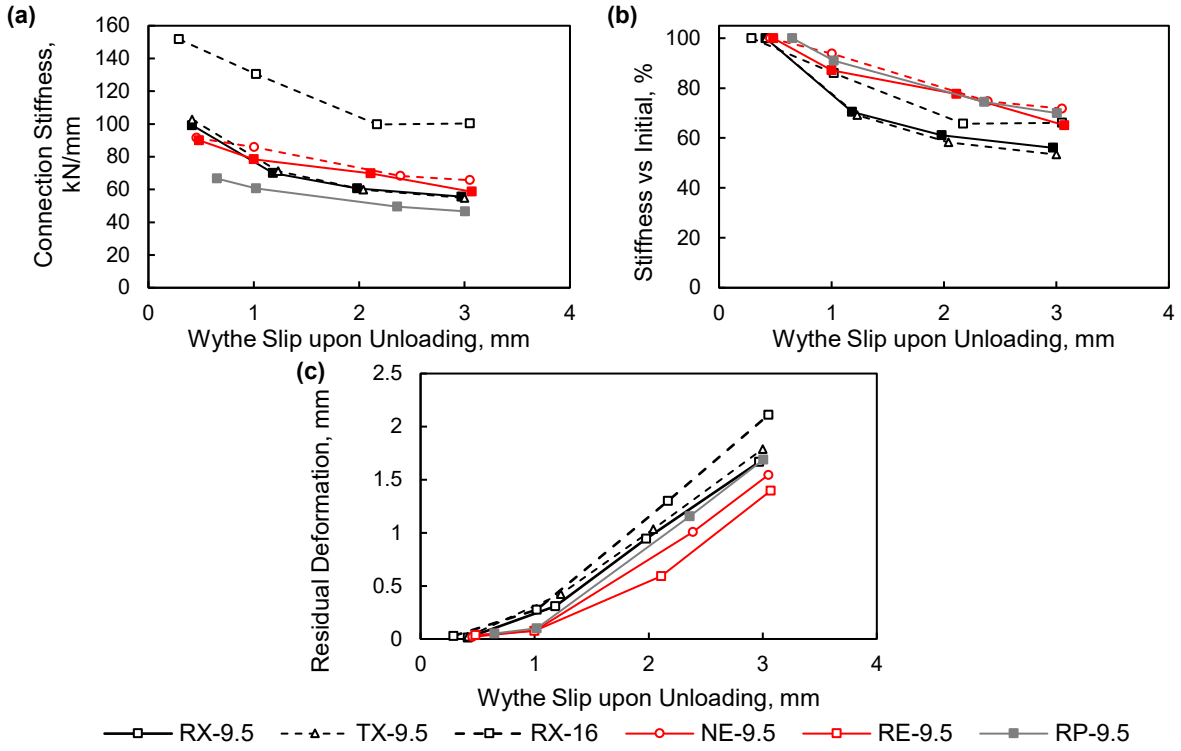

Figure 3.12: Load-unload cyclic test results illustrating changes in connection stiffness and residual deformation as the maximum wythe slip before unloading increases. Plots include (a) Connection stiffness degradation (kN/mm), (b) connection stiffness degradation (as a percentage of the first loading cycle), and (c) residual deformation (mm).

3.9 GENERAL ASSESSMENT

For panels with XPS insulation, the notch mechanism is effective as the peak load increased on average by 50% and 27% when rectangular and trapezoidal notches are used in combination with 9.5 mm connectors. When larger connector sizes are used, the peak load was also boosted by 12%.

Another means of comparison is shear flow and stiffness. The normalized parameter per metre (kN/m/m) is the value from each test in kN/m multiplied by $1/l_{rp}$, where $l_{rp}$is the height (m) of panels used in various studies. The results in Table 3.3 show higher shear flow capacity and stiffness in systems with notches, as well as for the unnotched case due to the connectors.

The X-shaped protruded GFRP connectors utilized in this test were stiffer in comparison with other connectors. This is due to the additional contribution from the compression member which is absent for other inclined connector types such as the grid type connector used in Bunn (2011) and Sopal (2013). Though the connectors were stiff, the contribution of the insulation notches was still observed. The notch contribution was smallest with the stiffest connectors (16 mm diameter)

but is expected to be more effective if smaller connectors or dowel type (rather than truss type) connectors were used.

3.10 CHAPTER SUMMARY AND CONCLUSIONS

The contribution of notches (trapezoidal, rectangular) on sandwich panel systems with different types of foam (EPS, PIR, XPS), as well as stiff X-shaped GFRP bars (9.5 mm and 16 mm) as shear connectors, was evaluated using experimental push-through testing. The following was concluded from this experimental study.

1. Notches are effective at increasing the strength and stiffness of shear connections with XPS insulation where the insulation-concrete bond is expected to fail under low levels of slip. Notches are less effective in panels made with PIR and EPS as these insulation types are adequately bonded to concrete throughout testing, at least over the short term. In addition to surface roughness, notch effectiveness also increases as the tensile strength and stiffness of the insulation increase and as the shear connector strength and stiffness decrease.
2. The rectangular notches enabled proper locking mechanism which allows the insulation to actively contribute structurally after insulation-concrete bond failure. Trapezoidal notches were also effective, but their inclined surfaces caused prying of the insulation that reduced friction between concrete and insulation and prompted a different connector failure mode (rupture rather than pullout). Though weaker and softer, systems with trapezoidal notches gave more warning of failure than those with rectangular notches.
3. All the tested shear connection systems lost stiffness and experienced permanent deformation during load-unload cycling. Significant (around 30%) stiffness loss in panels with notched XPS insulation and 9.5 mm shear connectors occurred even under low levels of slip (1 mm). This loss is not as sudden in systems where the concrete-insulation bond remains active (i.e. EPS and PIR insulation) but still is quite large.
4. Though failure modes of connectors in insulated walls are challenging to assess due to the complex stress state in the connectors and surrounding concrete, the contribution of the

insulation can be evaluated effectively using DIC. With DIC, insulation contribution was grouped into three phases during loading that relate to the initial insulation-concrete bond failure, the onset of insulation tearing, and the complete rupture of the insulation.

4. EXPERIMENTAL LONGITUDINAL SHEAR TESTING OF NOVEL AND TRADITIONAL SHEAR CONNECTORS IN DOUBLE-WYTHE CAVITY MASONRY WALLS

4.1 INTRODUCTION

Double wythe cavity masonry walls are a common exterior wall system around the world (Baker et al. 2004). These walls have one outer and one inner layer (wythe). In Canada, the outer wythe is typically made of clay or concrete brick veneer for architectural and hygrothermal purposes (Vanpachtenbeke et al. 2020), while the inner wythe is generally made of Concrete Masonry Units (CMUs) (Baker et al. 2004, Wang et al. 1997). Clay bricks are often used in the outer layer due to their ease of production, lower cost, better regulation of indoor humidity, and superior durability (Cagnon et al. 2014, Gencel et al. 2020). Insulation is placed between the wythes for thermal purposes with its structural contribution assumed to be negligible in design calculations. An air-gap, at least 25 mm wide, is left between the insulation and the outer layer, serving as a drainage path (Allen and Iano 2009, Brick Industry Association 2018, TMS 402/602 2016, Brick Industry Association, 2020). A moisture or vapour barrier is installed next to the warmer side of the insulation to prevent the ingress of moisture or water vapour due to condensation (Clayford 2003, Hatzinikolas et al. 2015).

In modern double wythe cavity masonry walls, wythes are joined by connectors (Fig. 4.1a,b) (Sakr and Neis 2001, TEK 12-01B- 2011, Wang et al. 1997). A tie (Fig. 4.1b) is a type of connector that is designed to transmit axial force between the wall layers. Out-of-plane loads that result in axial load carried by ties may come from wind pressure and seismic forces arising from the mass in the façade. While the strength of a tie is dependent on factors such as the embedment length and size (diameter/thickness), the size is further limited by the thickness of the mortar joint where they are inserted (Fig. 4.1a). Most ties are made of steel in the form of plain single or welded round bars, as well as corrugated round bars or plates (Cascardi et al. 2020, Sandoval et al. 2021). To ensure adequate anchorage of ties to mortar, the diameter of circular and helical connectors is

restricted to two-thirds the thickness of the mortar joint, and half for flat configurations (CSA A370:14, 2018). According to CSA A370:14 (2018), when larger sizes are used, recesses containing mortar or grout should be created to provide adequate anchorage. Connectors are expected to be resistant to corrosion with maximum spacings of 600 and 800 mm in the vertical and horizontal directions, respectively (Brick Industry Association 2003, CSA A370:14 2018). Under tension and compression, the strength of the connector should be at least 1 kN CSA A370:14 (2018).

Double-wythe masonry cavity walls may be classified as full composite, non-composite, and partially composite walls (Drysdale and Hamid 2005, Hatzinikolas et al. 2015, TEK 05-01B 2003). Full composite walls are designed such that both wythes act as a single unit, and this is usually achieved by filling the collar joint (space between the masonry layers, TMS 402/602 2016) with grout or mortar, by joining the wythes with masonry headers, or by using specially designed connectors able to carry shear forces. In non-composite walls, wythes are designed to individually carry load based on their relative stiffnesses. Also, the outer wythe is not intended to resist load apart from its self-weight and is placed for aesthetic and hygrothermal purposes (Drysdale and Hamid 2005, TEK 16-01A 2006). In partially composite walls, the connectors are not stiff enough to create the shared load resistance seen in full composite walls (Brick Industry Association 2018) but are still stiff enough that their contribution cannot be ignored. Filling the collar joint with mortar or grout is not common in modern wall construction, as they induce thermal bridging which ultimately results in a reduction in the R-value of the wall (Ismaiel et al. 2022, TEK 06- 02C 2013). More so, typical connectors are not designed to carry shear forces. Therefore, modern double wythe cavity masonry walls are not designed as full composite and tend to mostly act as non- or partially-composite systems.

Testing on connectors has focused on the strength of connectors in compression and tension while shear (in-plane and longitudinal, Fig. 4.1) test results are scarce. This means the connector contribution towards composite action is uncertain, leading to thicker masonry wythes, and less

efficient designs in comparison to a wall made with other materials like concrete. In Williams and Hamid 2005), the in-plane shear capacity of adjustable steel ties was examined in a CMU-brick setup and reported increased stiffness and strength for ties used with a smaller slot size. However, most tests over the past decade focused on the behaviour of connectors in tension and compression (Arslan et al. 2021, Arslan et al. 2020), only with a recent recommendation to further examine connectors in shear (Arslan et al. 2020).

Increasing the amount of connectors in walls often results in improved structural response by coupling the veneer and CMU (Graziotti et al. 2016, Marziale and Toubia 2015, Miglietta et al. 2021). However, uncertainty about connector capacity translates into a larger number of connectors used in a wall, which results in additional thermal bridges that reduce the thermal efficiency of the system. This is critical for steel connectors, due to their high thermal conductivity (Brick Industry Association 2002). To improve the thermal performance of buildings, National Research Council of Canada (2017), the Energy Performance of Buildings Directive (EPBD) of the European Union, and similar codes around the world are requiring improved energy efficiency in buildings. This is often achieved with thicker insulation. For example, in Alberta, Canada (climate Zone 7A), an insulation thickness of 150 mm is becoming prescriptive nowadays, a departure from an earlier insulation thickness of 75 mm for walls above ground level. Therefore, an investigation into the effect of increased insulation thickness is needed, as the connectors joining the wythes may lose stiffness which would reduce the wall's capacity.

A review of literature shows that the shear capacity of connectors is a topic that requires more investigation. This is evident in CSA A370:14 (2018) where the minimum strength under longitudinal shear is not specified. Experimental shear tests, relatively common for reinforced concrete insulated wall systems (Arevalo and Tomlinson 2020, Egbon and Tomlinson 2023, Woltman et al. 2013), should be conducted to understand the behaviour of connectors under longitudinal shear loading in masonry assemblies. Longitudinal shear testing will highlight the deficiencies in existing connectors, facilitate the prediction of the capacity of double wythe cavity

walls, better evaluate the degree of composite action, and aid in designing walls with larger cavities and thinner wythes.

The purpose of this study is to compare the experimental performance of existing plate connectors to an inclined novel connector that transmits load through truss action. To achieve this, longitudinal shear testing is carried out on the connectors, placed in masonry wallet assemblies built with CMU and bricks. As described in Section 1.1.4 and 3.1 of this thesis, longitudinal shear testing reveals the resistance of the shear connector to slip (relative movement between wythes), and this is similar to what is experienced by the shear connectors in full-scale walls.

The results are analyzed in terms of the strength and stiffness, and the effect of changing the outer wythe material between concrete and clay on failure mode is also examined.

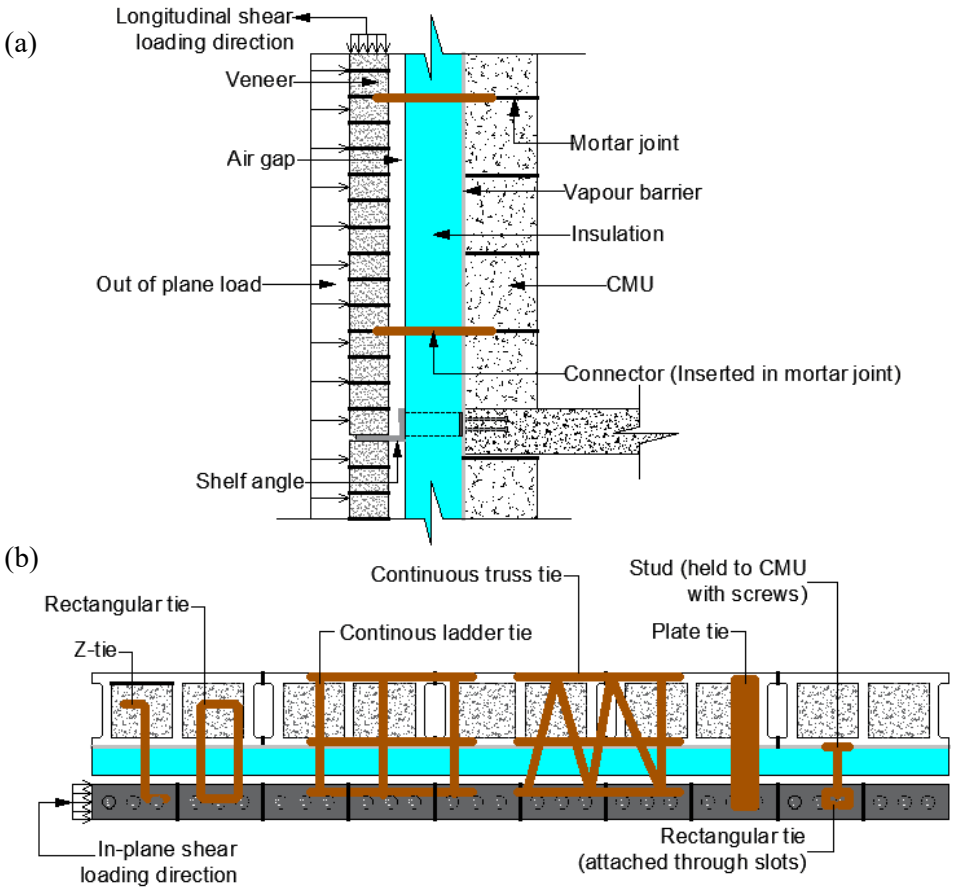

Figure 4.1: (a) Vertical section of a double wythe cavity wall with typical components (b) Plan view of masonry to masonry wall section showing commonly used ties.

4.2 EXPERIMENTAL PROGRAM

4.2.1 Specimen description

Masonry wallet samples were built using running bond with two and six courses of CMU and bricks (single unit per course), respectively. The CMU dimensions (length, height, thickness) were 390×190×190 mm while those of the clay and concrete bricks were 195×57×90 mm and 190×57×90 mm, respectively. Overall, samples were 390 mm wide, 390 mm high, and had a total thickness of 455 mm (Fig. 4.2). Type S mortar with a thickness of 10 mm was used in both wythes and the CMU was partially grouted with coarse grout and reinforced with 1-15M (cross-sectional area of 200 mm^2) steel rebar which is a minimum requirement for loadbearing walls according to CSA S304-14 (2019). Also following CSA A370:14 (2018), a surcharge load of 10 kPa was placed on the CMU to simulate the inner wythe carrying gravity load. Each clay and concrete brick weighed 17 and 17.5 N, respectively.

The cavity width was 175 mm, comprising 150 mm of insulation and a 25 mm airgap. The 150 mm insulation thickness was selected as it is a typical value used in Alberta, Canada (climate Zone 7A), to meet the new 3.08 m^2K/W RSI requirement for walls above ground level specified in NBC (2019). In this study, the intent was to capture only the capacity of the connectors. To achieve this, the specimens were built without insulation as it is assumed that insulation offers no support to connectors, especially for insulation with low stiffness such as fibreglass and mineral wool. However, we acknowledge that the presence of a relatively stiff insulation such as extruded polystyrene may influence the capacity and failure mode of the connector. Even in the cases in which the insulation is designed for this purpose, it may not be reliable throughout the service life of the wall (CSA A370:14 2018) due to degradation or shrinkage of the insulation material.

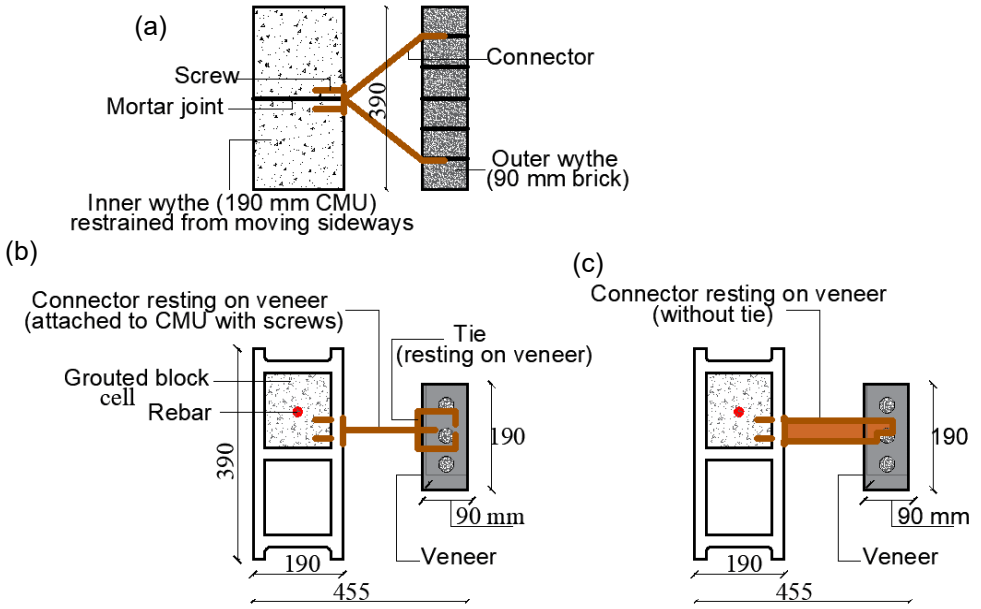

Figure 4.2: Specimen details (a) side view of inclined connector. Plan view of specimen with plate connector (b) inserted vertically (c) inserted horizontally (All dimensions in mm)

The connectors were made of two connected parts. One part was screwed to the CMU and the other part is a tie attached through slots. Both connector parts sit on the veneer (Fig. 4.2). The traditional connector was utilized in two forms. When laid horizontally, the plate connector was used without a tie (Fig. 4.2c). When laid vertically, the plate connector was used with a tie (Fig. 4.2b).

Connectors were made of plain (bare) steel, which makes the connectors appropriate for environments requiring Level 1 corrosion protection (no moisture exposure, CSA A370:14 2018). Even for environments requiring Level 2 and 3 protection, where galvanized steel is required per CSA A370:14 (2018), the test procedure and outcomes are assumed to be valid for a similarly sized connector, as the structural properties of plain and galvanized steel are comparable.

The traditional connectors have a flat shape and are placed either vertically or horizontally. Traditional connectors are designed to act only in tension and compression while the inclined connector was developed to resist shear loading. The plate connector was 3 mm thick and 50 mm wide (Fig. 4.3a,b), while the novel connector was also 3 mm thick and 20.2 mm wide, with an inclination of 36° (Fig. 4.3c,d). Slots were created in the connectors to reduce its self-weight and thermal bridging, while also serving as an opening to attach an embedded tie. The 36° inclination

was selected for constructability, ensuring the pre-cut slots in the connector align with a mortar joint in the veneer wythe. Although the connector thicknesses were the same, the width of the novel connector was made smaller, as it was expected it would structurally benefit from its inclination. Inclined connectors have been used in concrete sandwich panels and have shown improved connector performance (Arevalo and Tomlinson 2020, Egbon and Tomlinson 2023, Tomlinson et al. 2016).

The vertically placed plate connector had an additional rectangular-bent round tie attached through pre-cut slots (Fig. 4.2, 4.3). The rectangular-bent round tie had a diameter of 4.8 mm (Fig. 4.3e). The horizontally placed plate connector did not have the additional tie (Fig. 4.2c) and was omitted for constructability, where it would be difficult to place the additional tie in a head joint in the veneer wythe without hindrance by a brick in the running bond pattern, unlike the vertical plate connector where the additional tie is placed in the wider bed joint.

For the novel connector, two rectangular-bent round ties with a circular cross-section like the tie used with the vertical plate connector were placed in both inclined parts, sitting on the bed joint of the veneer. All connectors are held to the CMU with four Tapcon screws (Fig. 4.3f) of 6.25 and 68.8 mm in diameter and length, respectively.

4.2.2 Test matrix

The novel and traditional (vertically and horizontally placed) connectors were used to build thirteen specimen configurations, leading to 40 specimens total (Table 4.1) but two unfortunately failed during transportation. Specimens with the vertically placed plate connector and novel connector were identified using a three-character code. The first character represents the connector type (IP – inclined connector, VP – vertical plate connector, HP – horizontal plate connector), the second character is the veneer type (CN – concrete brick, CB – clay brick), and the third character is the embedment length of the round tie. To examine the effect of embedment length in the veneer, three embedment lengths were used (45, 60, and 75 mm). Due to the availability of materials, the 75 mm embedded tie was only used with the inclined connector and clay brick. Meanwhile,

specimens with the horizontally placed plate connector were identified using only the first two characters, since they did not have a tie attached. However, the horizontal and vertical plate connectors had a 54 mm embedment into the mortar head and bed joint of the veneer, respectively (Fig. 4.2b,c).

Table 4.1: Test Matrix

Specimen ID	Connector placement	Tie Diameter, mm	Tie Embedment length, mm	Number per connector	Veneer type
HP-CB*	Horizontal	N/A	54[a]	N/A	Clay
HP-CN					Concrete
VP-CB-45	Vertical	4.8	45	1	Clay
VP-CN-45					Concrete
VP-CB-60			60		Clay
VP-CN-60					Concrete
VP-CB-75			75		Clay
VP-CN-75					Concrete
IP-CB-45	Inclined		45	2	Clay
IP-CN-45*					Concrete
IP-CB-60			60		Clay
IP-CN-60					Concrete
IP-CB-75			75		Clay

* one specimen in the configuration failed during transport
[a] embedment length for the connector plate

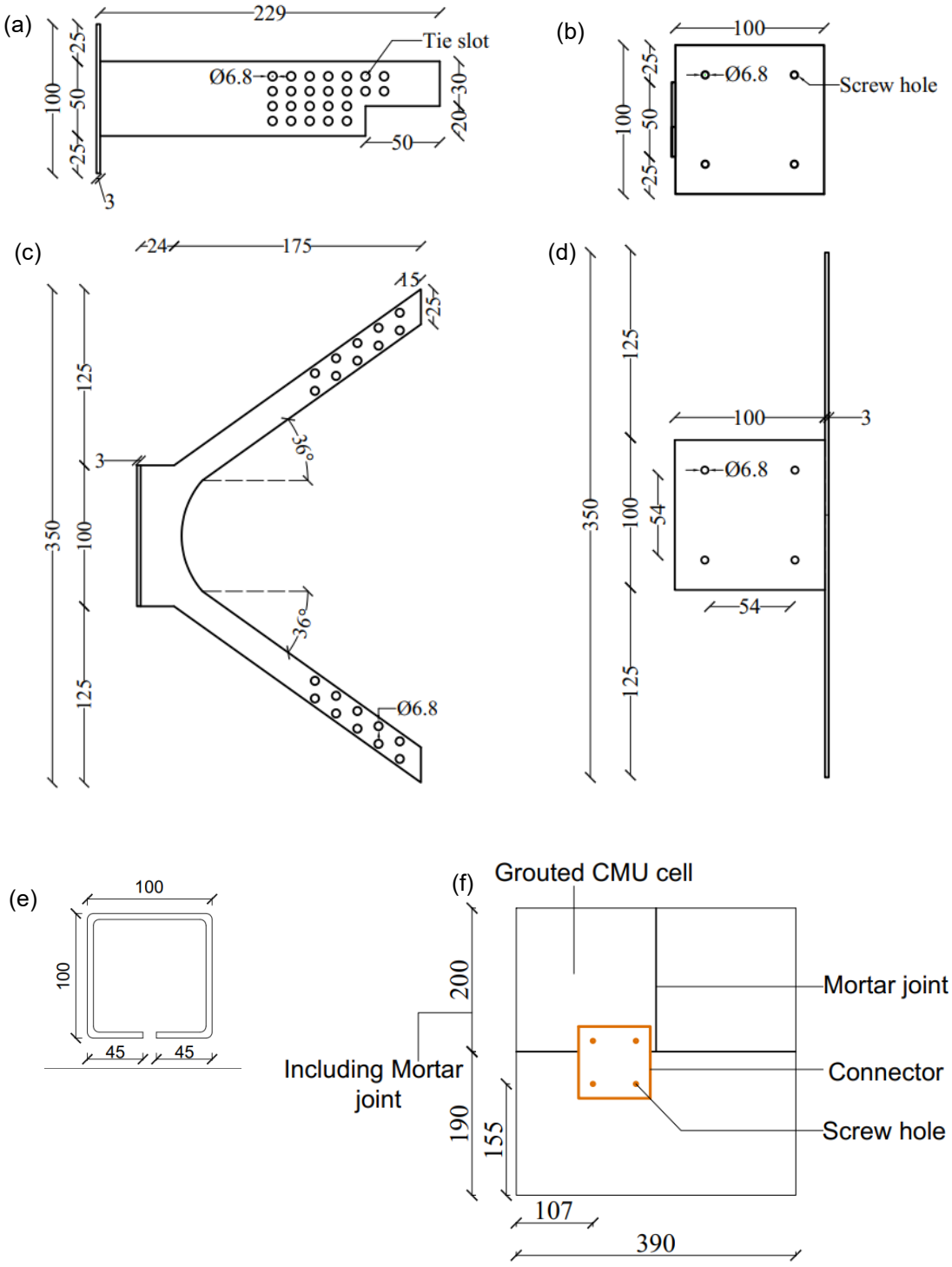

Figure 4.3: Connectors under study. Plate connector (a) Side view (b) back view. Inclined connector (c) Side view (d) back view I rectangular-bent round tie (f) connector position in specimen (All dimensions in mm)

4.2.3 Fabrication process

The construction of the specimens was done by a certified mason following Canadian masonry construction practices. Both courses of the CMU wythe were laid first, after which grout was poured into a cell containing the rebar and allowed to set (Fig. 4.4a,b). Holes were drilled into the CMU unit, then screws were inserted to anchor the HP, VP, and IP connector to the CMU (Fig.

4.4c). For the vertical plate and inclined connector, the anchored part (plate) was first placed in the veneer head joint, after Ih the ties were attached through the slots were placed on the bed joint in the veneer wythe (Fig. 4.2, 4.3, 4.4d, 4.4e). For the horizontal plate connector, the additional tie was not used, as described earlier, and was laid on the veneer at the same embedment length as the plate part of the vertical plate connector (Fig. 4.2b,c).

After the specimens were built, they were cured under a polyethylene sheet for the first seven days and then air-cured for at least 28 days before testing.

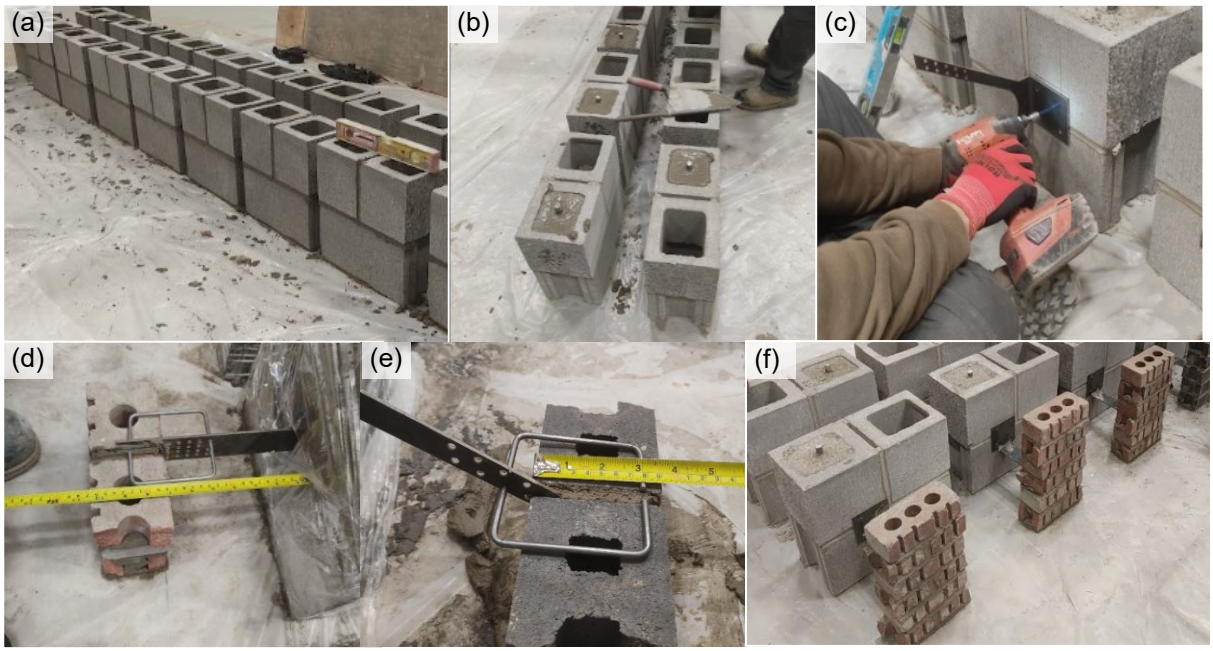

Figure 4.4: Specimen fabrication (a) Completed CMU courses (b) grouted cells (c) anchoring of connectors (IP connector shown) (d) VP connector and embedment tie placement in veneer I IP connector and embedment tie placement in veneer (f) completed specimen (HP connector shown).

4.2.4 Material properties

The compressive strength of the Type S mortar and coarse grout was determined per CSA-A179-14 (2019) using nine 50 mm cubes and seven 100 mm cylinders, respectively. Mortar and grout specimens were cured for at least 28 days, and the mean compressive strength of the mortar and grout were 16.9 and 27.1 MPa, respectively. The 28-day compressive strength for grouted and un-grouted prisms, tested per CSA A165.1 (2019), was 21.5 and 16.6 MPa respectively.

The steel used for the embedded tie and connector (plate and Inclined) had a yield strength of 569 $\pm$ 8.52 MPa and 234 $\pm$ 5.53 MPa, respectively. The steel rebar had a yield strength of 429 $\pm$

2.45 MPa, following ASTM E8 (2022). The elastic modulus of the tie and connector were 197 ± 6.6 Gpa and 194 ± 9.4 Gpa, respectively.

4.2.5 Test Setup and instrumentation

The specimens were tested under shear and the test setup is shown in Fig. 4.5.

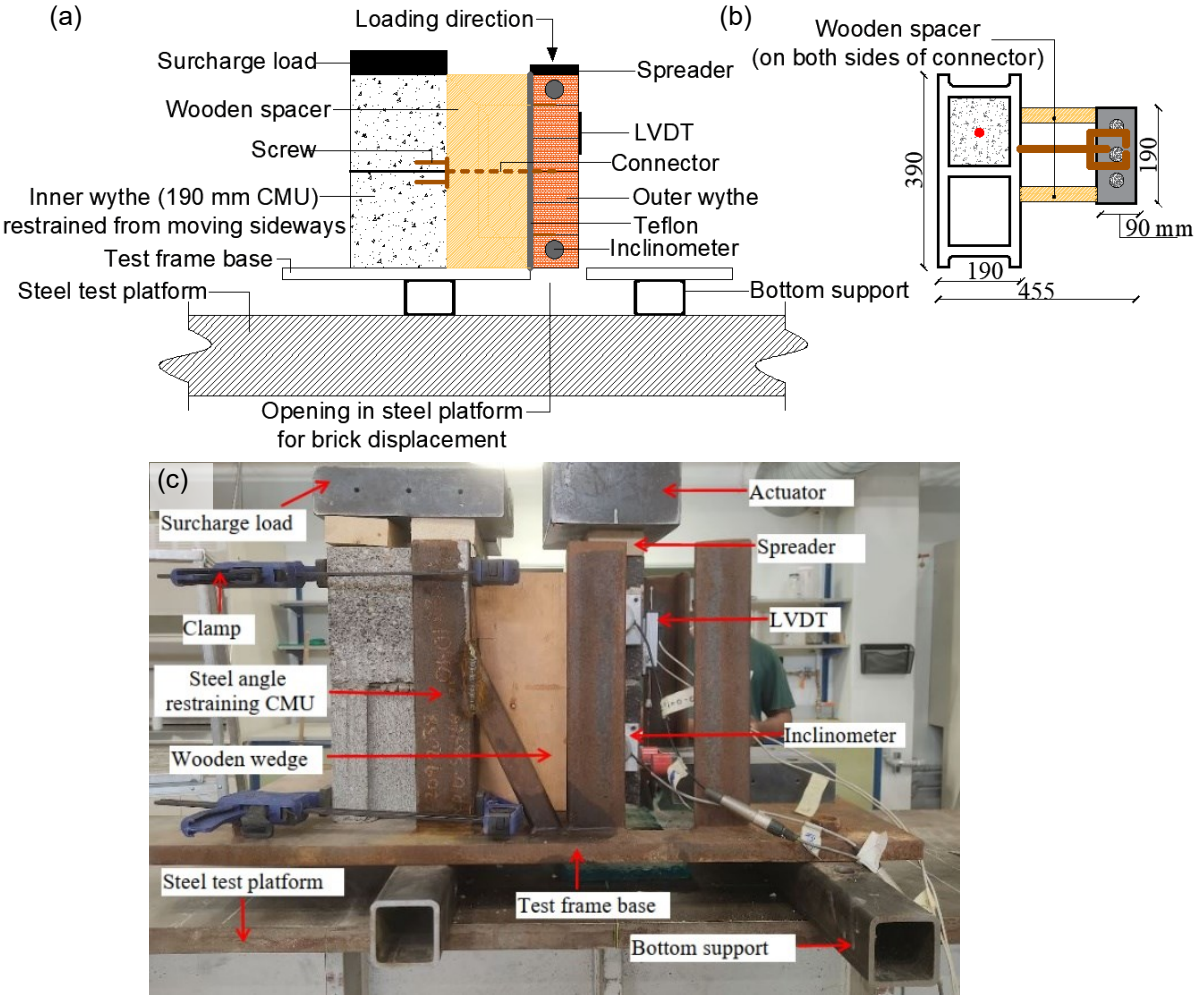

Figure 4.5: Schematic diagram of test frame (a) side view (b) plan view. (c) Photo of test setup

The frame had two steel angle members measuring 76×76×13 mm to restrain the CMU from horizontal movement. It allows the vertical displacement of the veneer through a recess. Four clamps were used to prevent overturning of the CMU during loading (Fig. 4.5c). To prevent rotation at the end of the wythes, therefore simulating pure longitudinal shear load between the CMU and veneer layers, a wood spacer was placed between the wythes, on both sides of the tie (Fig. 4.5b). The spacer was placed not to be tight to prevent bearing on the veneer, which would create unintended load paths. In addition, Teflon sheets were placed between the wood and the

veneer while giving some allowance to prevent friction and unintended load paths. Teflon serves a similar function as a vapour barrier in cavity walls and reduces friction between insulation and wythes. The use of the wooden spacer is similar to the use of a steel chute by Williams and Hamid (2005) to ensure a linear unidirectional in-plane motion under loading.

The spacer (Fig. 4.5b) was designed to enable the monitoring of the tie failure mode at the inner veneer interface. A constant cavity width, with wythes remaining parallel to each other across the height and width of the wall, would be assumed in walls with a standard-compliant number of connectors and are installed using typical construction practices. In addition, the snug placement of the veneer on a shelf angle could limit the out-of-plane sliding of the veneer through friction and mechanical interlock. If there is a small number of connectors or the support of the veneer is flexible, the wythes may not remain parallel. This situation warrants further investigation and was not part of the scope of this study.

Vertical loading was applied on the veneer through a hydraulic ram. The ram was hand-pump controlled at a displacement rate of 3 mm/min on average. The tests were halted when the load value dropped suddenly or when there was increasing deformation without a change in load value (up to the Linear Variable Differential Transformer (LVDT) capacity of 50 mm), indicating either a failure of the connector or collapse of the veneer.

Relative displacement between the CMU and veneer was measured using 2-50 mm LVDTs mounted on the exterior edge face of the veneer (Fig. 4.5a,c), while rotation of the veneer was monitored using two inclinometers attached to the sides of the veneer. Reported displacement readings were an average of the LVDT readings, and there was no considerable variation between the LVDT readings until after the peak load was reached.

4.3 RESULTS

4.3.1 General load-deformation relationship

Overall, the response of all specimens was categorized into three stages. The first stage starts from the initiation of loading up to the proportional limit (Fig. 4.6 i.e., the point where response first

becomes non-linear), with relatively high stiffness. As observed in most specimens, after the initially linear portion of the test, the response became non-linear due to the continuous formation of cracks in the mortar joint hosting the embedded tie. The second stage includes loads after the proportional limit, characterized by reduced stiffness and small load drops, due to cracks and debonding between the connector and mortar. The third stage occurred when the peak load was reached and is characterized by a large load drop, followed by delamination or collapse of the veneer wythe.

The averaged load-displacement curves for the three types of connectors are shown in Fig. 4.7, while load-displacement results for individual tests are shown in Fig. 4.8, 4.9, and 4.10. As wythe slip was monitored using two LVDTs, the average load value was obtained by interpolating fixed displacement intervals from both LVDT readings to the load values obtained from each load cell, after which the average was taken at equivalent displacement values. Numerical values for load and displacement are provided in Table 4.2. Variations for repetition specimens were similar to those observed in previously conducted shear tests of masonry and concrete systems (Williams and Hamid 2005, Martins et al. 2017, Tomlinson et al. 2016, Woltman et al. 2013), and this can be attributed to variability in materials and construction tolerances. The loads in Table 4.2 are the sum of the load measured by the load cell and the self-weight of the six courses of veneer (0.102 kN and 0.105 kN for clay and concrete bricks respectively).

4.3.2 Stiffness

The method for calculating the initial connector stiffness, k_p, shown in Table 4.2 follows the secant method used by Arevalo and Tomlinson (2020) and Egbon and Tomlinson (2021). Stiffness is calculated using load and displacement values at 10% and 40% of the peak load ($P_{U_{40\%}}, P_{U_{10\%}}, d_{U_{40\%}}, d_{U_{10\%}}$), as shown in Eq. 4.1. When $P_{U_{40\%}}$ was greater than the proportional limit, the proportionality limit was used as the value for $P_{U_{40\%}}$.

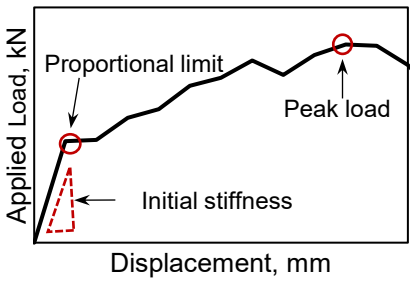

Figure 4.6: Illustration of proportional limit, initial stiffness, and peak load

$$k_p = \frac{P_{U_{40\%}} - P_{U_{10\%}}}{d_{U_{40\%}} - d_{U_{10\%}}} \tag{4.1}$$

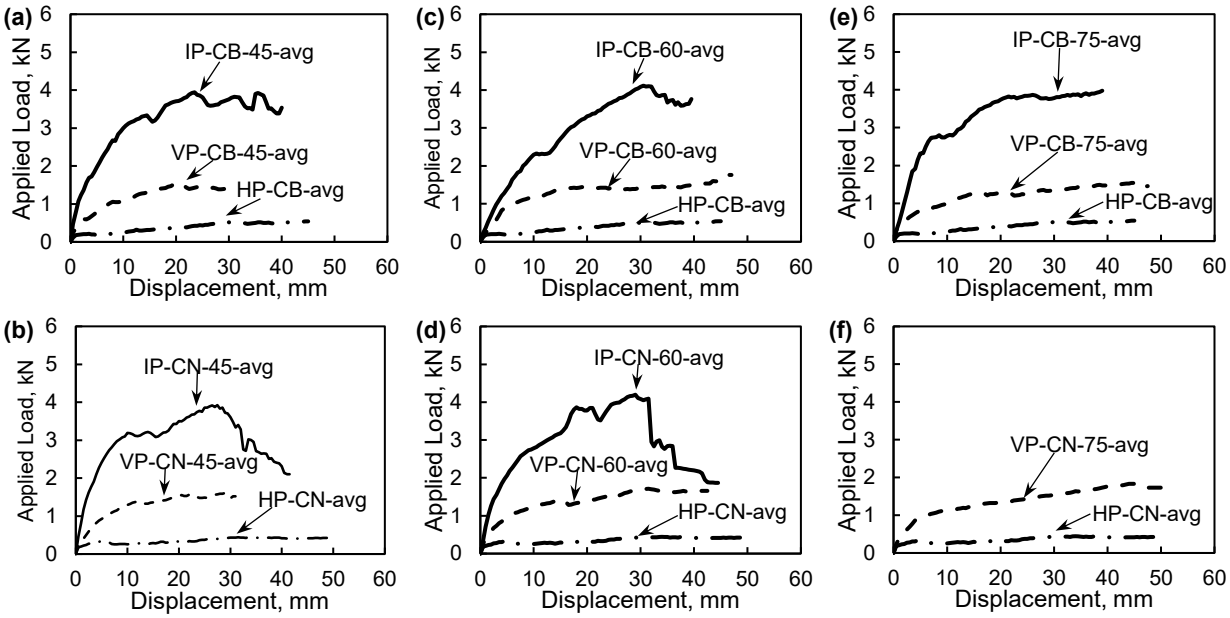

Figure 4.7: Averaged load-displacement responses for specimens with different embedment length and veneer material (average horizontal plate response included in each plot for reference) (a) CB-45 mm (b) CN-45 mm (c) CB-60 mm (d) CN-60 mm I CB-75 mm (f) CN-75 mm

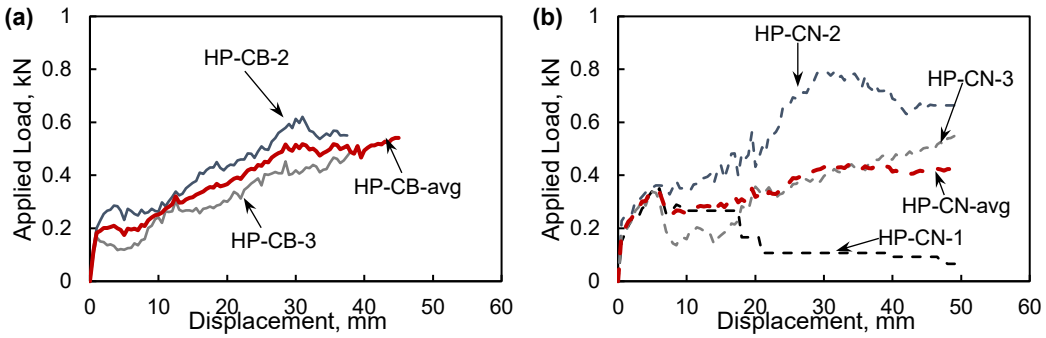

Figure 4.8: Individual load-displacement response for HP specimens (a) clay brick veneer (b) concrete brick veneer

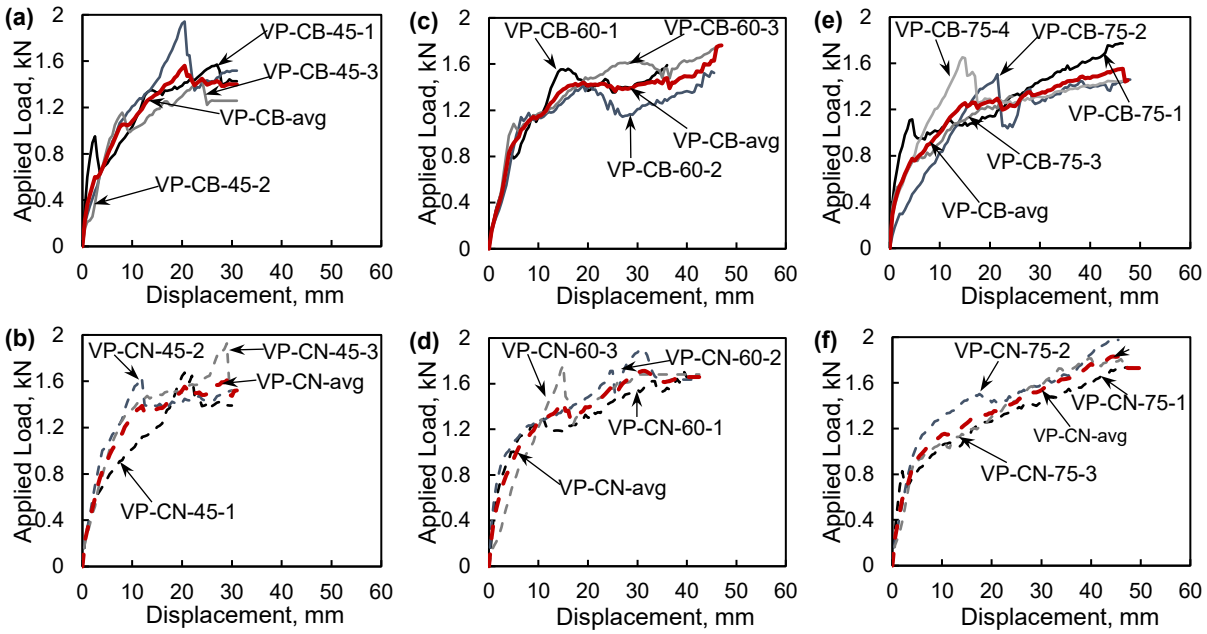

Figure 4.9: Individual load-displacement response for VP specimens. 45 mm embedment (a) clay brick veneer (b) concrete brick veneer. 60 mm embedment (c) clay brick veneer (d) concrete brick veneer. 75 mm embedment I clay brick veneer (f) concrete brick veneer

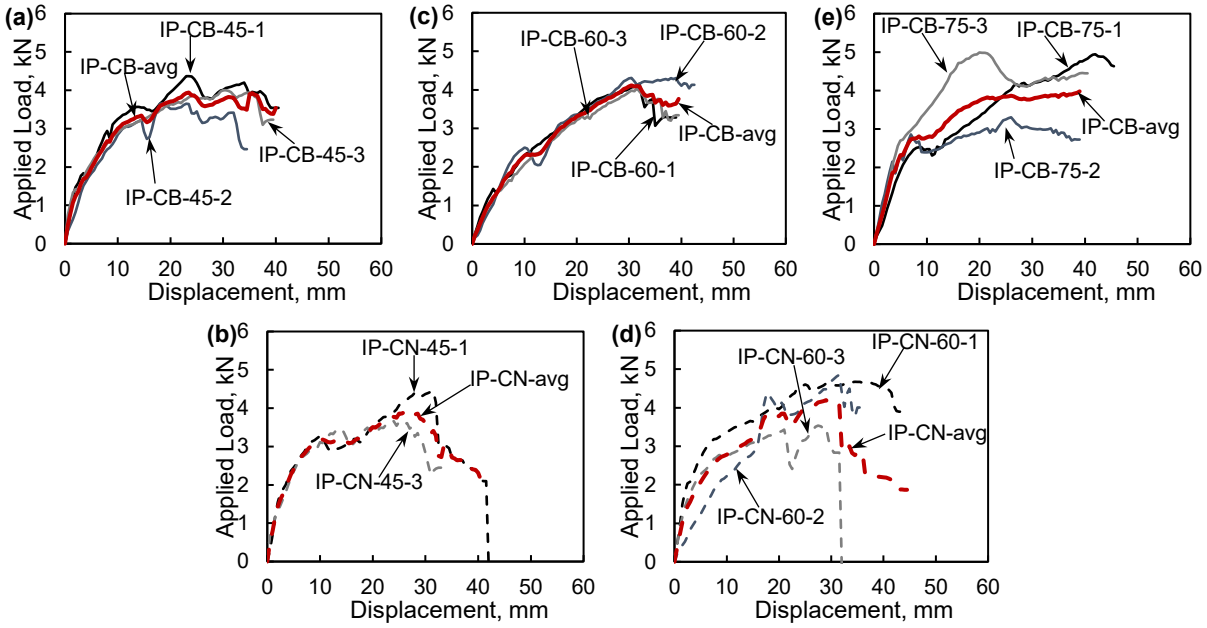

Figure 4.10: Individual load-displacement response for IP specimens. 45 mm embedment (a) clay brick veneer (b) concrete brick veneer. 60 mm embedment (c) clay brick veneer (d) concrete brick veneer. 75 mm embedment I clay brick

Table 4.2: Results from Shear Testing

ID	Proportional Limit, P.L.			Peak Load			Initial Stiffness	
	Load, kN	Mean Load ± Std, kN	Displacement at P.L, mm	Load, kN	Mean Load ± Std, kN	Displacement at peak, mm	Stiffness, kN/mm (Eq. 4.1)	Mean ± Std, kN/mm
HP-CB*	-- 0.13 0.10	0.12 ± 0.02	-- 0.51 0.50	-- 0.62 0.54	0.58 ± 0.06	-- 31.0 45.0	-- 0.32 0.23	0.28 ± 0.07
HP-CN	0.15 0.23 0.17	0.18 ± 0.04	0.50 0.50 0.49	0.35 0.79 0.56	0.57 ± 0.22	6.00 31.0 49.5	0.31 0.49 0.38	0.39 ± 0.09
VP-CB-45	0.35 0.21 0.16	0.24 ± 0.1	0.50 0.50 0.50	1.57 1.94 1.45	1.65 ± 0.26	27.0 20.5 24.0	0.64 0.53 0.51	0.56 ± 0.07
VP-CN-45	0.22 0.24 0.23	0.23 ± 0.01	0.50 0.50 0.50	1.68 1.63 1.93	1.75 ± 0.16	20.5 11.5 29.0	0.53 0.51 0.37	0.47 ± 0.08
VP-CB-60	0.20 0.15 0.15	0.17 ± 0.03	0.50 0.50 0.50	1.59 1.54 1.76	1.63 ± 0.12	36.0 45.0 47.0	0.41 0.30 0.31	0.34 ± 0.06
VP-CN-60	0.50 0.45 0.10	0.35 ± 0.22	1.00 0.60 0.50	1.70 1.91 1.76	1.79 ± 0.11	39.5 31.0 15.0	0.55 0.87 0.20	0.54 ± 0.33
VP-CB-75	0.39 0.30 0.36 0.29	0.34 ± 0.05	0.50 2.00 0.50 0.51	1.77 1.51 1.32 1.65	1.56 ± 0.2	46.0 21.5 24.0 14.5	0.71 0.10 0.79 0.78	0.6 ± 0.33
VP-CN-75	0.31 0.23 0.18	0.24 ± 0.07	0.49 0.50 0.49	1.74 2.00 1.82	1.85 ± 0.13	47.0 44.5 39.5	0.72 0.78 0.37	0.62 ± 0.22
IP-CB-45	1.25 0.32 0.75	0.77 ± 0.47	1.50 0.50 0.50	4.37 3.66 4.00	4.01 ± 0.36	23.5 18.5 30.5	0.86 0.64 1.79	1.08 ± 0.59
IP-CN-45*	0.60 -- 0.65	0.63 ± 0.04	0.85 -- 0.50	4.45 -- 3.66	4.06 ± 055	31.5 -- 24.0	0.78 -- 1.42	1.1 ± 0.45
IP-CB-60	0.75 0.16 0.3	0.41 ± 0.31	1.50 0.50 0.60	4.16 4.31 4.04	4.17 ± 0.14	32.0 30.5 31.5	0.53 0.33 0.50	0.45 ± 0.11
IP-CN-60	1.00 0.25 0.88	0.71 ± 0.4	1.00 0.50 1.00	4.67 4.85 3.54	4.35 ± 0.71	35.5 31.5 27.5	1.05 0.50 1.01	0.85 ± 0.31
IP-CB-75	0.23 1.05 0.74	0.67 ± 0.41	0.50 1.50 1.25	4.94 3.30 4.99	4.41 ± 0.96	42.0 26.0 20.5	0.46 0.77 0.69	0.64 ± 0.16

* one specimen in the configuration failed during transport

4.3.3 Specimen rotation

In the early stages of loading, low rotation values were observed in the veneer. As loading continued, rotation increased in varying magnitudes across specimens (Fig. 4.11), reaching a maximum average value of 4.5° at the peak load (IP-CB-75). The peak rotation values were observed at the peak load of the specimens, showing that there was no bearing action before the capacity of the connectors was reached. For the HP specimens (flat plate connector) the rotation at the proportional limit (P.L) was very small, with an average value of 0.1° (Fig. 4.11d). For the VP and IP specimens, the average rotation at PL was 0.38°. The cosine of 0.1 and 0.38° (veneer rotation at the proportional limit for the HP, VP, and IP specimens) or 4.5° (the highest rotation

recorded at peak for all specimens), is very close to unity (0.99). This makes the effect of the measured veneer rotations negligible for this small-scale test, and the peak load observed reflects the accurate capacity of the connectors.

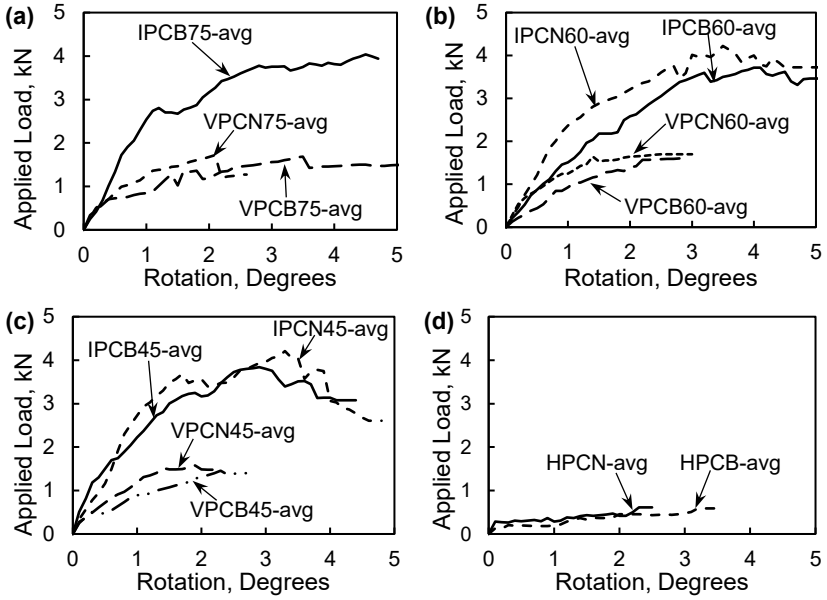

Figure 4.11: Average veneer rotation for specimens with various connectors and embedment lengths (a) 75 mm (b) 60 mm (c) 45 mm (d) horizontal plate

4.3.4 Failure modes and post-test inspection

Two distinct failure modes were observed. For the specimens with the horizontal (HP) and vertical (VP) plate connector, cracks initiated (Point A) at the mortar joint enclosing the connector and tie (Fig. 4.12a,b,d,e), after which failure of the connector occurred due to twisting (Point B, Fig. 4.12g,h).

For the inclined connector, failure was initiated by buckling of the compression member (Point A, Fig. 4.12c,f), transitioning to the pullout of the tie in the lower inclined member of the connector (Point B, Fig. 4.12i). The final failure of the three connectors was delamination of the mortar joint in the veneer wythe and/or collapse of the veneer wythe (Point C, Fig. 4.12j,k), which occurred after peak load. Cracks appeared in the later phases of deformation for specimens with concrete bricks, unlike samples with clay bricks where cracks appeared in the early stages of deformation. This may be attributed to the higher bond strength developed from the deeper and wider frogs present in the concrete veneer Rao et al. 1996).

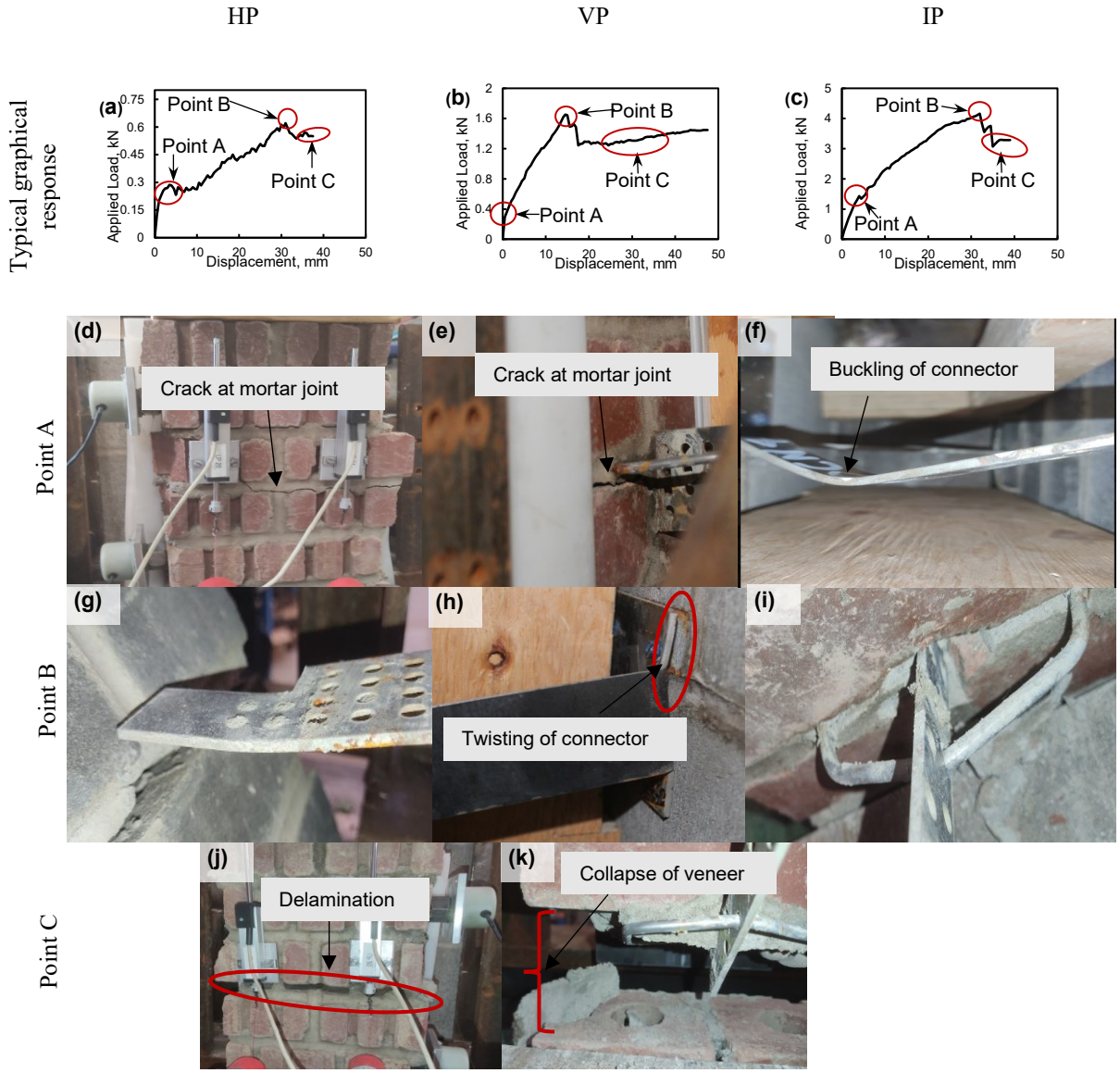

Figure 4.12: Failure mode and post-test investigation. Typical response of specimens with (a) HP connector (b) VP connector (c) IP connector. Failure/crack initiation in (d) HP specimens I VP specimens (f) buckling of compression of IP specimens. Second stage of failure (g) bending failure of HP connectors (h) twisting of VP connectors (i) failure of tension part IP connector (j) Delamination of veneer (k) collapse of veneer

4.4 GENERAL COMPARISON

At the time of this research, there have not been recent tests published on the longitudinal shear behaviour of connectors for masonry construction, with only Williams and Hamid (2005) examining the in-plane behaviour.

4.4.1 Effect of connector type

As anticipated, based on the mode of placement which changes the moment of inertia, the HP connectors (HP-CB, HP-CN) had lower stiffness and strength than the VP connectors under shear

loading. The average load at the proportional limit, stiffness, and peak load for the VP connectors was 1.74, 1.56, 2.97 times that of HP connectors. For IP connectors, the same parameters increased by 4.25, 2.46, 7.24 times compared to the HP connectors, and 2.44, 1,58, 2.46 times compared to the VP connectors. A major reason for the higher benefits seen with IP connectors is the better utilization of material. The IP connectors have a member that is in compression, and a tension part that is attached to an embedment tie that provides additional resistance. The tests show that the tie in the VP connector does not lead to increased capacity during the shear tests. This is because both the end of the VP connector and the tie rest on the veneer (Fig. 4.2b), with the connector taking the majority of the load. This renders the tie largely ineffective irrespective of embedment length. However, the tie would play a considerable role under pure tension and compression. The HP connector (plate connector laid horizontally) did not have an added tie.

The behaviour of the three connectors in the elastic range can be depicted as a beam with a fixed-hinge end condition (Fig. 4.13), where the part of the tie attached to the CMU with screws is assumed fixed while the end of the tie in the veneer is assumed to be a hinge. The maximum fixed end moment (M_{FE}) is obtained using Eq. 4.2. The dowel force (fixed-end shear, V_{FE}) is represented using Eq. 4.3 and the maximum fixed-end shear ($V_{max,FE}$)is obtained using Eq. 4.4.

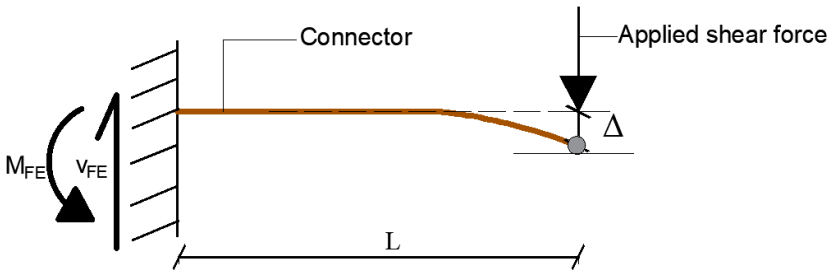

Figure 4.13: Fixed-hinge connector end condition.

$$M_{FE} = \frac{3EI}{L^2}\Delta \tag{4.2}$$

$$V_{FE} = \frac{3EI}{L^3}\Delta \tag{4.3}$$

$$V_{max,FE} = \frac{2f_y I}{Lh_c} \tag{4.4}$$

h_c is the height of the connector, Δ is the transverse displacement, f_y is the yield strength of the connector/tie, L is the connector length. The connectors are also examined for their critical moment (M_{cm}) due to lateral torsional buckling using Eq. 4.5.

$$M_{cm} = \frac{\pi\omega_2}{L}\sqrt{EI_y GJ} \tag{4.5}$$

G, J are the shear modulus and St. Venant torsional constant. ω_2 is the equivalent moment factor to account for a beam with unequal end moments, taken as 1.75 (Nethercot and Trahair 1976). The shear force (V_{cm}) associated with the moment M_{cm} can be obtained using Eq. 4.6.

$$V_{cm} = \frac{M_{cm}}{L} \tag{4.6}$$

Generally, according to Eq. 4.3 and 4.4, larger I results in a larger force carried by the connector. For the HP and VP connectors, the fixed end moment obtained using Eq. 4.5 was found to be larger than that obtained using Eq. 4.2. This means the HP and VP connectors will fail before lateral torsional buckling occurs (Table 4.3). Therefore, the maximum predicted force, using Eq. 4.4, for the HP and VP connector is obtained as 0.21 and 1.77 kN, respectively (including the average weight of clay and concrete bricks). The average predicted/test ratio of the HP connectors is 0.36, while that of the VP connector is 1.04. The failure of the inclined connector is a function of the capacity of its compression and tension members, along with that of the embedded ties (pullout), or breakout of the mortar in the joint hosting the tie. Buckling of the compression member in the IP connector was expected since its thickness and width were far smaller than its length. The mode of buckling can be explained using the Euler buckling formula (Eq. 4.7) to predict the buckling load (P_b).

$$P_b = \frac{\pi^2 EI}{(KL)^2} \tag{4.7}$$

where E, I is the elastic modulus and moment of inertia of the connector, while K is a factor accounting for the end condition. Buckling will be based on the connector axis with the smaller I

(weak axis), which is why the compression member of the IP connector buckled as shown in Fig. 4.12f.

The effective length factor is between 0.7 and 0.8, which are the theoretical and recommended design values for a fixed-hinged beam, respectively. For the IP member in tension, the capacity ($V_{y,T}$) can be estimated using Eq. 4.8.

$$V_{y,T} = A_{ns} f_y \tag{4.8}$$

A_{ns}, f_y are the net cross-sectional area and yield strength of the connector.

While the capacity of the embedded tie attached to the connector part in tension can be evaluated using Eq. 4.8, its contribution could also be limited to the pullout capacity, Eq. 4.9 (force needed to create an outward sliding of the tie when bond is lost with mortar). Equation 4.9 (V_{pT}), was initially developed by Kuhn and Shaikh (1996) for the pullout strength of anchors embedded in masonry and concrete.

$$V_{pT} = \sqrt{f_{mr}} \left(0.15\pi\emptyset(l_{hk} + l_{em} + \emptyset) + \left(1.5\sqrt{f_{mr}}\emptyset l_{hk}\right)\right) \tag{4.9}$$

f_{mr} is the mortar strength, $l_{hk}, l_{em}, \emptyset,$ are the hooked length (45 mm), embedded length, diameter, and area of the embedded tie.

The contribution of the tie is also limited to the mortar breakout capacity (outward formation of a cone-like shape of mortar as the tie tries to slide outward). The breakout capacity is evaluated using Eq. 4.10 based on provisions in TMS 402/602 (2016).

$$V_{br} = 0.33\sqrt{f_{mr}} A_{pt} \tag{4.10}$$

where A_{pt} is the projected tension breakout area, obtained using Eq. 4.11.

$$A_{pt} = 2 l_{em} t + {l_{em}}^2 \left(\frac{\pi\theta}{180} - \sin\theta\right) \tag{4.11}$$

where θ is the angle of breakout, obtained using Eq. 4.12.

$$\theta = 2\sin^{-1}\left(\frac{0.5t}{l_{em}}\right) \tag{4.12}$$

t is the thickness of the mortar joint.

Table 4.3: Model Results

Connector type	$V_{max,FE}$ (Eq. 4.4), kN	V_{cm} (Eq. 4.6), kN	P_b (Eq. 4.7), kN		$V_{y,T}$ (Eq. 4.8), kN	V_{pT} (Eq. 4.9), kN	V_{br} (Eq. 4.10), kN	Average test value, kN	Predicted /test ratio
			$K(0.7)$	$K(0.8)$					
HP	**0.21**	84.3	14.4	10.9	16.0	-	-	0.58	0.36
VP	**1.77**	84.3				-	-	1.71	1.04
IP	**0.32**	1.65	2.19	1.68	9.41	12.7[a], 13[b], 13.2[c]	**2.45[a], 3.26[b], 4.08[c]**	4.20	0.85

Governing load in bold (including self-weight of brick). The strength of the IP connector was obtained by adding values in bold from Eq. 4.4 and Eq. 4.10

[a,b,c] Computed values are for the attached tie to the IP connector with 45, 60, and 75 mm embedment length, respectively

4.4.2 Effect of tie embedment length

Test results of different embedment lengths for the VP and IP connectors are shown in Table 4.2 (the HP connector did not have a tie and was only attached to the CMU with screws).

For the VP connector with tie embedment lengths of 60 and 75 mm the average load at the proportional limit, peak, and stiffness, was 1.08, 1.01, 0.85 and 1.21, 1.01, 1.17 times that of the 45 mm embedment respectively. Similarly, for the IP connector, the ratios were 0.8, 1.06, 0.60 and 0.96, 1.09, 0.59 when the embedment length was increased from 45 mm to 60 and 75 mm, respectively. Physically examining the end of the VP connector that also rests on the veneer as the rectangular-bent round tie (Fig. 4.2b), loading was always on the connector, which renders the rectangular-bent round tie largely ineffective irrespective of embedment length (Fig. 4.14a,b) in shear testing. From shear testing conducted in this study, it can be inferred that those instances of minimal increase in capacities with larger tie embedment length in the VP connector may be attributed to variability in construction, rather than a direct effect of the tie.

After buckling of the compression member in the IP connector, the tie attached to the tension member still provides resistance. With continued deformation, as observed in most specimens for all embedment lengths, ties began to stretch (Fig. 4.12i). After peak load, pullout occurred, followed by the collapse of the veneer (Fig. 4.12k). This suggests that even the smallest embedment length (45 mm) tested in this study, is sufficient in preventing pullout of the tie before peak load is reached., explaining why specimens with 45, 60, and 75 mm embedment lengths achieved similar capacities (Table 4.2, 4.3).

Using Eq. 4.7, the buckling load for the compression member of the IP connector results in 1.62 and 1.25 kN, for the theoretical and recommended effective length factors, respectively (Table 4.3). Its moment capacity from bending (Eq. 4.2) is 0.04 kNm, while its lateral torsional buckling capacity obtained using Eq. 4.5, is 0.35 kNm. The pullout capacity (Eq. 4.9) for the 45, 60, and 75 mm are 12.7, 13, and 13.2 kN, respectively. The net section tensile capacities for tie were obtained using Eq. 4.8 was 10.3 kN, while that for the traditional and inclined connector were 16 and 9.41 kN, respectively. The breakout capacity for the 45, 60, and 75 mm embedment lengths are 2.45, 3.26, and 4.08 kN, respectively (Table 4.3). This means mortar breakout at the veneer will occur before connector pullout for all embedment lengths. Therefore, the failure load for the IP connector will be a combination of bending of the compression member and mortar breakout in the bottom embedded tie. For the 45, 60, and 75 mm embedment, the predicted load was 2.75, 3.58, and 4.40 kN, respectively (including the self-weight of the brick). When compared to test results, it gives an average prediction/test ratio of 0.85 (Fig. 4.14b).

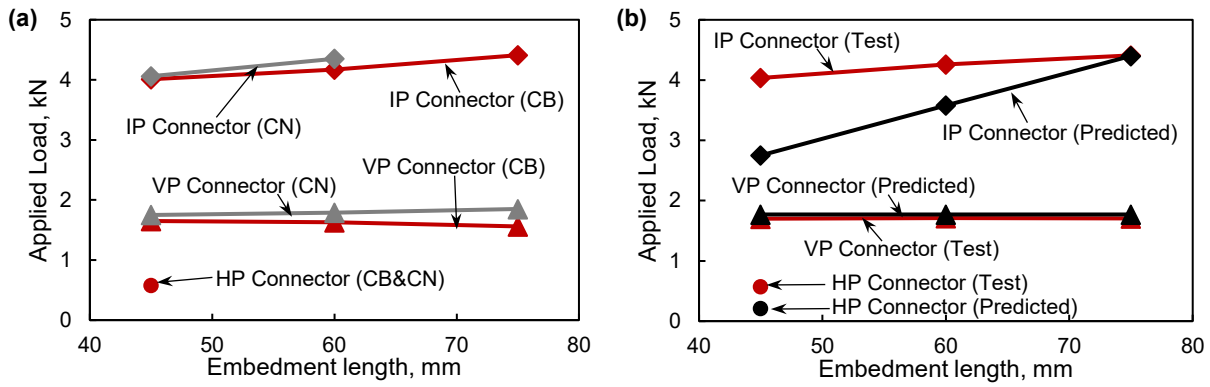

Figure 4.14: (a) Effect of change in embedment length, connector type, and embedded length (b) test vs predicted results

4.4.3 Effect of veneer type

The effect of the veneer type (clay and concrete brick) is shown in Table 4.2 and Figs. 4.7-4.10. The average capacity ratio between CB and CN specimens at the proportional limit, peak load, and stiffness, was 0.9 ± 0.1, 0.94 ± 0.1, and 0.84± 0.1, respectively. This suggests that apart from architectural purposes and the slower progression of cracks to the exterior of the veneer made with

concrete bricks, as mentioned earlier, there was no significant difference in the response of the specimens constructed from clay bricks compared to those with concrete bricks.

4.4.4 Implications to wall design

While there are other sources of connector loading, such as thermal loading, the only loading considered in this section is a uniformly distributed pressure over the veneer wythe (i.e., a wind load). Under out-of-plane load, the shear connectors are activated to create partial composite action (Fig. 4.15). The response of the connectors can be investigated with a shear testing scheme such as the one used in this study.

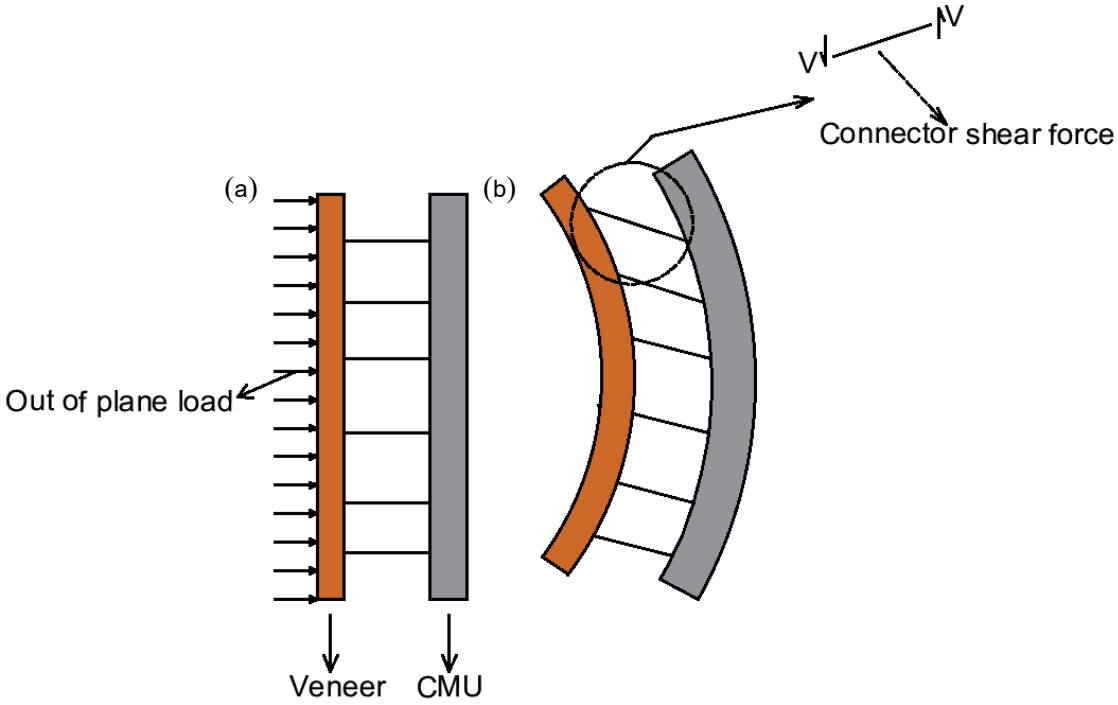

Figure 4.15: (a) cavity wall under out-of-plane loading (b) response of cavity wall under out-of-plane loading

Overall, the IP connector has larger shear stiffness and strength than the HP and VP connectors, respectively, which gives it a structural advantage in a full-scale wall. While the net cross-sectional area of the IP connector is only 80% that of the VP and HP connectors, connectors with larger shear stiffness tend to attract more thermal bowing (Brick Industry Association 2003, Pozo-Lora 2018, Stonkuvienė et al. 2021, Arevalo and Tomlinson 2020).

It is worth mentioning that the specimens tested in this Investigation were built without insulation material in the cavity. The presence of insulation may influence the results (for instance,

laterally supporting the connector). However, the contribution of the insulation was neglected assuming an extreme case where the lateral support from the insulation could not be relied on, as stated in CSA A370:14 (2018). It is also noted that a full-scale wall may have a shelf angle supporting the veneer, which reduces the gravity load on the connector. For low-rise buildings, designers may consider supporting the weight of bricks with shelf angles only up to the first row of connectors from the bottom, while connectors (especially the IP connectors) carry the weight of the bricks upwards, with expansion joints provided.

4.5 CHAPTER SUMMARY AND CONCLUSIONS

The longitudinal shear performance of a novel IP connector was analyzed against traditional plate connectors. The cavity width studied was made to reflect increasing insulation thicknesses seen across energy codes. The novel inclined connector is a first in literature for masonry construction (research and practice). This connector has been shown to offer more capacity per unit area, leading to savings in material. The following was concluded from this study.

1. Due to its diagonal shape, the IP connector attained larger strength and stiffness than the existing plate connector. Overall, the average normalized strength-to-connector cross-sectional ratio for the IP connector was 35 $\mathrm{N/mm^2}$, while that of the HP and VP connectors were 3.83 and 11.4 $\mathrm{N/mm^2}$, respectively.
2. Cracks appeared in the later stages of deformation for samples with concrete bricks, while cracks appeared early on in samples having clay bricks. In addition, there was no substantial difference in the stiffness and strength when concrete and clay bricks were used as veneer.
3. The rectangular-bent round tie used with the vertical plate connector appeared not to affect the results in this shear test irrespective of the embedment length. This is because the end of the VP connector also sits on the veneer as the rectangular-bent round tie. Similarly, for the IP connector, there was no major difference in the results for 45, 60, and 75 mm embedment lengths. However, the embedment length of the rectangular-bent round tie

would have a considerable role under pure tension and compression. It is recommended that tie embedment lengths lesser than 45 mm be tested to see the optimal amount of embedment needed to prevent the pullout of the tie.

4. The thickness of the connectors and ties can be increased to 5 and 6.7 mm respectively to increase the strength contribution based on larger sectional properties while maintaining limitations (mortar thickness of 10 mm) set by CSA A370:14 (2018). In jurisdictions where a 15 mm mortar thickness is prevalent, the sizes of the connector and tie can be increased further.
5. The average predicted-to-test ratio for the VP and IP connectors were 1.04 and 0.85, respectively. Meanwhile, the predicted-to-test ratio for the HP connector was less accurate (0.36), and appropriate characterization of the end-condition is critical in predicting the strength and failure mode of the connector.

5. SIMPLIFIED LOAD-DEFLECTION ANALYTICAL MODEL FOR PARTIALLY COMPOSITE INSULATED CONCRETE WALL PANELS UNDER FLEXURAL LOADING

5.1 INTRODUCTION

Precast concrete insulated wall panels (IWP), also known as sandwich wall panels typically consist of two concrete layers (wythes) that surround an insulation layer. Insulation is placed for thermal purposes and its low density helps IWPs achieve its lightweight nature compared to solid concrete wall panels. IWPs are generally precast which facilitates better quality control than cast-in-place solutions, making IWPs effective for exterior walls in many buildings (Leung 1984, Choi et al. 2015).

Panels are classified as non-composite (wythes act as separate units to carry the load), fully composite (wythes act together with no strain discontinuity between them), and partially composite where the load transfer between the wythes is a fraction of a fully composite panel. Attaining full composite action by strength does not translate to full composite action by stiffness, and vice-versa (Al-Rubaye et al. 2019, Chen et al. 2020). A fully composite panel by strength means there are sufficient connectors needed to make both wythes act together at peak load; for a fully composite panel by stiffness, there is no slip (i.e., strain discontinuity) between the wythes meaning that the full moment of inertia of the panel can be used. Though fully composite panels have structural advantages over other classes, this comes at the expense of thermal efficiency and increased thermal bowing (Arevalo and Tomlinson 2020). This makes some designers opt for non-composite panels that have thicker wythes but with limited bowing.

Wythes are joined by shear connectors which are the main facilitators of composite action between the wythes (Bunn 2011, Gara et al. 2012, Tomlinson and Fam 2016a). Connectors such as solid concrete zones and steel wire trusses are used to attain higher strength and stiffness (Benayoune et al. 2008, Bush and Stine 1994, Joseph et al. 2019) but permit significant thermal bridging which reduces IWP thermal efficiency (Frankl et al. 2008, PCI 2011, Rizkalla et al. 2009,

Woltman et al. 2017). Connectors made from Fibre-Reinforced Polymer (FRP) connectors are used as an alternative due to their low thermal conductivity (Erki and Rizkalla 1993, Alnahhal et al. 2006) which has been seen in experiments (Keenehan et al. 2012, Kinnane et al. 2020). However, the lower stiffness of FRPs (especially Glass FRP (GFRP)) relative to steel leads to lower composite action than a similarly designed panel with steel connectors (Chen et al. 2015, Yossef and Chen 2018). The initial use of FRP connectors in the 1980s was as pin types (Waldron 2004), with trusses, grid and inclined connectors introduced later to increase stiffness and strength (Arevalo and Tomlinson 2020, Bunn 2011, Bush and Stine 1994, Egbon and Tomlinson 2021, Hassan and Rizkalla 2010, Kim and You 2015, Sopal 2013).

Though connectors are the main source of composite action between wythes, the insulation also contributes. This is evident in panels with Expanded Polystyrene (EPS) insulation having larger shear capacity than those with other insulation types such as Extruded Polystyrene (XPS) or Polyisocyanurate (PIR) (Bunn 2011, Kazem et al. 2015). The structural contribution of insulation was also evident when the insulation-concrete bond of XPS was improved through surface roughening (Oh et al. 2013). Similarly, Egbon and Tomlinson (2023) utilized rectangular and trapezoidal notches in panels made with XPS and a 9.5 mm connector, leading to a 50 and 27% increase in the peak load, and a 12% when a 16 m connector was used. However, the structural contribution of the insulation layer is still a cause of debate among designers with some only considering its contribution during handling and erection of the panel, and neglected during its service life (PCI 2011).

The design of non and fully composite panels follows practices in reinforced concrete taught in many undergraduate civil engineering programs. However, for partially composite panels, the process is not straight-forward due to the need to quantify the longitudinal shear transferred by the connectors between the wythes (PCI 2011).

Early analytical models for composite structures were based on differential equations for steel-concrete composites and timber structures (Granholm 1949, Newmark et al. 1951, Stüssi 1947).

These studies served as a foundation for numerical formulations for concrete wall panels by Holmberg and Plem (1965). Afterwards, Allen (1969) proposed comparable analytical expressions for sandwich beams with thick and thin exterior wythes, but most of the formulations are for panels with a soft core (insulation) and thin skins (such as metal or fibreglass) and do not include the contribution of shear connectors like those used in insulated concrete wall panels. Just like earlier models, models such as that of Bai and Davidson (2015), provided complex formulations for the displacement, wythe slip, and stiffness of a panel.

The beam-spring model by Olsen and Maguire (2016) only predicts up to cracking. In Al-Rubaye et al. 2021), an iterative and simplified method was developed to estimate the load-deflection properties of panels. However, the iterative and simplified method only predicts the load and deflection at panel cracking, and not up to yielding of the panel longitudinal reinforcement as well as panel peak load which is of interest to designers. Similarly, Al-Rubaye (2017) developed a model for cracking and ultimate capacity prediction with an assumption of a linear slip along the panel length, which produced agreeable results compared to experimental results. In addition, the end connector contribution at cracking was assumed to be at the proportional limit while the panel was assumed to have failed when the end-connector reached its peak capacity. However, deflections were only computed up to cracking. In Tomlinson and Fam (2016a), the connector slip is obtained by integrating differential strain along the panel length and also including constitutive models to estimate insulation and shear connector contribution, which makes the solution more complicated. A similar procedure was implemented by Gombeda et al. (2017) using the principle of virtual work to evaluate the panel rotation from which shear connector forces were obtained. Meanwhile, Teixeira et al. (2016) developed a 2-dimensional model using beam elements for the wythes and link elements for the connectors, and also accounting for material non-linearity in concrete and steel. While the model by Teixeira et al. (2016) utilized a simplified bilinear curve from experimental connector test data to represent the

link element properties, a simplification of the model by Tomlinson and Fam (2016a), it still involves several iteration steps making it complex to use.

In this study, a designer-friendly model based on a simplified moment-curvature response is used to generate the load-displacement response of partially composite panels. Designer-friendly in this context means most computations are well within the daily practice of a designer and can be executed using simple-to-use spreadsheet software. The curvature approach is different from the strength approach commonly used for steel-concrete composite beams where full composite action is assumed (Hassan and Rizkalla 2010, Teixeira et al. 2016). Consequently, the number of studs required to achieve a desired level of composite action can be easily obtained for steel-concrete composite beams by multiplying the number of studs needed for full composite action with the ratio of the desired level of composite action and that for full composite action (100%). However, for partially composite concrete and cavity masonry walls, the number of connectors needed to attain a desired level of composite action cannot be easily obtained. This is because for partially composite concrete and cavity masonry walls, the connectors experience different amount of slip at various stages of loading, necessitating an iterative process for determination.

The moment-curvature approach developed in this thesis is suitable to determine the degree of composite action at different curvatures. In addition, the model only predicts the behaviour for simply supported panels under one-way bending while the analysis for panels under two-way bending is beyond the scope of this study. Other discontinuities that may be in a wall, such as doors and windows, are also not considered here.

The model was verified with results from 32 tests in literature where experimental shear data of the connector used was presented alongside that of full walls or could be traced to a previous publication. In addition, a parametric study was used to show the effect of panel length, reinforcement ratio as well as wythe thickness, connector diameter, connector spacing, connector inclination, and connector material. Formulations for the shear connector contribution as well as a design example are presented in Appendix A and B, respectively.

5.2 MODEL DESCRIPTION

The difficulty in predicting the load carried by IWPs at various load stages is the determination of the connector contribution at any degree of composite action. The proposed approach uses sectional geometry, strain compatibility, and a simplified moment-curvature relationship obtained for various levels of composite action to predict the load-curvature response. The approach is developed for non-prestressed simply supported members under symmetric flexural loading and can be completed using a simple spreadsheet, while prestressed panels are beyond the scope of this work. The approach is also suitable for panels with unequal wythes and in the next sections, the assumptions for the materials along with the formulations to determine the connector capacity are presented.

5.3 DETERMINATION OF CONNECTOR CONTRIBUTION (V_{cn})

When possible, a designer can obtain connector contribution from a separate shear connector testing program. Similarly, when assessing the performance of panels from literature the connector contribution can be obtained from published results if the panels have the same properties such as the insulation thickness, concrete strength, and connector size. This is important for connectors whose geometries are not regular such that properties (e.g., moment of inertia) cannot be determined easily or vary along the connector length. When connector shear test results are not available, they can be obtained using the formulations discussed below though limited to circular connectors.

The shear contribution is from various mechanisms which Include insulation, as well as dowel and truss action (Fig. 5.1).

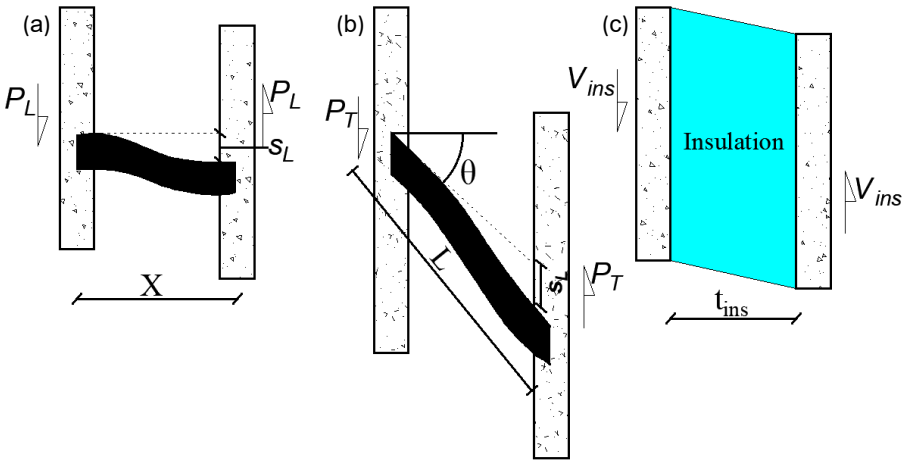

Figure 5.1: Shear transfer (a) dowel action (b) truss action (c) insulation

If the insulation is bonded to the concrete in a panel, the panel strength and stiffness are often larger than that of a panel where the insulation is not bonded (Hodicky et al. 2013, Oehlers et al. 1997, Tomlinson et al. 2016). When the insulation is bonded to concrete the insulation contribution (V_{is}) with increasing slip (s_L), can be obtained using Eq. 5.1 and is limited to the tensile strength of the insulation subjected to shear.

$$V_{ins} = \frac{G_{is}A_{is}s_L}{t_{is}} \leq f_{is,t}A_{is} \tag{5.1}$$

G_{is}, A_{is}, t_{is}, $f_{is,t}$ are the shear modulus, shearing area, thickness, and tensile strength of the insulation, respectively.

5.3.1 Dowel action

For dowel action, the dowel force (P_L) with increasing slip is obtained using Eq. 5.2 or Eq. 5.3. Equation 5.2 provides the connector flexural strength while Eq. 5.3 provides the shear strength under a dowel force (P_L). The smaller of the two values governs the connector capacity.

$$P_L = \frac{12E_bI_{cn}}{X^3}s_L \leq \frac{4f_{u,c}I_{cn}}{XD} \tag{5.2}$$

$$P_L = \frac{12E_bI_{cn}}{X^3}s_L \leq \frac{A_{cn}f_{u,rn}}{k} \tag{5.3}$$

where X, D, A_{cn}, I_{cn}, E_b are the horizontal length, diameter, cross-sectional area, moment of inertia, and flexural modulus of the connector, respectively. k is a constant accounting for the ratio of the maximum and average shear stress which equals 1.33 for circular cross-sections. $f_{u,rn}$ is the

tensile strength of the resin, and $f_{u,c}$ is taken as the compressive strength for an FRP connector and the yield strength for a connector made with steel. The compressive strength of FRP is different from its tensile strength and can be taken as 55% of its tensile strength (Khorramian and Sadeghian 2019).

For FRP connectors under dowel action, the connector utilizes its flexural properties while for FRP connectors under truss action, the connector utilizes its axial and bending properties. This is why in Eq. 5.3 (dowel action) E_b is the flexural modulus of elasticity. Meanwhile, for truss action (Eq. 5.4), E_l in the first part of Eq. 5.4 (axial part) is the longitudinal modulus of elasticity while that for the second part of Eq. 5.4 (bending action) is the flexural modulus of elasticity. Unlike steel, the flexural modulus of elasticity for FRP is different from its longitudinal modulus of elasticity. For small FRP connector sizes, the flexural modulus of elasticity is similar to the longitudinal modulus of elasticity as the fibres in the bar are better engaged under bending. For larger FRP connector sizes, the flexural modulus of elasticity deviates from the longitudinal modulus of elasticity (Benmokrane et al. 2017).

5.3.2 Truss action (tension)

The connector force from a connector under truss action before material failure (P_T) is obtained using Eq. 5.4.

$$P_T = \left(E_l \left(\frac{\sqrt{(X\tan\theta + s_L)^2 + (X)^2} - L}{L} \right) + \frac{3E_b D}{X^2} s_L \right) A_{cn} \sin\left(tan^{-1}\left(\frac{X\tan\theta + s_L}{X} \right) \right) \quad (5.4)$$

X is the horizontal connector length and θ is the angle of inclination, E_l is the longitudinal modulus of elasticity for the connector. Derivations for Eq. 5.1 to 5.4 are shown in Appendix A.

The resistance for a connector in tension is limited to the shear force at pullout (P_{bf}). For a connector made with FRP, P_{bf} is taken from CAN/CSA S806-12 (2021) (rearranged as Eq. 5.5) while that of a connector made with steel is obtained from CSA-A23.3-19 (2019) (rearranged as Eq. 5.6). In Eq. 5.5 and 5.6, it is assumed that the pullout strength is directly proportional to the embedment length considering the small embedment of connectors. As connectors are anchored

in the concrete wythes without being tied to the wythe's reinforcement, sufficient embedment length ensures the connectors do not fail (pullout) after the concrete wythe cracks. Also from shear connector tests (Arevalo and Tomlinson 2020, Egbon and Tomlinson 2023), pullout of connectors was not observed where sufficient embedment was provided.

$$P_{bf} = \left(\frac{l_e d_{cs}\sqrt{f_c'}}{1.15k_1k_2k_3k_4k_5}\right)\sin\theta \tag{5.5}$$

$$P_{bf} = \left(\frac{l_e d_{cs}\sqrt{f_c'}}{1.15k_1k_2k_3k_5}\right)\sin\theta \tag{5.6}$$

l_e is the embedment length of the connector, f_c' is the concrete strength, d_{cs} is the distance from the closest concrete surface to the connector, k_1, k_2, k_3, k_4, k_5 are factors accounting for the connector location, concrete density, connector size, FRP type, and surface profile.

Failure could also be due to concrete breakout due to the accumulation of stresses around the connector which eventually pushes out the surrounding concrete, especially those with a diameter of at least 10 mm (Cox et al. 2019, Egbon and Tomlinson 2021). The concrete breakout capacity (P_{br}) is shown in Eq. 5.7 CSA-A23.3-19 (2019), which was developed for steel headed anchors in concrete.

$$P_{br} = \left(\sqrt{Df_c'}c^{1.5}\left(\frac{l_e}{D}\right)^{0.2}\right)\sin\theta \tag{5.7}$$

c is the wythe thickness.

5.3.3 Truss action (compression)

While the demand on a connector in compression can be determined using Eq. 5.4, the strength of a connector in compression is limited to the buckling (P_{bu}) and material failure (Eq. 5.8,5.9).

$$P_{bu} = \left(\frac{\pi^2 E_{cn} I_{cn}}{(0.66L)^2}\right)\sin\theta \tag{5.8}$$

$$P_m = (f_{mc}A_{cn})\sin\theta \tag{5.9}$$

The connector is taken as a fixed-fixed beam with an effective length factor of 0.66, and f_{mc} is the connector's compressive strength. For FRP connectors f_{mc} is taken as the compressive strength,

which is taken as 55% of its tensile strength (Khorramian and Sadeghian 2019). For steel connectors f_{mc} is the yield stress, f_y.

5.4 MATERIAL RELATIONSHIPS

5.4.1 Concrete

Under tension, concrete cracks when it reaches its modulus of rupture (f_r) shown in Eq. 5.10 (CSA-A23.3-19 (2019). The concrete tensile contribution is zero after cracking. Under compression, concrete is modelled to be linear up to the yielding of the panel longitudinal reinforcement. At the yielding of panel longitudinal reinforcement, the linear assumption for concrete (under compression) produced similar values as when concrete was assumed to be non-linear, as shown in section 5.6.2. As shown in section 5.6.3, α_1 and β_1 from CSA-A23.3-19 (2019) were used to estimate the capacity at ultimate (concrete crushing). The tensile contribution of concrete after cracking via tension stiffening was considered negligible at panel longitudinal reinforcement yielding and concrete crushing (Lin 2010). The modulus of concrete in the elastic range, E_c, is obtained using Eq. 5.11 (CSA-A23.3-19 2019).

$$f_r = 0.6\sqrt{f_c'} \tag{5.10}$$

$$E_c = \left(3300\sqrt{f_c'} + 6900\right)\left(\frac{\gamma_c}{2300}\right)^{1.5} \tag{5.11}$$

f_c', γ_c are the compressive strength and density of concrete.

5.4.2 Steel

The reinforcing steel rebar is assumed to behave as an elastic-perfectly plastic material i.e. having constant stress after yield, with an elastic modulus E_s (Fig. 5.2). Welded Wire Fabric (WWF) is modelled using a bilinear curve (Fig. 5.2), having the same elastic modulus as the steel rebar (E_s) and a post-yield modulus (E_{py}) which terminates at its ultimate stress. E_{py} is obtained using Eq. 5.12.

$$E_{py} = \frac{f_{su} - f_y}{\varepsilon_{su} - \varepsilon_y} \tag{5.12}$$

5.4.3 FRP

FRP is assumed to behave as a linear elastic material up to failure, having an elastic modulus, E_{frp} (Fig. 5.2).

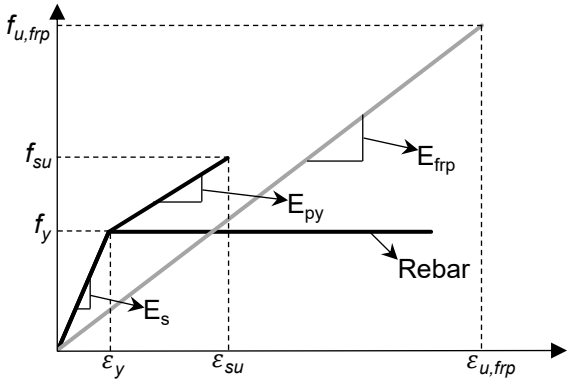

Figure 5.2: Constitutive model for steel rebar, WWF, and FRP (ε_y, f_y are the yield strain and stress for the steel rebar, respectively. $\varepsilon_{u,frp}$, $f_{u,frp}$ are the strain and stress and failure) while ε_{su}, f_{su} refers to the ultimate strain and stress for the WWF.

5.5 DEVELOPMENT OF MOMENT-CURVATURE RESPONSE

The development of the moment-curvature response is essential to the determination of the load-deflection response. To determine the moment-curvature response for a partially composite panel, it is essential to note that its response is between that of a non (NC) and fully (FC) composite panel. Previous analytical models like Gombeda et al. (2017) and Tomlinson and Fam (2016a) use a cumbersome process to determine the moment-curvature response for partially composite walls, which are not easy to follow by designers and may create a barrier to usage.

In this study, the moment-curvature response is simplified by carrying out evaluations at only three points: first cracking (concrete wythe), yielding (panel longitudinal reinforcement), and ultimate (concrete crushing)/rupture of longitudinal reinforcement. These points were selected since each is familiar to designers.

5.6 NON AND FULLY COMPOSITE SECTIONS

5.6.1 Analysis before cracking

The cracking moment (M_{cr}) is obtained using Eq. 5.13.

$$M_{cr} = \frac{f_r I_t}{y_t} \tag{5.13}$$

For non- and fully composite sections, y_t is the distance from the centroid ($\bar{y}$) to extreme fibre tension, I_t is the transformed moment of inertia, f_r is the modulus of rupture of the extreme tension fibre. For wythes with large flexural reinforcement ratio away from the middle, I_g (gross moment of inertia) underestimates the capacity of the section. For non-composite sections, the dimensions of the individual wythes are used for computation while for the fully composite section, the section is considered as a beam having top and bottom reinforcement with height (h) as shown in Fig. 5.3 and Table 5.1. For non-composite sections, M_{cr} is obtained for individual wythes and added together.

The curvature (φ_{cr}) is assumed equal in both wythes. This means the wythes are displaced by equal amounts (Hassan and Rizkalla 2010) and obtained using Eq. 5.14. In non-composite panels with similar wythe thicknesses, cracking will occur in both wythes at the same curvature. For sections with different wythe thicknesses, the respective sections are checked to see which cracks first.

$$\varphi_{cr} = \frac{M_{cr}}{E_c I_t} \tag{5.14}$$

The dimensions referenced in Table 5.1 are for rectangular wythes shown in Fig. 5.3. A_{s1} and A_{s2} are the area of reinforcement in the top and bottom wythes, respectively while n is the modular ratio (ratio of the elastic modulus of longitudinal reinforcement to that of concrete).

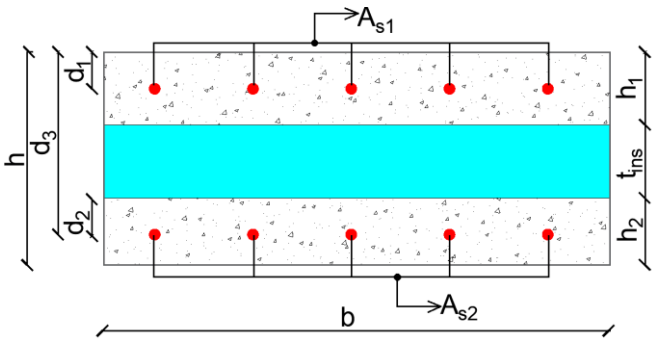

Figure 5.3: Panel cross-section

Table 5.1: Uncracked Properties of non and fully composite sections

Properties	Non -composite section	Fully composite section
$\bar{y}$	$\left(\frac{\frac{bh_2^2}{2}+(n-1)A_{s2}d_2}{bh_2+(n-1)A_{s2}}\right)$	$\left(\frac{\frac{bh^2}{2}++(n-1)A_{s1}d_1+(n-1)A_{s2}d_3}{bh+(n-1)A_{s1}+(n-1)A_{s2}}\right)$
I_t	$\left(\frac{bh_2{}^3}{12}+bh_2\left(\frac{h_2}{2}-\bar{y}\right)^2+(n-1)A_{s2}(d_2-\bar{y})^2\right)$	$\left(\frac{bh^3}{12}+bh\left(\frac{h}{2}-\bar{y}\right)^2+(n-1)A_{s1}(d_1-\bar{y})^2\right.$ $\left.+(n-1)A_{s2}(d_3-\bar{y})^2\right)$
I_g	$\frac{bh_2{}^3}{12}$	$\frac{bh^3}{12}$
y_t	$h_2-\bar{y}$	$h-\bar{y}$

- Dimension of bottom wythe shown here for non-composite section analysis

5.6.2 Analysis at yielding

At yielding, concrete was assumed to be linear, and this assumption is reasonable for under-reinforced concrete sections under which most insulated concrete wall panels fall. Concrete may also be assumed to be non-linear at yielding and the difference with the linear case, for moment and curvature, to be less than 2%. This check was done using the Hognestad model and similar results would be expected with other models.

For a non-composite section, the yielding moment (M_y) is obtained from Fig. 5.4a using Eq. 5.15 (moment for bottom wythe shown). For a fully composite section, the moment is obtained from Fig. 5.4b using Eq. 5.16.

$$M_y = A_{s2}f_y\left(d_2-\frac{kd_2}{3}\right) \tag{5.15}$$

$$M_y = A_{s1}f_s\left(d_1-\frac{kd_w}{3}\right)+A_{s2}f_y\left(d_3-\frac{kd_w}{3}\right) \tag{5.16}$$

d_w is the weighted average depth of $d_1$and d_3 found using Eq. 5.17.

$$d_w = \frac{A_{s1}d_{1+}A_{s2}d_3}{A_{s1}+A_{s2}} \tag{5.17}$$

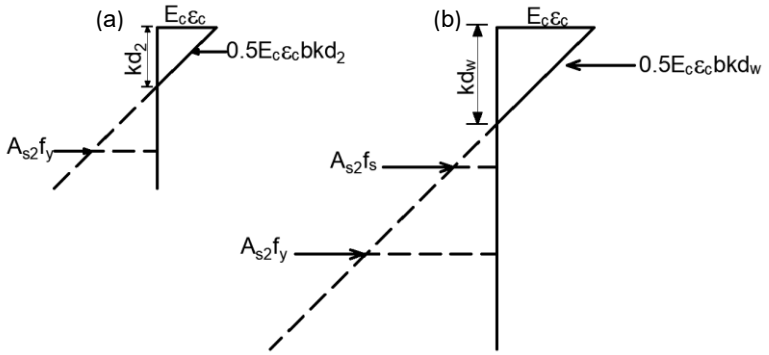

Figure 5.4: Stress profile for (a) non composite section (bottom wythe shown only) (b) fully composite section.

f_s is the steel stress in the top reinforcing layer, f_y is the yield stress of the reinforcement. k is the elastic cracked neutral axis factor. The curvature at yielding (φ_y), reinforcement ratio (ρ) along with other parameters are defined in Table 5.2.

Table 5.2: Cracked Properties of non and fully composite sections

Properties	Non -composite section	Fully composite section
ρ	$\frac{A_{s2}}{bd_2}$	$\frac{A_{s1}+A_{s2}}{bd_w}$
k	$\sqrt{2\rho n+(\rho n)^2}-\rho n$	
I_{cr}	$\left(\frac{b(kd_2)^3}{3}+nA_{s2}(d_2-(kd_2))^2\right)$	$\left(\frac{b(kd_w)^3}{3}+nA_{s1}(d_1-(kd_w))^2+nA_{s2}(d_2-(kd_w))^2\right)$
φ_y	$\frac{\varepsilon_y}{d_2-kd_2}$	$\frac{\varepsilon_y}{d_3-kd_w}$

- Dimension of bottom wythe shown here for non-composite section analysis

ε_y is the yielding strain for the reinforcement ($\varepsilon_y=\frac{f_y}{E_s}$).

5.6.3 Analysis at peak

For panels with steel rebar as reinforcement, the strength at peak is evaluated at concrete crushing. For panels with WWF as longitudinal reinforcement, there is a possibility that the WWF may rupture at its tensile strength due to its lower ductility and reinforcement ratio compared to rebar, and the strength is taken as the lesser of the strength at steel rupture and that due to concrete crushing. For sections where the steel ruptures the concrete is assumed to be non-linear at this stage and evaluated using equivalent stress block factors α and β (Fig. 5.5a,b). For concrete crushing, equivalent stress block factors of α_1 and β_1 are used (Fig. 5.5c,d).

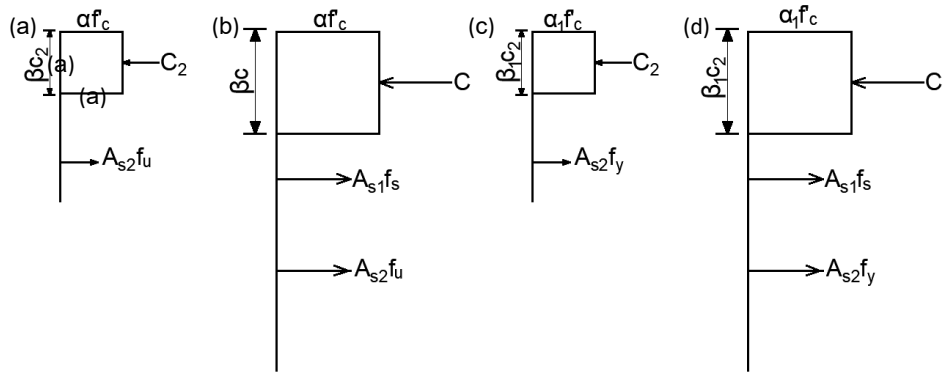

Figure 5.5: Stress profile for section strength for: Longitudinal reinforcement rupture (a) non composite (b) fully composite. Concrete crushing: (c) non composite (d) fully composite.

The moment and curvature at concrete crushing ($M_{u,c}$, $\varphi_{u,cc}$) and that at steel rupture ($M_{u,r}, \varphi_{u,r}$) for non and fully composite sections are shown in Table 5.3.

Table 5.3: Section properties at peak

Properties	Non composite section[a]	Fully composite section
α[b]	$\frac{2}{3}\left(\frac{\varepsilon_c(3\varepsilon_{co}-\varepsilon_c)^2}{(\varepsilon_{co})^2(4\varepsilon_{co}-\varepsilon_c)}\right)$	
β[b]	$\left(\frac{4-\left(\frac{\varepsilon_c}{\varepsilon_{co}}\right)}{6-\left(\frac{\varepsilon_c}{\varepsilon_{co}}\right)}\right)$	
α_1	$0.85-0.0015f_c'$	
β_1	$0.97-0.0025f_c'$	
$M_{u,c}$[c]	$A_{s2}f_y\left(d_2-\frac{\beta_1 c_2}{2}\right)$	$A_{s1}f_s\left(d_1-\frac{\beta_1 c}{2}\right)+A_{s2}f_y\left(d_3-\frac{\beta_1 c}{2}\right)$
$M_{u,r}$[c]	$A_{s2}f_u\left(d_2-\frac{\beta c_2}{2}\right)$	$A_{s1}f_s\left(d_1-\frac{\beta c}{2}\right)+A_{s2}f_u\left(d_3-\frac{\beta c}{2}\right)$
$\varphi_{u,cc}$	$\frac{\varepsilon_{cu}}{c_2}$	$\frac{\varepsilon_{cu}}{c}$
$\varphi_{u,r}$	$\frac{\varepsilon_{su}}{c_2}$	$\frac{\varepsilon_{su}}{d_3-c}$

[a] Dimension of bottom wythe shown for non-composite section analysis
[b] α and β are used for sections controlled by reinforcement rupture and α was multiplied by 0.9 to account for the difference between the test cylinder value and the in-place value of concrete
[c] Moment taken from concrete force C in fully composite sections

ε_{cu} is the ultimate concrete compression strain taken as 0.0035.

5.7 ANALYSIS FOR PARTIALLY COMPOSITE SECTIONS

For the non (NC) and fully (FC) composite section, the moment-curvature at cracking (concrete wythe), yielding (panel rebar), and ultimate (concrete crushing) can now be shown in plots (Fig. 5.6). Subsequently, the moment-curvature response for a partial composite section i.e. percentage composite action between 0% (NC) and 100% (FC), can be determined using the following steps.

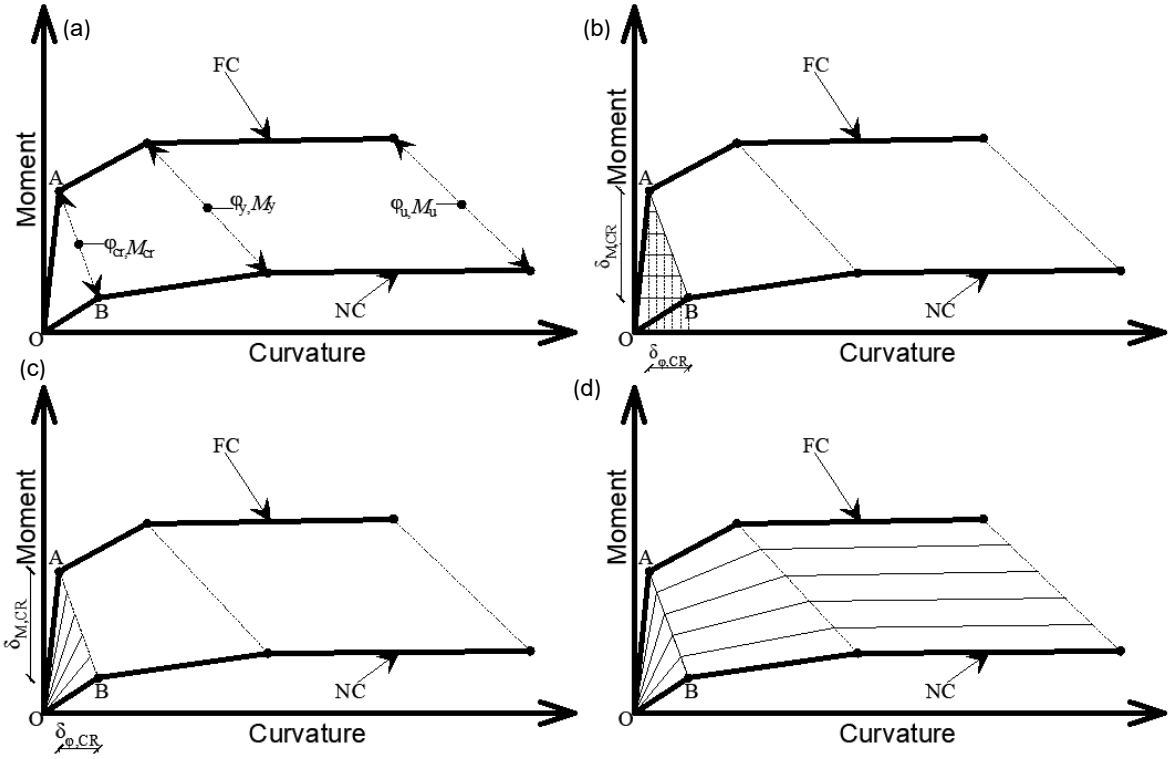

Figure 5.6: (a) Moment-curvature response for NC and FC sections (b) Off set of Moment-curvature values (20% increments of intermediate composite action shown) (c) connection from origin to moment-curvature coordinates (d) Fully developed moment-curvature responses for intermediate levels of composite action

1. Starting from cracking, the difference in moment ($\delta_{M,CR}$) and curvature ($\delta_{\varphi,CR}$) values between the FC and NC sections are offset at desired percentages of composite action (Fig. 5.6a).
2. Lines are drawn from point O to meet the offset-intersections along line AB (Fig. 5.6b).
3. A similar offsetting process is carried out at yielding and ultimate to obtain the entire moment-curvature response for all intermediate degrees of composite action (Fig. 5.6c,d).

With the moment-curvature established for NC (0%) and FC (100%) sections, the partially composite response of a panel can then be determined by accounting for the shear connection contribution. The strain discontinuity (ε_{sc}, Eq. 5.18) varies linearly with the shear connection contribution (V_{cn}) and is maximum in the NC section where the shear connector contribution is zero ($V_{cn,NC}$). In FC sections there is no strain discontinuity between the wythes, and the maximum shear is transferred between the wythes (V_{cn} equals $V_{cn,FC}$). For simply supported panels, the connector contribution (V_{cn}) is zero at the end of the panel and accumulates at each connector

location towards the middle of the panel, resulting in the maximum shear connection contribution for a section, $V_{cn,T}$ (Fig. 5.7). At a given curvature, $V_{cn,FC}$ is obtained as the difference in the compressive (or tensile) force in the FC section and that in the NC section.

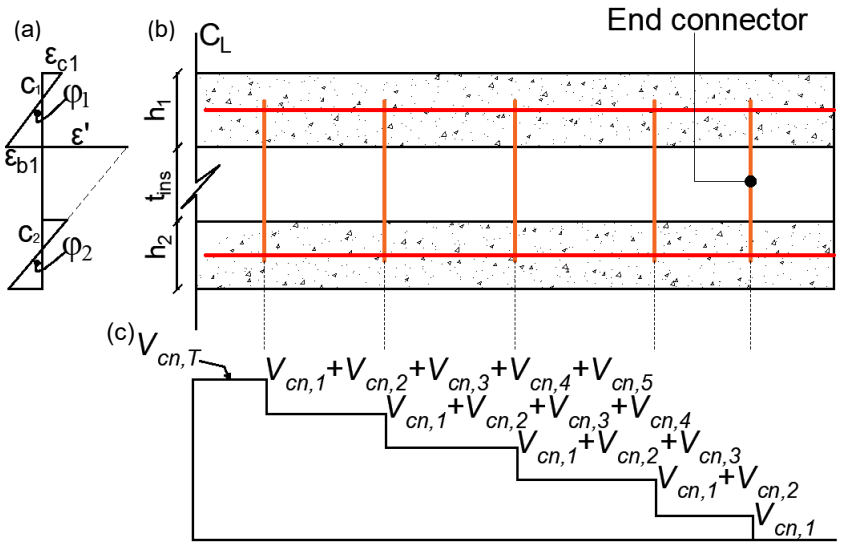

Figure 5.7: (a) Panel strain profile (b) panel showing end-connector (c) shear contribution accumulation

$$\varepsilon_{sc} = \varphi(c_2 + t_{ins}) + (\varphi h_1 + \varepsilon_{c1}) \tag{5.18}$$

where ε_{c1} is negative), c_2 is the neutral axis depth in the bottom wythe, φ is the curvature and equal for both wythes.

Generally, connectors with large stiffness limit the slip between the wythes to ensure enhanced load-sharing between the wythes, which also increases the degree of composite action in full-scale walls. For panels with more than one connector across the width, the individual connector contributions are lumped together to represent the connector contribution for the row of connectors. Also, for panels with different connector types and placement (dowel and truss) across various rows, the respective connector shear response is formulated using provisions shown in Section 5.2, and the contributions (V_{cn}) are lumped together towards the middle of the panel as described above as well in previous studies (Tomlinson and Fam 2016a, Gombeda et al. 2017).

The load-deflection response is therefore obtained using the following steps (Fig. 5.8).

The potential failure modes include connector (pullout, yielding, rupture, buckling, cone breakout) and wythe material failure (concrete crushing, rebar rupture). The connector failure

modes are slip-dependent as shown in Eq. 5.1 to 5.9, while the wythe material failure depends on the applied moment and shear contribution at the point of interest. Connector failure occurs when the end-connector, which carries the largest shear load, fails at the least slip value that causes one of the failures in Eq. 5.1 to 5.9 to occur (while also ensuring the initially assumed slip profile in Step 2 equals that in Step 5 in Fig. 5.8). On the other hand, wythe material failure occurs when the applied moment exceeds the moment capacity for concrete crushing or rebar rupture at a given curvature, and the applied moment is also lesser than that which would cause the end-connector to reach its failure slip.

Overall, peak load for the full-scale wall is determined as the out-of-plane (step 1 in Fig. 5.8) at which one of the failure modes mentioned above occurs first.

1. Apply load to the panel (3, 4-point or UDL) and determine the moment (M), at connector locations along the panel.

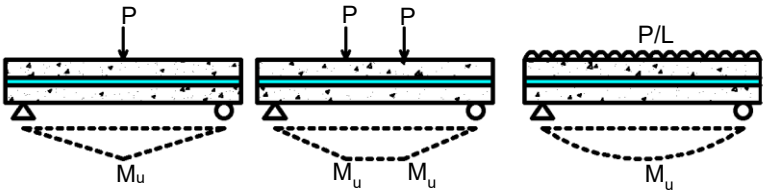

2.Assume a linear slip profile with the end connector having the largest slip ($\delta_{sc,1}$) and zero slip at the middle of the panel.

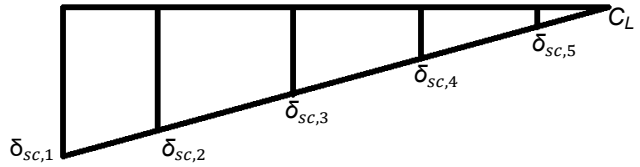

3.Obtain V_{cn} at each connector location by correlating assumed slip with shear connector load-slip relationship. If the insulation is bonded to the concrete, the insulation contribution is added. Sum V_{cn} towards the middle of panel.

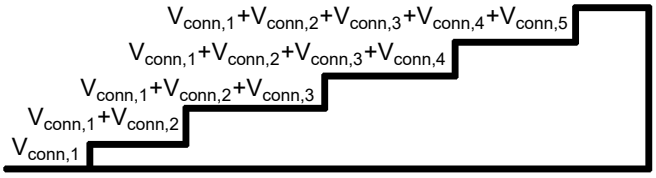

4.Relate V_{cn} at each connector location to the degree of composite action and obtain strain discontinuity (ε_{sc}).

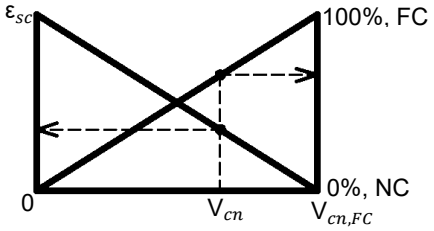

5.Integrate strain discontinuity at connector locations to get a new slip profile. Accounting for this slip is similar to accounting for deformations using Timoshenko beam theory. Repeat step 2 to 5 till new slip profile equals that in step 2.

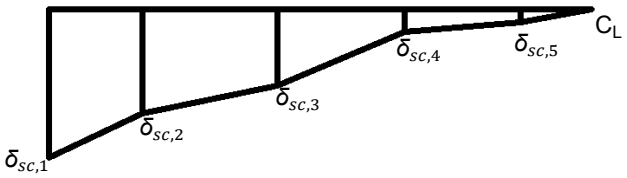

6.Obtain curvature (φ_i) by interpolating moment at connector location (M_i) to moment-curvature relationship with corresponding degree of composite action.

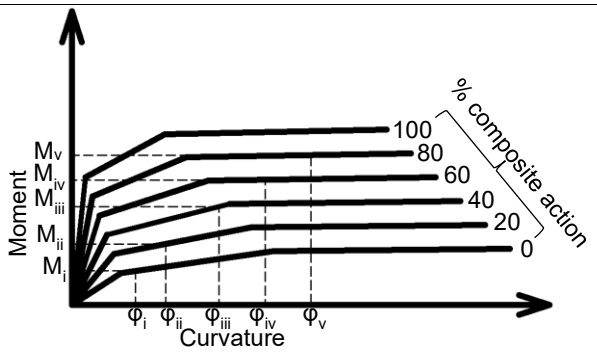

7. Integrate curvature to obtain deflection for the applied load, using to the moment-area approach.

8.Increase applied load value, and Step 2 to 7 is then done again to obtain a new point for the load-deflection response for the partial composite panel.

Figure 5.8: Generation of load-displacement response for partial composite panels

5.8 VERIFICATION OF MODEL WITH EXPERIMENTAL DATA

Verification of the model was done by comparing the load-deflection response to results for full-scale walls from literature in which the push-through test data or properties for the connector were included or could be traced to a previous publication. The tests include those by Cox et al. (2019), Huang et al. (2018), Huang and Dai 2020, Naito et al. 2011, Tomlinson and Fam 2015). Panels in Huang and Dai (2020) were made of geopolymer concrete whose tensile strength and elastic modulus are slightly larger and lesser, respectively, than portland cement (Prachasaree et al. 2020, Tempest et al. 2016). However, properties such as f_r and E_c were not reported in all tests and obtained using Eq. 5.10 and 5.11, respectively, in absence of data or design standard information on geopolymer concrete. More research into developing these design expressions in future is recommended. The panels were tested under four-point bending and uniformly distributed load (UDL). The panel dimensions and properties are shown in Table. 5.4.

The load-deflection response from analytical modelling is compared to the experimental results for different tests in literature (Table 5.5, Fig. 5.9). From Table 5.5 the panels examined were controlled by serviceability requirements as expected since most of the panels are lightly reinforced. In addition, comparison of the model and test results was done at initial cracking, initial stiffness, as well as service and peak load, and the comparison was expressed in terms of the mean and coefficient of variation (COV). Generally, the COV (standard deviation/mean) is suitable when the mean value is nonzero but it could still give misleading results for a data set with nonzero negative and positive values, which would make the mean close to zero.

For unimodal data set, the central tendency is measured using the mean and as such, the COV is appropriate for statistical evaluation. For bimodal data set, the central tendency is best measured using the mode and as such, the COV is not appropriate for statistical evaluation. Specifically, the COV (a unitless parameter) was chosen for statistical assessment in this study because the data set contains only positive values and for any developed model, designer/researchers would be

interested in the closeness of the predictions to the test values. From the test results, there were no outliers and the COV was suitable in statistical evaluation of model predictions.

The differences in predicted and test load-deflection response can be attributed to variations in the reported material properties as well as differences in the predicted shear connector response and that from the test. Similarly, some tests had variations within a sample set which also created variations with predicted values. An average strength predicted to test ratio (K) of 1.06 with a coefficient of variation (COV) of 17.5 %, was obtained. The model gave reasonable predictions for the panel cracking strength and initial stiffness. The K and COV for cracking load were 1.03, 29.2 while that for initial stiffness was 0.98, 31.9. This shows that expressions from CSA-A23.3-19 (2019) for the modulus of rupture and elastic modulus (Eq. 5.10, 5.11) provide a reasonable estimate for wall behaviour at panel cracking, even for panels made of geopolymer concrete. The K appears to be large for the cracking load and initial stiffness. This is because these properties are sensitive to specimen fabrication and placement of displacement measuring devices, which causes large variations even within similar test specimens, reported test data, as seen in specimen PCS7 of Naito et al. (2011).

Most of the predicted failure modes matched with reported test failure modes but could not be compared to some as they were not reported in the publication. From the analytical modelling in this study, connector failure was determined to occur when the slip for the end-connector in the panel reached that corresponding to the strength from the shear connection relationship. Concrete crushing or steel rupture was determined to be the failure mode when they occurred respectively before connector failure.

Table 5.4: Matrix for completed experimental tests in literature

Study		f_c', MPa		Span, mm	Wythe thickness, mm	Reinforcement			$\rho = A_s/bh)$, %	Connector type (spacing, mm)
		Top wythe	Bottom wythe			Type	f_y, MPa	f_u, MPa		
Huang and Dai (2020)	P-300-S	40.4	40.4	2340	75	Steel	401	546	0.52	GFRP (300)
	P-300-S						413	528	0.75	(300)
	P-300-B					Basalt	-	1150	0.52	(300)
	P-300-B					FRP	-	1080		(300)
	H-525-S	40.3	40.3			Steel	413	528	0.75	(525)
	H-300-S						413			(300)
	H-525-B					Basalt	-	1080		(525)
	H-300-B					FRP	-			(300)
Huang et al. (2018)	SP 1-1	44.7	44.7	3000	60	Steel	514	-	0.12	GFRP (500)
	SP 1-2	44.7	44.7							(300)
	SP 2-1	24.4	24.4							(500)
	SP 2-2	24.4	24.4							(300)
Naito et al. (2011)[a]	TS1	32.1	35.2	3600	150	Steel	481	-	0.2	GFRP (400)
	TS2	32.1	35.2		75				0.4	
	PCS7	61.1	61.1						0.5	
Cox et al.(2019)	70-50-70	29	51.9	3300	70	Steel	453	-	0.23	GFRP (540)
	70-100-70	29	47.3	4200	70				0.18	(600)
	70-50-70	40	54.6	4200	70				0.23	(600)
	90-50-90	34.7	34.7	3300	90				0.19	(540)
	90-50-90	44.5	44.5	4200	90				0.19	(600)
	90-100-90	29	47.3	3300	90				0.16	(540)
	90-100-90	40	54.5	4200	90				0.16	(600)
Tomlinson and Fam (2015)	SPF	57.7	57.7	2630	60, 150	Steel	600	680	0.38	Steel (600)
	SSF								0.38	
	HPF	70.4	70.4						0.38	BFRP (600)
	BPF	60.9	60.9			BFRP	-	1100	0.37	

Table 5.5: Results of model prediction

Study		Cracking Load, kN			Initial stiffness × 10^{11}, Nmm^2			Peak Load, kN			Service Deflection (L/360)			Failure mode	
		Test	Model	K_c	Test	Model	K_i	Test	Model	K_u	Test	Model	K_s	Test	Model
Huang and Dai (2020)	P-300-S-10	8.90	8.23	0.92	6.52	7.33	1.12	30.8	27.8	0.90	11.3	9.24	0.82	CF	CF
	P-300-S-12	8.70	8.36	0.96	6.37	7.45	1.17	35.5	32.3	0.91	12.5	10.5	0.84	CF	CF
	P-300-B-10	9.40	8.38	0.89	6.33	7.51	1.19	27.3	28.1	1.03	10.5	10.3	0.98	CF	CF
	P-300-B-12	9.00	9.36	1.04	6.37	7.48	1.17	29.8	31.0	1.04	9.57	11.1	1.16	CF	CF
	H-525-S-12	10.0	8.57	0.86	6.40	4.98	0.78	30.3	32.7	1.08	13.1	9.76	0.75	CC	CC
	H-300-S-12	10.8	7.58	0.70	8.30	7.40	0.89	40.2	44.4	1.10	17.5	10.7	0.61	CC	CC
	H-525-B-12	10.3	7.26	0.70	6.53	5.55	0.85	29.4	31.2	1.06	13.3	9.63	0.72	CC	CF
	H-300-B-12	10.1	9.36	0.93	8.05	5.01	0.62	36.2	42.1	1.16	13.6	11.2	0.82	CC	CC
Huang et al. (2018)	SP 1-1	19.7	18.0	0.91	13.8	13.9	1.01	29.5	36.1	1.22	19.6	18.1	0.92	CF	CF
	SP 1-2	19.6	19.2	0.98	13.5	14.7	1.09	33.6	47.9	1.43	20.6	19.7	0.96	CF	CF
	SP 2-1	17.2	13.0	0.76	11.1	10.3	0.93	37.1	41.9	1.13	17.9	13.1	0.73	CF	CF
	SP 2-2	17.7	19.4	1.10	11.3	15.1	1.34	42.8	36.1	0.84	19.4	20.2	1.04	CF	CF
Naito et al. (2011)[a]	TS1	6.82		0.65	48.2		0.83	11.0		1.28	7.33		1.18		
		7.73	4.45	0.58	26.9	39.8	1.48	8.34	14.1	1.69	8.54	8.68	1.02	[b]	CF
		8.51		0.52	22.8		1.75	10.9		1.29	6.23		1.39		
	TS2	2.85		1.72	18.3		1.15	13.6		0.93	6.33		1.30		
		3.44	4.89	1.42	27.5	21.0	0.76	13.9	12.7	0.91	6.33	8.22	1.30	[b]	CF
		3.69		1.33	42.1		0.50	13.6		0.93	6.33		1.30		
	PCS7	8.47		1.00	39.7		0.68	31.6		0.96	14.7		0.62		
		5.85	8.5	1.45	15.3	26.9	1.76	33.0	30.4	0.92	14.9	9.13	0.61	[b]	CF
		5.89		1.44	33.8		0.80	26.4		1.15	13.1		0.70		
Cox et al. (2019)[a]	70-50-70-3.3	16.1	16.4	1.02	58.5	48.1	0.82	27.8	27.6	0.99	20.5	19.1	0.93	[b]	CF
	70-100-70-4.2	13.2	23.0	1.74	54.1	54.5	1.01	33.2	32.0	0.96	16.2	23.3	1.44	[b]	CF
	70-50-70-4.2	16.5	21.3	1.29	49.2	50.4	1.02	26.3	28.4	1.08	19.4	20.7	1.07	[b]	CF
	90-50-90-3.3	21.5	17.2	0.80	81.1	48.9	0.60	47.0	35.1	0.75	38.2	17.5	0.46	[b]	CF
	90-50-90-4.2	22.1	20.3	0.92	110	78.3	0.71	43.7	36.0	0.82	30.7	22.2	0.72	[b]	CF
	90-100-90-3.3	24.7	24.0	0.97	81.4	46.1	0.57	37.3	37.6	1.01	31.3	24.7	0.79	[b]	CF
	90-100-90-4.2	22.9	24.3	1.06	87.9	75.6	0.86	38.8	38.7	1.00	25.2	29.8	1.18	[b]	CF
Tomlinson and Fam (2015)	SPF	22.7	20.0	0.88	69.3	73.4	1.06	99.3	100	1.01	51.5	47.3	0.92	RR	RR
	SSF	18.2	24.1	1.32	32.7	20.4	0.62	72.7	81.3	1.12	46.5	35.9	0.77	RR	RR
	HPF	21.2	21.5	1.01	38.6	42.0	1.09	88.9	92.4	1.04	38.9	36.2	0.93	RR	RR
	BPF	20.1	23.2	1.15	36.7	48.4	1.32	58.6	65.8	1.12	31.1	22.3	0.72	RR	CF
Mean, K (Predicted/Test)				1.03			0.98			1.06			0.93		
COV (%)				29.2			31.9			17.5			27.1		

[a] Load reported as moment values
[b] Failure mode not reported
[c] CC – Concrete crushing, CF – Connector failure, RR – Reinforcement rupture

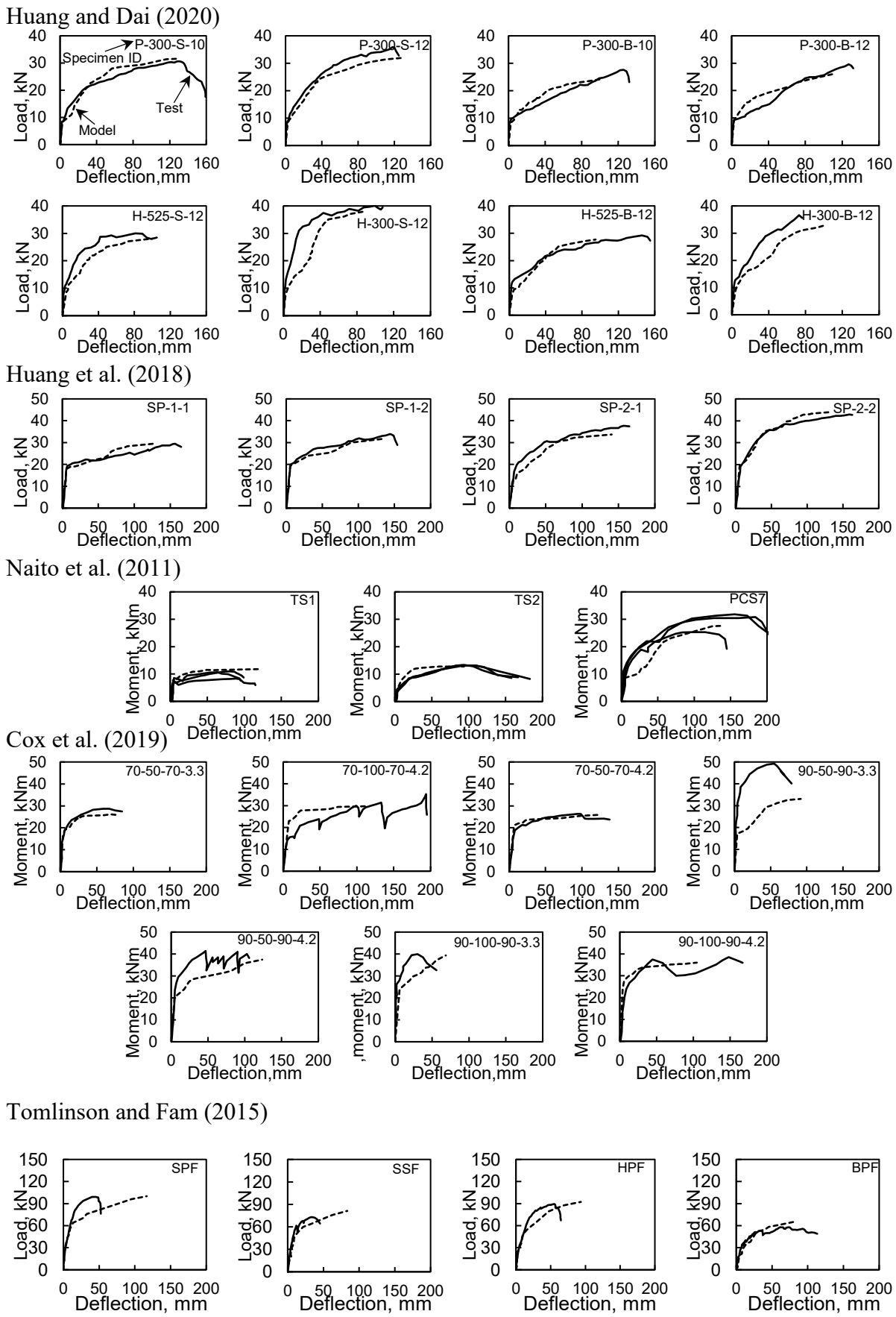

Figure 5.9: Comparison of test and model load-deflection response for panels examined from literature. (Dashed lines are model predictions and solid lines are test results)

5.9 PARAMETRIC ANALYSIS

In this section, the effect of several parameters on the load-deflection response is examined. The parameters include panel length, insulation and concrete wythe thickness, reinforcement ratio, connector spacing and diameter, connector material (FRP and steel), and connector inclination. These parameters are shown in Table 5.6 and are evaluated using a 1000 mm wide panel reinforced with steel longitudinal bars with a yield stress of 400 MPa and loaded as shown in Fig. 5.10.

A base panel length of 3200 mm was selected to represent a typical storey height. Other panel lengths of 5600 and 8500 mm were chosen to reflect taller storey heights found in commercial and institutional structures, as well as in literature (Gonzalez 2022, Zmavc 1991). A base insulation and concrete thickness of 75 mm was chosen to reflect the common thickness used by designers in Canada for walls above ground level. However, thicknesses of 100 and 150 mm were examined to reflect increasing insulation thickness currently prescribed by designers to meet stricter energy requirements set by the National Energy Code of Canada for Buildings (NECB 2017), the Energy Performance of Buildings Directive (EPBD) of the European Union, and comparable codes around the world. Similarly, concrete thicknesses of 100 and 150 mm were selected to reflect walls with larger fire ratings and concrete cover.

A base reinforcement ratio of $0.005A_g$ (A_g is the gross section area) was selected as it was greater than the minimum reinforcement ratio of 0.001 stipulated in CSA-A23.3-19 (2019) for non-prestressed walls and to reflect reinforcement ratios in literature. The selected connector material, spacing, inclination and diameter were chosen as they reflect parameters that are usually considered when a panel is built, and the values were selected to reflect a range seen in literature.

In addition, the effect of the parameters mentioned above on the degree of composite action by strength (D_u) as well as service stiffness (D_s) were examined using Eq. 5.19 and 5.20. This is important as panels with larger strength (peak load) do not translate to a section with comparable composite action by stiffness, as shown in the following sections.

$$D_u = \frac{P_m - P_{NC}}{P_{FC} - P_{NC}} \tag{5.19}$$

$$D_s = \frac{P_{m,s} - P_{NC,s}}{P_{FC,s} - P_{NC,s}} \tag{5.20}$$

P_m, P_{NC}, and P_{FC} are the strength values at peak for the partial composite, non-composite, and full-composite panels, respectively while $P_{m,s}$, $P_{NC,s}$, and $P_{FC,s}$ are load values corresponding to panel deflection values of span/360 (mm).

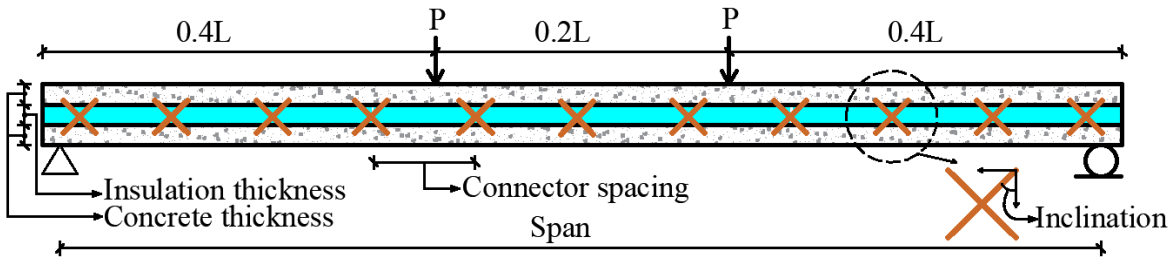

Figure 5.10: Loading arrangement for parametric analysis

Table 5.6: Numerical values for examined parameters.

Parameters	Values
Panel span (mm)	3200, 5600, 8500
Insulation thickness (mm)	75, 100, 150
Concrete thickness (mm)	
Reinforcement ratio (%)	0.5, 0.7, 1
Connector spacing (mm)	150, 300, 600
Connector diameter (mm)	6, 8, 10, 12, 16
Inclination (degrees)	0, 30, 45
Connector material	GFRP, steel
Tensile strength of GFRP (MPa)	1420
Tensile strength of steel (MPa)	400
Modulus of Elasticity for steel (MPa)	200000
Longitudinal modulus of Elasticity for all FRP sizes (MPa)	60500
Flexural modulus of Elasticity for 6, 8, and 10 mm GFRP bars (MPa)	60500
Flexural modulus of Elasticity for 12 mm GFRP bar (MPa)	57400
Flexural modulus of Elasticity for 16 mm GFRP bar (MPa)	50200

5.10 RESULTS FROM PARAMETRIC ANALYSIS

5.10.1 Effect of connector material

Overall, panels with shear connectors made of steel exhibited strength compared to a similarly sized panel with GFRP connectors (Fig. 5.11). Similarly, the degree of composite action (D_u, D_s) was larger for panels with steel connectors (Fig. 5.12). The lower stiffness for panels with GFRP connectors is because the modulus of elasticity for GFRP is smaller compared to steel.

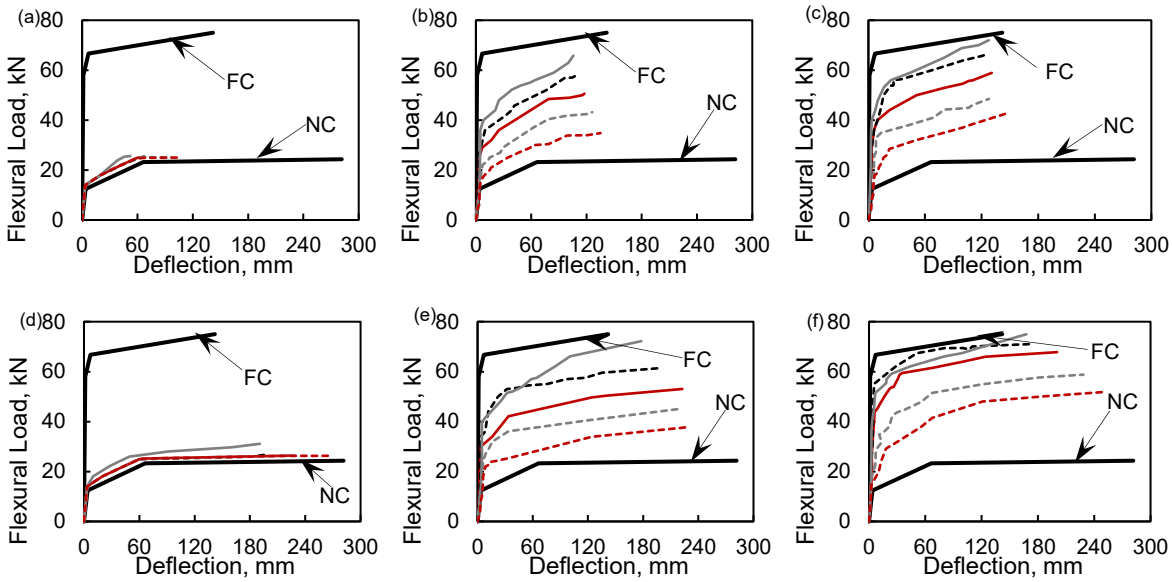

6 (-----), 8 (-----), 10 (——), 12 (-----), 16 mm(——) diameter shear connector

Figure 5.11: Effect of Connector material, diameter, and connector inclination (a) GFRP connector 0° (b) GFRP connector 30° (c) GFRP connector 45° (d) Steel connector 0° (c) Steel connector 30° (f) Steel connector 45°. (All panels analyzed with 0.005 flexural reinforcement ratio and 300 mm connector spacing)

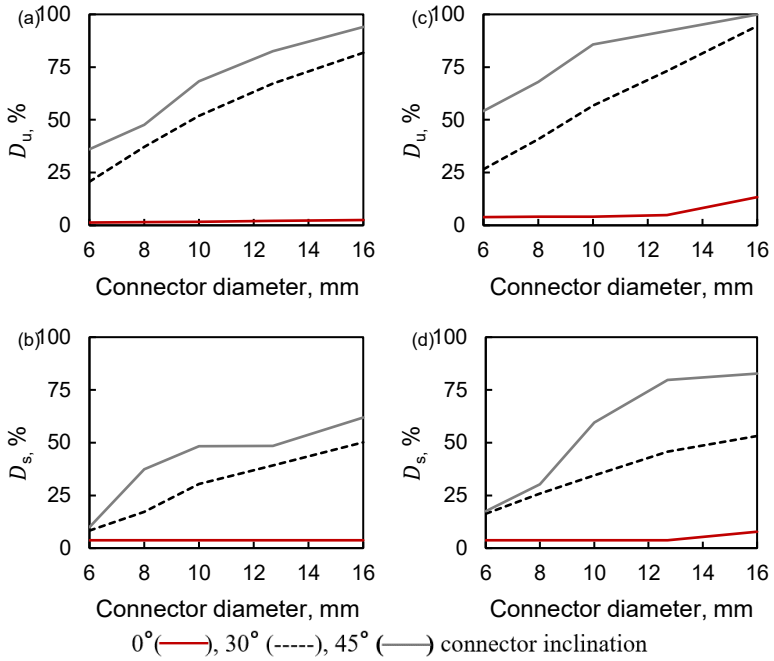

Figure 5.12: Effect of connector material type on D_u, D_s for connector made of (a,b) GFRP (c,d) Steel (All panels with flexural reinforcement ratio of 0.005 and connector spacing of 300 mm).

5.10.2 Effect of flexural reinforcement ratios

As the panel flexural reinforcement ratio increased for the same shear connector reinforcement ratio, the strength and stiffness of the panel increased (Fig. 5.13). Although the strength of the panels increased with flexural reinforcement ratios, the D_u and D_s reduced (Fig. 5.14), more evident for the 300 and 600 mm connector spacing for all connector diameters in this study. This is because moment resistance increases essentially linearly with the reinforcement ratio (if tension controlled) which requires additional shear flow from the connectors. However, since the connector contribution remains the same, the connector is unable to contribute more towards shear flow thereby reducing the connector contribution to composite action.

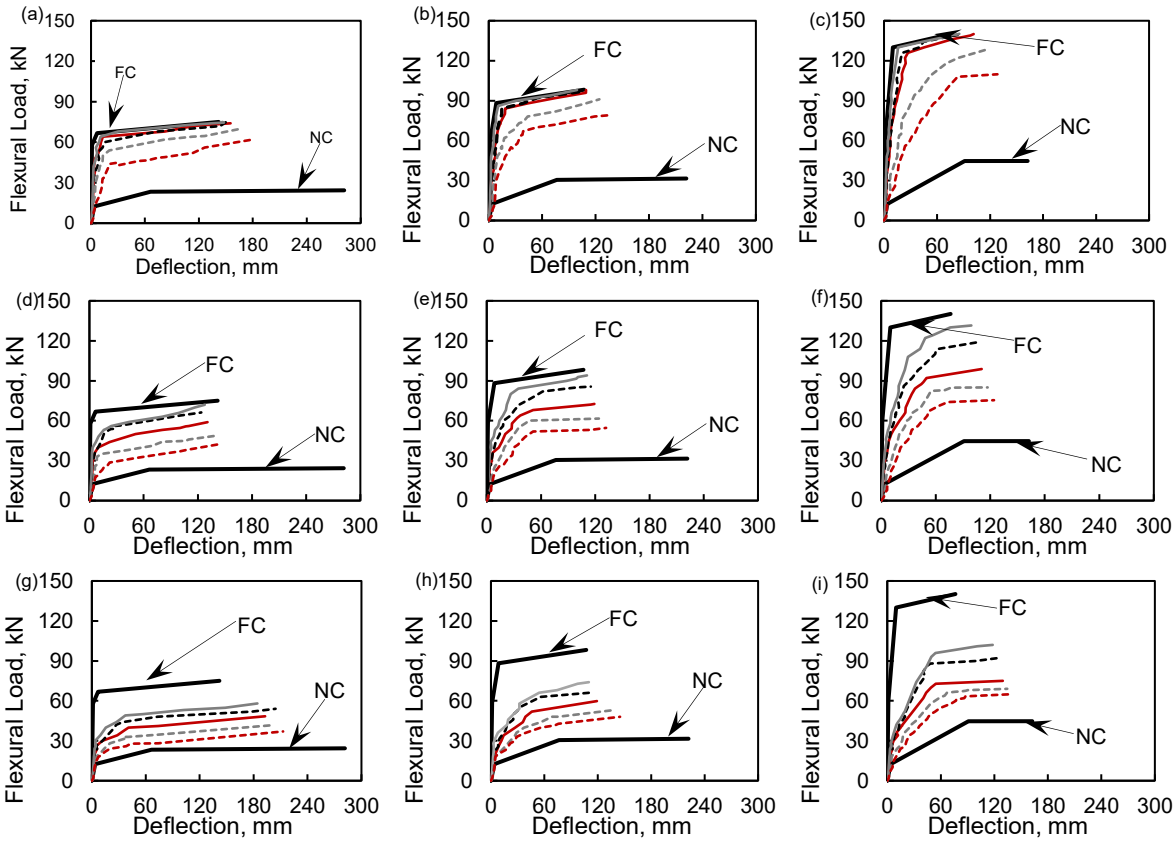

6 (-----), 8 (-----), 10 (——), 12 (-----), 16 mm(——) diameter shear connector

Figure 5.13: Effect of flexural reinforcement ratio with 150 mm connector spacing (a) 0.005 (b) 0.007 (c) 0.01. 300 mm connector spacing (d) 0.005 I 0.007 (f) 0.01. 600 mm connector spacing (g) 0.005 (h) 0.007 (i) 0.01. (All connectors are GFRP inclined at 45 degrees)

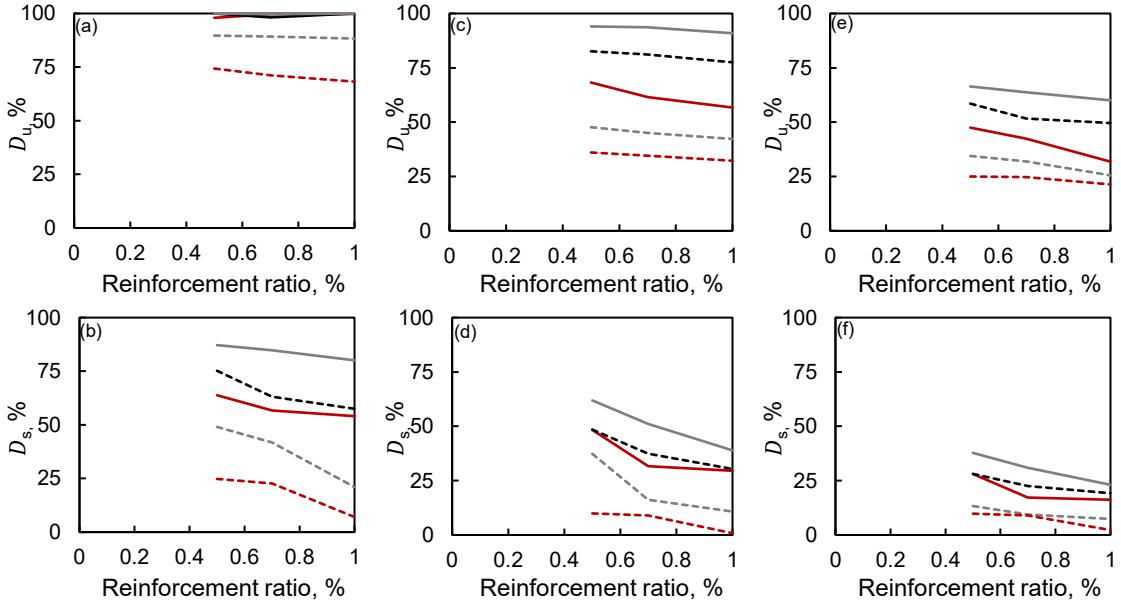

6 (-----), 8 (-----), 10 (——), 12 (-----), 16 mm(——) diameter shear connector

Figure 5.14: Effect of flexural reinforcement ratio on D_u, D_s. (a,b) 150 mm connector spacing (c,d) 300 mm connector spacing (e,f) 600 mm connector spacing

5.10.3 Effect of connector diameter

Generally, as the connector diameter increased, the stiffness, strength, and degree of composite action of the panel (D_u, D_s) increased (Fig. 5.11,5.12,5.13,5.14). This benefit was more evident with larger spacing (300 and 600 mm used in this study).

However, the effect of increasing the shear connector diameter from 6 to 16 mm on the degree of composite action is negligible when the connector angle of insertion was zero degrees, especially with the GFRP connector (Fig. 5.11). This is because flexural failure governs based on the connector lengths and diameters, and the flexural modulus of elasticity governs connectors inserted at 0° (dowel action). The flexural modulus of elasticity for FRP is similar in value to the longitudinal modulus of elasticity for small connector sizes (for the 6-10 mm diameter connector used in this study) as the fibres in the bar are better engaged under bending. For larger connector sizes, the flexural modulus of elasticity significantly deviates from the longitudinal modulus of elasticity (for the 12 and 16 mm diameter connector used in this study) due to the likelihood of the misalignment of fibres during production and defects (Benmokrane et al. 2017). Also under dowel action, only the outermost fibres experience high stresses. Therefore, for large connector sizes, only a small number of fibres are fully engaged which makes it attain lower flexural modulus even when compared to a smaller connector size with similar fibre content.

Overall, the average strength ratio when sequentially changing from the 6 to 16 mm connector was not proportionate with the ratios of the connector areas.

5.10.4 Effect of connector inclination

As the connector inclination increased from 0° to 30° and 45° the strength, stiffness, and degree of composite action (D_u D_s.) increased for panels with steel and GFRP connectors, and all connector diameters (Fig. 5.11,5.12). This is because the inclined connectors are placed to benefit from truss action, and connectors made with GFRP can utilize both the longitudinal and flexural modulus of elasticity. In addition, panel ductility increased with an increase in connector inclination, notably for panels with GFRP connectors which failed due to connector failure while

panels with steel connectors failed due to concrete crushing. While panels with connectors inclined at zero degrees had the least strength and composite action, designers may still prefer such panels as they may be less susceptible to thermal bowing (Pozo-Lora 2018).

5.10.5 Effect of connector spacing (connector reinforcement ratio) and arrangement

The effect of connector spacing is analogous to the effect of connector reinforcement ratio. As connector spacing reduced the strength, D_u, and D_s of the panel increased (Fig. 5.13, 5.14). The reason for this is that for closely spaced connectors, the slip is better resisted by the connectors and more shear force is accumulated towards the middle of the panel. The effect of connector arrangement was checked where a panel with two connectors per row produced similar strength as that of a panel with one connector per row (similar reinforcement ratio, Fig. 5.15a,b). Also using a larger number of smaller connector sizes (10 mm) produced similar panel strength (Fig. 5.15c) as a smaller number of larger connector sizes (12, 16 mm at the same connector reinforcement ratio).

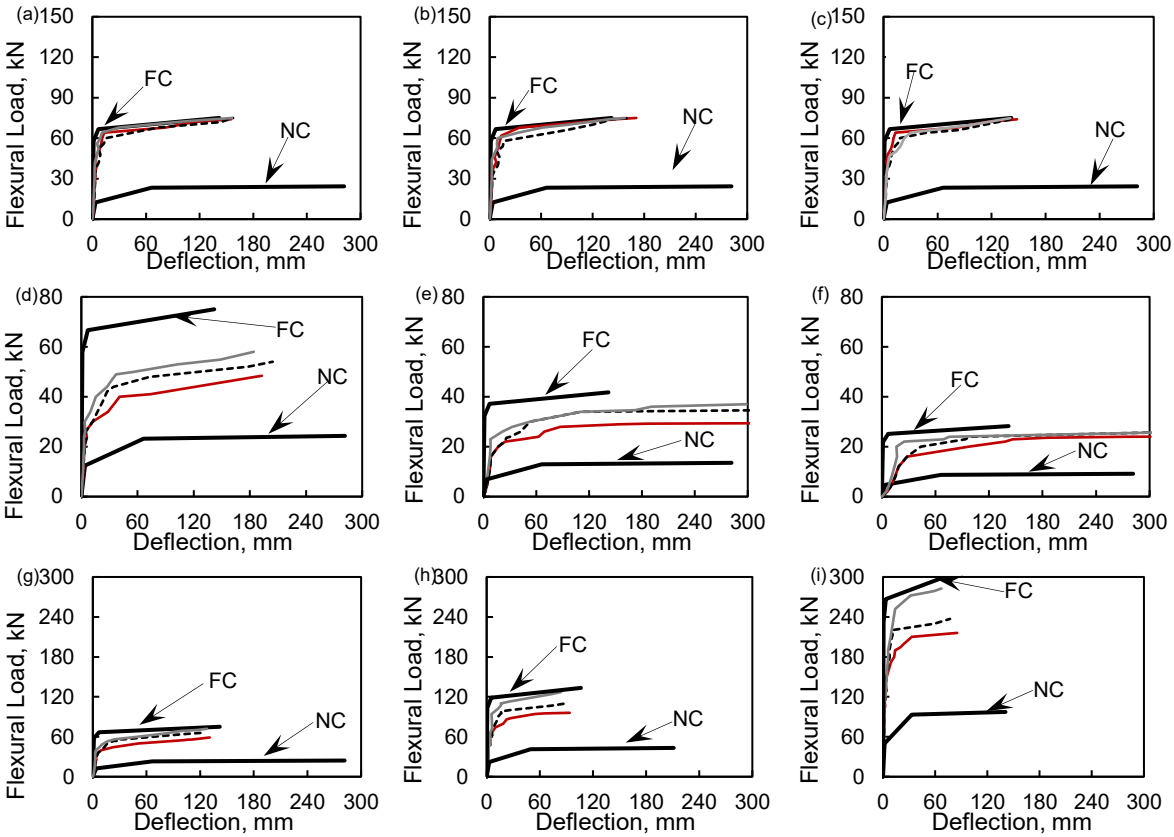

Figure 5.15: Effect of connector arrangement (a)10 connectors (one per row) at 150 mm spacing (b) 10 connectors (2 per row) at 300 mm spacing (c) Effect of similar connector reinforcement ratio using different connector diameters (150 mm spacing). Effect of panel length (d) 3200 mm I 5600 mm (f) 8500 mm. Effect of wythe thickness (concrete and insulation) (g) 75 mm (h) 100 mm (i) 150 mm. All panels with flexural reinforcement ratio of 0.005).

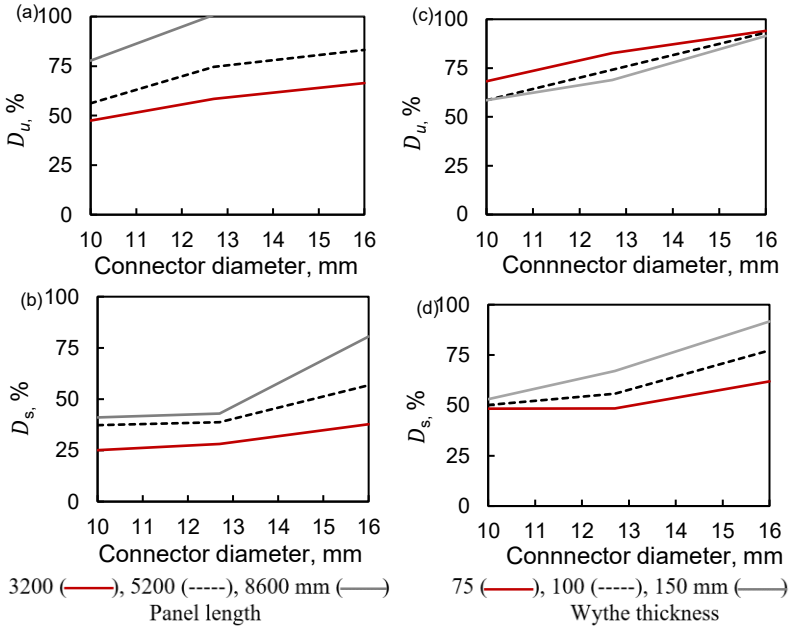

Figure 5.16: (a,b) Effect of panel length on D_u, D_s. (c,d) Effect of wythe thickness (concrete and insulation) on D_u, D_s. (All panels with flexural reinforcement ratio of 0.005).

5.10.6 Effect of panel length

The design and analysis of partially composite panels are length-dependent due to the presence of shear connectors along the length and differ from the typical flexural design of non and fully composite panels which is based on cross-section. As panel length increased the degree of composite action (D_u,D_s) increased (Fig. 5.16a,b). This is due to a larger aggregation of connector shear contribution towards the middle of the panel, which makes the peak load closer to that of the full composite section. However, the peak load capacity reduced as panel length increased (Fig. 5.15d,e,f).

Panels with larger lengths (5600 and 8500 mm in this study) had larger deflections. In addition, the limiting service load calculated using L/360 shows that the maximum service load reduces with an increase in panel length, and the panels are controlled by serviceability requirements. Considering this, designers can make the wythes thicker and also use closely spaced connectors to improve the service performance.

5.10.7 Effect of panel wythe thickness

Generally, panel peak load increased as the wythe thickness increased (Fig. 5.15g,h,i). While the D_s increased with wythe thickness (Fig. 5.16d), the D_u reduced with an increase in panel wythe thickness due to the additional demand put on the connectors (Fig. 5.16c). While also considering that the panel weight increases with wythe thickness, the option of increasing the panel thickness may not be attractive to a designer who desires a lightweight wall section.

5.11 LIMITATIONS OF PROPOSED MODEL

The proposed model was developed for simply supported panels where the end moments are negligible and would need to be modified to account for different support conditions. Also, the model was developed for panels without axial load and would need to be modified to account for axial load eccentricities and second-order effects. The model is only applicable to panels under one-way bending and the behaviour of panels under two-way bending was not considered in the

study. Therefore, further work on two-way responses of walls and accounting for factors like doors and windows are recommended.

5.12 CHAPTER SUMMARY AND CONCLUSIONS

The major aim of this study was to develop a designer-friendly analytical model to predict the load-deflection response of partially composite panels. The model was validated using experimental tests in literature where the panel components where published or could be traced to a previous publication. In addition, a parametric study was performed on the effect of the panel length, wythe thickness, reinforcement ratio, connector spacing, connector diameter, connector material, and connector inclination, on the strength and degree of composite action. The following was concluded from this study:

1. The proposed model accurately predicts the strength and failure mode of simply supported panels with reduced computational rigour compared to other models. The model is developed with reduced barrier to entry and designers are familiar with the steps which can be done using a simple spreadsheet.
2. The connector inclination and connector spacing influenced the strength and degree of composite action to a larger extent than others.
3. While an increase in flexural reinforcement ratio and wythe thickness increased the strength of panels the degree of composite action reduced due to extra demand put on the connectors.
4. The effect of certain parameters was more pronounced under certain conditions. For example, the effect of increasing the connector diameter from 10 to 16 mm was more evident with larger connector spacing and diminished when the connector spacing was smaller. Therefore, it would be more beneficial in terms of cost for a designer to use smaller connectors at small spacing than large connectors at small spacing.

Even if panel strength reduces with smaller connector sizes, it may be beneficial in reducing thermal bowing and should be confirmed through tests. It is recommended that researchers always

report the properties of all panel materials to aid in independent assessments like that carried out in this study.

6. ANALYTICAL FLEXURAL MODEL FOR PARTIALLY COMPOSITE DOUBLE WYTHE CAVITY MASONRY WALLS

6.1 INTRODUCTION

Double wythe cavity masonry walls consist of outer and inner layers also known as wythes. Double wythe cavity masonry walls are usually constructed onsite, where the outer wythe is made of clay or concrete veneer bricks, while the inner wythe is made of Concrete Masonry Units (CMUs) (Baker et al. 2004, Wang et al. 1997). Due to their ease of production, lower cost, better regulation of indoor humidity, and superior durability in comparison to concrete bricks, clay bricks are often used in the outer wythe (Banerjee et al. 2019, Cagnon et al. 2014, Gencel et al. 2020).

The cavity contains insulation, which is placed for thermal purposes and assumed to not contribute to the structural response of the wall in design (Fig. 6.1). An air-gap of at least 25 mm is created after the veneer and serves as a drainage path (Langmans et al. 2017, Brick Industry Association 2018, Allen and Iano 2009). A vapour or moisture barrier is attached to the warmer side of the insulation to prevent the entry of water vapour due to condensation (Clayford 2003, Hatzinikolas et al. 2015). Similar to insulated concrete walls, modern double-wythe cavity masonry walls are joined using connectors which transfer load from the outer wythe to the inner wythe, and are the main contributors to strength and stiffness for walls under flexural and axial loading (Sakr and Neis 2001, Wang et al. 1997). Common connectors for masonry walls are discrete in application and usually made of galvanized steel although there have been attempts to develop masonry connectors made from Fibre reinforced polymers (FRP) (Lissel and Shrive 2001). The structural contribution from a connector depends on its size (diameter/thickness) and embedment length. Connector sizes are also influenced by the thickness of the mortar joint which typically ranges between 10 and 15 mm (Cascardi et al. 2020, Petersen et al. 2012, Martins et al. 2017). CSA A370:14 (2018) limits the size of flat and round connectors to 50% and 67% of the mortar thickness, respectively, to ensure adequate cover and bond with surrounding mortar.

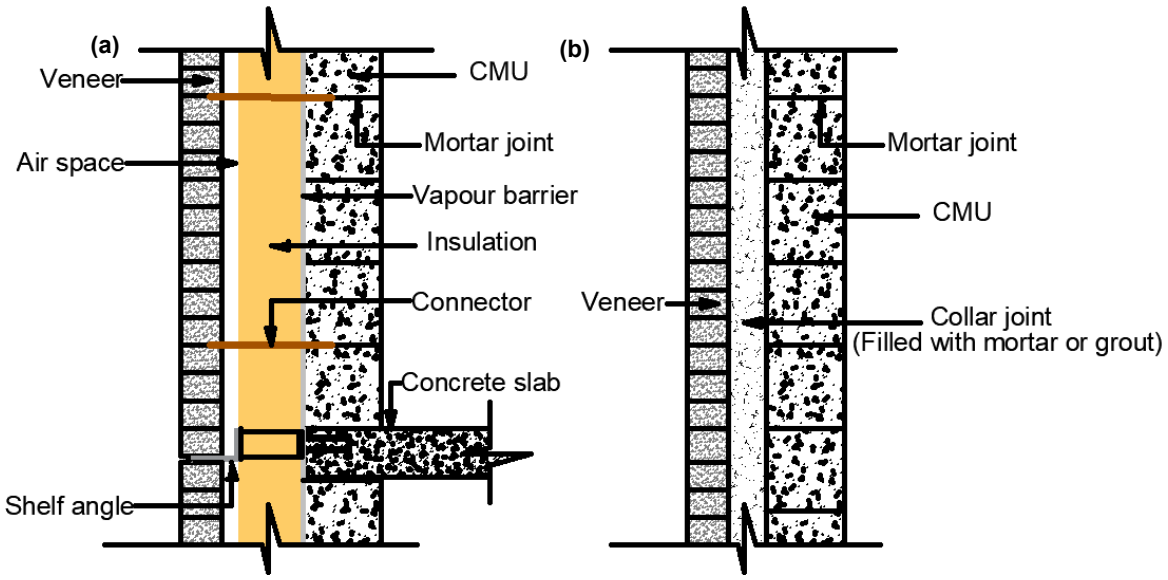

Figure 6.1: (a) Vertical section of a double-wythe cavity masonry wall with connectors (b) vertical wall section with grouted collar joint

Double-wythe masonry cavity walls tend to act within three classes which are non-composite, partially composite, and full composite (Drysdale and Hamid 2005, TEK 05-01B 2003, Hatzinikolas et al. 2015). In non-composite walls, both wythes act individually and carry load based on their relative stiffnesses. In most applications of non-composite walls, the outer wythe is made of bricks and the bricks are only placed for aesthetic and hygrothermal purposes (Brown and Elling 1979 , Reneckis et al. 2004, Drysdale and Hamid 2005, TEK 16-01A 2006), thereby acting structurally as a single wythe reinforced CMU wall (Drysdale and Hamid 2005). In fully composite walls, there is a shared load resistance and both wythes act as a single unit. This is usually achieved by filling the collar joint (space between the masonry layers) with grout or mortar, although it may initiate thermal bridging and permanent moisture damage which leads to a reduction in the R-value of the wall (Reicher and Farahmandpour 2016, TEK 06- 02C 2013, Ismaiel et al. 2022). In partially composite walls, the connectors joining the wythes are not stiff enough to make both wythes act as a single unit, as seen in full composite walls (Brick Industry Association 2018).

The design of non and fully composite walls follows methods taught in many masonry courses. However, the design for partially composite double-wythe cavity masonry walls is complicated due to the presence of shear forces transferred by the shear connectors between the wythes.

Only a few attempts have been made to predict the load-deflection response of double-wythe cavity masonry walls. Initial analytical models for double wythe cavity masonry walls like Pacholok (1989) and Papanikolas et al. (1990) were developed using finite element modelling where the part of the connector embedded in CMU mortar was modelled as fixed while the connector part at the veneer joint was modelled as a hinge. However, these finite element models were time-consuming and only predicted the load and deflection up to cracking. Zmavc (1991) developed analytical expressions which were compared to the previous finite element models. Though the time for computation was reduced, the model just like the previous finite element models, only predicted the load and deflection up to cracking based on the respective stiffness of the CMU and brick wythes. Overall, the studies highlighted factors such as the connector property and relative stiffnesses of the wythes as key factors affecting the stiffness and load-carrying capacity of walls. This means proper material characterization of the wythes and connectors is needed for accurate wall evaluation.

In this paper, an analytical model based on simplified moment-curvature relationships is used to create the load-displacement response of partially composite double-wythe cavity masonry walls. As discussed in Section 5.1 of this thesis, the moment-curvature approach is different from the strength approach commonly used for steel-concrete composite beams where full composite action is assumed (Hassan and Rizkalla 2010, Teixeira et al. 2016). Additional differences in the strength and curvature approach are also discussed in Section 5.1 of this thesis.

The model is also implemented to evaluate the degree of composite action created by a novel connector (Fig. 6.2). In addition, the computations are made such that they can be completed using simple-to-use spreadsheet software. Since the goal of this study was to quantify the degree of composite action generated by connectors in double wythe cavity walls, the examined wall was loaded under flexural load while the axial load considered was due to self-weight of the wall (effect of super imposed axial load is not within the scope of this study). The effect of various parameters on wall strength and degree of composite action were also examined. These include cavity width,

connector type and spacing, wall length, loading direction (pressure and suction), and flexural reinforcement ratio. To evaluate the role of shelf angles towards composite action, walls were examined with a very stiff metal (L-shaped steel angle) at the bottom of the wall.

6.2 DEVELOPMENT OF NOVEL CONNECTOR

Many masonry wythe connectors are not designed to transfer shear forces, this means the amount of composite action developed by connectors becomes negligible, therefore making most double-wythe cavity masonry walls be characterized as non-composite systems.

With increasing insulation thickness being prescribed to improve the thermal performance of buildings, walls are expected to lose composite action. This is why longitudinal shear testing was carried out as shown in chapter 4 of this Thesis on a novel inclined connector as well as existing plate connectors (Fig. 6.2a). The novel inclined connector resists load through truss action and is anticipated to contribute more towards composite action and aid in designing walls with larger cavities and thinner wythes. The existing connector is a plate connector that is inserted vertically or horizontally, with only the vertically placed plate connector having an additional rectangular-bent round tie (Fig. 6.2b) attached through pre-cut circular slots with a diameter of 6.8 mm (Fig 6.2c). The slots were created in the connectors to serve as an opening to attach embedment ties while also reducing their self-weight and influence on thermal bridging. The novel connector is inserted with two similar rectangular-bent round ties as with the existing plate connectors. The diameter of the rectangular-bent round tie was 4.8 mm (Fig. 6.2b) while the thickness of the plate and novel connector was 3 mm.

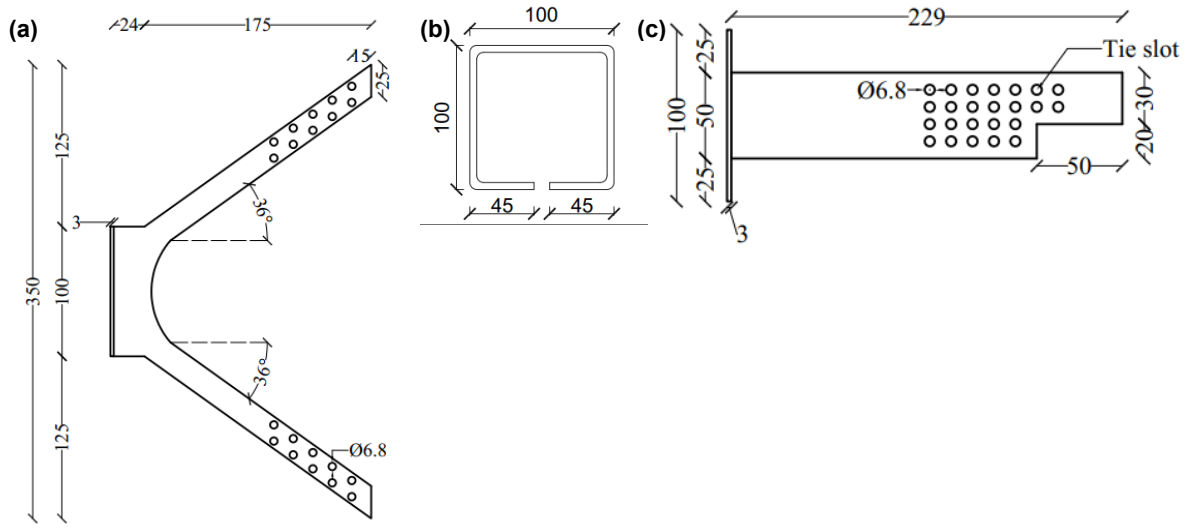

Figure 6.2: (a) Inclined connector (b) embedment tie (c) existing connector (All dimensions in mm)

6.3 WALL EVALUATION

Some cavity masonry walls are built to resist a combination of superimposed axial loads and out-of-plane lateral loads, or in some residential applications where they resist only out-of-plane lateral load without superimposed axial loads also known as non-load bearing walls (Hatzinikolas et al. 2015). Out-of-plane lateral loads come from sources like wind and result in out-of-plane bending moment (Fig. 6.3), while axial loads can be from the roof or the self-weight of the masonry. The superimposed roof load tends to act concentrically or eccentrically on the masonry, with self-weight usually assumed to act concentrically.

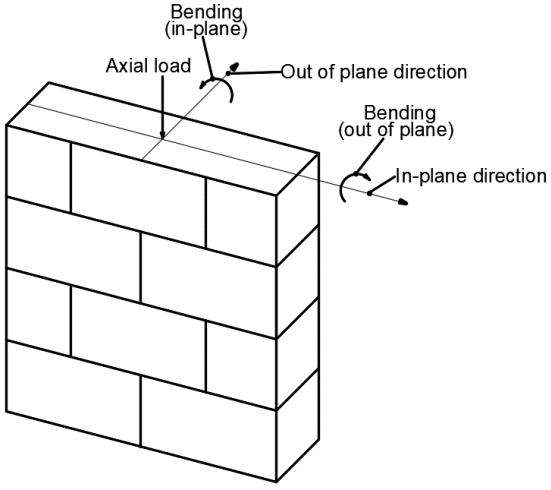

Figure 6.3: Loading direction for walls

The response of single wythe masonry walls is symmetrical under pressure and suction for loadbearing walls with rebar placed at the middle of the cell. This is similar to most double wythe

insulated concrete panels which have the rebar at similar positions of the wythe. However, for most double wythe cavity masonry walls, only the CMU is reinforced which makes the response different under pressure and suction. The brick wythe is placed for aesthetic purposes which is usually unreinforced with its structural contribution in tension neglected after cracking. In double-wythe masonry walls, the self-weight of the brick wythe is carried by shelf angles while the connectors transfer out-of-plane load from the brick wythe to the CMU.

Most masonry walls are slender. Following CSA S304-14 (2019), slenderness effects can be ignored if the slenderness ratio is less than $10 - 3.5e_1/e_2$ (e_1 and e_2 are the smaller and larger of the two end eccentricities, respectively). For 140, 190, and 290 mm CMU block wythes with pin support conditions, slenderness can only be neglected for 910, 1235, and 1885 mm wall heights, respectively. These wall heights are smaller than the 2400-3000 mm height typical for even low-height residential and office storeys in Canada. In terms of composition, double wythe cavity masonry walls are similar to double wythe insulated concrete walls, with inner and outer wythes that are joined by shear connectors. When both walls act non-compositely (Fig. 6.4a), i.e. when they act separately, strain discontinuity is created between the wythes. This strain discontinuity accumulates along the wall in the form of slip between the wythes and is largest at the end of the wall. This slip is then resisted by the connectors in the form of longitudinal shear contribution. For partially composite walls (Fig. 6.4b), the strain discontinuity is lesser compared to non-composite sections while in fully composite sections, there is no strain discontinuity (Fig. 6.4c). As the load transfer mechanism is similar for both wall types, this means analytical models developed for partially composite double wythe insulated concrete walls can be used to analyze double wythe cavity masonry walls. In addition, there are similarities in design provisions for both wall types contained in respective concrete and masonry design codes (CSA-A23.3 2019, CSA S304-14 2019), (ACI 318 2019, TMS 402/602 2016), (Eurocode 2, Eurocode 6).

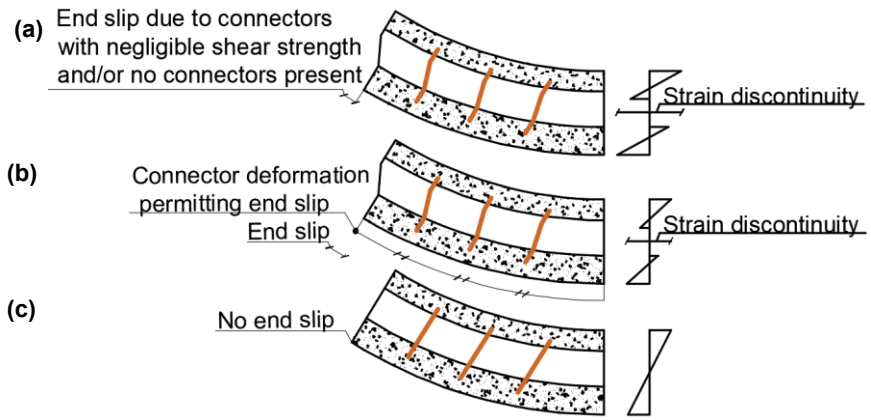

Figure 6.4: Wall classification (a) Non composite (b) partially composite (c) fully composite

While both wall types resist load through the same mechanism, a major difference is that the outer wythe in double wythe cavity masonry walls are usually unreinforced which makes similarly sized insulated concrete walls have larger strength. The absence of reinforcement in the outer wythe also makes the response of double wythe cavity masonry walls under pressure different from that under suction.

6.4 WALL BEHAVIOUR

The total moment applied on a slender wall is composed of a primary moment and a secondary moment. The primary moment is generated from out-of-plane loading, the eccentric axial load, or a combination of both. Secondary moments occur due to deflections, δ, created by primary moments which makes the axial load, P, act at an eccentricity (or additional eccentricity if the axial load was initially acting eccentrically), thereby creating second-order effects. CSA S304-14 (2019) accounts for second-order effects using either the $P-\delta$ or the moment-magnifier method. The $P-\delta$ method calculates the secondary moment that is to be added to the primary moment through the iteration process while the moment magnifier method calculates the total moment directly by amplifying the primary moment. While the moment magnifier method is less time-consuming to execute, it is an approximate method derived from the $P-\delta$ method, and deviates from the $P-\delta$ method as the slenderness ratio increases (ratio of the height to wall thickness ratio, kh_w/t_u, where k is an effective length factor based on boundary conditions at the top and bottom

of the wall (Annex B of CSA S304-14 2019), h_w is the wall height, while t_u is the thickness of the unit).

The extent to which the secondary moment affects the wall is determined by the slenderness ratio. CSA S304-14 (2019) outlines that slenderness (secondary effects) can be ignored if the slenderness ratio is less than $10 - 3.5\mathrm{e}_1/\mathrm{e}_2$, with e_1 and e_2 being the smaller and larger of the two end eccentricities, respectively. When the slenderness ratio is greater than $10 - 3.5\mathrm{e}_1/\mathrm{e}_2$ but less than or equal to 30, slenderness effects are applied. When $\mathrm{kh_w/t_u}$ is greater than 30, special slenderness provisions apply.

As the aim of this study was to evaluate the contribution of the novel connector toward composite action, the only axial load considered is from the self-weight ($\mathrm{P_{sw}}$) of the wall. This is similar to Goyal et al. (1994) where double-wythe walls were only tested under out-of-plane flexural loading while examining the performance of a specially made CMU block. The self-weight, $\mathrm{P_{sw}}$ (kN), is obtained using Eq. 6.1. At connector locations (h_{cl}), the self weight is obtained by multiplying Eq. 6.1 by h_{cl}/h_w, and the self weight reduces from the bottom of the wall to zero at the top of the wall.

$$P_{sw} = \left(st_u P_{solid}\rho_{unit} + b_{gr}t_u\rho_{gr}P_{hollow}\right)h_w g \tag{6.1}$$

s is the rebar spacing, t_u is the thickness of the unit, b_{gr} is the width of the grouted cell, P_{solid} and P_{hollow} are the percentage of the solid and hollow parts of the masonry wall, $g = 9.81\ m/s^2$, ρ_{unit} and ρ_{gr} are the density for the CMU and grout, respectively.

6.5 CONNECTOR CONTRIBUTION (V_{CN})

The contribution of connectors towards composite action is determined by their ability to transfer shear load. For connectors to transmit shear load, their axial stiffness ($E_{cn}A_{cn}/X$) should be larger than the flexural stiffness of the wythes ($E_{wythe}I_{wythe}/{h_w}^3$), and this sufficient axial stiffness ensures that the wythes bend with the same curvature (Brown and Elling 1979, Sakr and Neis

2001) (X is the connector length, E_{wythe}, I_{wythe} are the modulus of elasticity and moment of inertia of the wythe, $E_{cn,}A_{cn}$ are the modulus of elasticity and cross-sectional area of the connector).

When connector properties such as the yield strength and modulus of elasticity are not available, they can be obtained from a separate shear connector test program such as that shown in chapter 4 of this thesis. Also, when evaluating the behaviour of walls from literature, the connector contribution can be obtained from previously published results if the walls have the same properties such as cavity width, connector dimension, and mortar strength. When shear test results are not available, they can be obtained using the formulations discussed below for rectangular and circular-shaped connectors.

6.5.1 Dowel action

A shear connector can be depicted as a beam with a fixed-hinge end condition, with the part of the connector attached to the CMU assumed fixed while the end in the veneer is assumed to be a hinge (as the end in the veneer is unable to resist moment, Fig. 6.5). This boundary condition has also been used in previous analytical models for similar connector types and shown to produce reasonable results.

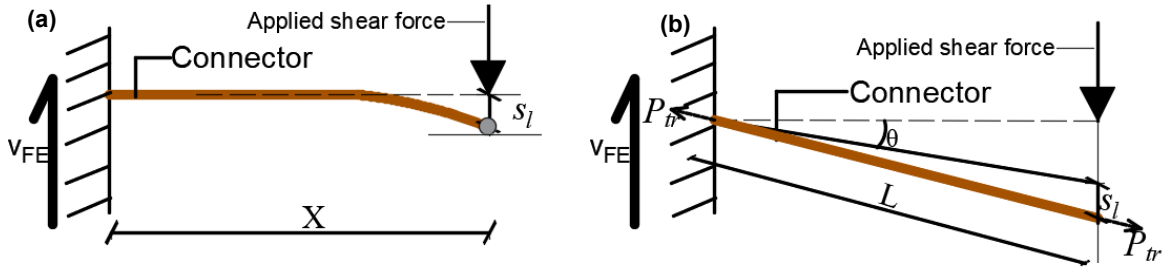

Figure 6.5: Fixed-hinge connector end condition (a) Dowel action (b) Truss connector (s_l is the slip, P_{tr} is the connector contribution under truss action)

The maximum fixed-end shear ($V_{max,FE}$) is obtained using Eq. 6.2.

$$V_{max,FE} = \frac{2f_y I_{cn}}{X t_c} \tag{6.2}$$

t_c, I_{cn} are the thickness in the direction of loading, modulus of elasticity, and moment of inertia of the connector of the connector, respectively. f_y is the yield strength of the connector, X is the horizontal connector length within the cavity.

6.5.2 Truss action

The demand on a connector under tension and compression (P_T) is obtained using Eq. 6.3, which was adopted from connectors in concrete walls as shown in chapter 5 of this thesis.

$$P_T = \left(E_{cn} \left(\frac{\sqrt{(X \tan\theta + \Delta)^2 + (X)^2} - L}{L} \right) + \frac{1.5 E_{cn} t_c}{X^2} \Delta \right) A_{cn} \sin\left(\tan^{-1}\left(\frac{X \tan\theta + \Delta}{X} \right) \right) \qquad (6.3)$$

θ, A_{cn}, L are the angle of inclination, cross-sectional area, and inclined connector length.
The connectors are also examined for their critical moment due to lateral torsional buckling, and elastic buckling. Other failure modes are the pullout and yield strength of the connector, as well as the masonry breakout strength. These are presented in Appendix C for convenience as well as a design example shown in Appendix D.

6.5.3 Axial behaviour of connectors

For walls under pressure and suction, the axial force distribution is largest in the top and bottom end-connectors, and closer to zero for the connector near the middle of the wall (McGinley et al. 1988, Dryscale and Hamid 2005). However, there is no conclusive method to determine the axial forces carried by connectors in walls under out-of-plane loading. In this study, the veneer is assumed to span between the floor height, with the top and bottom row of connectors apportioned the full out-of-plane load on the veneer, i.e., the top and bottom row of connectors acting as reactions supporting the veneer load. Meanwhile, the axial force in other connectors is obtained based on their relative distance from the end connectors. This ensures there is a progressive axial failure of connectors, starting from the end connectors which carry more of the shear load and have been shown to fail first when axial failure of connectors governs wall failure (Goyal et al. 1994).

For walls under pressure and suction, the value of the end-connector reactions is compared to the compressive and tensile strength of the connectors, respectively.

6.6 MATERIAL RELATIONSHIPS

6.6.1 Masonry

Masonry (CMU and brick) is taken to have cracked when it reaches its cracking strength (f_t), and the structural contribution of the brick is not considered after cracking as it is usually unreinforced. In the absence of test values, the design value for f_t can be obtained from Table 5 of CSA S304-14 (2019).

The modulus of elasticity for masonry, E_m, is obtained using Eq. 6.4 (CSA S304-14 2019).

$$E_m = 850 f'_m \tag{6.4}$$

f'_m is the design compressive strength of masonry.

6.6.2 Steel

Reinforcing steel and connectors are assumed to behave as an elastic-perfectly plastic material i.e. having constant stress after yield, with an elastic modulus E_s of 200 and 194 Gpa, respectively (Fig. 6.6). The yield strength (f_y) for the reinforcing steel and connectors was 400 and 234 MPa, respectively while the yield strain was 0.002 and 0.001, respectively.

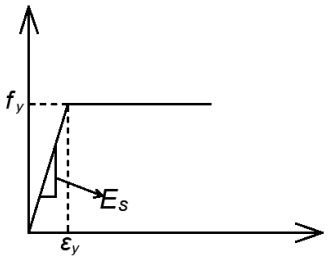

Figure 6.6: Constitutive model for steel rebar and connector (ε_y, f_y are the yield strain and stress)

6.7 MOMENT-CURVATURE RESPONSE (PRESSURE AND SUCTION)

The development of the moment-curvature response is vital to the determination of the load-deflection response. The moment-curvature response for partially composite double-wythe cavity walls is between that of a non (NC) and fully (FC) composite wall. Previous analytical models like Sakr and Neis (2001) use a cumbersome process to determine the moment-curvature response for double wythe cavity masonry walls and also rely on empirical factors which may create a

barrier to usage. This is similar to most analytical models for insulated concrete walls such as Tomlinson and Fam (2016a), and Gombeda et al. (2017) that involve several iteration steps and are cumbersome to follow, which makes it difficult to apply to masonry walls.

In this study, a simplified moment-curvature response is obtained by carrying out evaluations at only three points: cracking, yielding of reinforcement, and masonry crushing. These points were selected since each is familiar to designers.

6.8 NON AND FULLY COMPOSITE SECTIONS

The behaviour of a partial composite wall (Fig. 6.7a) is between that of a non and fully composite wall, and the presence of connectors makes the determination of its behaviour challenging. In the analysis of non-composite sections, it is assumed that the veneer and CMU resist the load independently (Fig. 6.7b), with an effective depth d for the CMU. For a fully composite section, it is assumed that there is no strain discontinuity between the brick and CMU wythe and the moment of inertia is calculated using the properties of brick and CMU, with an increased effective depth of d_1 (Fig. 6.7c).

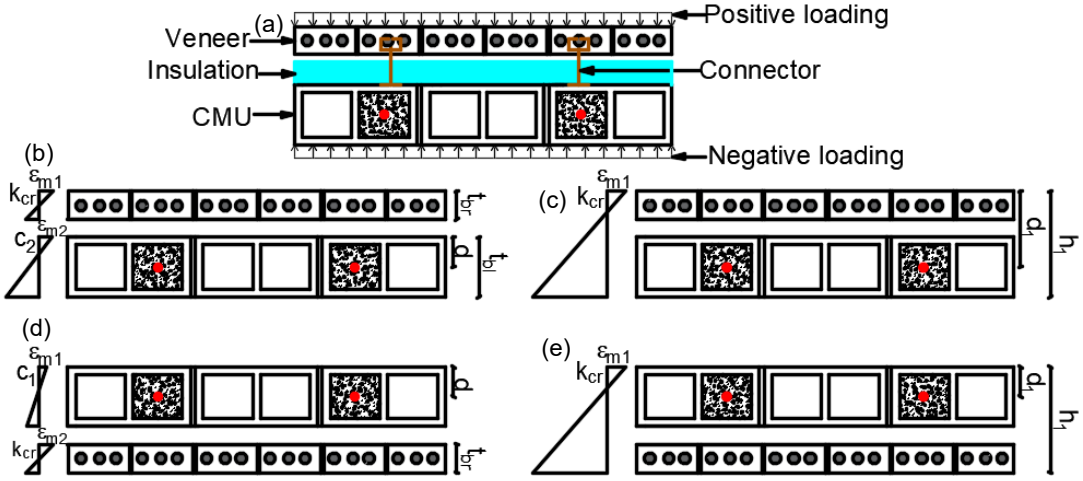

Figure 6.7: (a) Wall under loading (b,c) Non-composite (NC) and Fully composite action (FC) under pressure (d,e) Non-composite (NC) and Fully composite action (FC) under suction

6.8.1 Analysis before cracking

The cracking moment (M_{cr}, (kNm/m)) is obtained using Eq. 6.5.

$$M_{cr} = \left(f_t + \frac{P_{sw}}{A_{em}}\right)\frac{I_{tr}}{y_t} \tag{6.5}$$

A_{em} is the effective mortar bedded area. For NC, the respective A_{em} for the brick and CMU are used, while a summation of the effective area of both wythes is used for FC analysis.

For non and fully composite sections, y_t is the distance from the centroid ($\bar{y}$) to extreme tension fibre, f_t is the rupture stress in the extreme tension fibre. In partially grouted walls, a weighted value for f_t is used for calculation (Eq. 6.6). I_{tr} is the transformed moment of inertia, and in non and fully composite sections, it accounts for the transformation of the rebar into an equivalent CMU area. Additionally, for the fully composite section, the transformation of the brick wythe into an equivalent area of CMU is also accounted for by multiplying the effective width (b_{eff}) by a factor n_b which is the ratio of the elastic modulus of the brick to that of CMU. The effective width,b_{eff}, is taken as the lesser of the reinforcement spacing and 4 times the CMU wythe thickness, and this ensures successive rebars are coupled under bending (CSA S304-14, 2019).

The curvature at cracking (φ_{cr}) is obtained using Eq. 6.7. Since most double wythe cavity masonry walls have unequal wythe thicknesses, the respective wythes are checked to see which cracks first.

$$f_{t,weighted} = \frac{A_{gr}f_{t,gr} + A_{ug}f_{t,ug}}{A_{gr} + A_{ug}} \tag{6.6}$$

$A_{gr}, f_{t,gr}, A_{ug}, f_{t,ug}$ are the area and tensile strength of the grouted (gr) and un-grouted sections (ug), respectively. The uncracked properties are shown in Table 6.1 for pressure and can be modified for suction cases.

$$\varphi_{cr} = \frac{M_{cr}}{E_c I_{tr}} \tag{6.7}$$

Table 6.1: Uncracked properties of non and fully composite sections (pressure shown for FC)

Properties	Non -composite section	Fully composite section
$\bar{y}$	$\frac{t_{bl}}{2}$	$\left(\frac{\left(n_b t_{br} b_{eff} \times \frac{t_{br}}{2}\right) + \left(A_{e,bl} \times \left(t_{br} + t_{cj} + \frac{t_{bl}}{2}\right)\right)}{n_b t_{br} b_{eff} + A_{e,bl}}\right)$
		$= I_{br} + I_{bl}$
I_{tr}	$\frac{b_{eff} h^3}{12} - \frac{\left(b_{eff} - t_g\right)\left(t_{bl} - 2t_f\right)^3}{12}$	$\left(\frac{n_b b_{eff} {t_{br}}^3}{12} + t_{br} n_b b_{eff} \left(\frac{t_{br}}{2} - \bar{y}\right)^2\right) + \left(I_{bl} + A_{e,bl}\left(t_{br} + t_{cj} + \frac{t_{bl}}{2} - \bar{y}\right)^2\right)$
y_t	$t_{bl} - \bar{y}$	$h_1 - \bar{y}$

- Properties for partially grouted CMU section shown for non-composite section
- $A_{e,bl}$, I_{bl} are the effective area and moment of inertia for the effective width area of the CMU, and can be taken from Table 1-13 of TEK 14-1B (2007) depending on the nature of grouting. In the absence of such Tables in TEK 14-1B (2007), the centroid for the fully composite section can be obtained using the dimensions of the flange and grout components of the CMU.
- t_{br}, t_{cj}, t_{bl} are the thickness of the brick, collar joint, and CMU
- t_f, t_g are the thickness of the CMU flange and grouted cells, respectively.

6.8.2 Analysis at yielding

Basically, for walls under pressure, a fully composite section is considered as a masonry wall with similar reinforcement as a single CMU but with increased effective depth (d_1) as shown in Fig. 6.7 and Table 6.2. For walls under suction, the reinforcement in the fully composite section is considered to have an effective depth similar to that of a single CMU wall and smaller than that for pressure (Fig. 6.7d,e). At yielding, masonry is assumed to have a linear stress distribution, and this assumption is rational for under-reinforced masonry walls (similar to under-reinforced insulated concrete walls) under which most double-wythe masonry walls fall. Masonry may also be assumed to be non-linear at yielding, and using the Kent and Park (1971) model, the difference with the linear case was less than 6% for moment and curvature. For a non-composite section (pressure and suction), the yielding moment (M_y (kNm/m)) is obtained from Fig. 6.8a using Eq. 6.8 (moment for CMU wythe shown). For a fully composite section under pressure, the moment is obtained from Fig. 6.8c using Eq. 6.9 while that for a wall under suction is shown in Fig. 6.8b,d.

$$M_y = 0.5 E_m \varepsilon_m b_{eff} k_{cr} d \left(d - \frac{k_{cr} d}{3}\right) \tag{6.8}$$

$$M_y = A_s f_y \left(d_1 - \frac{k_{cr} d_1}{3}\right) + P_{sw} \left(\bar{y} - \frac{k_{cr} d_1}{3}\right) \tag{6.9}$$

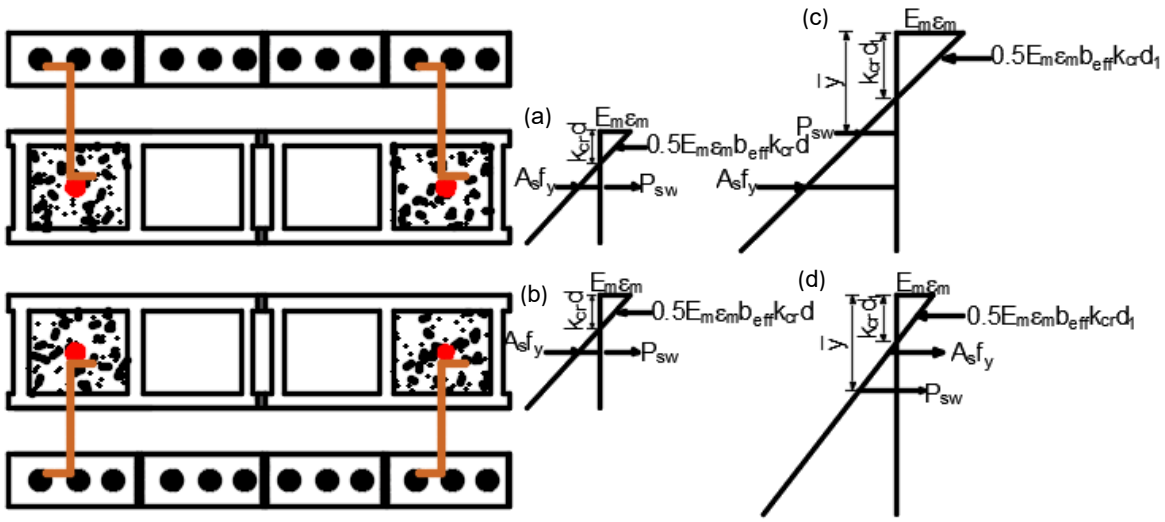

Figure 6.8: Cracked, elastic stress profile for (a,b) NC section (pressure and suction, CMU wythe shown only). FC section I pressure (d) suction

f_y is the yield stress of the reinforcement. k_{cr} is the elastic cracked neutral axis factor. The curvature at yielding (φ_y), reinforcement ratio (ρ) along with other parameters are defined in Table 6.2.

Table 6.2: Cracked Properties of non and fully composite sections

Properties	Non -composite section	Fully composite section
ρ	$\frac{A_s}{b_{eff}d}$	$\frac{A_s}{b_{eff}d_1}$
k_{cr}	$\sqrt{2\rho n + (\rho n)^2} - \rho n$	
I_{cr}	$\left(\frac{b_{eff}(k_{cr}d)^3}{3} + nA_s(d - k_{cr}d)^2\right)$	$\left(\frac{b_{eff}(k_{cr}d_1)^3}{3} + nA_s(d_1 - k_{cr}d_1)^2\right)$
φ_y	$\frac{\varepsilon_y}{d - k_{cr}d}$	$\frac{\varepsilon_y}{d_1 - k_{cr}d_1}$

- Dimension of CMU wythe shown here for non-composite section analysis
- n is the ratio of the elastic modulus for masonry to that of steel
- ε_y is the yielding strain for the reinforcement ($\varepsilon_y = \frac{f_y}{E_s}$)

6.8.3 Analysis at peak

The strength at peak is evaluated at masonry crushing, and CSA S304-14 (2019) assumes the equivalent rectangular stress block acts over a stress of $0.85\chi f'_m$ (Fig. 6.9), with equivalent stress block factor of β_1 shown in Table 6.3. The moment and curvature at masonry crushing (M_u, φ_u) are shown in Table 6.3.

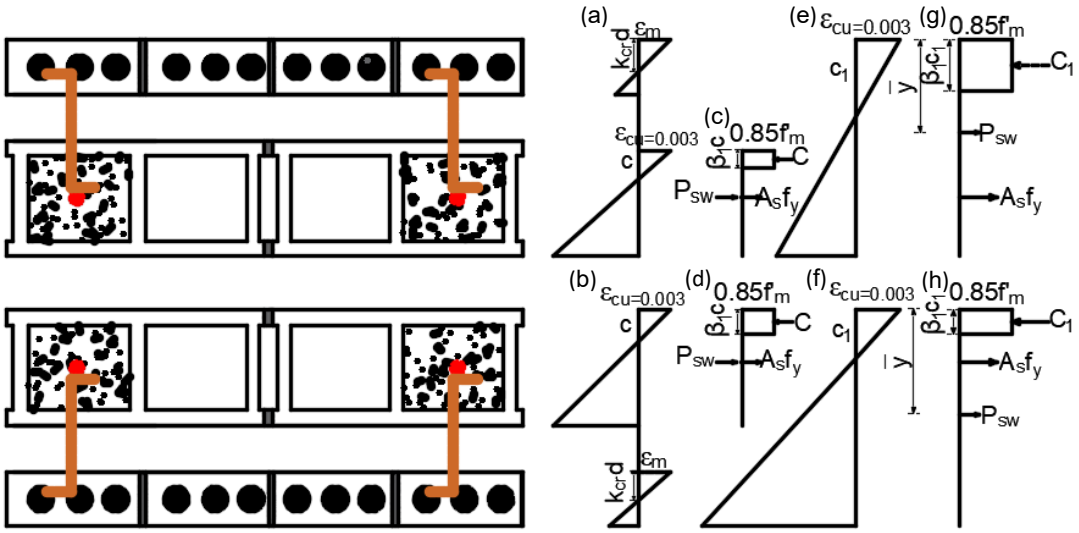

Figure 6.9: Strain profile at ultimate for NC section (a) pressure (b) suction. Load profile for NC section (c) pressure (d) suction. Strain profile for FC section I pressure (f) suction. Load profile for FC section (g) pressure (h) suction

Table 6.3: Section properties at peak

Properties	Non -composite section	Fully composite section
β_1	$0.8 - 0.1\left(\frac{f'_m - 20}{10}\right) \leq 0.8$	
M_u (kNm/m))	$C\left(d - \frac{\beta_1 c}{2}\right)$	$A_s f_y\left(d_1 - \frac{\beta_1 c_1}{2}\right) + P_{sw}\left(\bar{y} - \frac{\beta_1 c_1}{2}\right)$
φ_u	$\frac{\varepsilon_{cu}}{c}$	$\frac{\varepsilon_{cu}}{c_1}$

- Dimension of CMU Wythe shown here for non-composite section analysis
- ε_{cu} is the ultimate masonry compressive strain taken as 0.003.

6.9 EFFECTIVE WALL STIFFNESS

CSA S304-14 (2019) provides formulation for the effective wall stiffness, EI_{eff}, which aids to easily calculate second-order effects. This provision enables the application of elastic formulations in the calculation of deflection after cracking. For unreinforced masonry EI_{eff} is taken as $0.4E_mI_o$ while for reinforced masonry it is obtained using Eq. 6.10. Further for reinforced masonry, EI_{eff} should not be taken greater than $0.25E_mI_o$ and not less than E_mI_{cr}.

$$EI_{eff} = E_m\left(0.25E_mI_o - (0.25E_mI_o - E_mI_{cr})\left(\frac{e - e_k}{2e_k}\right)\right) \quad (6.10)$$

e *i*s the end eccentricity and e_k *i*s the kern eccentricity $= I_o/(A_e \times \bar{y})$, A_e is the effective area.

6.10 ANALYSIS FOR PARTIALLY COMPOSITE DOUBLE-WYTHE CAVITY MASONRY SECTIONS

For the non (NC) and fully (FC) composite sections, the moment-curvature at cracking and yielding can now be shown in plots for pressure and suction (Fig. 6.10a). Subsequently, the moment-curvature response for a partially composite double-wythe cavity masonry wall at percentage composite action between 0% (NC) and 100% (FC) can be determined by interpolating between the cracking and yielding for pressure and suction, respectively (Fig. 6.10b).

In the development of the moment-curvature response for NC sections, the contribution of the brick layer is only considered up to cracking. This is because the brick wythe in most partially composite cavity masonry walls are not reinforced and only aid after cracking in transferring the out of plane load to the backup wythe through the shear connectors. If the bricks were reinforced, its contribution in NC sections would be considered beyond cracking like the CMU. The absence of this rebar makes a partially composite cavity masonry wall reach lesser capacity in comparison to a similarly sized insulated concrete wall, and this can be improved by adding rebar at various intervals as in the CMU wythe. In this thesis, the cavity masonry walls examined were made of unreinforced brick layers.

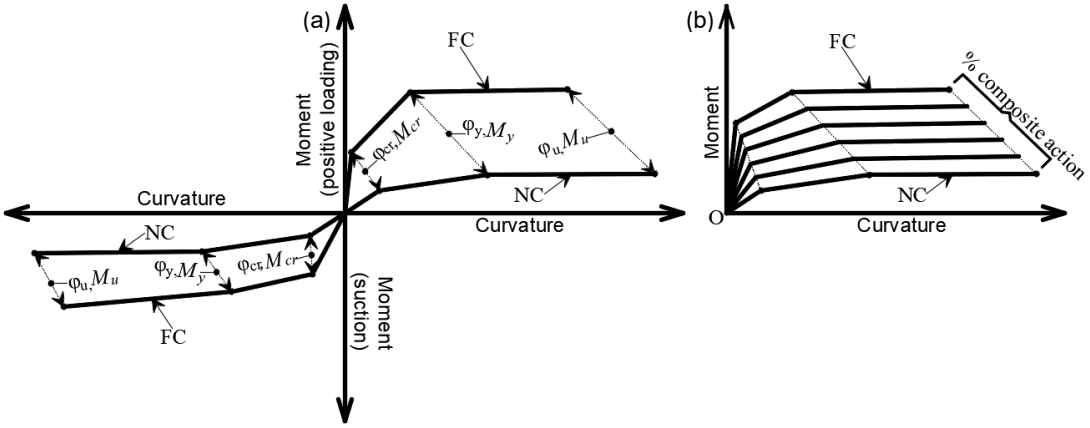

Figure 6.10: (a) Moment-curvature for pressure and suction (b) Full moment-curvature responses for intermediate levels of composite action

The response of a partially composite double-wythe cavity masonry wall can be determined by accounting for the shear contribution from the connectors. The strain discontinuity (ε_{sc}, Eq. 6.11, Fig. 6.4) varies linearly with the shear connection contribution (V_{cn}) and is maximum in the NC

section where the shear connector contribution is zero ($V_{cn,NC}$). In FC sections which are composite sections made of brick, collar joint, and CMU, there is no strain discontinuity between the wythes, and the maximum shear is transferred (V_{cn} equals $V_{cn,FC}$). For fully composite multi-wythe masonry walls, CSA S304-14 (2019) prescribes a value V_{cj} as the shear bond resistance between the collar joint (mortar or grout) and the neighbouring masonry (Eq. 6.12). The maximum shear force ($V_{cn,FC}$) in a section is obtained using Eq. 6.13. The connector contribution (V_{cn}) is accumulated at each connector location towards the middle of the wall, resulting in the maximum shear connection contribution for a section, $V_{cn,T}$ (Fig. 6.11).

$$\varepsilon_{sc} = \varphi(c_2 + t_{cj}) + \varphi(t_{br} - kd_{br}) \tag{6.11}$$

c_2 is the neutral axis depth in the CMU wythe (for pressure), φ is the curvature. As highlighted in Section 6.5, for connectors to be able to transmit shear load, they should possess sufficient axial stiffness and this sufficient axial stiffness ensures the two wythes have equal curvature when loaded (Brown and Elling 1979, Sakr and Neis 2001). Also, the strength of the connectors determines the amount they can contribute to longitudinal shear (i.e. composite action) in a wall. After cracking, the neutral axis for the brick wythe ($k_{cr}d_{br}$) can be obtained using the effective stiffness for unreinforced masonry ($0.4E_mI_o$).

$$V_{cj} = \frac{vI_{tr}b_{eff}}{Q} \tag{6.12}$$

$$V_{cn,FC} = \left(\frac{V_{cj}Q}{I_{tr}}\right)\frac{h_w}{2} \tag{6.13}$$

v is given in CSA S304-14 (2019) as the shear bond factor which is taken as 0.1 and 0.2 for mortared and grouted collar joints, respectively. An average value of 0.15 was used in this study. Q (Eq. 6.14) is the first moment of area of the masonry wythe adjacent to the plane under consideration about the centroid of the section.

$$Q = n_b t_{br} b_{eff}\left(\bar{y} - \frac{t_{br}}{2}\right) \tag{6.14}$$

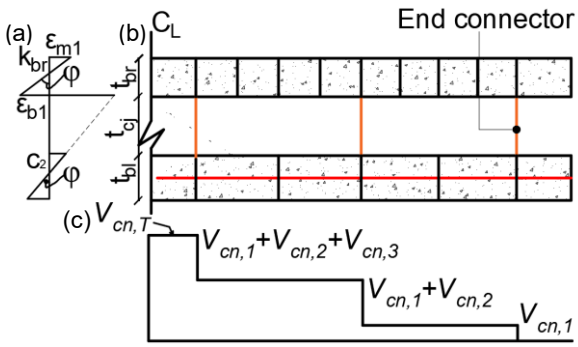

Figure 6.11: (a) wall strain profile (b) wall showing end-connector (c) accumulated shear contribution.

The load-deflection response is therefore obtained using the following steps (Fig. 6.12).

As discussed in Section 5.7 of this thesis, the wall failure mode is either from connector or wythe material failure, and the process to determine the failure mode is also described in Section 5.7. In addition, for double wythe cavity masonry walls, the connector capacity (and failure) is also limited by the axial capacity of the connectors as described in Section 6.5.3.

1.Apply out of plane load (OP), w (kN/m^2), to the wall and determine the moment, M (kNm/m), at connector locations along the wall. Similar procedure can be done for 3 and 4 point bending.

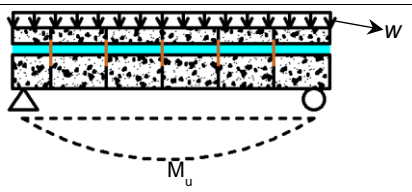

2.Assume a linear slip profile with end connector having the largest slip ($\delta_{sc,1}$) and zero slip at the middle of the wall.

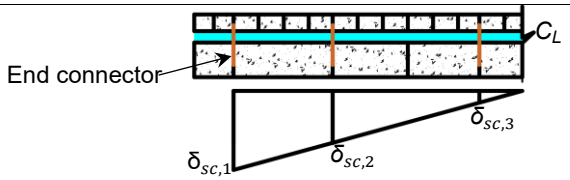

3.Find V_{cn} at each connector location by correlating assumed slip with shear connector load-slip relationship. Sum V_{cn} towards the middle of wall.

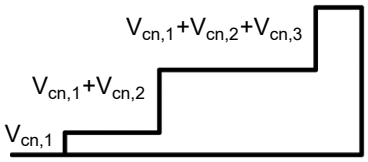

4.Use V_{cn} at each connector location to get strain discontinuity (ε_{sc}).

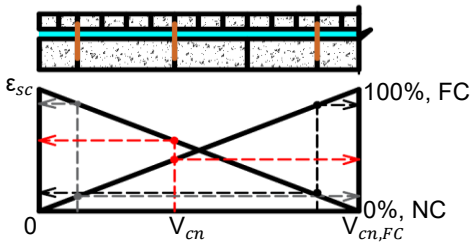

5.Integrate strain discontinuity at connector locations to get a new slip profile. Repeat step 2 to 5 till new slip profile equals that in step 2.

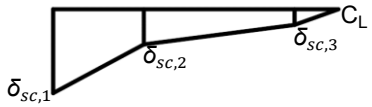

6.Interpolate moment at connector location (M_i) to get curvature (φ_i) corresponding to the degree of composite action.

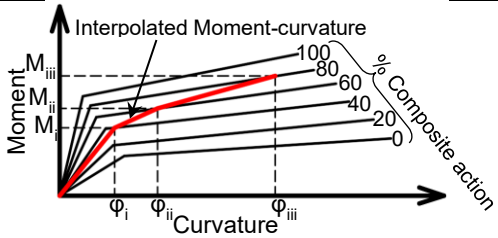

7.Integrate curvature to obtain primary deflection (Δ_0) for OP, using the moment-area approach.

8.Use EI_{eff} to iterate and get secondary deflection (Δ_1) and secondary moment ($P(\Delta_0 + \Delta_1)$). At mid wall height using the *P*-Δ method, $\Delta_1 = \frac{5P_{sw}(\Delta_0+\Delta_1)h_w^2}{48EI_{eff}}$ (P_{sw} is the self-weight of the wall). Self-weight reduces from the bottom to the top of wall. EI_{eff} along the wall can be obtained by correlating the degree of composite action at connector locations to the end of the wall. Add secondary deflection (Δ_1) to primary deflection (Δ_0) to obtain total deflection and secondary moment. With secondary moment, repeat step 1 to 5 to find additional connector slip due to second-order effects.

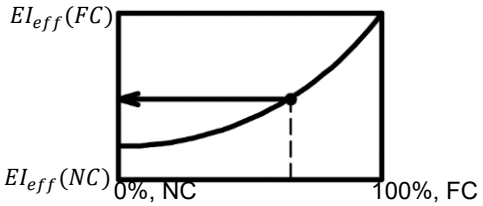

9.Increase OP load, and Step 2 to 8 is executed to obtain a new point for the OP load-deflection response for the partial composite double -wythe cavity masonry wall.

Figure 6.12: Generation of load-deflection response for partial composite double-wythe cavity masonry wall

6.11 VERIFICATION OF MODEL WITH EXPERIMENTAL DATA

Verification of the model was done by comparing the load-deflection response to results for full-scale walls from literature in which properties for wall components such as connectors, CMU, and brick are given or could be traced to a previous publication. Unlike insulated concrete walls, not many experimental tests have been conducted for double wythe masonry walls under flexural loading. The test used for verification was Goyal et al. (1994) and the properties of wall components are shown in Table 6.4. The bar yield strength was taken as 300 MPa as it represents a lower bound value used in other tests by some of the authors (Wang et al. 1996), while the properties for similar connectors were obtained from (Zmavc 1991). These complimentary sources from which wall properties were taken (Wang et al. 1996, Zmavc 1991) were selected as they were conducted by similar research groups. The tensile strength of CMU, brick, and grout was taken from Table 5 of CSA S304-14 (2019) as 0.4, 0.65, and 0.65 MPa, respectively. The compressive strength of the brick was taken as 16 MPa as it represents the typical strength of a Canadian brick (where the study was conducted).

The load-deflection response from analytical modelling is compared to experimental data and service response comparison was done at a load value corresponding to deflection of span/360 (mm). The deflection criteria for service load was selected as it is usually critical for architectural walls (Table 6.5, Fig. 6.13). As mentioned in Section 5.8 of this thesis, comparison of the model and test results was expressed in terms of the mean and coefficient of variation (COV). This is because the COV (a unitless parameter) evaluates the relative closeness of the predictions to the test values, which is of interest in any developed model. From the test results, there were no outliers and the COV was suitable in statistical evaluation of model predictions.

From Table 6.5 the average test to predicted strength ratio was 0.72 with a coefficient of variation (COV) of 29.4%. The overprediction can be attributed to the assumed wall properties, especially the connector properties (compressive strength) which may be lesser in the test than that from the complimentary source. Considering construction imperfections which can create an

out-of-straightness effect on the connectors, as well as possible effects of combined axial/shear forces on the connectors, the capacity of the connectors would be reduced under loading. Future investigations should evaluate this combined axial/shear effect. In addition, the predicted initial stiffness was stiffer than the test values. A reason for this is that the CMUs were produced with sawdust replacing 50% of the lightweight aggregates which reduced the compressive strength by up to 30% and is likely to have a similar effect on the tensile strength. Also, provisions such as Eq. 6.4 (CSA S304-14 2019) overestimates the modulus of elasticity, which was also reported by Gayed and Korany (2012). The tensile strength for masonry in Table 5 of CSA S304-14 (2019) was developed for masonry without partial replacement of aggregates with materials like sawdust, and it appears to overestimate the tensile strength for masonry with partial replacement of aggregates with sawdust, thereby leading to stiffer wall responses. In Batool et al. (2021) and Olaiya et al. (2023), an adverse reduction in tensile strength was reported for concrete with sawdust content larger than 15-20%. Therefore, test standards should be developed and material property expressions developed for masonry where aggregates are partially replaced with alternative materials which would follow similar processes used in reinforced concrete design. The failure mode of most walls was due to connector buckling which occurred when the compression capacity of the end-connector was reached.

Table 6.4: Matrix of experimental test

Study		Wall height, mm	Cavity width, mm	Brick size, mm	CMU, mm	Rebar area, mm2	Rebar spacing, mm	Yield strength of rebar, MPa	f'_m, MPa (CMU)	f'_m, MPa (brick)	f'_m, MPa (Grout)
Goyal et al. (1994)	S1D	3000	100	100	150	200	600	300[a]	10[b]	16[c]	20
	S2C	4200									
	S2D	5400									
	S3B	3000			200						
	S3C	4200									
	S3D	5400									
	S4A	3000			100						
	S4C	2400									

[a] Obtained from Wang et al. 1996
[b] Average of test range values of 9 and 11 MPa
[c] Obtained from Table 4 of CSA S304-14 (2019)

Table 6.5: Result for model prediction

Study		Peak Load, kPa		D_u	Service Load at deflection (L/360), kPa		D_s	Failure mode	
		Test	Model		Test	Model		Test	Model
Goyal et al. (1994)	S1D	3.35	6.33	0.53	2.33	3.88	1.67	CB	CB
	S2C	3.25	4.52	0.72	1.49	3.08	2.07	CB	CB
	S2D	1.67	2.98	0.56	0.88	1.44	1.64	CB	CB
	S3B	5.31	6.33	0.84	*	*		CB	CB
	S3C	4.51	4.52	1.00	2.57	4.21	1.64	CB	CB
	S3D	3.58	3.52	1.02	1.53	2.77	1.81	CB	CB
	S4A	3.34	6.33	0.53	1.83	2.50	1.37	CB	CB
	S4C	4.28	7.92	0.54	1.56	2.32	1.49	CB	CB
Mean D (Test/Predicted)				0.72			0.61		
COV (%)				29.4			13.1		

*Wall failed in service
CB – Connector buckling
CR– Masonry crushing

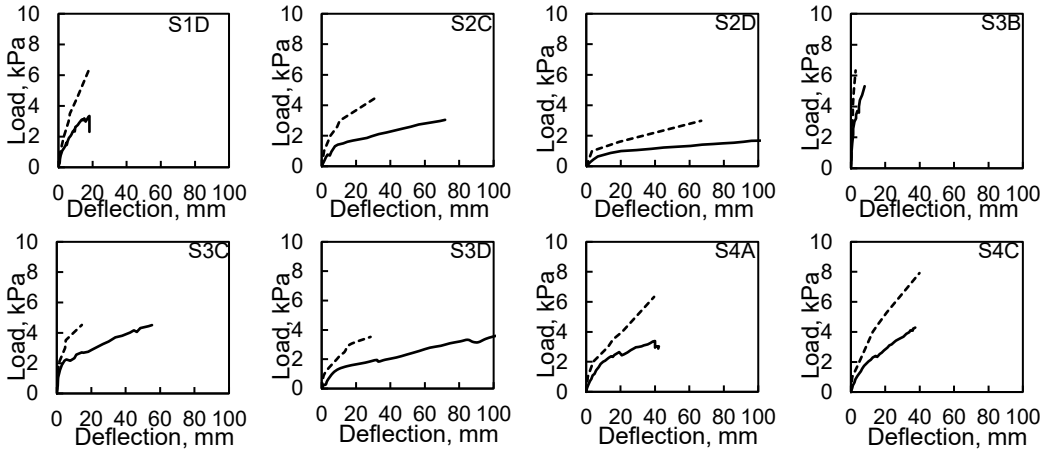

Figure 6.13: Comparison of test and model load-deflection response for Goyal et al. (1994) (Dashed lines are model predictions and solid lines are test results)

6.12 PARAMETRIC ANALYSIS

In this section, the effect of several parameters on the load deflection of double-wythe masonry walls response is examined. These include reinforcement ratio, cavity width, wall length, connector spacing, strength, and stiffness. The chosen parameters are shown in Table 6.6 and are evaluated using a 190 and 90 mm thick CMU and brick, respectively. The rebar was spaced at 600 mm intervals with a yield strength of 400 MPa, as shown in Fig. 6.14. As most walls are slender, they are usually partially grouted to reduce self-weight. However, the same procedure can be applied to fully grouted walls.

The CMU is assumed to have a specified compressive strength of 20 MPa which is common in literature, while that of the brick is taken as 16 MPa which represents the minimum strength for

Canadian manufactured brick (Dryscale and Hamid 2005). This specified compressive strength is interpreted from Table 4 of CSA S304-14 (2019) to get design values of 16, 13, and 10 MPa for the brick, CMU, and grout, respectively. Similarly, the design tensile strength of all masonry components is taken from Table 5 of CSA S304-14 (2019), to get design values of 0.65, 0.4, and 0.65 MPa for the brick, CMU, and grout, respectively.

A base cavity width of 100 mm (75 mm insulation and a 25 mm air gap) was selected to represent existing cavity widths used in Canada for walls above ground level. A maximum cavity width of 175 mm was selected to reflect increasing insulation thickness currently prescribed by designers to meet stricter energy requirements set by the National Energy Code of Canada for Buildings (NECB 2017) and comparable codes around the world. A minimum wall length of 3000 mm was selected to represent a typical storey height. Other wall lengths of 6000 and 8500 mm were chosen to reflect taller storey heights found in commercial and institutional structures. The minimum longitudinal spacing for the novel connector (NP) was selected as 400 mm to allow for proper construction considering it is 350 mm high while the minimum spacing for the existing connectors (HP, VP) was selected as 200 mm. For both connector types, the maximum spacing was 600 mm, to represent the maximum longitudinal spacing prescribed for connectors in CSA A370:14 (2018). The horizontal spacing is limited to the spacing of the grouted cells (600 mm).

Three rebar sizes, 10M, 15M, and 20M, placed in the centre of the CMU cell, were selected to reflect a range of rebar sizes seen in literature and to study the effect of reinforcement ratio on wall strength. In addition, the effect of the parameters mentioned above on the degree of composite action by strength (K_u) as well as service stiffness (K_s) were examined using Eq. 6.15 and 6.16. This is vital as walls with larger strength (peak load) do not translate to a wall with equivalent composite action by stiffness, as seen in insulated concrete walls (Huang et al. 2018, Tomlinson and Fam 2015) and shown in the following sections.

$$K_u = \frac{P_m - P_{NC}}{P_{FC} - P_{NC}} \tag{6.15}$$

$$K_s = \frac{P_{m,s} - P_{NC,s}}{P_{FC,s} - P_{NC,s}} \tag{6.16}$$

P_m, P_{NC}, and P_{FC} are the strength of the partial composite, non-composite, and full-composite walls, respectively while $P_{m,s}$, $P_{NC,s}$, and $P_{FC,s}$ are strength values at span/360 (mm). The factor of 360 was selected instead of 180 as a masonry veneer is attached and the air gap provides a drainage path for moisture ingress (CSA S304-14 2019).

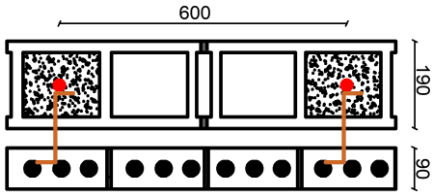

Figure 6.14: Double-wythe masonry cross-section for parametric analysis

Table 6.6: Numerical values for examined parameters.

Parameters	Values
Wall length (mm)	3000, 6000, 8500
Cavity width (mm)	100, 150, 175
CMU thickness (mm)	190
Bar sizes	10M, 15M, 20M
Connector longitudinal spacing (mm)	200, 400, 500, 600
Rebar and connector horizontal spacing	600
Connector material	Steel
Tensile strength of Rebar (MPa)	400
Tensile strength of connector plate (MPa)	234
Modulus of Elasticity for rebar (MPa)	200000
Modulus of Elasticity for connector (MPa)	194000
f'_m (brick, MPa)	16
f'_m (CMU, MPa)	13
f'_m (grout, MPa)	10
f_t (brick, MPa)	0.65
f_t (CMU, MPa)	0.4
f_t (grout, MPa)	0.65
Shelf angle (Steel)*	L102 × 102 × 13

*The horizontal leg of the shelf angle was selected to be larger than the thickness of a typical brick (90 mm) and the design procedure was adopted from (Hagel et al. 2019)

6.13 RESULTS FROM PARAMETRIC ANALYSIS

6.13.1 Effect of connector type

Generally, for walls with similar connector reinforcement ratio and cavity width, the novel connector (NP) exhibited larger strength, K_u, and K_s than those made with the VP and HP connectors (Fig. 6.15,6.16,6.17). On average, the K_u of the wall with the NP connector was 1.6

and 3.4 times that of a wall with VP and HP connectors, respectively while that for K_s was 1.2 and 2.6, respectively (Table 6.7). This is because the novel connector transmits load through truss action which enables better material utilization.

6.13.2 Effect of rebar size

As the wall rebar size increased from 10M to 20M rebar, for a wall with similar connector spacing and cavity width, the strength and service load at $L/360$ increased (Fig. 6.15). Although there was an increase in strength with larger rebar sizes, the larger moment resistance of the wall puts more demand on the connector, which causes a reduction in the connector's contribution to composite action (K_u, K_s, Fig. 6.16). This is similar to trends seen for the effect of larger reinforcement ratios in insulated concrete walls (Trasborg 2014, Teixeira 2015).

Table 6.7: Results from parametric analysis

ID	Pressure				Suction			
	Load, kN/m2		K_u,%	K_s, %	Load, kN/m2		K_u	K_s
	Peak load	L/360			Peak load	L/360		
HP-100-600	12.4	6.87	6.72	4.23	9.82	6.43	*	12.5
HP-150-600	12.2	6.67	4.64	2.85	9.82	6.15	*	9.23
HP-175-600	12.1	6.29	3.96	1.57	9.82	5.95	*	3.22
HP-175-200	12.4	6.36	4.82	1.77	9.82	6.51	*	13.3
HP-175-400	12.2	6.31	4.21	1.60	9.82	5.98	*	3.67
VP-100-600	14.2	7.80	14.3	7.69	9.13	6.93	*	21.4
VP-150-600	14.2	7.39	11.3	5.07	9.13	6.81	*	18.8
VP-175-600	14.0	7.05	9.80	3.71	9.13	6.54	*	14.4
VP-175-200	16.5	8.31	17.6	7.22	9.13	7.02	*	22.1
VP-175-400	14.2	7.18	10.4	4.04	9.13	6.76	*	15.3
VP-175-400-1.25	15.8	7.77	15.4	5.69	9.13	6.71	*	16.8
VP-175-400-1.5	15.8	8.18	15.4	6.84	9.13	6.98	*	21.4
VP-175-400-1.75	17.2	8.32	19.7	7.26	9.13	7.17	*	24.7
VP-175-400-2.0	17.6	8.62	20.9	8.07	9.13	7.17	*	24.7
NP-100-600	15.1	8.07	18.4	8.67	11.0	7.03	17.4	23.3
NP-150-600	15.0	7.80	14.3	6.31	11.0	7.01	10.1	22.2
NP-175-600	14.0	7.34	9.80	4.52	10.9	6.58	1.89	14.6
NP-175-400	15.6	8.08	14.8	6.44	10.9	6.86	3.29	20.1
NP-175-500	15.3	7.62	13.1	5.38	10.9	6.81	1.89	19.4
NP-175-400A	4.07	1.72	14.9	6.78	2.89	1.58	12.6	21.6
NP-175-400B	2.08	0.77	15.9	7.64	1.52	0.65	22.1	22.7
NP-175-600C	8.40	5.95	9.80	4.76	6.20	5.61	5.37	58.9
NP-175-600D	19.3	9.53	9.45	4.56	13.3	8.24	*	12.7

* The tensile strength of the connector governed and wall strength was lesser than the NC value
A,B represent walls with 6000 and 8500 mm high walls, respectively. Other walls are 3000 mm high.
C,D represent walls with 10M and 20M rebar sizes, respectively. Other walls have 15M rebars.

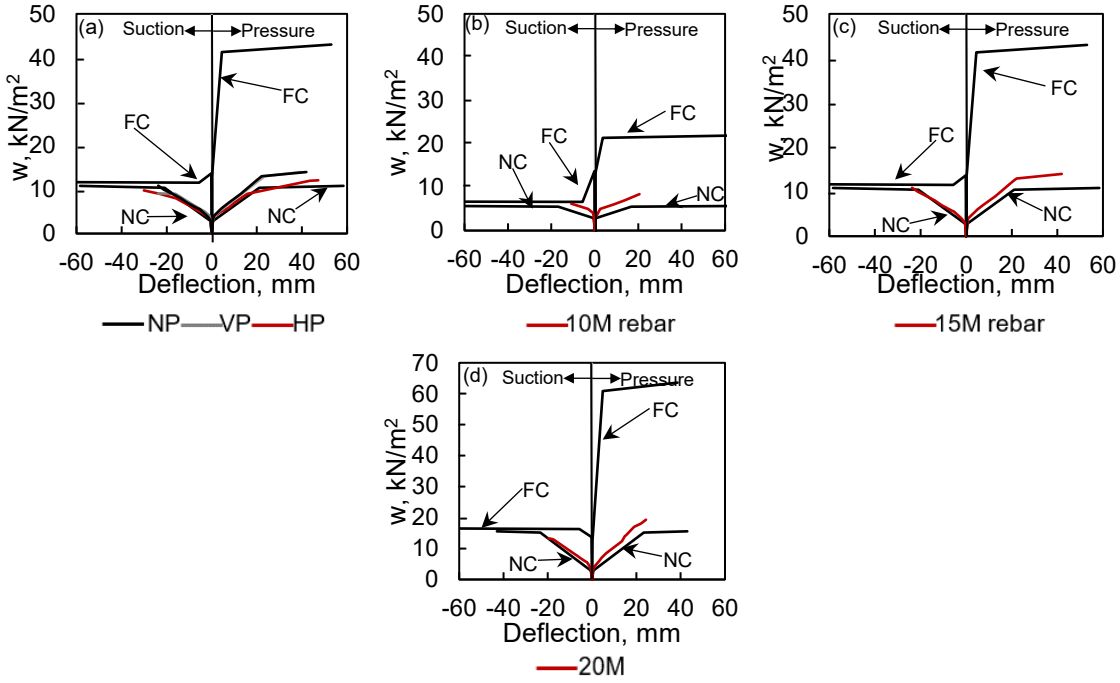

Figure 6.15: (a) Effect of connector type (175 mm cavity). Effect of rebar size (175 mm cavity) (b) 10M (c) 15M (d) 20M. (All walls with 3000 mm wall length and 600 mm connector spacing)

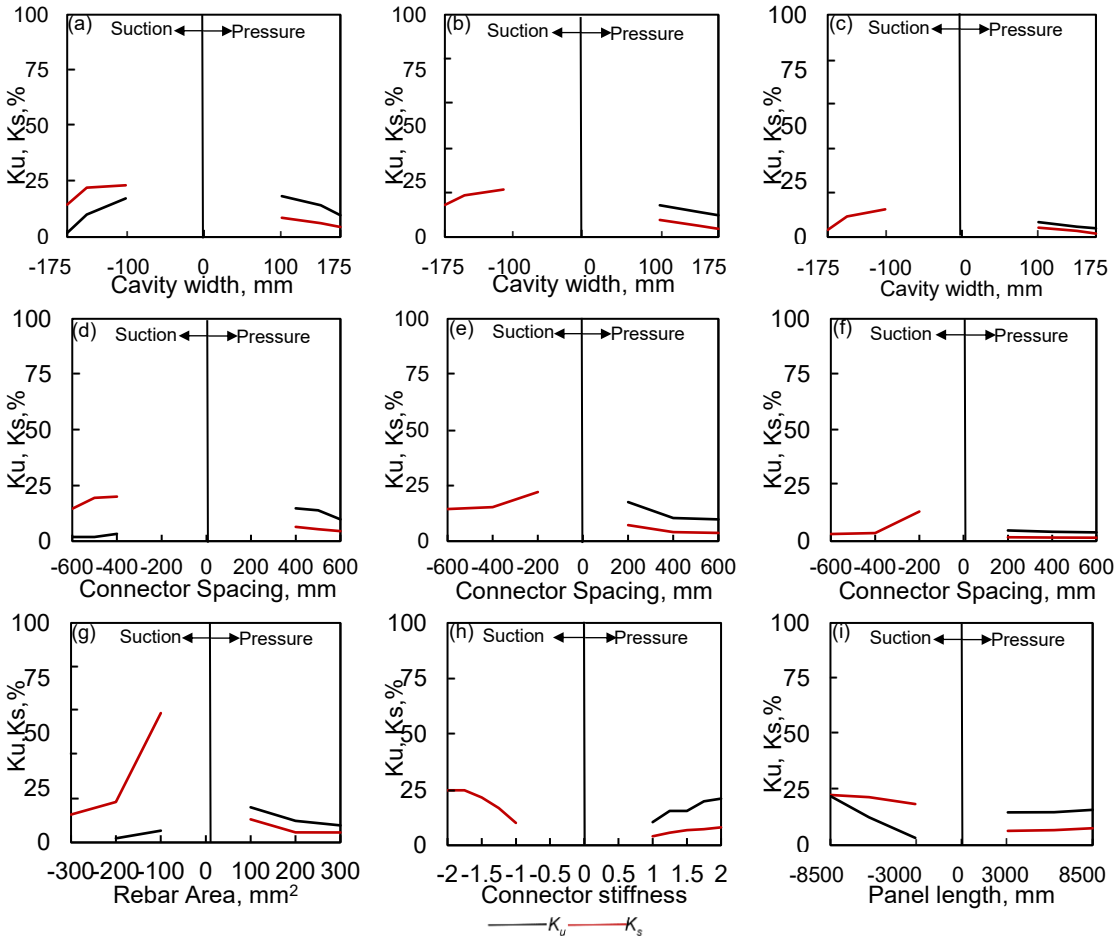

Figure 6.16: Effect of parameters on K_u and K_s. Cavity width (a) NP (b) VP (c) HP. Connector spacing (d) NP I VP (f) HP (g) Rebar size (h) Connector stiffness (i) Wall length

6.13.3 Effect of cavity width

The strength, K_u, and K_s of walls decreased with an increase in cavity width (Fig. 6.16,6.17a,b,c) due to loss of connector strength and stiffness. Similarly, the increased moment demand owing to larger section size is not resisted by connectors in the form of shear flow, thereby reducing the degree of composite action of the wall. An increase in insulation thickness by designers (currently up to 150 mm plus an air gap) which affects the cavity width, necessitated the development of the novel connector and this novel connector resulted in larger strength per unit area of connector.

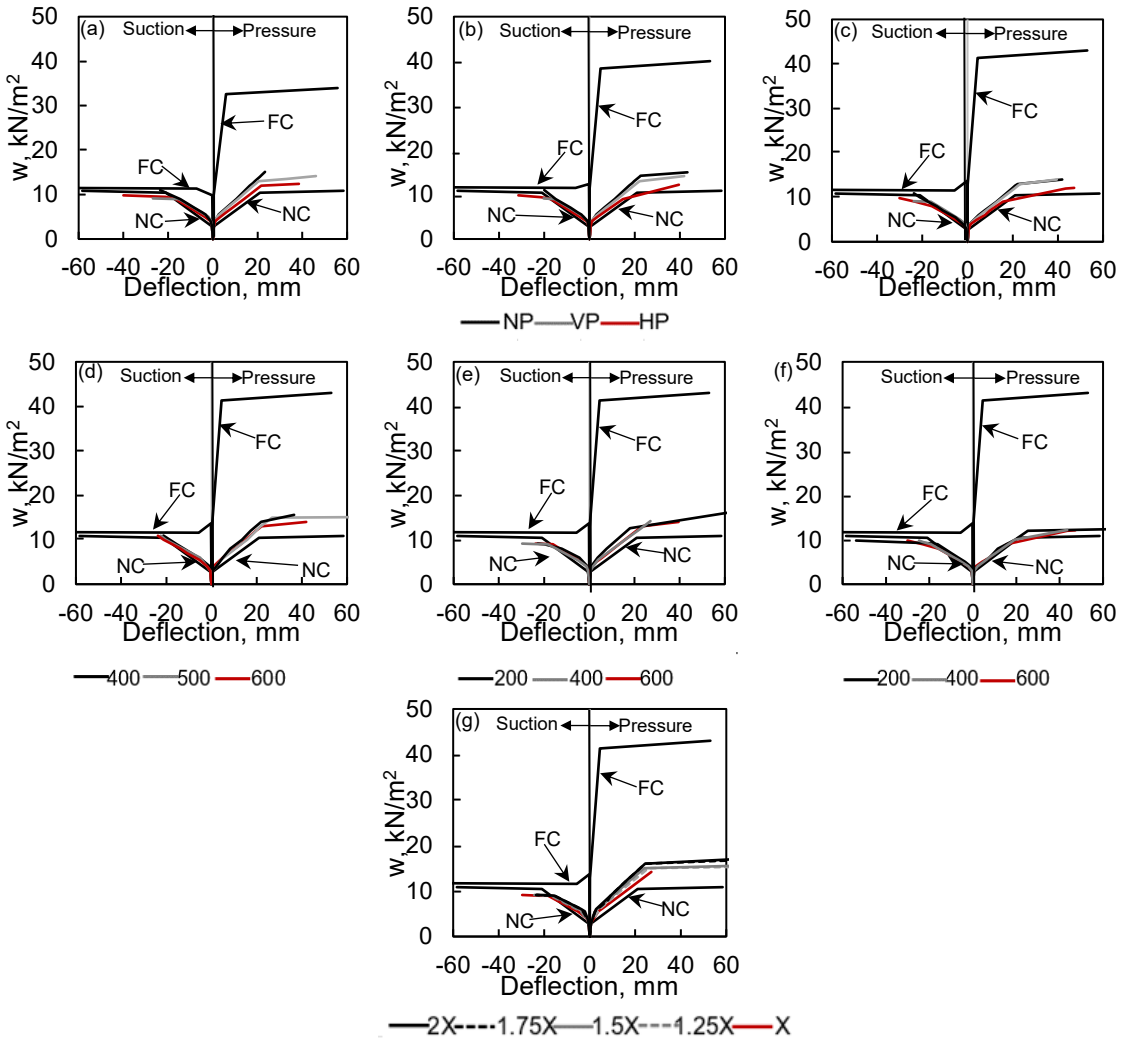

Figure 6.17: Effect of cavity width (a) 100 mm (b) 150 mm (c) 175 mm. Effect of connector spacing (3000 mm wall length and 175 mm cavity width) (d) NP I VP (f) HP (g) Effect of connector stiffness (X is a wall with VP connector with 400 and 175 mm connector spacing and cavity width, respectively. Digits before X represent walls with connectors at various multiples of stiffness.

6.13.4 Effect of loading direction

Unlike most reinforced concrete walls which have similar reinforcement placed at identical positions in respective wythes, double wythe cavity masonry walls only have the inner wythe reinforced which leads to an unsymmetrical response under pressure and suction, respectively. As anticipated, due to the larger moment arm of the rebar, the moment resistance and consequently the wall strength as well as service load at L/360 was larger for pressure (Fig. 6.15,6.16,6.17,6.18). On average, the K_u and K_s was larger for suction as the strength and stiffness values were closer to their respective NC and FC section values (similar rebar moment arm for NC and FC). This aligns with Sakr and Neis (2001) where it is noted that a partially composite wall under suction is expected to behave more like a non-composite wall i.e. a single CMU wythe. Considering the disadvantage, the strength of walls under suction can be improved by placing two rebars per cell preferably on opposite faces of the face shell within the CMU, which will also improve the strength under pressure.

6.13.5 Effect of connector spacing

As connector spacing reduced the strength, K_u, and K_s increased for all connector types, more evident in that for NP and VP connectors (Fig. 6.16,6.17). This is because the additional shear flow is accumulated towards the middle of the wall.

Although CSA A370:14 (2018) specifies the maximum horizontal connector spacing to be 800 mm, this would be impractical for connectors screwed to the CMU used in partially grouted walls with rebar spacing greater than 800 mm. This is because the screws in such connectors require adequate bonding with grout in the CMU cell to function adequately under loading. This limitation differentiates partially grouted walls from fully grouted walls, and likewise insulated concrete walls. To optimize connector spacing in partially grouted walls, the connectors can be developed without relying on the screws for fixity, such that they can be placed on the head joints of the CMUs.

6.13.6 Effect of wall length

As wall length increased, the strength and stiffness of the partially composite wall reduced. However, the K_u and K_s increased as wall length increased (Fig. 6.16,6.18) most especially for the 8500 mm wall. This is because as wall length increases, more longitudinal shear (V_{cn}) transfers between wythes towards the middle of the wall making the resistance closer to that of the sectional FC load capacity. In addition, the deflection increased with wall length (6000 and 8500 mm used in this study) and the service load calculated at L/360 shows the maximum service load reduces with an increase in wall length.

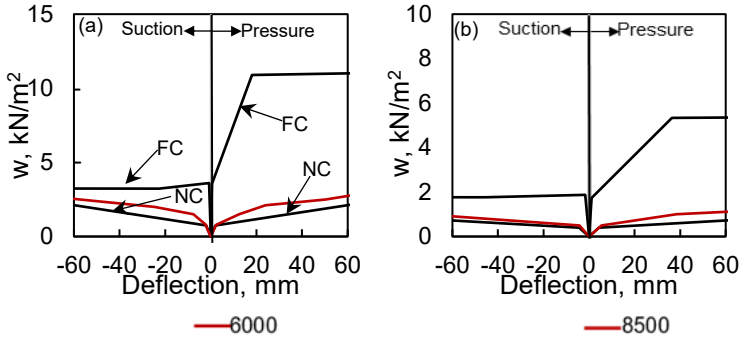

Figure 6.18: Effect of wall length (a) 6000 m (b) 8500 mm

6.13.7 Effect of connector strength, stiffness, and shelf angle

Although not proportionally, an increase in connector strength and stiffness resulted in a corresponding increase in wall strength, stiffness, K_u, and K_s (Fig. 6.16,6.17). This is because the connectors with larger strength were able to offer more shear flow in response to moment demand on the wall. Additionally, an increase in connector stiffness resulted in a corresponding increase in service load calculated at L/360 (Table 6.7).

Similarly, when the shelf angle was included in the analysis, the strength, stiffness, and degree of composite action of the wall increased to a larger extent than that resulting from the connectors thereby creating an upper bound for wall behaviour (Fig. 6.19,6.20). This is because the shear strength and stiffness of the shelf angle are far larger than that of the connectors examined (as well as conventional connectors), and the shelf angle attracts more of the load. As most double-wythe cavity walls are built with shelf angles, it could be interpreted that many walls are more composite

by strength and stiffness than may be believed. However, this may not be the case in walls with horizontal expansion joints that accommodate the slip in the brick wythe without having the shelf angle necessarily contributing to composite action. In addition, the shelf angle is usually anchored to a concrete pedestal under the CMU and not directly to the CMU to allow for continuous insulation between above-grade and below-grade walls (Hagel et al. 2019). This means the shelf angle only transfers the weight of the brick to the foundation without necessarily contributing to composite action.

When shelf angles are thought to contribute towards composite action, it is important to consider the effect on thermal bowing. Also, additional investigation on full wall performance is needed to develop comprehensive design expressions relating to the thermal and structural effects of the shelf angle.

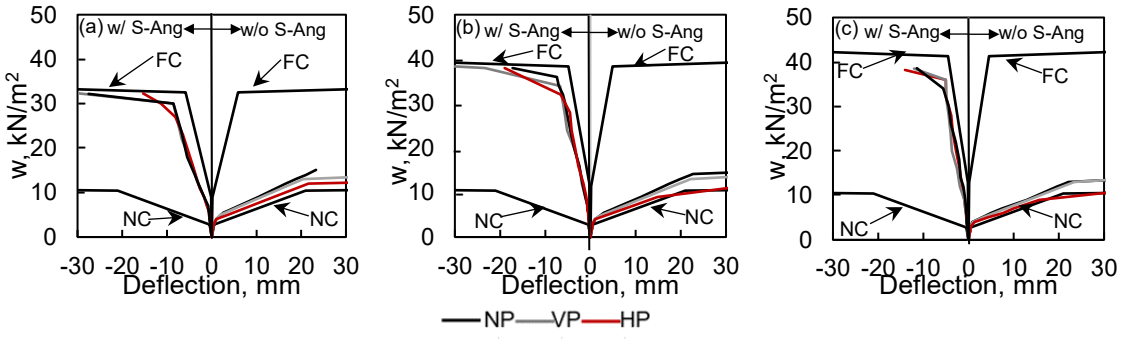

Figure 6.19: Effect of shelf angle (S-Ang) on wall strength. Cavity width (a) 100 m (b) 150 (c) 175 mm

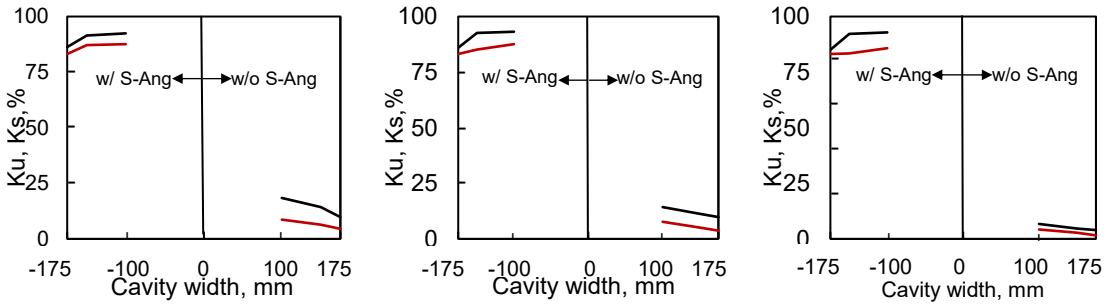

Figure 6.20: Effect of shelf angle (S-Ang) on K_u and K_s. Cavity width (a) IP (b) VP (c) HP

6.14 CHAPTER SUMMARY AND CONCLUSIONS

This study aimed to develop an easy-to-use analytical model to predict the load-deflection response of double-wythe cavity masonry walls and also examine the performance of a novel connector over traditional connectors in full-scale double wythe cavity masonry walls. The model

was validated using experimental tests in literature where the wall components where published or could be traced to a previous publication. A parametric analysis was performed on the effect of connector spacing and stiffness, cavity width, wall length, and flexural reinforcement ratio, on the strength and degree of composite action.

The following were concluded from this study:

1. The proposed model reduces the computational difficulty compared to other models and can be done using a simple spreadsheet.
2. The novel connector gave larger strength and degree of composite action per unit connector cross-sectional area than the existing connectors.
3. While increasing the flexural reinforcement ratio generally increases the wall strength, the degree of composite action is reduced due to additional shear flow demand on the connectors, which the connectors are not able to offer through resistance.
4. To improve composite action in walls, designers have a choice of using stiffer or more closely spaced connectors, of which smaller connector spacing influenced the wall strength and degree of composite action to a larger extent.
5. Proper characterization of wall properties (CMU, bricks, and connectors) that will aid in the assessment of wall behaviour. Also, other methods should be developed to determine the axial forces developed in connectors, especially the end-connectors, whose axial strength (tension and compression) could control the strength of walls. In addition, micro finite element models should be developed to better capture the interaction between connector elements and surrounding mortar.
6. From research (Liu and Dawe 2003, Liu and Hu 2007), the effective flexural stiffness formulation by CSA S304-14 (2019) is conservative. Further analysis should be carried out using other provisions for effective flexural wall stiffness.

7. CONCLUSION

7.1 RESEARCH SUMMARY

Insulated concrete and double wythe cavity masonry walls are common wall types in residential and commercial buildings. The major focus of this thesis was on developing methods to better assess the amount of composite action in insulated concrete and double wythe cavity masonry walls. The contributions from the preceding Chapters are highlighted below.

In Chapter 2, a critical review of literature identified major contributors to composite action for both wall types to be from the shear connection system. To this end, distinct methods were developed to improve the shear transfer mechanism. Chapter 3 was on the experimental push-through test on 18 notched and 6 unnotched insulated concrete walls. Some parameters examined were the insulation type, size of connectors, and type of notch. Chapter 4 examined a novel shear connector-tie system for double wythe cavity masonry walls under push-through tests and compared the results to that of traditional masonry connectors. In total, 38 small-scale specimens were examined and the parameters examined included the embedment length of the tie and type of brick.

Chapter 5 presented a unified analytical model to predict the load-deflection response of insulated concrete walls under flexural loading, and the model was verified using 32 experimental tests from literature. A parametric study was conducted to examine the effect of several parameters on composite action. These included longitudinal reinforcement ratio, connector material, wall length, connector spacing, size, and inclination. In Chapter 6, the analytical model developed in Chapter 5 was extended to predict the load-deflection response of non-load-bearing double wythe cavity masonry walls. The effect of connector type (novel and traditional connector tested in Chapter 4) cavity width, connector spacing, and wall length, on composite action were examined through a parametric analysis.

7.2 RESEARCH CONCLUSIONS

The following conclusions can be made for insulated concrete and double wythe cavity masonry walls, respectively.

7.2.1 Insulated concrete and double wythe cavity masonry walls

1. The novel shear connection system developed for insulated concrete and double wythe cavity masonry walls was effective in improving composite action. From Chapter 3 (Task 2), notches increased the strength and stiffness of shear connections of insulated concrete walls, especially those with XPS insulation due to their larger tensile strength and stiffness, in comparison to PIR and EPS. Rectangular notches aided the proper locking mechanism with the insulation, and resulted in larger strength than trapezoidal notches, while trapezoidal notches gave more warning before failure. From Chapter 4 (Task 3) the novel inclined masonry connector resulted in larger shear connection strength per unit area than traditional connectors, due to better utilization of material.
2. From Chapter 4 (Task 3), the influence of embedment ties appears to be insignificant when only examining the longitudinal shear behaviour of connectors. However, embedment ties will play a significant role when loaded under pure tension and compression.
3. The novel inclined connector produced larger wall flexural load and composite action per connector cross-sectional area than traditional connectors, as shown in Chapter 6 (Task 5). For insulated concrete walls, using larger-sized connectors was only significant for widely spaced connector arrangements (Chapter 5, Task 4).
4. For insulated concrete and double wythe cavity masonry walls, the connector spacing and inclination affected the strength of walls to a larger extent than other parameters examined, as shown in Chapters 5 and 6 (Tasks 4 and 5).
5. In Chapter 6 (Task 5), a large variation in the predicted strength and stiffness was observed for the double wythe cavity masonry walls used for model validation. This is because the model uses formulations for normal masonry such as the elastic modulus, which over-

estimates the modulus for the test specimens that were made of blocks with partial replacement of aggregates with sawdust. Also, the method used to apportion axial forces to the connectors may be unconservative, especially for the end-connectors whose failure could determine the strength of the walls. In addition, adequate wall properties were not given in the publication, which had to be obtained from tests by other researchers in the same research group.

Overall, this thesis developed methods to better assess composite action in insulated concrete and double wythe cavity masonry walls. This was achieved by experimentally conducting push-through tests on innovative inclined shear connection systems. In addition, a simplified analytical model was developed to assess the amount of composite action generated by various shear connection systems. The results indicate that for insulated concrete and double wythe cavity masonry walls, inclined connectors can reach larger shear connection strength than dowel connectors. In some instances, the inclined connector reached strength values that were 7.3 times that of a dowel connector. Using the simplified analytical model, the slip profile for connectors was non-linear even at wall cracking load. While it may be reasonable to assume a linear slip profile at cracking load, further evaluation is needed to test the adequacy of a linear slip profile assumption at yielding of wall longitudinal reinforcement and at ultimate load.

While the innovative shear connection schemes resulted in larger connection strengths which would lead to thinner and less-expensive wall sections, consideration should also be given to their effect on thermal bowing. This is because shear connectors with larger stiffness would lead to increased thermal bowing, and connectors with lesser stiffness resulting in reduced thermal bowing.

7.3 FUTURE RECOMMENDATIONS

As stated in the opening chapter of the thesis, there is a dire need to improve energy efficiency in walls such as insulated concrete and double wythe cavity masonry walls, and this is commonly achieved through larger insulation thickness. Larger insulation thickness reduces the composite

action in both walls, due to a reduction in stiffness of the connectors. This creates a coupled thermal and structural problem. However, only the structural effect was examined in this thesis, and further research in the following areas would enhance understanding of the behaviour of both wall types. Recommendations for each wall type are provided in the following sections.

7.3.1 Specific recommendations for insulated concrete walls

1. As with many infrastructure, freeze-thaw cycles occur due to repeated cycles of freezing and melting of water which initially penetrated the voids of wythes, consequently causing damage to the material. Damage to the material include degradation of the modulus of elasticity and tensile strength (Shiping et al. 2022). For insulated concrete walls without notches, the expansion and contraction from freeze-thaw cycles may also degrade the interaction (if any) between concrete and insulation, as well as for walls with notches that depend on the concrete-insulation bond for structural contribution.
2. Similar to the effect of freeze-thaw cycles, additional tests should be carried out on unnotched and notched walls to re-evaluate the effect of notches under sustained load (creep), as well as to determine the most suitable connector type under sustained load.
3. Carry out experimental tests on full-scale walls with notched insulation while also considering different notch sizes and connector types such as grids and pins (steel or FRP).

7.3.2 Specific recommendations for double wythe cavity masonry walls

1. Considerations for newer masonry shear connections should ensure that it can be anchored in the head joints of the CMU wythes, instead of relying on screws which can only be affixed to grouted cells.
2. While the similarly simplified analytical model predicts flexural (reinforcement yielding and rupture, and masonry crushing) and connector failure, it should be modified to predict other failure modes such as out-of-plane shear failure.
3. The combined axial/shear interaction of the connection system should be further assessed, to aid in better prediction of wall strength. In addition, other methods should be developed

to determine the axial forces developed in connectors, especially for the end-connectors, whose axial strength (tension and compression) could also control the strength of walls.

7.3.3 Recommendations that apply to both insulated concrete and double wythe cavity masonry walls

1. Examination of the integrity/residual strength of shear connection systems after exposure to elevated temperatures/fire. In addition, the contribution of the stiff connectors developed in this thesis towards thermal bowing should be evaluated to create walls with balanced thermal and structural performance.
2. Carry out longitudinal shear tests and full-scale tests on connection systems with thicker insulation (100-200 mm) as building energy codes continue to evolve to meet climate targets.
3. A parametric analysis considering more wythe thicknesses, reinforcement ratios, and connector spacing is needed as it would serve as standardized design curves for non-load bearing partially composite double wythe cavity masonry and insulated concrete walls.
4. The simplified model should be adjusted to account for superimposed concentric and eccentric axial loads, which could lead to instability failure.
5. The analytical model developed in this study is able to predict the global failure mode such as connector and wythe material failure. However, it is not able to capture the interaction between connectors and host element such as concrete and mortar which is better characterized using micro finite element modelling. The developed model is only applicable to walls under one-way bending, and further work through finite element modelling, is needed to analyse two-way response of walls while accounting for openings like doors and windows.

REFERENCES

AC422. (2010). Acceptance criteria for semicontinuous fiber-reinforced grid connectors used in combination with rigid insulation in concrete sandwich panel construction." AC422. Los Angeles, CA.

ACI 318. (2019). 318M–19: Building Code Requirements for Reinforced Concrete and Commentary, 473.

ACI PRC 440.2-23. (2023). Guide for the Design and Construction of Externally Bonded FRP Systems for Strengthening Concrete Structures. American Concrete Institute.

Al-Rubaye, S. A. (2017). Experimental and simplified analytical investigation of full scale sandwich panel walls. MSc.Thesis, Department of Civil and Environmental Engineering,Utah State University,Logan, Utah.

Al-Rubaye, S., Sorensen, T., Thomas, R. J., and Maguire, M. (2019). Generalized beam–spring model for predicting elastic behavior of partially composite concrete sandwich wall panels. Engineering Structures, 198(September 2018), 109533. https://doi.org/10.1016/j.engstruct.2019.109533

Al-Rubaye, Salam, Sorensen, T., and Maguire, M. (2021). Iterative and Simplified Sandwich Beam Theory for Partially Composite Concrete Sandwich Wall Panels. Journal of Structural Engineering, 147(10), 04021143.

Allen, E., and Iano, J. (2009). Fundamentals of Building Construction – Materials and Methods (Fifth Edit, Vol. 148). Hoboken, New Jersey: John Wiley and Sons, Inc.

Allen, H. G. (1969). Analysis and design of structural sandwich panels. (P. P. Oxford, Ed.).

Alnahhal, W. . I., Chiewanichakorn, M., Aref, A. J., and Alampalli, S. (2006). Temporal Thermal Behavior and Damage Simulations of FRP Deck. Journal of Bridge Engineering (ASCE), 11(4), 452–44. https://doi.org/10.1061/(ASCE)1084-0702(2006)11:4(452)

Arevalo, S. (2019). Experimental Investigation of Thermal Bowing for Concrete Insulated Wall Panels. MSc.Thesis, Department of Civil and Environmental Engineering, University of Alberta, Canada.

Arevalo, S., and Tomlinson, D. (2020). Experimental thermal bowing response of precast concrete insulated wall panels with stiff shear connectors and simple supports. Journal of Building Engineering, 30(January), 101319. https://doi.org/10.1016/j.jobe.2020.101319

Arslan, O., Messali, F., Smyrou, E., Bal, E., and Rots, J. G. (2021). Mechanical modelling of the axial behaviour of traditional masonry wall metal tie connections in cavity walls. Construction and Building Materials, 310(October), 125205.

Arslan, Onur, Messali, F., Smyrou, E., Bal, İ. E., and Rots, J. G. (2020). Experimental characterization of the axial behavior of traditional masonry wall metal tie connections in cavity walls. Construction and Building Materials, (xxxx).

ASHRAE. (2021). Fundamentals SI Handbook. https://doi.org/10.1055/b-0039-166526

ASTM C1611/C1611M-18. (2018). Standard test method for slump flow of self-consolidating concrete. ASTM International, 1–6. https://doi.org/10.1520/C1611

ASTM C165. (2017). Standard Test Method for Measuring Compressive Properties of Thermal Insulations. ASTM International (Vol. i). https://doi.org/10.1520/C0165-07R17

ASTM C39/C39M−20. (2020). Compressive Strength of Cylindrical Concrete Specimens. ASTM Standards, 1–7. https://doi.org/10.1520/C0039

ASTM E8. (2022). Standard test methods for tension testing of metallic materials. Annual Book of ASTM Standards, I, 1–31. https://doi.org/10.1520/E0008

Bai, F., and Davidson, J. S. (2015). Analysis of partially composite foam insulated concrete sandwich structures. Engineering Structures, 91, 197–209.

Baker, C., Marr, J. K., and Drysdale, R. G. (2004). Capacity of Single and Double Wythe Unreinforced Concrete Block Walls. In 13th International Brick and Block Masonry Conference. Amsterdam.

Banerjee, S., Nayak, S., and Das, S. (2019). Enhancing the flexural behaviour of masonry wallet using PP band and steel wire mesh. Construction and Building Materials, 194, 179–191.

Batool, F., Islam, K., Cakiroglu, C., and Shahriar, A. (2021). Effectiveness of wood waste sawdust to produce medium- to low-strength concrete materials. Journal of Building Engineering, 44(August), 103237. https://doi.org/10.1016/j.jobe.2021.103237

Belarbi, A., Dawood, M., and Acun, B. (2016). 20 – Sustainability of fiber-reinforced polymers (FRPs) as a construction material. In J. M. B. T.-S. of C. M. (Second E. Khatib (Ed.), Woodhead Publishing Series in Civil and Structural Engineering (pp. 521–538). Woodhead Publishing. https://doi.org/https://doi.org/10.1016/B978-0-08-100370-1.00020-2

Benayoune, A., Samad, A. A. A., Trikha, D. N., Ali, A. A. A., and Ellinna, S. H. M. (2008). Flexural behaviour of pre-cast concrete sandwich composite panel – Experimental and theoretical investigations. Construction and Building Materials, 22(4), 580–592.

Benmokrane, B., Manalo, A., Bouhet, J. C., Mohamed, K., and Robert, M. (2017). Effects of Diameter on the Durability of Glass Fiber-Reinforced Polymer Bars Conditioned in Alkaline Solution. Journal of Composites for Construction, 21(5), 1–12.

Binda, L., Pina-Henriques, J., Anzani, A., Fontana, A., and Lourenço, P. B. (2006). A contribution for the understanding of load-transfer mechanisms in multi-leaf masonry walls: Testing and modelling. Engineering Structures, 28(8), 1132–1148. https://doi.org/10.1016/j.engstruct.2005.12.004

Brick Industry Association. (2002). Energy Code Compliance of Brick Masonry Walls. TECHNICAL NOTES on Brick Construction, 4B(February).

Brick Industry Association. (2003). Wall Ties for Brick Masonry. TECHNICAL NOTES on Brick Construction, 44B(May).

Brick Industry Association. (2018). Technical Notes 28D – Brick Veneer/Concrete Masonry Walls. Technical Notes on Brick Construction 28D.

Brick Industry Association. (2020). Adding Brick Veneer to Existing Construction. TECHNICAL NOTES on Brick Construction (Vol. 28A).

Brown, R. H., and Elling, R. E. (1979). Lateral Load Distribution in Cavity Walls. Proceedings of the Fifth International Brick Masonry Conference,Washington, D.C, 351–359.

BS EN. (1992). Eurocode 2: Design of concrete structures-Part 1. General rules and rules for buildings. British Standards.

BS EN. (1992). Eurocode 6: Design of masonry structures (Part 1-1): General rules for reinforced and unreinforced masonry structures.

Bunn, W. G. (2011). CFRP Grid/Rigid Foam Shear Transfer Mechanism for Precast, Prestressed Concrete Sandwich Wall Panels. MSc. Thesis, Graduate Faculty of North Carolina State University.

Bush, T. D., and Stine, G. L. (1994). Flexural Behavior of Composite Precast Concrete Sandwich Panels With Continuous Truss Connectors. PCI Journal, 39(2), 112–121. https://doi.org/10.15554/pcij.03011994.112.121

Cagnon, H., Aubert, J. E., Coutand, M., and Magniont, C. (2014). Hygrothermal properties of earth bricks. Energy and Buildings, 80, 208–217. https://doi.org/10.1016/j.enbuild.2014.05.024

CAN/CSA S806-12. (2021). Design and Construction of Building structures with Fibre-Reinforced Polymer, CAN/CSA S806-12. Canadian Standards Association.

Carbonari, G., Cavalaro, S. H. P., Cansario, M. M., and Aguado, A. (2012). Flexural behaviour of light-weight sandwich panels composed by concrete and EPS. Construction and Building Materials, 35, 792–799. https://doi.org/10.1016/j.conbuildmat.2012.04.080

Cascardi, A., Leone, M., and Aiello, M. A. (2020). Transversal joining of multi-leaf masonry through different types of connector: Experimental and theoretical investigation. Construction and Building Materials, 265, 120733.

Chen, A., Norris, T. G., Hopkins, P. M., and Yossef, M. (2015). Experimental investigation and finite element analysis of flexural behavior of insulated concrete sandwich panels with FRP plate shear connectors. Engineering Structures, 98, 95–108.

Chen, A., Yossef, M., and Hopkins, P. (2020). A comparative study of di ff erent methods to calculate degrees of composite action for insulated concrete sandwich panels. Engineering Structures, 212(February), 110423. https://doi.org/10.1016/j.engstruct.2020.110423

Choi, I., Kim, J. H., and You, Y. C. (2016). Effect of cyclic loading on composite behavior of insulated concrete sandwich wall panels with GFRP shear connectors. Composites Part B: Engineering, 96, 7–19. https://doi.org/10.1016/j.compositesb.2016.04.030

Choi, K. B., Choi, W. C., Feo, L., Jang, S. J., and Yun, H. Do. (2015). In-plane shear behavior of insulated precast concrete sandwich panels reinforced with corrugated GFRP shear connectors. Composites Part B: Engineering, 79, 419–429.

Choi, W., Jang, S. J., and Yun, H. Do. (2019). Design properties of insulated precast concrete sandwich panels with composite shear connectors. Composites Part B: Engineering, 157(August 2018), 36–42. https://doi.org/10.1016/j.compositesb.2018.08.081

Clayford, G. T. (2003). Using Air Barriers in Masonry Walls. Concrete Construction.

Corradi, M., Borri, A., Poverello, E., and Castori, G. (2017). The use of transverse connectors as reinforcement of multi-leaf walls. Materials and Structures/Materiaux et Constructions, 50(2), 1–14. https://doi.org/10.1617/s11527-016-0977-3

Correia, J. R., Branco, F. A., Ferreira, J. G., Bai, Y., and Keller, T. (2010). Fire protection systems for building floors made of pultruded GFRP profiles: Part 1: Experimental investigations. Composites Part B: Engineering, 41(8), 617–629.

Cox, B., Syndergaard, P., Al-Rubaye, S., Pozo-Lora, F. F., Tawadrous, R., and Maguire, M. (2019). Lumped GFRP star connector system for partial composite action in insulated precast concrete sandwich panels. Composite Structures, 229(July), 111465.

CPCI. (2020). Insulated Wall Panel-Technical Guide. Ottawa, Ontario.

CSA-A179-14. (2019). National Standard of Canada CAN / CSA-A179-14 Mortar and grout for unit masonry.

CSA-A23.3-19. (2019). Design of concrete structures for buildings. Standards Council of Canada. Standards Council of Canada, Ottawa, Ontario, Canada.

CSA A165.1. (2019). CSA Standards on concrete masonry units.

CSA A370:14. (2018). Connectors for masonry. Mississauga, Ontario, Canada.

CSA S304-14. (2019). Design of Masonry Structures. Canadian Standards Association, Mississauga, Ontario, Canada.

CSA S807:19. (2019). Specification for fibre-reinforced polymers. National Standard of Canada.

Daniel, I. M., and Ori lsha. (2006). Engineering Mechanics of Composite Materials. Oxford University Press (Vol. 2nd Editio). https://doi.org/10.1016/B978-1-84569-385-5.50021-0

Davies, J. M. (2001). Lighweight Sandwich Construction. John Wiley and Sons. John Wiley and Sons.

De Munck, M., Tysmans, T., El Kadi, M., Wastiels, J., Vervloet, J., Kapsalis, P., and Remy, O. (2019). Durability of sandwich beams with textile reinforced cementitious composite faces. Construction and Building Materials, 229, 116832. https://doi.org/10.1016/j.conbuildmat.2019.116832

Dizhur, D., Griffith, M., and Ingham, J. (2014). Out-of-plane strengthening of unreinforced masonry walls using near surface mounted fibre reinforced polymer strips. Engineering Structures, 59, 330–343. https://doi.org/10.1016/j.engstruct.2013.10.026

Dryscale, R. G., and Hamid, A. A. (2005). Masonry Structures Behaviour and Design – Canadian Edition. Canada Masonry Design Council.

Dutton, M. (2012). Digital Image Correlation for Evaluating Structural Engineering Materials. Department of Civil Engineering, Queen's University Kingston, Ontario, Canada. https://doi.org/10.1016/S1369-7021(10)70235-2

Dzaye, E. D., Tsangouri, E., Spiessens, K., De Schutter, G., Aggelis, D. G., MICHAEL, D., … Sause, M. G. R. (2012). Digital image correlation. Archives of Civil and Mechanical Engineering, 242(1), 122. https://doi.org/10.1016/j.acme.2018.10.003

Egbon, B., and Tomlinson, D. (2023). Structural Evaluation of Notched Insulation in Precast Concrete Sandwich Panels. Lecture Notes in Civil Engineering (Vol. 241). Springer Nature Singapore. https://doi.org/10.1007/978-981-19-0511-7_25

Egbon, Benedict, and Tomlinson, D. (2021). Experimental investigation of longitudinal shear transfer in insulated concrete wall panels with notched insulation. Journal of Building Engineering, 43(103173). https://doi.org/https://doi.org/10.1016/j.jobe.2021.103173

Einea, A. (1992). Structural and thermal efficiency of precast concrete sandwich panel systems. PhD Thesis. https://doi.org/10.1016/j.jaci.2012.05.050

Einea, A., Salmon, D. C., Tadros, M. K., and Culp, T. . (1994). A New Structurally and Thermally Efficient Precast Sandwich panel. PCI Journal, 39(4), 90–101.

Erki, M. A., and Rizkalla, S. H. (1993). FRP Reinforcement for Concrete Structures. Concrete International, 48–53.

Ferdous, W., Manalo, A., Aravinthan, T., and Fam, A. (2018). Flexural and shear behaviour of layered sandwich beams. Construction and Building Materials, 173, 429–442. https://doi.org/10.1016/j.conbuildmat.2018.04.068

Frankl, Bernard A, Lucier, G. W., Hassan, T. K., and Rizkalla, S. H. (2011). Behavior of precast, prestressed concrete sandwich wall panels reinforced with CFRP shear grid. PCI Journal, 56(2), 42–54. https://doi.org/10.15554/pcij.03012011.42.54

Frankl, Bernard Anthony, Lucier, G., Rizkalla, S., Blaszak, G., and Harmon, T. (2008). Structural Behavior of Insulated Precast Prestressed Concrete Sandwich Panels Reinforced with CFRP Grid. Fourth International Conference on FRP Composites in Civil Engineering (CICE2008), 243. https://doi.org/10.1002/pbc.24544

Gara, F., Ragni, L., Roia, D., and Dezi, L. (2012). Experimental tests and numerical modelling of wall sandwich panels. Engineering Structures, 37, 193–204. https://doi.org/10.1016/j.engstruct.2011.12.027

Gayed, M., and Korany, Y. (2012). Masonry Chair Report: Modulus of Elasticity Prediction for Hollow Concrete Masonry.

Gencel, O., Erdugmus, E., Sutcu, M., and Oren, O. H. (2020). Effects of concrete waste on characteristics of structural fired clay bricks. Construction and Building Materials, 255, 119362. https://doi.org/10.1016/j.conbuildmat.2020.119362

Gleich, H. . (2007). New Carbon Fiber Reinforcement Advances Sandwich Wall Panels. Structure Magazine, (April), 61–63.

Gombeda, M. J., Trasborg, P., Naito, C. J., and Quiel, S. E. (2017). Simplified model for partially-composite precast concrete insulated wall panels subjected to lateral loading. Engineering Structures, 138, 367–380. https://doi.org/10.1016/j.engstruct.2017.01.065

Gonzalez, R. (2022). Study Of A Slender Masonry Wall Tested In An Innovative Device. MSc.Thesis, Department of Civil and Environmental Engineering, University of Alberta, Canada.

Goudarzi, N., Korany, Y., Adeeb, S., and Cheng, R. (2016). Characterization of the shear behavior of Z-shaped steel plate connectors used in insulated concrete panels. PCI Journal, 23–37. https://doi.org/10.15554/pcij.03012016.23.37

Goyal, A., Rashwan, M. S., Hatzinikolas, M. A., and Zervos, S. (1994). Structural performance of cavity walls constructed with units containing sawdust and shear connected to the brick veneer. Canadian Journal of Civil Engineering, 21(4), 576–584. https://doi.org/10.1139/l94-059

Granholm, H. (1949). Om sammansatta balkar och pelare med särskild hänsyn till spikade träkonstruktioner -On composite beams and columns with particular regard to nailed timber structures.

Graziotti, F., Tomassetti, U., Penna, A., and Magenes, G. (2016). Out-of-plane shaking table tests on URM single leaf and cavity walls in two-way bending. Engineering Structures, 125, 455–470.

Hagel, M., Moses, D., and Jonkman, R. (2019). Shelf-Angle and Brick Ledge Design for Brick Veneer on Mid-rise Wood Frame Buildings.

Hammant, B. (1971). The use of 4-point loading tests to determine mechanical properties. Composites, 2(4), 246–249. https://doi.org/10.1016/0010-4361(71)90154-6

Hassan, T., and H. Rizkalla, S. (2010). Analysis and design guidelines of precast, prestressed concrete, composite load-bearing sandwich wall panels reinforced with CFRP grid. PCI Journal, 55(2), 147–162. https://doi.org/10.15554/pcij.03012010.147.162

Hatzinikolas, M., Longworth, J., and Warwaruk, J. (n.d.). Strength and behaviour of Metal Ties in 2-Wythe Masonry Walls. 1979.

Hatzinikolas, M A, Elwi, A. E., Warwaruk, J., and Papanikolas, P. K. (1990). Experimental and Analytical Results for Shear Connected Cavity Walls.

Hatzinikolas, Michael A., Lee, R., Longworth, J., and Warwaruk, J. (1983). Drilled-in Inserts in Masonry Construction.

Hatzinikolas, Michael, Korany, Y., and Brzev, S. (2015). Masonry Design For Engineers and Architects.

Hodicky, K., Hulin, T., Schmidt, J. W., and Stang, H. (2013). Structural Performance of New Thin-Walled Concrete Sandwich Panel System Reinforced with BFRP Shear Connectors. 4th Asia-Pacific Conference on FRP in Structures, (December), 6.

Hodicky, K., Sopal, G., Rizkalla, S., Hulin, T., and Stang, H. (2014). Experimental and numerical investigation of the FRP shear mechanism for concrete sandwich panels. Journal of Composites for Construction, 19(5), 1–12. https://doi.org/10.1061/(ASCE)CC.1943-5614.0000554

Holmberg, A., and Plem, E. (1965). Behaviour of load-bearing sandwich- type structures. (S. B. Lund, Ed.).

Hou, H., Ji, K., Wang, W., Qu, B., Fang, M., and Qiu, C. (2019). Flexural behavior of precast insulated sandwich wall panels: Full-scale tests and design implications. Engineering Structures, 180(December 2018), 750–761. https://doi.org/10.1016/j.engstruct.2018.11.068

Huang, J.-Q., and Dai, J.-G. (2019). Direct shear tests of glass fiber reinforced polymer connectors for use in precast concrete sandwich panels. Composite Structures, 207(September 2018), 136–147. https://doi.org/10.1016/j.compstruct.2018.09.017

Huang, J., Jiang, Q., Chong, X., Ye, X., and Wang, D. (2018). Experimental study on precast concrete sandwich panel with cross-shaped GFRP connectors. Magazine of Concrete Research, 72(3), 149–162. https://doi.org/10.1680/jmacr.18.00258

Huang, J. Q., and Dai, J. G. (2020). Flexural performance of precast geopolymer concrete sandwich panel enabled by FRP connector. Composite Structures, 248(December 2019), 112563. https://doi.org/10.1016/j.compstruct.2020.112563

Huang, Q., and Hamed, E. (2019). Nonlinear finite element analysis of composite precast concrete sandwich panels made with diagonal FRP bar connectors. Composite Structures, 212(March 2018), 304–316. https://doi.org/10.1016/j.compstruct.2019.01.019

Huovila, P., Juusela, M. A., Melchert, L., Pouffary, S., Cheng, C. C., Urge-Vorsatz, D., … Svenningsen, N. (2009). Buildings and Climate Change. UNEP SBCI -Sustainable Buildings and Climate Initiative. https://doi.org/10.1055/s-2003-37012

Insel, E., Olsen, M. D., Tanner, J. E., and Dolan, C. W. (2006). Carbon Fiber Connectors for Concrete Sandwich Panels. Conrete International, (October), 33–38.

Ismaiel, M. (2022). A Practical Method to Estimate the Effective Thermal Resistance of Exterior Masonry Walls. Ph.D. Thesis, Department of Civil and Environmental Engineering, University of Alberta, Canada.

Imjai, T., Guadagnini, M., and Pilakoutas, K. (2017). Bend Strength of FRP Bars: Experimental Investigation and Bond Modeling. *Journal of Materials in Civil Engineering*, *29*(7), 1–11. https://doi.org/10.1061/(asce)mt.1943-5533.0001855

Ismaiel, M., Chen, Y., Cruz-Noguez, C., and Hagel, M. (2022). Thermal resistance of masonry walls: a literature review on influence factors, evaluation, and improvement. Journal of Building Physics, 45(4), 528–567. https://doi.org/10.1177/17442591211009549

Jagadeesh, P., Mavinkere Rangappa, S., Suyambulingam, I., Siengchin, S., Puttegowda, M., Binoj, J. S., and Cuadrado, M. M. M. (2023). Drilling characteristics and properties analysis of fiber reinforced polymer composites: A comprehensive review. *Heliyon*, *9*(3), e14428. https://doi.org/10.1016/j.heliyon.2023.e14428

Jaiden, T. O. (2017). Developing a General Methodology for Evaluating Composite Action in Insulated Wall Panels. MSc Thesis. Utah State University. Retrieved from https://digitalcommons.usu.edu/cee_facpub/3531

Jakobsen, J., Bozhevolnaya, E., and Thomsen, O. T. (2007). New peel stopper concept for sandwich structures. Composites Science and Technology, 67(15–16), 3378–3385. https://doi.org/10.1016/j.compscitech.2007.03.033

Joseph, J., Prabakar, J., and Alagusundaramoorthy, P. (2017). Precast concrete sandwich one-way slabs under flexural loading. Engineering Structures, 138, 447–457. https://doi.org/10.1016/j.engstruct.2017.02.033

Joseph, J., Prabakar, J., and Alagusundaramoorthy, P. (2018). Flexural behavior of precast concrete sandwich panels under different loading conditions such as punching and bending. Alexandria Engineering Journal, 57(1), 309–320. https://doi.org/10.1016/j.aej.2016.11.016

Joseph, J., Prabakar, J., and Alagusundaramoorthy, P. (2019). Experimental studies on through-thickness shear behavior of EPS based precast concrete sandwich panels with truss shear connectors. Composites Part B: Engineering, 166(January), 446–456. https://doi.org/10.1016/j.compositesb.2019.02.030

Kandola, B. K., Horrocks, A. R., Myler, P., and Blair, D. (2002). The effect of intumescents on the burning behaviour of polyester-resin-containing composites. Composites – Part A: Applied Science and Manufacturing, 33(6), 805–817. https://doi.org/10.1016/S1359-835X(02)00026-X

Kazem, H., Bunn, W. G., Seliem, H. M., Rizkalla, S. H., and Gleich, H. (2015). Durability and long term behavior of FRP/foam shear transfer mechanism for concrete sandwich panels. Construction and Building Materials, 98, 722–734.

Keenehan, J., Concannon, K., Hajializadeh, D., and McNally, C. (2012). Numerical Asessment of The Thermal Performance of Structural Precast Panels. In Numerical Modeling Strategies for Sustainable Concrete Structures, Aix-en-Provence, France, May 29-June 1, 2012 (pp. 1–10).

Kent, D. C., and Park, R. (1971). Structural Division : STRUCTURAL DIVISION Proceedings of the American Society of Civil Engineers, 97(7).

Khorramian, K., and Sadeghian, P. (2019). Material characterization of GFRP bars in compression using a new test method. Journal of Testing and Evaluation, 49(2), 1037–1052. https://doi.org/10.1520/JTE20180873

Kim, J., and You, Y. (2015). Composite behavior of a novel insulated concrete sandwich wall panel reinforced with GFRP shear grids: Effects of insulation types. Materials, 8(3), 899–913. https://doi.org/10.3390/ma8030899

Kinnane, O., West, R., and Hegarty, R. O. (2020). Structural shear performance of insulated precast concrete sandwich panels with steel plate connectors. Engineering Structures, 215(October 2019), 110691. https://doi.org/10.1016/j.engstruct.2020.110691

Kuhn, D. P., and Shaikh, F. A. (1996). Slip-Pullout Strength of Hooked Anchors. Research Report, University of Wisconsin-Milwaukee, Submitted to the National Codes and Standards Council.

Langmans, J., Indekeu, M., and Roels, S. (2017). The impact of workmanship on the thermal performance of cavity walls with rigid insulation boards: Where are we today? Energy Procedia, 132, 255–260. https://doi.org/10.1016/j.egypro.2017.09.711

Lee, B.J., and Pessiki, S. (2008). Revised zone method R-value calculation for precast concrete sandwich panels containing metal wythe connectors. PCI Journal, 53(5), 86–100. https://doi.org/10.15554/pcij.09012008.86.100

Lee, B. J., and Pessiki, S. (2006a). Thermal behavior of precast prestressed concrete three-wythe sandwich wall panels. AEI 2006: Building Integration Solutions – Proceedings of the 2006 Architectural Engineering National Conference, 2006, 3.

Lee, B. J., and Pessiki, S. (2006b). Thermal performance evaluation of precast concrete three-wythe sandwich wall panels. Energy and Buildings, 38(8), 1006–1014. https://doi.org/10.1016/j.enbuild.2005.11.014

Leung, A. (1984). Structural Design and Analysis of Concrete Sandwich Panels and their Practical Application. M. Eng Thesis, Memorial University of Newfoundland.

Lin, Y. (2010). Tension stiffening model for reinforced concrete based on bond stress slip relation. MSc.Thesis, College of Engineering,The Pennsylvania State University, USA.

Liu, Y., and Dawe, J. L. (2003). Analytical modeling of masonry load-bearing walls. Canadian Journal of Civil Engineering, 30(5): 795–806. Canadian Science Publishing.

Liu, Y., and Hu, K. (2007). Experimental study of reinforced masonry walls subjected to combined axial load and out-of-plane bendingThis article is one of a selection of papers published in this Special Issue on Masonry. Canadian Journal of Civil Engineering, 34(11): 1486–1494.

Lissel, S. L., and Shrive, N. G. (2001). Glass Fibre Reinforced Polymer (GFRP) Shear Connectors For Masonry. In 9th Canadian Masonry Symmposium. Fredericton, New Brunswick.

Losch, E. (2003). Bowing of insulated precast concrete wall panels. PCI Journal, 48(6), 126–129.

Theriaule, M., and B. Benmokrane. (1998). Effects of FRP Reinforcement Ratio and Concrete Strength. Journal of Composites for Construction, 2(February), 7–16. https://doi.org/10.1061/(ASCE)1090-0268(1998)2:1(7)

Maccarini, H., Vasconcelos, G., Rodrigues, H., Ortega, J., and Lourenço, P. B. (2018). Out-of-plane behavior of stone masonry walls: Experimental and numerical analysis. Construction and Building Materials, 179, 430–452. https://doi.org/10.1016/j.conbuildmat.2018.05.216

Magenes, G., Penna, A., Rota, M., Galasco, A., and Senaldi, I. (2012). Shaking table test of a full scale stone masonry building with stiffened floor and roof diaphragms. 15th World Conference on Earthquake Engineering, (2012), 24–28.

Maranan, G., Manalo, O., Karunasena, K., Benmokrane, B. (2015). Bond Stress-Slip Behavior: Case of GFRP Bars in Geopolymer Concrete, J. Mater. Civ. Eng. 27 1–9. https://doi.org/10.1061/(asce)mt.1943-5533.0001046.

Martins, A., Vasconcelos, G., and Campos Costa, A. (2016). Experimental study on the mechanical performance of steel ties for brick masonry veneers. Brick and Block Masonry: Trends, Innovations and Challenges - Proceedings of the 16th International Brick and Block Masonry Conference, IBMAC 2016, (July), 1723–1732. https://doi.org/10.1201/b21889-214

Martins, A., Vasconcelos, G., and Costa, A. C. (2017). Experimental assessment of the mechanical behaviour of ties on brick veneers anchored to brick masonry infills. Construction and Building Materials, 156, 515–531. https://doi.org/10.1016/j.conbuildmat.2017.09.013

Marziale, S. A., and Toubia, E. A. (2015). Analysis of brick veneer on concrete masonry wall subjected to in-plane loads. Structures, 2, 1–7. https://doi.org/10.1016/j.istruc.2014.11.001

Mathieson, H., and Fam, A. (2014). Axial Loading Tests and Simplified Modeling of Sandwich Panels with GFRP Skins and Soft Core at Various Slenderness Ratios. Journal of Composites for Construction, 19(2), 04014040. https://doi.org/10.1061/(asce)cc.1943-5614.0000494

Maximos, H. N., Pong, W. A., Tadros, M. K., and Martin, L. D. (2007). Behavior and Design of Composite Precast Prestressed Concrete Sandwich Panels with NU-Tie.

McCall, W. C. (1985). Thermal Properties of Sandwich Panels. Concrete International, 7(1), 35–41.

McGinley, W. M., Warwaruk, J., Longworth, J., and Hatzinikolas, M. (1988). Masonry Veneer Wall Systems. Structural Engineering Report.

Miglietta, M., Damiani, N., Guerrini, G., and Graziotti, F. (2021). Full-scale shake-table tests on two unreinforced masonry cavity-wall buildings: effect of an innovative timber retrofit. Bulletin of Earthquake Engineering (Vol. 19). Springer Netherlands.

Mitra, N. (2010). A methodology for improving shear performance of marine grade sandwich composites: Sandwich composite panel with shear key. Composite Structures, 92(5), 1065–1072. https://doi.org/10.1016/j.compstruct.2009.10.005

Morcous, G., Henin, E., Lafferty, M., and Tadros, M. K. (2011). Design and testing of tornado-resistant precast/prestressed concrete sandwich panels with GFRP Ties. PCI/NBC, 1–21.

Mostafa, A., Shankar, K., and Morozov, E. V. (2013). Effect of shear keys diameter on the shear performance of composite sandwich panel with PVC and PU foam core: FE study. Composite Structures, 102, 90–100. https://doi.org/10.1016/j.compstruct.2013.03.003

Naito, C., Hoemann, J., Beacraft, M., and Bewick, B. (2012). Performance and Characterization of Shear Ties for Use in Insulated Precast Concrete Sandwich Wall Panels. Journal of Structural Engineering, 138(1). https://doi.org/https://doi.org/10https://doi.org/10.1061/(ASCE)ST.1943-541X.0000430

Naito, C. J., Hoemann, J. M., Shull, J. S., Saucier, A., Salim, H. A., Bewick, B. T., and Hammons, Michael, I. (2011). Precast/prestressed concrete experiments performance on non-load bearing sandwich wall panels. Final Technical Report.

Nanni, A., Rizkalla, S., Bakis, C. E., Conrad, J. O., and Abdelrahman, A. A. (1998). Characterization of GFRP Ribbed Rod Used for Reinforced Concrete Construction. In Proceedings of the International Composites Exhibition (ICE-98). Nashville, TN, pp. 16A/1-6.

National Research Council of Canada. (2017). National Energy Code of Canada for Buildings.

Natural Resources Canada. (2020). Energy efficiency for homes.

Natural Resources Canada. (2021). Keeping The Heat In - Section 7: Insulating Walls: insulating, renovating and building additions.

NBC. (2019). National Building Code - 2019 Alberta Edition.

Nethercot, D. A., and Trahair, N. S. (1976). Lateral Buckling Approximations for Elastic Beams. The Structural Engineer, 54(6), 197–204.

Newberry, C. M. (2011). Finite Element Simulation and Assessment of Single-Degree-of-Freedom Prediction Methodology for Insulated Concrete Sandwich Panels Subjected to Blast Loads. Masters Thesis. Auburn University.

Newmark, N. ., Siess, C. ., and Viest, I. M. (1951). Tests and analysis of composite beams with incomplete interaction. Society for Experimental Stress Analysis, 9(1), 75–92.

Noël, N. (2012). Material selection by architects for green building design. MSc.Thesis, Faculty of Graduate Studies, University of British Columbia, Canada.

Norris, T. G., and Chen, A. (2016). Development of insulated FRP-confined Precast Concrete Sandwich panel with side and top confining plates and dry bond. Composite Structures, 152, 444–454. https://doi.org/10.1016/j.compstruct.2016.05.053

O'Hegarty, R., and Kinnane, O. (2020). Review of precast concrete sandwich panels and their innovations. Construction and Building Materials, 233, 117145. https://doi.org/10.1016/j.conbuildmat.2019.117145

Oehlers, D. J., Nguyen, N. T., Ahmed, M., and Bradford, M. A. (1997). Partial Interaction in Composite Steel and Concrete Beams with Full Shear Connection. Journal of Constructional Steel Research, 41(2–3), 235–248. https://doi.org/10.1016/S0143-974X(97)80892-9

Oh, T. S., Jang, S. J., Lee, K. M., and Yun, H. Do. (2013). Insulation Type Effect on the Direct Shear Behavior of Concrete Sandwich Panel (CSP) with Non-Shear Connectors. Advanced Materials Research, 663, 154–158. https://doi.org/10.4028/www.scientific.net/amr.663.154

Olaiya, B. C., Lawan, M. M., and Olonade, K. A. (2023). Utilization of sawdust composites in construction—a review. SN Applied Sciences, 5(5). https://doi.org/10.1007/s42452-023-05361-4

Olsen, J., and Maguire, M. (2016). Shear testing of preast concrete sandwich wall panel composite shear connectors. PCI/NBC, (June).

Pacholok, K. W. (1989). Shear connectors in masonry cavity walls.

Pantelides, C. P., Surapaneni, R., and Reaveley, L. D. (2008). Structural Performance of Hybrid GFRP/Steel Concrete Sandwich Panels. Journal of Composites for Construction, 12(5), 570–576. https://doi.org/10.1061/(asce)1090-0268(2008)12:5(570)

Papanikolas, K., Hatzinikolas, M., and Warwaruk, J. (1990). Behaviour of Shear Connected Cavity Walls. Structural Engineering Report No. 169, Department of Civil Engineering, University of Alberta, Edmonton, Canada.

PCI. (2010). PCI Design Handbook 7th Edition. Precast Concrete Institute, Chicago, IL.

PCI. (2011). State of the Art of Precast/Prestressed Concrete Sandwich Wall Panels. PCI Journal, 56(2), 131–176.

Peng, C. (2016). Calculation of a building's life cycle carbon emissions based on Ecotect and building information modeling. Journal of Cleaner Production, 112, 453–465. https://doi.org/10.1016/j.jclepro.2015.08.078

Pessiki, S., and Mlynarczyk, A. (2003). Experimental Evaluation of the Composite Behavior of Precast Concrete Sandwich Wall Panels. PCI Journal, 48, 54–71.

Petersen, M. R., Chen, A., Roll, M., Jung, S. J., and Yossef, M. (2015). Mechanical properties of fire-retardant glass fiber-reinforced polymer materials with alumina tri-hydrate filler. Composites Part B: Engineering, 78, 109–121. https://doi.org/10.1016/j.compositesb.2015.03.071

Petersen, R. B., Ismail, N., Masia, M. J., and Ingham, J. M. (2012). Finite element modelling of unreinforced masonry shear wallettes strengthened using twisted steel bars. Construction and Building Materials, 33, 14–24. https://doi.org/10.1016/j.conbuildmat.2012.01.016

Pope, H. (2021). Improving the Fire Resistance of Concrete Masonry Walls. Ph.D.Thesis, Department of Civil and Environmental Engineering, Carleton University,Ottawa, Ontario, Canada.

Post, A. W. (2006). Thermal and fatigue Testing of Fiber Reinforced Polymer Tie Connectors used in Concrete Sandwich Walls. MSc.Thesis,Retrospective Theses and Dissertations. 851. https://lib.dr.iastate.edu/rtd/851 This.

Pozo-Lora, F. Thermal bowing of concrete sandwich panels with flexible shear connectors, 102 (2018). https://doi.org/10.1016/j.jobe.2019.101124

Pozo-Lora, F., and Maguire, M. (2020). Thermal bowing of concrete sandwich panels with flexible shear connectors. Journal of Building Engineering, 29(July 2019), 101124. https://doi.org/10.1016/j.jobe.2019.101124

Prachasaree, W., Limkatanyu, S., Hawa, A., Sukontasukkul, P., and Chindaprasirt, P. (2020). Manuscript title: Development of strength prediction models for fly ash based geopolymer concrete. Journal of Building Engineering, 32(July), 101704. https://doi.org/10.1016/j.jobe.2020.101704

Reicher, P., and Farahmandpour, K. (2016). Evaluating Water Leakage in Mass Masonry Walls. Interface-International Institute of Building Enclosure Consultants.

Reneckis, D., LaFave, J. M., and Clarke, W. M. (2004). Out-of-plane performance of brick veneer walls on wood frame construction. Engineering Structures, 26(8), 1027–1042. https://doi.org/10.1016/j.engstruct.2004.02.013

Rizkalla, S. H., Hassan, T. K., and Lucier, G. (2009). FRP Shear Transfer Mechanism for Precast, Prestressed Concrete Sandwich Load-Bearing Panels. ACI Special Publication, 265, 603–626. https://doi.org/10.14359/51663315

S. Suryani, and N. Mohamad. (2012). Structural Behaviour of Precast Lightweight Foamed Concrete Sandwich Panel under Axial Load : An Overview. International Journal of Integrated Engineering, 4(3), 47–52.

S.H. Rizkalla and G. Lucier, T. K. H. (2009). FRP Shear Transfer Mechanism for Precast, Prestressed Concrete Sandwich Load-Bearing Panels. ACI Special Publication, 265, 603–626. https://doi.org/10.14359/51663315

Sakr, K. M., and Neis, Vernon, V. (2001). Load-Deflection Analyses of Double Wythe Unreinforced Masonry Walls. Jornal of Structural Engineering, 127(9), 1101–1108.

Sakr, Khaled M., and Neis, Vernon, V. (1997). The Structural Behaviour of Double-Wythe Masonry Walls: Experimental Results And Analysis. 11th International Brick/block Masonry Conference, Tongji University, Shanghai, China.

Salmon, D. C., and Einea, A. (1995). Partially Composite Sandwich Panel Deflections. Journal of Structural Engineering, 121(4), 778–783.

Salmon, D. C., Einea, A., Tadros, M. K., and Culp, T. D. (1997). Full Scale Testing of Precast Concrete Sandwich Panels. ACI Structural Journal, 94(4), 354–362. https://doi.org/10.14359/486

Sandoval, O. J., Takeuchi, C., Carrillo, J., and Barahona, B. (2021). Performance of unreinforced masonry panels strengthened with mortar overlays reinforced with welded wire mesh and transverse connectors. Construction and Building Materials, 267, 121054.

Sause, M. G. R. (2016). Digital image correlation. Springer Series in Materials Science, 242(12), 57–129. https://doi.org/10.1007/978-3-319-30954-5_3

Shahari, S., Fathullah, M., Abdullah, M. M. A. B., Shayfull, Z., Mia, M., and Budi Darmawan, V. E. (2021). Recent developments in fire retardant glass fibre reinforced epoxy composite and geopolymer as a potential fire-retardant material: A review. Construction and Building Materials, 277, 122246. https://doi.org/10.1016/j.conbuildmat.2021.122246

Shiping, Y., Linli, F., Shilang, X., Xiangming, H., Yuqing, W., and Chuanxiu, L. (2022). Study on the bonding properties of the interface between ECC and thermal insulation materials under freeze-thaw environment. Construction and Building Materials, 333(April), 127399. https://doi.org/10.1016/j.conbuildmat.2022.127399

Skroumpelou, G., Messali, F., Esposito, R., and Rots, J. G. (2018). Masonry Today Mechanical Characterization of Wall Tie Connection in. In 10th Australasian Masonry Conference, Sidney, Australia.

Sopal, G. J. (2013). Use Of CFRP Grid As Shear Transfer Mechanism For Precast Concrete Sandwich Wall Panels. PhD Thesis. North Carolina State University, Raleigh, North Carolina, USA.

Soriano, J. G. (2013). GFRP Shear Grid for Precast, Prestressed Concrete Sandwich Wall Panels. MSc.Thesis, Graduate Faculty, North Carolina State University, Raleigh, North Carolina, USA.

Stinson, S. (2017). Energy Efficiency in the Buildings Sector: Presentation to the Senate Committee on Energy, the Environment and Natural Resources.

Stonkuvienė, A., Bliūdžius, R., Burlingis, A., and Ramanauskas, J. (2021). The impact of connector's thermal and geometrical characteristics on the energy performance of facade systems. Journal of Building Engineering, 35(July 2020). https://doi.org/10.1016/j.jobe.2020.102085

Stüssi, F. (1947). Zusammengesetzte vollvandträger - Built-up girders. International Association for Bridge and Structural Engineering, IABSE, 8.

Sylaj, V., Fam, A., Hachborn, M., and Burak, R. (2018). Next Generation of UHPC Double Wythe Insulated Precast Concrete Wall Panels.

Szyszka, M., Jasieńko, J., and Ochsendorf, J. A. (2018). Out-of-plane behavior of two-layered free-standing masonry walls: Analytical solutions and small-scale tests. Engineering Structures, 163(April 2017), 11–24. https://doi.org/10.1016/j.engstruct.2018.02.011

Teixeira, Nanthan, and Queen's university kingston, ontario, C. (2015). Connection and fatigue behaviour of precast concrete insulated sandwich panels, (September), 1–169.

Teixeira, N., Tomlinson, D. G., and Fam, A. (2016). Precast concrete sandwich wall panels with bolted angle connections tested in flexure under simulated wind pressure and suction. PCI Journal, 65–83.

TEK 05-01B. (2003). Concrete Masonry Veneer Details. National Concrete Masonry Association, 1–7.

TEK 06- 02C. (2013). R - Values And U - Factors of Single Wythe Concrete Masonry Walls. National Concrete Masonry Association, 1–13.

TEK 12-01B. (2011). Anchors And Ties for Masonry. National Concrete Masonry Association, 1–9.

TEK 14-1B. (2007). Section Properties of Concrete Masonry Walls (Vol. 06).

TEK 16-01A. (2006). Multiwythe Concrete Masonry Walls. National Concrete Masonry Association, 1–9.

Tempest, B., Gergely, J., and Skipper, A. (2016). Reinforced geopolymer cement concrete in flexure: A closer look at stress-strain performance and equivalent stress-block parameters. PCI Journal, 61(6), 30–43.

TMS 402/602. (2016). Building Code Requirements for Masonry Structures. Building Code Requirements and Specification for Masonry Structures.

Tomek, R. (2017). Advantages of Precast Concrete in Highway Infrastructure Construction. Procedia Engineering, 196(June), 176–180. https://doi.org/10.1016/j.proeng.2017.07.188

Tomlinson, D. (2015). Behaviour of partially composite precast concrete sandwich panels under flexural and axial loads. Doctorate Thesis.

Tomlinson, D., and Fam, A. (2014). Experimental investigation of precast concrete insulated sandwich panels with glass fiber-reinforced polymer shear connectors. ACI Structural Journal, 111(3), 595–605. https://doi.org/10.14359/51686621

Tomlinson, D., and Fam, A. (2015). Flexural behavior of precast concrete sandwich wall panels with basalt FRP and steel reinforcement. PCI Journal, 60(6), 51–71. https://doi.org/10.15554/pcij.11012015.51.71

Tomlinson, D., and Fam, A. (2016a). Analytical approach to flexural response of partially composite insulated concrete sandwich walls used for cladding. Engineering Structures, 122, 251–266. https://doi.org/10.1016/j.engstruct.2016.04.059

Tomlinson, D., and Fam, A. (2016b). Combined Loading Behavior of Basalt FRP–Reinforced Precast Concrete Insulated Partially-Composite Walls. Journal of Composites for Construction, 20(3), 04015060. https://doi.org/10.1061/(ASCE)CC.1943-5614.0000611

Tomlinson, D., and Fam, A. (2018). Axial load-bending moment-interaction diagram of partially composite precast concrete sandwich panels. ACI Structural Journal, 115(6), 1515–1528. https://doi.org/10.14359/51710834

Tomlinson, Douglas G., Teixeira, N., and Fam, A. (2016). New Shear Connector Design for Insulated Concrete Sandwich Panels Using Basalt Fiber-Reinforced Polymer Bars. Journal of Composites for Construction, 20(4), 04016003. https://doi.org/10.1061/(asce)cc.1943-5614.0000662

Trasborg, P. (2014). Analytical and Experimental Evaluation of Precast Sandwich Wall Panels Subjected to Blast, Breach, and Ballistic Demands. Lehigh University,Bethlehem, PA.

Van Geem, M. G., and Shirley, S. T. (1987). Heat Transfer Characteristics of Insulated Concrete Sandwich Panel Walls.

VanGeem, M. (2006). Achieving sustainability with precast concrete. PCI Journal, 51(1).

Vanpachtenbeke, M., Van Den Bulcke, J., Van Acker, J., and Roels, S. (2020). Hygrothermal performance of timber frame walls with brick veneer cladding: A parameter analysis. E3S Web of Conferences, 172, 1–8. https://doi.org/10.1051/e3sconf/202017207002

Venu Madhava Rao, K., Venkatarama Reddy, B. V., and Jagadish, K. S. (1996). Flexural bond strength of masonry using various blocks and mortars. Materials and Structures/Materiaux et Constructions, 29(2), 119–124. https://doi.org/10.1007/bf02486202

Vervloet, J., Van Itterbeeck, P., Verbruggen, S., El Kadi, M., De Munck, M., Wastiels, J., and Tysmans, T. (2019). Experimental investigation of the buckling behaviour of Textile Reinforced Cement sandwich panels with varying face thickness using Digital Image Correlation. Construction and Building Materials, 194, 24–31. https://doi.org/10.1016/j.conbuildmat.2018.11.015

Waldron.P. (2004). The use of FRP as embedded reinforcement in concrete. In FRP Composites in Civil Engineering – CICE (pp. 83–92). https://doi.org/10.1017/CBO9781107415324.004

Wang, R., Elwi, A. E., and Hatzinikolas, M. A. (1997). Numerical Study of Tall Masonry Cavity Walls Subjected to Eccentric Loads. Journal of Structural Engineering, 123(10), 1287–1294. https://doi.org/10.1061/(asce)0733-9445(1997)123:10(1287)

Wang, R., Elwi, A. E., Hatzinikolas, M. A., and Warwaruk, J. (1997). Tests of Tall Cavity Walls Subjected To Eccentric Loading. Journal of Structural Engineering, 123(7), 912–919.

Wang, Ru, Elwi, A. E., Hatzinikolas, M. A., and Warwaruk, J. (1996). Behaviour of Masonry Cavity Walls Under Vertical Eccentric Loads.

Williams, C. R., and Hamid, A. A. (2005). In-Plane Stiffness and Strength of Adjustable Wall Ties. In 10th Canadian Masonry Symposium. Banff, Alberta.

Woltman, Greg. (2014). Structural and Steady-State Thermal Experimental Investigations of an Insulated Sandwich Panel. MASc.Thesis, Department of Civil Engineering, Queen's University, Kingston, Ontario, Canada.

Woltman, G., Tomlinson, D., and Fam, A. (2013). Investigation of Various GFRP Shear Connectors for Insulated Precast Concrete Sandwich Wall Panels. Journal of Composites for Construction, 17(5), 711–721. https://doi.org/10.1061/(ASCE)CC.1943-5614.0000373

Woltman, Gregory, Noel, M., and Fam, A. (2017). Experimental and numerical investigations of thermal properties of insulated concrete sandwich panels with fiberglass shear connectors. Energy and Buildings, 145, 22–31. https://doi.org/10.1016/j.enbuild.2017.04.007

Yossef, M., and Chen, A. (2018). A solution considering partial degree of composite action for insulated sandwich panels with general configuration flexible shear connectors. Engineering Structures, 162(February), 135–150. https://doi.org/10.1016/j.engstruct.2018.02.019

Zmavc, R. (1991). Simplified Analysis of Shear Connected Cavity Walls. MSc.Thesis, Department of Civil Engineering, University of Manitoba, Canada.

APPENDIX A: FORMULATIONS FOR THE LOAD-SLIP RESPONSE OF CONNECTORS IN INSULATED CONCRETE WALLS

Derivation of shear connection relationships (Eq. 5.1 to 5.4).

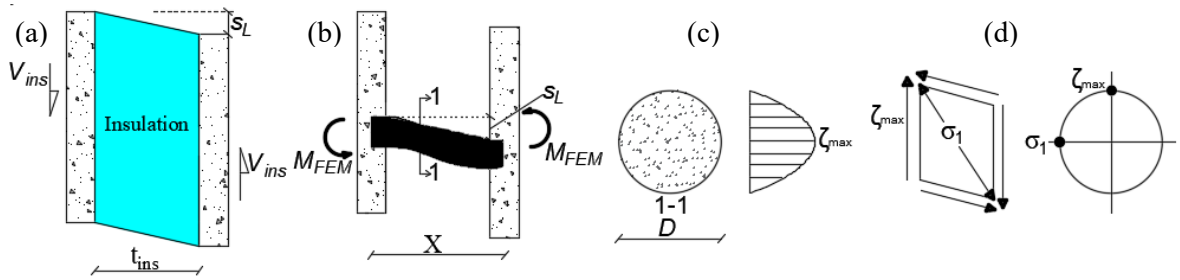

Figure A.1: (a) insulation shear resistance (b) Dowel connector with fixed-fixed end condition (c) connector shear stress (τ_{max}) (d) Mohr's Circle with principal (σ_1) and shear stress (τ_{max})

The shear stress ($\boldsymbol{\tau_{s,is}}$) acting on the insulation area (Fig. A.1a) is given as Eq. A.1

$$\tau_{s,is} = G_{is}\gamma_{s,is} \tag{A.1}$$

G_{ins} is the insulation shear modulus and $\gamma_{s,ins}$ is the shear strain and taken as s_L/t_{ins}. Multiplying the insulation shear stress ($\tau_{s,ins}$) by the insulation shear area (A_{is}), we arrive at the left hand side of Eq. 5.1.

$$V_{ins} = \frac{G_{is}A_{is}}{t_{is}}$$

The maximum insulation shear stress is the tensile strength of the insulation ($f_{is,t}$). Therefore, replacing $\tau_{s,is}$ in Eq. A.1 with $f_{is,t}$, and multiplying by the insulation shear area (A_{is}), we have the right hand side of Eq. 5.1

$$V_{ins} \leq f_{is,t}A_{is}$$

From structural analysis text, a beam with fixed-fixed end condition has a stiffness ($k_{s,cn}$, Eq. A.2)

$$k_{s,cn} = \frac{12E_bI_{cn}}{X^3} \tag{A.2}$$

E_b is the flexural modulus of elasticity. Multiplying Eq. A.2 by the slip (s_L) we have the left hand side of Eq. 5.1 and 5.2.

$$P_L = \frac{12E_bI_{cn}}{X^3}s_L$$

For dowel action (Fig. A.1b), since the connectors are assumed as beams with fixed-fixed end condition (Fig. A.1), the fixed-end moment (M_{FEM}, Eq. A.3, from structural analysis texts) is obtained as;

$$M_{FEM} = \frac{6E_b I_{cn}}{X^2} \tag{A.3}$$

Relating M_{FEM} to the bending stress (f_u), Eq. A.4

$$M_{FEM} = \frac{f_u I_{cn}}{y} \tag{A.4}$$

y is the centroid of the round connector which is obtained as $D/2$, where D is the connector diameter. Equating Eq. A.3 to A.4, the maximum bending stress is obtained as Eq. A.5.

$$f_u = \frac{3E_b D s_l}{X^2} \tag{A.5}$$

From Eq. A.5, substitute $E_b = f_u X^2/(3Ds_l)$ into the left hand side of Eq. 5.2 to have the right hand side of Eq. 5.2;

$$P_L \leq \frac{4f_u D I_{cn}}{XD}$$

The maximum shear stress in the connector ($\boldsymbol{\tau_{max}}$) due to shear force (P_L), is at the middle (Fig. A.1c) and obtained using Eq. A.6

$$\boldsymbol{\tau_{max}} = \frac{kP_L}{A_{cn}} \tag{A.6}$$

A_{cn} is the cross sectional area of the connector, k is a constant accounting for the ratio of the maximum and average shear stress which equals 1.33 for circular cross-sections. From Mohr's Circle (Fig. A.1c,d) the maximum shear stress ($\boldsymbol{\tau_{max}}$) is equal to the principal tensile stress (σ_1), and when the tensile strength of the FRP resin ($\boldsymbol{f_{u,rn}}$) is reached, the FRP experiences shear failure. Therefore, replacing $\boldsymbol{\tau_{max}}$ with $\boldsymbol{f_{u,rn}}$ in Eq. A.6, we obtain the right hand side of Eq. 5.3:

$$P_L \leq \frac{A_{cn} f_{u,rn}}{k}$$

For the inclined connector (Fig. A.2), the stress in Eq. 5.4 is a combination of the axial contribution of the connector as well as bearing action. The axial stress (f_{ax}) is obtained as $E_l \varepsilon_{cn}$, where ε_{cn} is

the axial strain and obtained as l_{ax}/L. The axial extension (l_{ax}) is obtained using Eq. A.7 and the axial stress (f_{ax}) is shown in Eq. A.8.

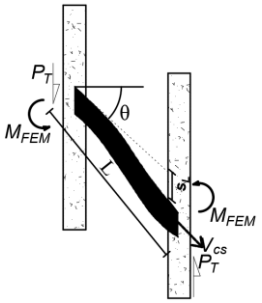

Figure A.2: Inclined connector

$$l_{ax} = \frac{\sqrt{(X\tan\theta + s_L)^2 + (X)^2} - L}{L} \tag{A.7}$$

$$f_{ax} = E_l\left(\frac{\sqrt{(X\tan\theta + s_L)^2 + (X)^2} - L}{L}\right) \tag{A.8}$$

E_l is the longitudinal modulus of elasticity. Adding the axial $(f_{ax}, \text{Eq. A. 8})$ and bending $(f_u, \text{Eq. A. 5})$ stresses, and multiplying by the connector cross-sectional area (A_{cn}) we have the strength of the connector (V_{cs}, Eq. A.9);

$$V_{cs} = \left(E_l\left(\frac{\sqrt{(X\tan\theta + s_L)^2 + (X)^2} - L}{L}\right) + \frac{3E_bD}{X^2}s_L\right)A_{cn} \tag{A.9}$$

Resolving V_{cs} in the direction of shearing, we arrive at P_T(Eq. 5.4)

$$P_T = \left(E_l\left(\frac{\sqrt{(X\tan\theta + s_L)^2 + (X)^2} - L}{L}\right) + \frac{3E_bD}{X^2}s_L\right)A_{cn}\sin\left(tan^{-1}\left(\frac{X\tan\theta + s_L}{X}\right)\right)$$

APPENDIX B: DESIGN EXAMPLE FOR INSULATED CONCRETE WALL UNDER FLEXURAL LOADING

Table B.1 shows parameters for a design example (baseline panel used in the parametric analysis) showing how the model generates the load-displacement curve. The loading set up as well as output from the model are shown in Fig. B.1.

Table B.1: Parameters for design example

E_s (MPa)	200000	h_1 (mm)	75
Span (mm)	3200	h_2 (mm)	75
t_{is} (mm)	75	d_2 (mm)	37.5
f_y (MPa)	400	f_c' (Mpa)	50
d_1 (mm)	37.5	Connector spacing, (mm)	300
A_{s1} (mm2)	562.5	Panel width (mm)	1000
A_{s2} (mm2)	562.5	Connector diameter (mm)	10
Connector inclination (degrees)	0	Connector material	GFRP
E_b (MPa)	60800	Connector length (mm)	176.8
$f_{u,c}$ (MPa)	781	I_{cn}	491
$f_{u,rn}$ (MPa)	70	Connectors per location	2

1. Apply a load P = 8 kN (sample load, Fig. B.1a) and obtain moment profile (Fig. B.1b)
2. Assume a slip, s_l (converged slip for illustration in Fig. B.1c)
3. Obtain shear connector force (multiplied by 2 since two connectors per location)

$$V_{cn} = \begin{pmatrix} V_{cn,1} \\ V_{cn,2} \\ V_{cn,3} \\ V_{cn,4} \\ V_{cn,5} \end{pmatrix} = \frac{12E_bI_{cn}}{L^3}s_l = 2 \times \begin{pmatrix} \frac{12(60800)(491)}{176.8^3} \times 1.36 \\ \frac{12(60800)(491)}{176.8^3} \times 1.33 \\ \frac{12(60800)(491)}{176.8^3} \times 1.25 \\ \frac{12(60800)(491)}{176.8^3} \times 1.14 \\ \frac{12(60800)(491)}{176.8^3} \times 0.71 \end{pmatrix} = \begin{pmatrix} 180 \\ 170 \\ 160 \\ 150 \\ 90 \end{pmatrix} \text{N}$$

Check if the end connector has failed. For flexure controlled failure the maximum force is obtained as:

$$P_{L,max} = \frac{4f_{u,c}I_{cn}}{LD} = \frac{4(781)(491)}{176.8(10)} = 870 \text{ N}$$

For shear controlled failure the maximum shear force is obtained as:

$$P_{L,max} = \frac{f_{u,rn}A_{cn}}{k} = \frac{70(78.5)}{1.33} = 4130 \text{ N}$$

The slip at which the connector will fail, governed by flexure failure, is obtained as;

$$\frac{12 \times 60800 \times 491}{176.8^3} \times s_{l,max} = 870$$

$$s_{l,max} = 13.4 \text{ mm}$$

4. The connector load-slip response is shown in Fig. B.1d.
5. Aggregate shear contribution at the middle ($V_{cn,T}$) of the panel (Fig. B.1e)

$$V_{cn,T} = V_{cn,1} + V_{cn,2} + V_{cn,3} + V_{cn,4} + V_{cn,5}$$

90+150+160+170+180=750 N

6. Correlating the moment value at each location to the moment-strain relationship (process for connector at the middle shown in Fig. B.1f), the strain discontinuity (ε_{sc}) profile from the middle of the panel (0 mm) is shown in Fig. B.1g.
7. Sum areas under the strain discontinuity profile to obtain a new slip profile (calculation for end-connector shown here). Note that if the new slip values at each connector location are different from that in Step 2 of this Appendix, a new slip value is assumed again in Step 2 and the process is re-evaluated until the slip converges (converged slip assumed already in Step 2).

$\left[(1500-1200)\frac{(\varepsilon_{sc,2}+\varepsilon_{sc,1})}{2}\right]+\left[(1200-900)\frac{(\varepsilon_{sc,3}+\varepsilon_{sc,2})}{2}\right]+\left[(900-600)\frac{(\varepsilon_{sc,4}+\varepsilon_{sc,3})}{2}\right]+\left[(600-300)\frac{(\varepsilon_{sc,5}+\varepsilon_{sc,4})}{2}\right]+\left[(300-0)\frac{(\varepsilon_{sc,5}+\varepsilon_{sc,5})}{2}\right] = 1.36$ mm

(where $\varepsilon_{sc,1} = 4.63 \times 10^{-5}, \varepsilon_{sc,2} = 1.85 \times 10^{-4}, \varepsilon_{sc,3} = 3.23 \times 10^{-4}, \varepsilon_{sc,4} = 4.62 \times 10^{-4}, \ \varepsilon_{sc,5} = 2.37 \times 10^{-3}$)

8. The curvature ($\boldsymbol{\varphi}$) at connector locations is obtained as Fig. B.1h.
9. Integrate curvature to get deflection. For instance, using the moment area method where curvature is broken into 10 shapes (Fig B.1h) as;

$(0.5\times100\times\boldsymbol{\varphi_1}\times(\frac{2}{3}\times100)) + (300\times\boldsymbol{\varphi_1}\times250) + (0.5\times(\boldsymbol{\varphi_2}-\boldsymbol{\varphi_1})\times300\times((\frac{2}{3}\times300)+100)) + (\boldsymbol{\varphi_2}\times300\times550) + (0.5\times(\boldsymbol{\varphi_3}-\boldsymbol{\varphi_2})\times300\times((\frac{2}{3}\times300)+400)) + (300\times\boldsymbol{\varphi_3}\times850) + (0.5\times(\boldsymbol{\varphi_4}-\boldsymbol{\varphi_3})\times300\times((\frac{2}{3}\times300)+700)) + (0.5\times(\boldsymbol{\varphi_5}-\boldsymbol{\varphi_4})\times300\times((\frac{2}{3}\times300)+1000)) + (\boldsymbol{\varphi_4}\times300\times1150) + (\boldsymbol{\varphi_5}\times300\times1450) = 11.3$ mm

(where $\boldsymbol{\varphi_1} = 3.13 \times 10^{-7}$ mm^{-1}, $\boldsymbol{\varphi_2} = 1.25 \times 10^{-6}$ mm^{-1}, $\boldsymbol{\varphi_3} = 2.19 \times 10^{-6}$ mm^{-1}, $\boldsymbol{\varphi_4} = 3.13 \times 10^{-6}$ mm^{-1}, $\boldsymbol{\varphi_5} = 1.58 \times 10^{-6}$ mm^{-1})

Therefore, for a value of P (8 kN), the load (**2P**) and deflection values are obtained as 16 kN and 11.3 mm, respectively.

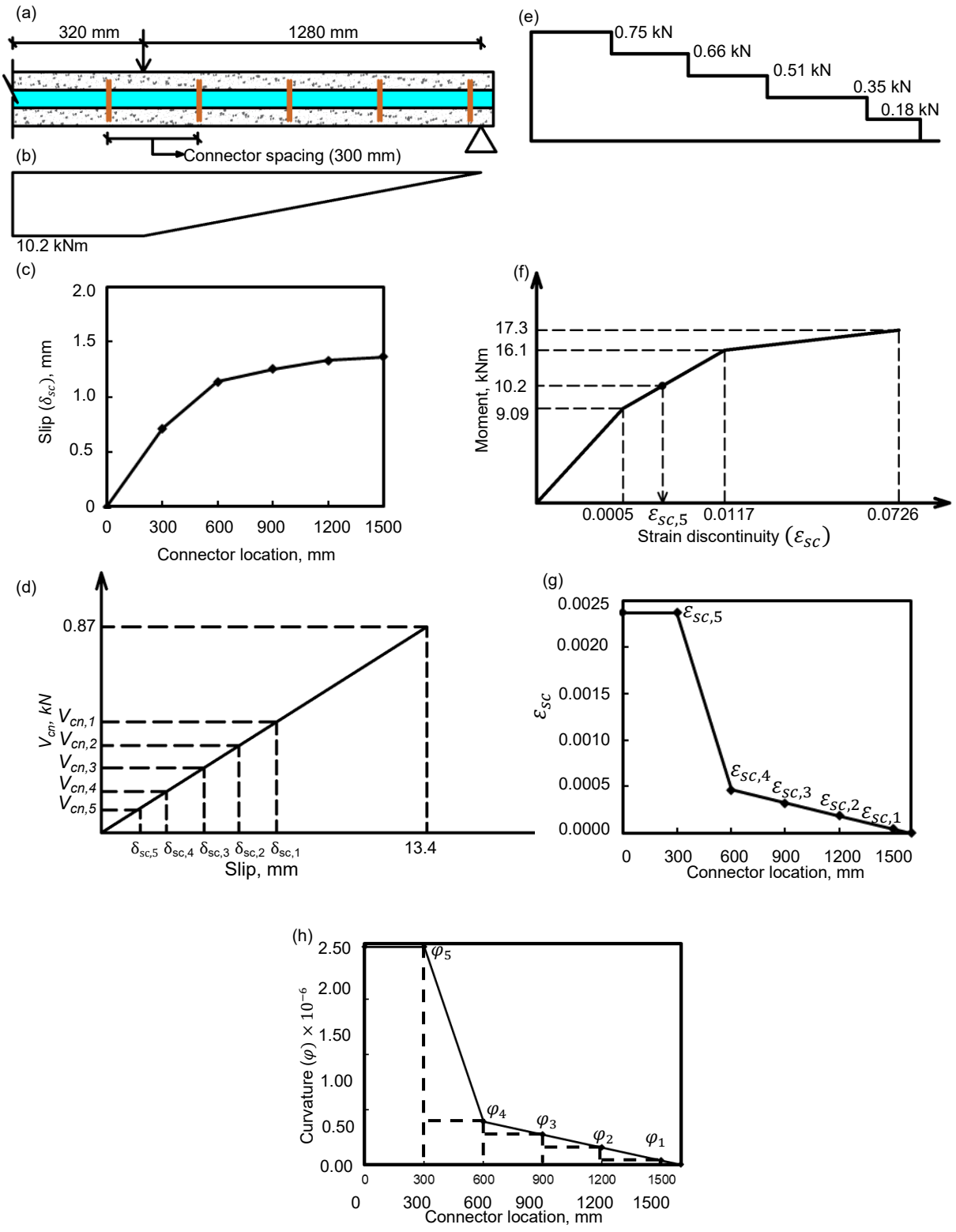

Figure B.1: Output of design example

APPENDIX C: FORMULATIONS FOR THE LOAD-SLIP RESPONSE OF MASONRY CONNECTORS

This section shows formulation used in predicting the load slip response of connectors in masonry walls.

The load-slip relationship for the connectors is presented as follows.

A.1. Connector buckling

For connectors under compression the buckling capacity is obtained using Eq. C.1.

$$P_b = \frac{\pi^2 E_{cn} I_{cn}}{(KL)^2} \tag{C.1}$$

K is a factor accounting for end condition.

A.2. Connector yielding

The tension capacity of a connector ($V_{y,T}$) can be estimated using Eq. C.2.

$$V_{y,T} = A_{cn} f_y \tag{C.2}$$

A_{cn} is the cross -sectional area of the connector.

A.3. Lateral torsional buckling

The end force due to lateral torsional buckling ($V_{L,T}$) can be estimated using Eq. C.3.

$$V_{L,T} = \frac{\pi \omega_2}{L^2} \sqrt{E I_y G J} \tag{C.3}$$

G, J are the shear modulus and St. Venant torsional constant. ω_2 is the equivalent moment factor to account for a beam with unequal end moments, taken as 1.75 (Nethercot and Trahair 1976).

A.4. Pullout capacity

The pullout capacity, Eq. C.4, (force needed to create an outward sliding of the connector when bond is lost with mortar) was initially developed by Kuhn and Shaikh (1996) for the pullout strength of anchors embedded in masonry.

$$V_{pT} = \sqrt{f_{mr}}\left(0.15\pi D(l_{hk} + l_{em} + D) + \left(1.5\sqrt{f_{mr}} D l_{hk}\right)\right) \quad \text{(C.4)}$$

f_{mr} is the mortar strength, $l_{hk}, l_{em}, D,$ are the hooked length, embedded length, and diameter of the connector.

A.5. Mortar breakout

The mortar breakout capacity (outward formation of a cone-like shape of mortar as the connector tries to slide outward) is evaluated using Eq. C.5 based on provisions in TMS 402/602 (2016).

$$V_{br} = 0.33\sqrt{f_{mr}} A_{pt} \quad \text{(C.5)}$$

where A_{pt} is the projected tension breakout area, obtained using Eq. C.6.

$$A_{pt} = 2l_{em}t + {l_{em}}^2\left(\frac{\pi\theta}{180} - sin\,\theta\right) \quad \text{(C.6)}$$

where θ is the angle of breakout, obtained using Eq. C.7.

$$\theta = 2\,sin^{-1}\left(\frac{0.5t}{l_{em}}\right) \quad \text{(C.7)}$$

t is the thickness of the mortar joint.

APPENDIX D: DESIGN EXAMPLE FOR DOUBLE WYTHE CAVITY MASONRY WALL UNDER FLEXURAL LOADING

Table D.1 shows parameters for a design example using the novel connector in a wall under pressure. It also shows how the model generates the load-displacement curve. The loading set up as well as output from the model are shown in Fig. D1.

Table D.1: Parameters for design example

E_s (MPa)	200000	t_c (mm)	20
h_w (mm)	3000	t_c (horizontal direction, mm)	3
t_{bl} (mm)	190	f'_m (brick, MPa)	16
t_{br} (mm)	90	f'_m (CMU, MPa)	13
t_{cj} (mm)	175	f'_m (grout, MPa)	10
Rebar	15M	f_{mr} (brick, MPa)	16
E_{cn} (connector, MPa)	194000	f_t (brick, MPa)	0.65
f_y (rebar, MPa)	400	f_t (CMU, MPa)	0.4
f_y (connector, MPa)	234	f_t (grout, MPa)	0.65
l_{em} (mm)	45	Connector vertical spacing, (mm)	600
l_{hk} (mm)	45	Connector horizontal spacing, (mm)	600
D (mm)	4.8	Rebar spacing (mm)	600
Connector inclination (θ_1, degrees)	36	Rebar material	Steel

Check connector's axial stiffness against wall bending stiffness;

$$\frac{E_{cn}A_{cn}}{X} = \frac{194000 \times 60}{175} = 66.5 \text{ kN/mm}$$

$$\frac{E_{wythe}I_{wythe}}{{h_w}^3} = \frac{13600 \times 36450000}{3000^3} = 0.018 \text{ kN/mm}$$

Therefore, connector has sufficient axial stiffness to transmit out of plane load.

Derive connector response;

Checking the connector part in compression against elastic buckling (Eq. C.1), using effective length factors of 0.7 and 0.8 which are the theoretical and recommended design value of K for a fixed-hinged beam, respectively.

$$P_b = \left(\frac{\pi^2(194000)(45)}{(0.7 \times 215)^2}\right)\sin(36) = 2.24 \text{ kN}$$

$$P_b = \left(\frac{\pi^2(194000)(45)}{(0.8 \times 215)^2}\right)\sin(36) = 1.71 \text{ kN}$$

The tension capacity of the connector ($V_{y,T}$) using Eq. C.2;

$$V_{y,T} = (60 \times 234)\sin(36) = 8.17 \text{ kN}$$

Checking the pullout capacity of the embedment tie (V_{pT}), Eq. C.4;

$$V_{pT} = \sqrt{16}\left(0.15 \times \pi \times 4.8(45 + 45 + 4.8) + \left(1.5 \times \sqrt{16} \times 4.8 \times 45\right)\right) = 6.04 \text{ kN}$$

Checking the connector against lateral torsional buckling ($V_{L,T}$), using Eq. C.3;

$$V_{L,T} = \left(\frac{\pi \times 1.75}{215^2}\sqrt{194000 \times 45 \times 80833 \times 180}\right)\cos 36 = 1.08 \text{ kN}$$

Checking the connector (upper inclined part) against flexural bending (V_{FE}), Eq. 6.2;

$$V_{FE} = \left(\frac{2 \times 234 \times 2000}{215 \times 20}\right)\cos 36 = 0.18 \text{ kN}$$

Checking the slip (s_{l1}) at which this occurs;

$$s_{l1} = \frac{0.18 \times 215^3 \times 1000}{3 \times 194000 \times 2000} = 1.5 \text{ mm}$$

Checking the mortar breakout capacity (Eq. C.5,C.6,7);

$$\theta = 2\sin^{-1}\left(\frac{0.5 \times 10}{45}\right) = 12.8^{\circ}$$

$$A_{pt} = (2 \times 45 \times 10) + 45^2\left(\frac{\pi \times 12.8}{180} - \sin 12.8\right) = 904 \text{ mm}^2$$

$$V_{br} = 2 \times \left(0.33 \times \sqrt{16} \times 904\right) = 2.45 \text{ kN}$$

(multiplied by 2 because of the two legs of the embedment tie)

From the computations above, the breakout capacity is lesser than the yield strength of the inclined member, and the slip at which this occurs can be obtained using Eq. 6.3

$$2450 = \left(194000\left(\frac{\sqrt{(175\tan 36 + s_l)^2 + (175)^2} - 215}{215}\right) + \left(\frac{1.5 \times 194000 \times 20}{175^2}\right)s_l\right)60\sin\left(\tan^{-1}\left(\frac{175\tan 36 + s_l}{175}\right)\right)$$

$$s_{l2} = 0.11 \text{ mm}$$

1. Apply a load w = 9 kN/m^2 (sample load, Fig D.1a) and obtain moment (kN.m/m) profile (Fig D.1b)

2. Check if connector fails under axial compression. For the 9 kN/m^2 external load over the 3 m high wall and 600 mm horizontally spaced connectors, the reaction per end-connector is obtained as;

$$= \frac{9(3)(0.6)}{4} = 4.05 \text{ kN}$$

This reaction value is less than the connector's compressive strength which was obtained from compression tests at the University of Alberta as 8.7 kN.

3. Assume a slip, s_l (converged slip for illustration in Fig. D.1c)

4. Obtain shear connector force at connector location (Fig. D.1d)

$$V_{cn} = \begin{pmatrix} V_{cn,1} \\ V_{cn,2} \\ V_{cn,3} \end{pmatrix} = 2 \begin{pmatrix} 1000 \\ 2450 \\ 2450 \end{pmatrix} = \begin{pmatrix} 2000 \\ 4900 \\ 4900 \end{pmatrix} \text{N}$$

5. Aggregate shear contribution at the middle ($V_{cn,T}$) of the wall (Fig. D.1e)

$$V_{cn,T} = V_{cn,1} + V_{cn,2} + V_{cn,3}$$

$$4900+4900 + 2000=11.8 \text{ kN}$$

6. Correlating the moment value at each location to the moment-strain relationship (process at the middle of wall shown in Fig. D.1f), the strain discontinuity (ε_{sc}) profile from the middle of the wall (0 mm) is shown in Fig. D.1g.

7. Sum areas under the strain discontinuity profile to obtain a new slip profile due to primary load (calculation for end-connector shown here). Note that if the new slip values at each connector location are different from that in Step 2 of this Appendix, a new slip value is assumed again in Step 2 and the process is re-evaluated until the slip converges (converged slip assumed already in Step 2).

$$\left[(1300-700)\frac{(\varepsilon_{sc,2}+\varepsilon_{sc,1})}{2}\right]+\left[(700-100)\frac{(\varepsilon_{sc,3}+\varepsilon_{sc,2})}{2}\right]+\left[(100-0)\frac{(\varepsilon_{sc,3}+\varepsilon_{sc,3})}{2}\right]=2.92\text{ mm}$$

(where $\varepsilon_{sc,1}=1.30\times10^{-4},\varepsilon_{sc,2}=2.37\times10^{-3},\varepsilon_{sc,3}=3.65\times10^{-3}$)

8. The curvature (φ) due to primary load at connector locations is obtained as Fig. D.1h.

9. Integrate curvature to get primary deflection (Δ_0). For instance, using the moment area method where curvature is broken into 7 shapes (Fig D.1h) as;

(0.5×200×φ_1×($\frac{2}{3}$×200)) + (600×φ_1×500) + (0.5× (φ_2 - φ_1) ×600× 600) + (φ_2×600×1100) + (0.5×(φ_3 − φ_2)×600×1200) + (100×φ_3×1450) + (0.5× ($\varphi_4-\varphi_3$) ×100× (($\frac{2}{3}$×100)+1400)) = 11.3 mm (where $\varphi_1=0.43\times10^{-6}$ mm^{-1}, $\varphi_2=9.59\times10^{-6}$ mm^{-1}, $\varphi_3=14.8\times10^{-6}$ mm^{-1}, $\varphi_4=14.9\times10^{-6}$ mm^{-1})

10. Account for secondary effect due to self-weight. At middle of wall, the self-weight (P_{sw}, N/m) is obtained as;

$$P_{sw}=\big((0.6\times0.19\times0.6\times2100)+(0.2\times0.19\times0.4\times2100)+(0.6\times0.09\times2000)\big)\times3\times\frac{9.81}{0.6}\times\frac{1.5}{3}=6954.3\text{ N/m}$$

At connector locations, the self-weight is obtained as;

$$\begin{pmatrix}P_{sw,mid}\\P_{sw,1}\\P_{sw,2}\\P_{sw,3}\end{pmatrix}=\begin{pmatrix}6954\\6540\\3760\\974\end{pmatrix}\text{N/m}$$

11. Obtain effective wall stiffness (Nm^2/m) at connector locations (Fig. D.1i, middle of wall shown)

12. Using the P − δ to obtain secondary deflection (Δ_1) at middle of wall;

$$\Delta_{1,mid}=\frac{5P_{sw}(\Delta_{0,mid}+\Delta_{1,mid})h_w^2}{48EI_{eff}}=\frac{5\times6954\,(0.011+\Delta_{1,mid})\times3^2}{48\times534277}$$

Iterating, $\Delta_{1,mid}=0.00014$ m

Total deflection is obtained as;

$$\Delta_{0,mid}+\Delta_{1,mid}=0.0113+0.00014=11.4\text{ mm}$$

Secondary moment at middle of wall and other locations is obtained as;

$$\begin{pmatrix} 72.5 \\ 53.7 \\ 6.75 \\ 0.01 \end{pmatrix} \mathrm{Nm/m}$$

Check additional slip on connectors from secondary moments

Repeating steps 2 to 5 of the model and the additional slip is obtained as;

$$\begin{pmatrix} 0.0000 \\ 0.0003 \\ 0.0011 \\ 0.0014 \end{pmatrix} \mathrm{mm}$$

Therefore, for a value of $\mathrm{w} = 9\ \mathrm{kN/m^2}$ the total deflection is 11.4 mm.

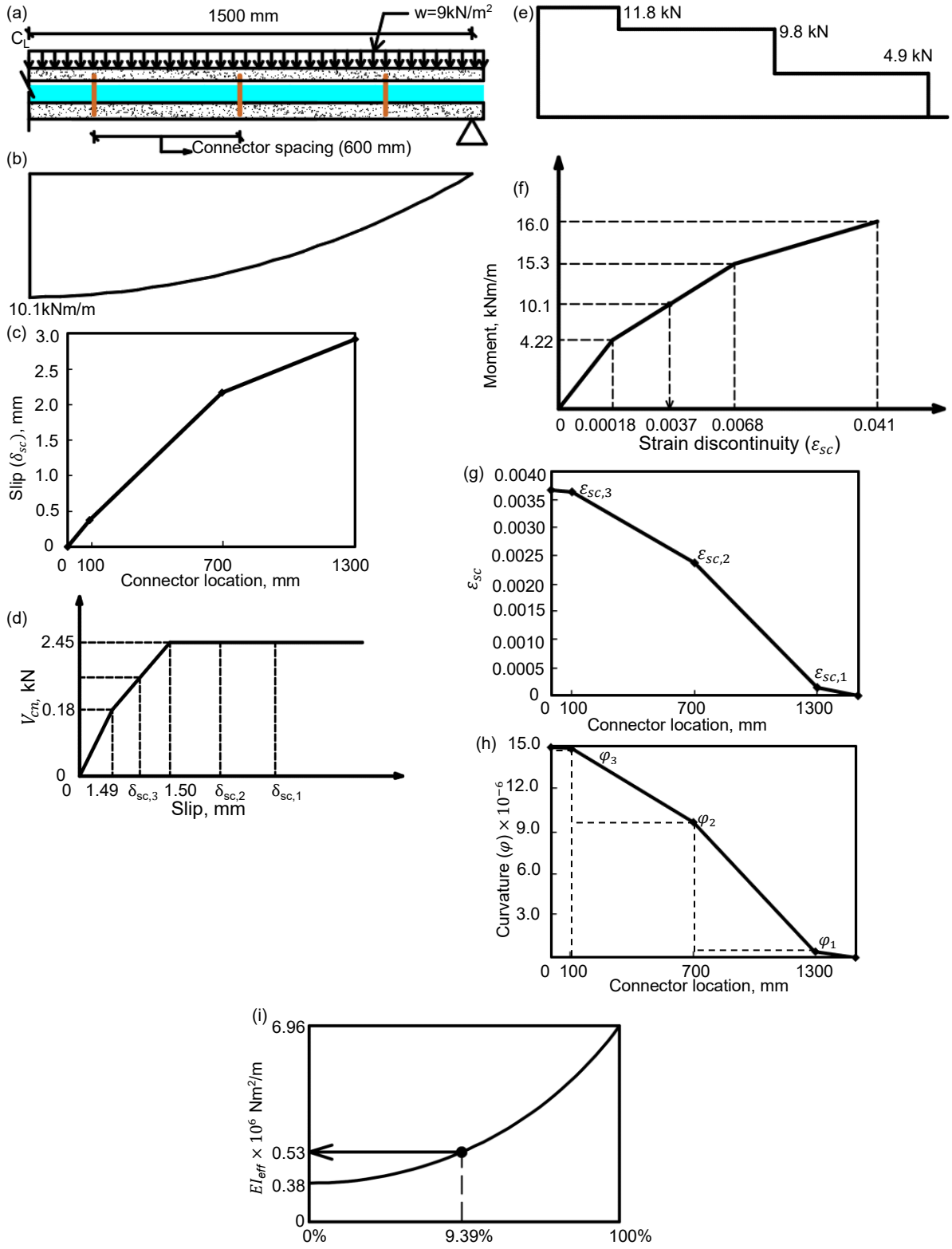

Figure D.1: Output of design example